# The use of Design of Experiments and Machine Learning to Optimise 3D Bioprinted bone repair Scaffolds




Ghayadah Al-Kharusi, BSc

Submitted for the degree of Doctor of Philosophy

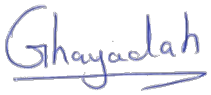
School of Mechanical and Manufacturing Engineering
Dublin City University

Supervised by:
Dr Tanya Levingstone
Prof. Nicholas Dunne
Prof. Suzanne Little

April 2024

# Declaration

I hereby certify that this material, which I now submit for assessment on the programme of study leading to the award of PhD is entirely my own work, and that I have exercised reasonable care to ensure that the work is original, and does not to the best of my knowledge breach any law of copyright, and has not been taken from the work of others save and to the extent that such work has been cited and acknowledged within the text of my work.

Signed:  ID No.: 15103579 Date: 20/08/2024

# Acknowledgement

Embarking on this PhD journey has been one of the most challenging yet rewarding experiences of my life. The completion of this thesis marks not just an academic achievement, but a personal milestone shaped by the unwavering support and encouragement of those around me. Foremost, my deepest gratitude to my husband Saif, whose patience, understanding, and belief in my capabilities have been unwavering. Your support extended beyond the personal sacrifices, providing me with both the space and the encouragement to pursue my research even when it demanded long hours and constant focus.

To my parents, who taught me the value of determination and education, thank you for your endless love and support. To my entire family, who have cheered me especially my sister and best friend AlAnoud, your faith in me has been a source of constant motivation. This thesis is dedicated to the memory of my siblings (Ibrahim, Zakiya and Saeed) whose absence has been a profound silence in my life during this journey. I honour your memory today and always, carrying forward the light of your spirits in this accomplishment.

To the friends who have become family John, Halima, Goli, Sen, Angela, Nicoletta, Beth and Srishti thank you for understanding the trials that this path entails, for the laughter that eased the stress, and for always being a call away when I needed a break from the demands of research. Lastly, Thanks to my supervisors for all the guidance. I would like to sincerely thank the CRT-AI group especially Angela Lally for being there for us till the end. My appreciation also goes to the GIOTTO group for the invaluable internship experience and for facilitating the collaboration with Politecnico Di Torino, which was instrumental in providing the data necessary for my work.



## Research Publications

### Journal Articles

(1) S. McGivern, H. Boutouil, **G. Al-Kharusi,** S. Little, N. J. Dunne, and T. J. Levingstone, "Translational Application of 3D Bioprinting for Cartilage Tissue Engineering," *Bioengineering*, vol. 8, no. 10, p. 144, 2021, doi: 10.3390/bioengineering8100144.

(2) **G. Al-Kharusi,** N. J. Dunne, S. Little, and T. J. Levingstone, "The Role of Machine Learning and Design of Experiments in the Advancement of Biomaterial and Tissue Engineering Research," *Bioengineering*, vol. 9, no. 10, 2022, doi: 10.3390/bioengineering9100561

This paper highlights the significant impact ML and DoE methodologies have on the field of tissue engineering. It demonstrates how the fusion of ML with DoE can lead to the refined design and predictive analysis of biomaterials, addressing a critical gap in traditional experimental approaches. This work underlines the importance of a collaborative computational and experimental framework, which can streamline scaffold optimisation, enhance material characterisation.

(3) I. Corvaglia, **G. Al- Kharusi**, F. Banche- Niclot, A. Manca, T. j. Levingstone, S. Little, S.Fioril li, N. Dunne , C. Vitale-Brovaron "Comprehensive study through imaging techniques of the degradation of a resorbable calcium sulphate-based composite bone cement," Open Ceramics, vol. 17, Mar. 2024, doi: 10.1016/j.oceram.2024.100542.

The image analysis program developed using Python has significantly improved the assessment of scaffold degradation rates. Its rapid and precise measurements are instrumental in understanding scaffold behaviour using micro-CT images, providing a foundation for further computational analysis in biomaterial research.

### Conferences

(1) Oral podium presentation **'Collagen Bioink Optimisation or 3D Bioprinting Using Artificial Intelligence**'. 26th Annual BINI Conference, Mount Wolseley, Carlow (Jan-2020).

(2) Virtual oral presentation **'Application of Image Analytics to Assess the Degradation Rate of 3D Bioprinted Scaffolds'**. 31st Conference of the European Society of Biomaterials (ESB), (Sep- 2021).

(3) Podium poster presentation **'3D Bioprinted Scaffold Degradation Study Using Image Analytics'**. Worlds Biofabrication Conference 2022 (Pisa), (Sep-2022).

(4) Oral podium presentation **'Assessment of the Degradation Rate of 3D Bioprinted Collagen- Based Scaffolds Using Image Analytics and Machine Learning**'. 27th Annual BINI Conference, Enfield, Co. Meath (Jan-2023)

# Table of Contents

*Declaration* ..... *III*

*Acknowledgement* ..... *V*

**Research Publications** ..... **VII**

**Journal Articles** ..... VII

**Conferences** ..... VII

*Nomenclature* ..... *XV*

*Abstract* ..... *XXXVII*

*1. Chapter 1: Introduction* ..... *1*

**1.1. Introduction** ..... **2**

**1.2. Objectives** ..... **4**

**1.3. Thesis outline** ..... **5**

*2. Chapter 2: Literature review* ..... *7*

**2.1. Bone** ..... **9**

**2.1.1. Bone structure** ..... 9

**2.1.2. Natural bone repair** ..... 12

**2.1.3. Bone defects** ..... 13

**2.2. Tissue Engineering (TE)** ..... **14**

**2.2.1. Freeze-drying** ..... 14

**2.2.2. Electrospinning** ..... 15

**2.2.3. Injectable cements** ..... 15

**2.2.4. 3D Bioprinting** ..... 15

**2.3. Design of Experiments (DoE)** ..... **29**

**2.3.1. Factorial experiments** ..... 31

**2.3.2. Taguchi Designs** ..... 32

**2.3.3. Response Surface Methodology (RSM)** ..... 32

**2.3.4. Statistical Tools** ..... 34

**2.3.5. Comparison of the DoE Techniques** ..... 34

**2.4. Application of DoE Methods in Biomaterials and TE Research** ..... **34**

**2.5. Machine Learning** ..... **36**

**2.5.1. Supervised Learning** ..... 37

**2.6. Applications of ML in Biomaterials and TE Research ..... 41**

**2.7. Classical ML Techniques Compared with DoE Methods ..... 46**

**2.8. Research Gap ..... 49**

***3. Chapter 3: Development and Optimisation of a 3D bioprinted collagen-hydroxyapatite scaffold using Design of Experiments ..... 51***

**3.1. Introduction ..... 52**

**3.1.1. Chapter Aims** ..... 53

**3.2. Materials and methods ..... 53**

**3.2.1. Ink preparation** ..... 53

**3.2.2. 3D Bioprinting** ..... 55

**3.2.3. Crosslinking** ..... 56

**3.3. Characterisation Methods ..... 57**

**3.3.1. Ink characterisation methods** ..... 57

**3.3.2. Scaffold characterisation method** ..... 63

**3.3.3. Statistical analysis** ..... 67

**3.3.4. DoE Methodology** ..... 67

**3.4. Study 1 Results and Discussion ..... 69**

**3.4.1. Study 1: Ink characterisation** ..... 69

**3.4.2. DoE Study 1 Optimisation of COL ink formulation and scaffold properties** ..... 74

**3.5. Study 2 Results and Discussion ..... 95**

3.5.1. Study 2: Ink characterisation ..... 95

**3.5.2. DoE Study 2: COL/HA printing parameter optimisation** ..... 110

**3.6. Conclusion ..... 131**

***4. Chapter 4: Predicting degradation of three tissue engineering scaffold applications from image data using convolutional neural network (CNN) model and Long short-term memory (LSTM) ..... 133***

**4.1. Introduction ..... 134**

**4.1.1. Chapter Aims** ..... 135

**4.2. Methodology ..... 136**

4.2.1. Material fabrication ..... 136

**4.2.2. Data collection** ..... 139

**4.2.3. Image analysis method** ..... 140

**4.2.4. ML application to predict scaffold degradation** ..... 142

**4.3. Results and Discussion** ..... **151**

**4.3.1. Computational vs traditional methods (Image analysis tool)** ..... 151

**4.3.2. CNN and LSTM models** ..... 159

**4.4 Conclusions** ..... **164**

***5. Chapter 5: Predicting pore sizes and porosity in Micro-CT images of degraded injectable cements using CNN model*** ..... ***166***

**5.1. Introduction** ..... **168**

**5.1.1. Chapter Aims** ..... 168

**5.2. Methodology** ..... **169**

**5.2.1. Sample fabrication** ..... 169

**5.2.2. *In vitro* degradation test** ..... 170

**5.2.3. Micro-CT images** ..... 170

**5.2.4. Pore detection and porosity measurements using image analysis tool** ..... 170

**5.2.5. CNN model to predict pore sizes and porosity** ..... 172

**5.3. Results and Discussion** ..... **176**

**5.3.1. Image analysis tool** ..... 176

**5.3.2. CNN evaluation** ..... 178

**5.4. Conclusion** ..... **181**

***6. Chapter 6: Overall thesis discussion, conclusions and future work*** ..... ***183***

**6.1. Overall discussion** ..... **184**

**6.2. Concluding Remarks** ..... **186**

***References*** ..... ***188***

***Appendix A*** ..... ***215***

**Plus test G-code** ..... **215**

***Appendix- B*** ..... ***216***

# Nomenclature

| | |
|---|---|
| 3D | Three-Dimensional |
| ANN | Artificial neural networks |
| BO | Bayesian optimisation |
| CNN | Convolutional neural network |
| DoE | Design of Experiments |
| ECM | Extracellular Matrix |
| FT-IR | Fourier-transform infrared spectroscopy |
| HA | hydroxyapatite |
| hr | hour |
| LAB | Laser-assisted bioprinting |
| Micro-CT | |
| min | minute |
| ML | Machine learning |
| MRI | Magnetic resonance imaging |
| PBS | Phosphate Buffer Saline |
| RPM | Revolutions per minute |
| RSM | Response Surface Methodology |
| SEM | Scanning Electron Microscope/Microscopy |
| SLSQP | Sequential Least Squares Programming |
| TE | Tissue engineering |
| β-TCP | Beta-tricalcium phosphate |

## Units

| | |
|---|---|
| °C | Degrees Celsius |
| cm/mm/µm/nm | Centimetre / Micrometre / Micrometre / Nanometre |
| $cm^2$ | Centimetre squared |
| $g/cm^3$ | Grams per centimetre cubed |
| kPa | Kilopascals |
| mg/mL | Milligrams per millilitre |
| N | Newton |
| Pa | Pascal |
| % (w/v) | Weight per volume percentage |

# Table of Figures

**Figure 1.1:** Schematic representation of the DoE and ML workflow to optimise the material that will be used for the TE applications. ..... 4

**Figure 1.2**: Outline of this thesis including a more detailed description. ..... 6

Figure 2.1: Bone composition composed of three parts organic, water and minerals, adapted from [4]. ..... 9

**Figure 2.2:** Long bone anatomy schematic showing diaphysis and epiphysis regions [34]. ..... 10

**Figure 2.3**: Overall schematic of the periosteum and endosteum of the bone [34]. ..... 11

**Figure 2.4:** Four different cell categories can be found within the bones such as osteocyte, osteoblast, osteogenic and osteoclast [34]. ..... 11

**Figure 2.5:** The four stages of bone repair and remodelling, including the hematoma and granulation process at the fracture site followed by the development of cartilaginous and bony callus leading to the final stage which is the bone remodelling. ..... 13

**Figure 2.6:** Bioprinting methods used to build 3D scaffolds., for instance Inkjet bioprinting deposits drop-by-drop method, extrusion- based bioprinting deposits hydrogels via applied force or air pressure, and laser-assisted bioprinting method. ..... 19

**Figure 2.7:** A framework for sequentially characterising 3D bioprinting, from assessing ink properties to evaluating scaffold performance..... 25

**Figure 2.8:** Rheological behaviour that affects the bioinks fidelity. A) The evaluation of the bioinks shear stress and viscosity using cone-and-plate rheometer. B) The effect of loss tangent parameter on the filament uniformity. C-D) The effect of bioinks viscosity on cell viability where the pink represents the dead cells and green illustrates the live cells (C) shows bioinks with low viscosity and (D) high viscosity bioinks [131]. ..... 27

**Figure 2.9:** The influence of print speed on the scaffold printing quality. a) Schematic illustrating standard printing on a flat surface, showing the push and pull forces between the deposited ink and the ink yet to be deposited. b) Diagram of a proposed parallel line model. c) Example images of printed structures with various configurations of $v_{ink}$ and$v_{noz}$. [134]. ..... 27

**Figure 2.10:** DoE workflow for the process optimisation. ..... 31

**Figure 2.11:** P-diagram. A P-diagram is used to classify the variables associated with the product into input energy, signal or user intent (M), noise factors (Z), design parameters (X) and output/key product characteristics, functions, performance, etc. (Y). ..... 32

**Figure 2.13:** Number of experimental runs required for each design for 3 factors investigated at 3 levels. ..... 33

**Figure 2.14:** Overview of the ML types that can be used for different applications, supervised, unsupervised and reinforcement learning. ..... 37

**Figure 2.15:** Schematic diagram of the input data (from the material characterisation results) and the output prediction using ML methods [24]. ..... 43

**Figure 2.16:** (A) Three-dimensional bioprinting optimisation processes. (B) Computer vision method used for the optimisation and correction of 3D bioprinting using ML approaches [18]. .... 45

**Figure 2.17:** Summarised workflow, describing the link between ML and the DoE, where the DoE data is being used as an input for the ML model. Active learning can occur when the ML result is used as an input suggestion to design a new experiment [218]. ..... 48

**Figure 2.18:** Core processes for the Design of DoE and ML, including human and software-based parts [216]. ..... 49

**Figure 3.1:** COL and COL/HA inks protocol. First COL was combined with acetic acid. The slurry was then blended at high speed before being passed through a custom dual syringe system fitted with meshes to homogenize the ink. ..... 55

**Figure 3.2:** Scaffold designing process illustrating the conversion of STL 3D object and sliced using the Slic3r software that can be read by the bioprinter specifying the infill density of the object. ... 56

**Figure 3.3:** Test apparatus and necessary set up to determine the extent of injectability using Zwick equipment. ..... 58

**Figure 3.4:** A) Plot of ink ejection of a continuous flow, B) Plot force vs displacement presenting ink clogging. ..... 59

**Figure 3.5:** Schematic representation of the extrusion process through a syringe and nozzle setup. The diagram shows the velocity profile in the needle where L = needle length, $P_0$= initial pressure, $P_L$ = outlet pressure (at the tip of the needle) and R= inner needle radius. ..... 61

**Figure 3.6:** At the needle's tip, the bioink on the left created a liquid drop. When extruded, the bioink on the right showed the potential of a material for 3D bioprinting by forming a filament. ..... 62

**Figure 3.7:** Filament Collapse Test: CAD design for testing rig and manufactured using 3D printer, deflection measurement schematic. ..... 63

**Figure 3.8:** Pores size distribution of the 3D printed scaffolds analysing the microscopic images using ImageJ. ..... 65

**Figure 3.9:** Degradation analysis procedure. ..... 66

**Figure 3.10:** FTIR Spectra of collagen at various concentrations, indicating the interaction between the components. ..... 70

**Figure 3.11:** Spectra demonstrating collagen crosslinking, with changes in amide bands reflecting the crosslinking degree. ..... 71

**Figure 3.11:** Standard force vs extrusion of collagen injectability test for three concentration 4, 5 and 6% collagen tested with three needle sizes 21G, 22G and 23G..... 73

**Figure 3.12**: Normal probability plots for A] printing pressure, B] Young's modulus and C] pore sizes for 3D bioprinted pure collagen scaffold. ..... 78

**Figure 3.13:** Studentised residuals versus predicted values plots for A] printing pressure, B] Young's modulus and C] pore sizes for 3D bioprinted pure collagen scaffold. ..... 79

**Figure 3.14:** Predicted versus actual values plots for A] printing pressure, B] Young's modulus and C] pore sizes for 3D bioprinted pure collagen scaffold. ..... 80

**Figure 3.15:** Studentised residuals versus run number plots for A] printing pressure, B] Young's modulus and C] pore sizes for 3D bioprinted pure collagen scaffold. ..... 81

**Figure 3.16:**A] Perturbation plot displaying the sensitivity of Factor A (collagen concentration ) and Factor D (needle size) to pressure parameter. B] Interaction effects of collagen concentration and needle size on printing pressure..... 83

**Figure 3.17:** A] Contour plot of printing pressure as influenced by collagen concentration and needle size. B] 3D response surface showing the effect of needle size and collagen concentration on printing pressure. ..... 83

**Figure 3.18:** A] Perturbation plot illustrating the effects of fabrication parameters on Young's modulus. B]-C] Interaction plots demonstrating the effect of collagen concentration and crosslinking concentration and time on Young's modulus. ..... 85

**Figure 3.19:** A] Contour plot of Young's modulus against Collagen and tannic acid concentration. B] 3D Response Surface of Young's modulus against collagen and tannic acid concentration. C] Contour plot of Young's Modulus against collagen concentration and crosslinking time. D] 3D Response Surface of Young's modulus against collagen concentration and crosslinking time..... 86

**Figure 3.20:** A] Perturbation Plot for Pore Size Response. B] Interaction Effect of collagen and tannic acid concentration on pore size. C] Effect of Collagen concentration and crosslinking time on pore size. D] Effect of crosslinking time and needle size on pore size. ..... 88

**Figure 3.21:** A] Contour plot for pore size response with factor A and factor C. B] 3D surface plot for pore size response with factor A and factor C. C] Contour plot for pore size response with factor d and factor c. D] Surface plot for pore size response with factor D and factor C. E] Contour plot for

pore size response with factor B and factor C. F] 3D surface plot for pore size response with factor B and factor C. ..... 90

**Figure 3.22:** RSM confirmation experiment A] Stress vs. strain curve for a scaffold with 4 %(w/v) collagen concentration. B] Binary image of 3D printed scaffold (scale bar= 1mm) C] Average pore area of 4 %(w/v) collagen. D]Average pore diameter of 4 %(w/v) collagen. With each test conducted in triplicate (n=3) for reliability and statistical significance..... 94

**Figure 3.23:** FTIR Spectra of Collagen Composites. Spectra of collagen with varying levels of HA, indicating the interaction between the components. ..... 96

**Figure 3.25:** Standard force vs extrusion of collagen injectability test for four different inks tested with three needle sizes 21G, 22G and 23G..... 98

**Figure 3.26:** Rheological Characterisation of Collagen Inks – A-B] A comparison of storage modulus (G') and loss modulus (G'') across a frequency sweep. C] complex viscosity across the same frequency range for Inks 1 to 4, demonstrating the viscoelastic properties. ..... 100

**Figure 3.27:** Correlation Plots of Measured vs. Predicted Shear Stress for Bioinks 1-4 Across Increasing Shear Rates. ..... 101

**Figure 3.28:** Evaluation of extrusion consistency for various inks across different needle gauges, with classification of PASS or FAIL based on the continuous flow of the ink through the needle. (scale bar 1mm). ..... 104

**Figure 3.29:** Filament collapse test for evaluating the rheological performance of bioprinting inks. This figure illustrates the comparative results of a filament collapse test for four different bioprinting inks (Ink 1 (COL) , Ink 2 (COLHA_0.05%), Ink 3 (COLHA_0.5%) and Ink 4 (COLHA_1%). (scale bar 1mm). ..... 105

**Figure 3.30**: 'Plus' test comparison for ink's 1 through 4, illustrating the ability of each ink to maintain structural integrity when printed in a layered cross pattern (scale bar 1mm 21G). ..... 107

**Figure 3.31:**Effect of print speed and number of layers on scaffold porosity. For print speeds of A] Average porosity for scaffold printed at 1 mm/s. B] Average porosity for scaffold printed at 3.5 mm/s. C] Average porosity for scaffold printed at 6 mm/s. (**** $p<0.0001$, n=3). ..... 109

**Figure 3.32:** Normal probability plots for A] printing pressure, B] scaffold degradation C] Young's modulus and D] pore sizes for 3D bioprinted pure collagen scaffold. ..... 114

**Figure 3.33:** Studentised residuals versus predicted values plots for A] printing pressure, B] scaffold degradation C] Young's modulus and D] pore sizes for 3D bioprinted pure collagen scaffold..... 115

**Figure 3.34:** Predicted versus actual values plots for A] printing pressure, B] scaffold degradation C] Young's modulus and D] pore sizes for 3D bioprinted pure collagen scaffold. ..... 116

**Figure 3.35:** Studentised residuals versus run number plots for A] printing pressure, B] scaffold degradation C] Young's modulus and D] pore sizes for 3D bioprinted pure collagen scaffold..... 117

**Figure 3.36:** Perturbation plot demonstrating the individual effects of HA concentration and printing speed on the printing pressure of a 3D bioprinted scaffold, along with an interaction plot highlighting their combined impact. ..... 118

**Figure 3.37:** Contour and 3D response surface plots demonstrating the effects of HA concentration and printing speed on the printing pressure of 3D bioprinted scaffolds. ..... 119

**Figure 3.38:** Perturbation and interaction plots showing the effect of HA concentration, layer number, and printing speed on scaffold degradation, with individual factor impacts and their two-way interactions. ..... 121

**Figure 3.39:** Contour and 3D response surface plots illustrating the impact of HA concentration, number of layers, and printing speed on the degradation percentage of 3D bioprinted scaffolds.. 123

**Figure 3.40:** Perturbation and interaction plots showing the influence of HA concentration and the number of layers on the Young's modulus of 3D bioprinted scaffolds. ..... 124

**Figure 3.41:** Contour and 3D response surface plots revealing the relationship between HA concentration, the number of layers, and the resultant Young's modulus of 3D bioprinted scaffolds. ..... 125

**Figure 3.42:** Perturbation and interaction plots showing the influence of HA concentration, number of layers and printing speed on the pore sizes of 3D bioprinted scaffolds. ..... 126

**Figure 3.43:** Contour and 3D response surface plots illustrating the effect of HA concentration, layer number, and printing speed on the pore size of 3D bioprinted scaffolds. ..... 127

**Figure 3.44:** Conformation results of the optimal scaffold properties identified in Study 2 of the DOE, with each test conducted in triplicate (n=3) for reliability and statistical significance ..... 130

Figure 4.1: Scaffold degradation analysis methods in tissue engineering. ..... 136

**Figure 4.2:** A] manual measurements collected from the lab and B] Image-based data taken from 3D bioprinted (scale bar 1 mm). ..... 139

**Figure 4.3:** A] Noise A 3x3 morphological ellipse structuring element. B] Initial scaffold binary image displaying noise artifacts. C] Result of morphological opening and closing using the ellipse, which cleans noise and closes gaps. Image axes are in pixels..... 141

**Figure 4.4:** Pre-processing steps involved in extracting the scaffold area and computing degradation. It includes converting the image to grayscale, applying morphological filters, thresholding, segmenting the scaffold, and measuring its area and scaffold degradation (Device 3). Images axes are in pixels. ..... 142

**Figure 4.5:** Data exploration ..... 143

**Figure 4.6:** The training process involves feature maps, sub-sampling, and flattened features, which capture important patterns related to degradation rate. Fully connected layers further learn complex relationships within the extracted features. The CNN model's output layer provides predictions for scaffold degradation rate. ..... 145

**Figure 4.7:** Illustrates of the use of VGG-16 and LSTM to forecast scaffold degradation at different time points. ..... 149

**Figure 4.8:** Comparison between image analysis (D_c), weight loss (D_w), and dimensional change (D_d) from Day 0 to 15 with images for . A] 4% COL/0%HA B] 4% COL/0.05%HA and C] 4% COL/0.5%HA. ..... 153

**Figure 4.9:** Device 1 comparison between image analysis (D_c), weight loss (D_w), and dimensional change (D_d) from Day 0 to 28 with scaffold images for A] PLLA/PCL/PHBV (5 x 3 mm) B] PLLA/PCL/PHBV (5 x 5 mm) C] PLLA/PCL/PHBV_nHA D] PLLA/PCL/PHBV_Sr_nHA. .... 155

**Figure 4.10:** Device 2 comparison image analysis (D_c), weight loss (D_w), and dimensional change (D_d) degradation measurements from Day 0 to 28 with images from each day for A] PEOT/PBT. B] PEOT/PBT_MBG. ..... 157

**Figure 4.11:** Device 3 comparison between image analysis (D_c), weight loss (D_w), and dimensional change (D_d) degradation measurements from Day 0 to 28 with images from each day. for A] 100 CSH B] 70CSH_MBG. ..... 158

**Figure 4.12:** CNN and LSTM models efficacy was gauged during their training phases using the mean squared error as the benchmark metric. A] CNN learning curve. B] LSTM learning curve. 160

**Figure 4.13:** Device 1 degradation prediction testing and comparing it with actual data. ..... 162

**Figure 4.14:** Web Interface displaying image degradation analysis results. The interface presents degradation weight and diameter percentages for selected days. ..... 163

**Figure 5.1:** A] Workflow of the pore detection algorithm coded in Phyton 3.9. B] Raw images of the reconstructed 100CSH (top) and 75CSH-MBG (bottom) formulations. C] Pre-processing methods (thresholding, contouring) applied to the reconstructed images. Scale bar represents 1 mm. ..... 171

**Figure 5.2:** Microstructural parameters obtained using the image analysis tool. A] Porosity percentage of 100CSH formulation over time. B] Porosity percentage of 75CSH-MBG formulation over time. ..... 176

**Figure 5.3:** Pore size distribution over time for 100CSH formulation analysed using image analysis tool. A] Pore size distribution of the cement before degradation testing. B] Pore size distribution at Day 3. C] Pore size distribution at Day 7. D] Pore size distribution at Day 14. E] Pore size distribution at Day 21. F] Pore size distribution at Day 28. ..... 177

**Figure 5.4:** Pore size distribution over time for 75CSH-MBG formulation using image analysis tool. A: Pore size distribution of the cement before degradation test. B: Pore size distribution at Day 3. C: Pore size distribution at Day 7. D: Pore size distribution at Day 14. E: Pore size distribution at Day 21. F: Pore size distribution at Day 28. ..... 178

**Figure 5.5:** The CNN model performance during training using mean absolute error as the evaluation metric. The blue and orange lines depict the training and validation errors, respectively. ..... 179

# Table of Tables

**Table 2.1:** T-score diagnosis for osteoporosis according to World Health Organization [43]. ..... 13

**Table 2.2:** Different bioprinting methods, comparing the printing parameters as well as the advantages and disadvantages of each method. ..... 19

**Table 2.3:** Comparative summary of natural hydrogels in bone scaffold bioprinting ..... 22

**Table 2.4:** Crosslinking methods, using chemical treatment, changing the percentage of concentration and the treatment time [120] ..... 24

**Table 2.5:** ML approaches that can be used in Biomaterials and TE applications. ..... 37

**Table 3.1:** Inks compositions for Study 1 and 2. ..... 54

**Table 3.2:** Numerical factors and their lower and upper levels for DoE study 1. ..... 67

**Table 3.3:** Numerical factors and their lower and upper levels for DoE study 2. ..... 68

**Table 3.4:** ANOVA for response surface quadratic model for printing pressure, Young's modulus and pore size. ..... 76

**Table 3.5:** Optimisation criteria for the scaffold properties ..... 91

**Table 3.6:** Optimal solutions as obtained by Design-Expert ..... 92

**Table 3.7:** Results of the DoE optimisation of the COL bioink composition demonstrate. The models were validated by comparing the difference between the expected responses for the optimal COL composition and crosslinking conditions and the actual values obtained from experimental data. . 94

**Table 3.8:** Flow Behaviour Index (n) and Consistency Coefficient (k). ..... 101

**Table 3.9**: Comparison of calculated power law pressures to the applied pressures on the CELLINK 3D bioprinter for different inks and needle sizes. ..... 103

**Table 3.10:** Measured extrusion pressures from the filament string test for Inks (Ink 1 (COL) , Ink 2 (COLHA_0.05% ), Ink 3 (COLHA_0.5% ) and Ink 4 (COLHA_1% ))., using 23G, 22G, and 21G needles, as recorded from the 3D Bioprinter. ..... 104

**Table 3.11:** Study 2 ANOVA for response surface quadratic model for printing pressure, Degradation, Young's modulus and pore sizes ..... 111

**Table 3.12:** Study 2 optimisation criteria for scaffold properties. ..... 128

**Table 3.13:** Optimal scaffold configurations derived from the RSM study, showcasing HA concentration, number of layers, printing speed, pressure, degradation, Young's modulus, pore size, and overall desirability. ..... 129

**Table 3.14:** Results of the DoE optimisation of the COL/HA bioink composition demonstrate. The models were validated by comparing the difference between the expected responses for the optimal COL/HA composition and the actual values obtained from experimental data. ..... 131

**Table 4.1:** Layers parameter used to build CNN model ..... 146

**Table 4.2:** Summary of model hyperparameters. ..... 147

**Table 4.3:** layers. parameters and hyperparameters to build LSTM model ..... 150

**Table 4.4:** Comparison between scaffold degradation traditional manual methods vs image analysis tool ..... 159

**Table 4.5:** Performance metrics comparison between CNN and LSTM models, including Mean Squared Error (MSE), Mean Absolute Error (MAE), R-squared (R2), and Accuracy..... 161

**Table 5.1:** PoreNet CNN model architecture summary ..... 174

**Table 5.2:** Summarised hyperparameters..... 174

**Table 5.3:** Model performance metric summery..... 180

# Table of Equations

**Equation 3.1**: Power-law model ..... 60

**Equation 3.2:** Pressure drop in pipe flow. ..... 60

**Equation 3.3:** Filament collapsing rate [%] ..... 62

**Equation 3.4:** Density formula for the scaffold density calculation. ..... 64

**Equation 3.5:** Formula for the calculation of the scaffold porosity (%), using the ratio between the density of scaffold and the solid density of the material. ..... 64

**Equation 3.6:** Mass loss, $W_0$ = Initial weight/dimensions (Day 1 post-crosslinking), $W_f$ = Final weight/ dimensions. ..... 66

**Equation 3.7:** Dimension loss, $D_0$ = Initial weight/dimensions (Day 1 post-crosslinking), $D_f$ = Final weight/ dimensions. ..... 66

**Equation 3.8:** Second-order polynomial equation, where Y is the predicted response, $\boldsymbol{\beta 0}$ is the intercept term, $\boldsymbol{\beta i}$ are the linear coefficients for the factors, $\boldsymbol{\beta ii}$ are the quadratic coefficients for the square of the factors, $\boldsymbol{\beta ij}$ are the interaction coefficients for the product of factors $\boldsymbol{Xi}$ and $\boldsymbol{Xj}$, $\boldsymbol{Xi}$ and $\boldsymbol{Xj}$ are the coded levels of the independent variables, and $\in$ is the random error term. ..... 74

**Equation 4.1:** Feature Maps Generation ..... 144

**Equation 4.2:** Rectified Linear Unit (ReLU) Activation ..... 144

**Equation 4.3:** Max Pooling Operation equation ..... 144

**Equation 4.4:** Mean Squared Error equation ..... 150

**Equation 4.5:** Root Mean Squared Error equation ..... 151

**Equation 5.1:** Residual weight percentage ..... 170

**Equation 5.2:** Mean Absolute Error equation. ..... 175

# Abstract

**Ghayadah Al-Kharusi**

**The use of Design of Experiments and Machine Learning to Optimise 3D Bioprinted bone repair Scaffolds**

Osteoporosis represents a significant clinical challenge, particularly in the aging population, leading to a heightened risk of fractures and long-term disability. Traditional therapeutic strategies often fall short, necessitating innovative approaches for effective fracture repair. Tissue Engineering (TE) has emerged as a transformative approach in regenerative medicine, focusing on developing three dimensional structures to facilitate the regeneration of damaged tissues. This thesis presents an investigation into the optimisation of 3D bioprinted scaffolds for bone repair, using Design of Experiments (DoE) and Machine Learning (ML) methodologies. The work details the development of a bioprinted collagen-hydroxyapatite scaffold for bone TE applications. Utilising DoE, the research optimises parameters affecting scaffold printability, mechanical integrity, and rheological properties. A significant advancement is made in automating scaffold degradation measurement through image analysis tools, comparing the efficacy of ML models such as Convolutional Neural Networks (CNN) and Long Short-Term Memory (LSTM) networks in scaffold degradation prediction using image-derived and numerical data. The thesis lays out the development of a ML framework that can quantify the structural integrity and functionality of bioprinted scaffolds over time. By doing so, it addresses critical challenges in bone TE, like the optimisation of scaffold properties and the real-time monitoring of degradation processes. An integral contribution of this thesis is the construction of a user-friendly interface platform that predicts scaffold degradation. Moreover, the research successfully develops an image analysis tool capable of detecting changes in pore size and porosity within scaffolds, validated using micro-CT images.

# Chapter 1: Introduction

## 1.1. Introduction

Osteoporosis is a systemic, degenerative disorder that predominantly affects postmenopausal women (1 out of 3) but also men at an advanced age (1 out of 5) [1]. It increases the risk of fractures, with osteoporotic fractures leading to death in one-fifth of cases and leaving half of the individuals dependent on assistance [1]. While anti-osteoporotic drugs are available, they have serious side effects and do not promote fracture healing. Addressing this challenge requires the development of innovative approaches for osteoporotic fracture repair [2].

In recent years, tissue engineering (TE) has become a pivotal field in regenerative medicine, focusing on the creation of three-dimensional (3D) structures that integrate cells into supportive frameworks. These constructs are implanted to repair or replace damaged tissues, influencing biomaterials and cell transplantation to encourage natural regeneration. Initially aimed at mitigating tissue and organ donor shortages, TE has significantly expanded to develop replacement tissues like cartilage, bone, blood vessels, and skin. It has also progressed to applications in drug delivery, disease modelling, and high-throughput screening, reflecting its broad impact and potential in therapeutic strategies and biomedical research [3], [4], [5], [6].

TE shows considerable potential in the study of osteoporosis for the creation of novel methods to speed up fracture repair and enhance patient outcomes [7]. TE employs specialised scaffolds designed to emulate bone's extracellular matrix, promoting cell proliferation and tissue regeneration [8]. These scaffolds are engineered with precise mechanical properties, such as appropriate strength and controlled degradation [9], along with the right architecture, including specific pore sizes and porosity [10]. This allows them to serve as bone substitutes and foster the formation of new bone tissue [11]. One advanced technique used in scaffold fabrication is bioprinting, a method that allows for precise layer-by-layer construction to replicate the complex structure of bone, enhancing the efficacy of bone tissue regeneration.

A one-at-a-time type of experimental strategy has been overtaken over the course of the previous decade by statistical experiments, such as Design of Experiments (DoE), where input variables can be varied simultaneously to acquire the highest amount of information from the least number of experiments [12]. This experimental approach involves a series of systematic tests that aim to find the factors that have the greatest effect on response variables [12]. The application of these statistical approaches enables the development of models that can predict the properties of biomaterials and tissue-engineered constructs, identify the relationships between properties and optimise their structural and performance outcomes with a reduction in experimental iterations, saving time, and reducing the consumption of laboratory resources and the overall cost of product development [13].

Several characterisation techniques are used for the assessment of TE scaffolds **Figure 1.1**, including physicochemical analysis, microstructural analysis, rheological assessment, mechanical testing, and

degradation measurements (**Figure 1.1**). Although DoE approaches are used in many studies for optimisation problems, these statistical methods may not be compatible for processing and predicting certain types of data, such as images, video, audio and high dimensional data, where the number of features is larger than the number of observations (**Figure 1.1**) [14]. Machine learning (ML) has shown the potential to overcome many of these existing experimental challenges, providing new methodologies for optimisation within the field of TE. ML plays a significant role in the world today and its impact is transformational, disrupting society and industry alike. The application of ML has shown the potential to bring about rapid process optimisation [15], [16].

Recently, the application of ML in biomaterials and TE research has been demonstrated with the successful use of prediction methods, artificial neural networks (ANN), convolutional neural networks (CNN), Bayesian optimisation (BO) and robot-based rapid prototyping systems, which can be used for prediction and optimisation in TE applications [17], [18], [19], [20], [21], [22]. Furthermore, ML has been combined with DoE to provide further enhancement of the optimisation process in biomaterials and TE research [23]. Despite evidence highlighting the benefits of application of ML reported in the literature, significant challenges remain, specifically in relation to effectively handling the preparation and representation of data generated from biomaterials and TE applications. The majority of studies focus on scaffold fabrication processes, such as 3D bioprinting and freeze-drying [14], [18], [24], [25], and scaffold properties [26], with only a few focussing in detail on how ML can be applied and the main outcomes and benefits that can be obtained from using ML methods [18], [27], [28].

Challenges relating to the implementation of ML in TE applications largely relate to the limitations in obtaining suitable datasets and the conversion of large datasets into easily accessible and utilisable formats as data is frequently gathered from manual processes [15], [17]. Thus, it is important to collect and explore a considerable amount of data to extract the right features and make it manageable. As a starting point, this literature review begins by examining the various applications of 3D bioprinting. It then proceeds to outline the foundational DoE methodologies that have become essential for process optimisation in this field. Following that, the review introduces recent applications of ML in biomaterials and tissue engineering, highlighting the benefits and challenges associated with their use in these specific areas. Finally, it contrasts the DoE and ML methodologies in the context of biomaterials and tissue engineering, discussing the unique aspects of each and exploring how combining these approaches may enhance optimisation and prediction in the field.

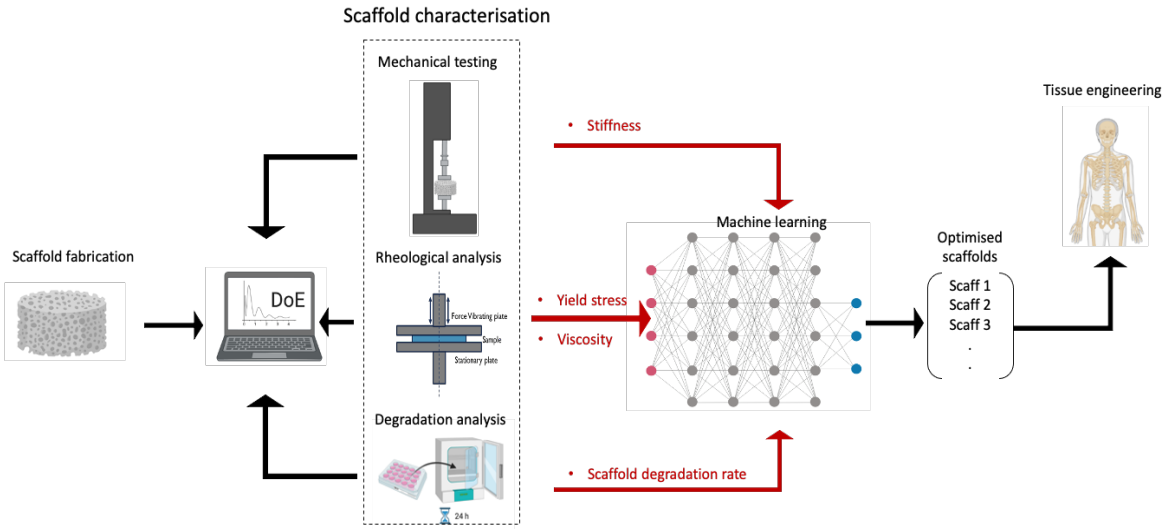



**Figure 1.1:** Schematic representation of the DoE and ML workflow to optimise the material that will be used for the TE applications.

## 1.2. Objectives

The overall aim of this thesis was to apply DoE and ML approaches for the optimisation of bioprinted scaffolds for bone tissue engineering applications, focusing specifically on the measurement of scaffold properties including degradation rate, pore size and porosity. The specific thesis objectives were:

**Objective 1:** To develop a collagen-hydroxyapatite bioprinted scaffold for bone tissue engineering applications and systematically evaluate and optimise the various parameters affecting printability, degradation, mechanical, and rheological properties using DoE.

**Objective 2:** To automate the measurement of scaffold degradation rates using image analysis tools and compare various machine learning models for predicting scaffold degradation with a combination of image-derived and numerical data.

**Objective 3:** To build interface platform to predict scaffold degradation.

**Objective 4:** To develop an image analysis tool capable of detecting pores and porosity within scaffolds, and to implement a CNN model to predict changes in pore size of degraded cement scaffolds using Micro-CT images.

## 1.3. Thesis outline

The outline of this thesis is also presented in **Figure 1.2**.

**Chapter 1: Introduction**

This chapter provides an overview of the thesis, establishing the context and significance of the research within the broader field of tissue engineering. It lays out the fundamental concepts and introduces the primary objectives and hypotheses that guide the research.

**Chapter 2: Literature Review**

The literature review chapter delves into previous studies relevant to tissue engineering, particularly focusing on the role of Machine Learning (ML) and Design of Experiments (DoE) in advancing biomaterial research. It synthesizes the current state of knowledge, identifying gaps that the present study aims to fill. This chapter has been partially published in the work "The Role of Machine Learning and Design of Experiments in the Advancement of Biomaterial and Tissue Engineering Research" [29].

**Chapter 3: Characterisation and Optimisation**

Here, the research develops collagen/collagen--hydroxyapatite inks and scaffolds, optimising them through DoE – addressing Objective 1. This process involves detailed analysis of the scaffolds' physical properties and their behaviour under different printing conditions, including the effects of hydroxyapatite content on the mechanical properties of the scaffolds.

**Chapter 4: Predicting Degradation**

Chapter 4 expands on the theme of scaffold degradation by employing ML algorithms. The chapter explores the development of image tool to measure scaffold degradation and the capability of ML models to predict degradation using both image data and numerical inputs – addressing Objectives 2 and 3. This predictive approach enhances the understanding of scaffold longevity and stability over time.

**Chapter 5: Pore Size and Porosity Prediction**

This chapter is centred on developing and implementing an image analysis tool that detects changes in pore size and porosity using Micro-CT images addressing Objective 4. It uses CNN models to predict alterations in the pore structure of cement scaffolds as they degrade. The published article "Comprehensive study through imaging techniques of the degradation of a resorbable calcium sulphate-based composite bone cement" [30] outlines part of the research conducted in this chapter.

**Chapter 6: Overall Conclusion and Future Work**

The final chapter draws conclusions from the research findings across all chapters, discusses the limitations encountered, and suggests avenues for future work. It synthesises the study's significant findings and reflects on the contribution of this research to the field of tissue engineering, particularly in the application of ML and image analysis to scaffold characterisation.

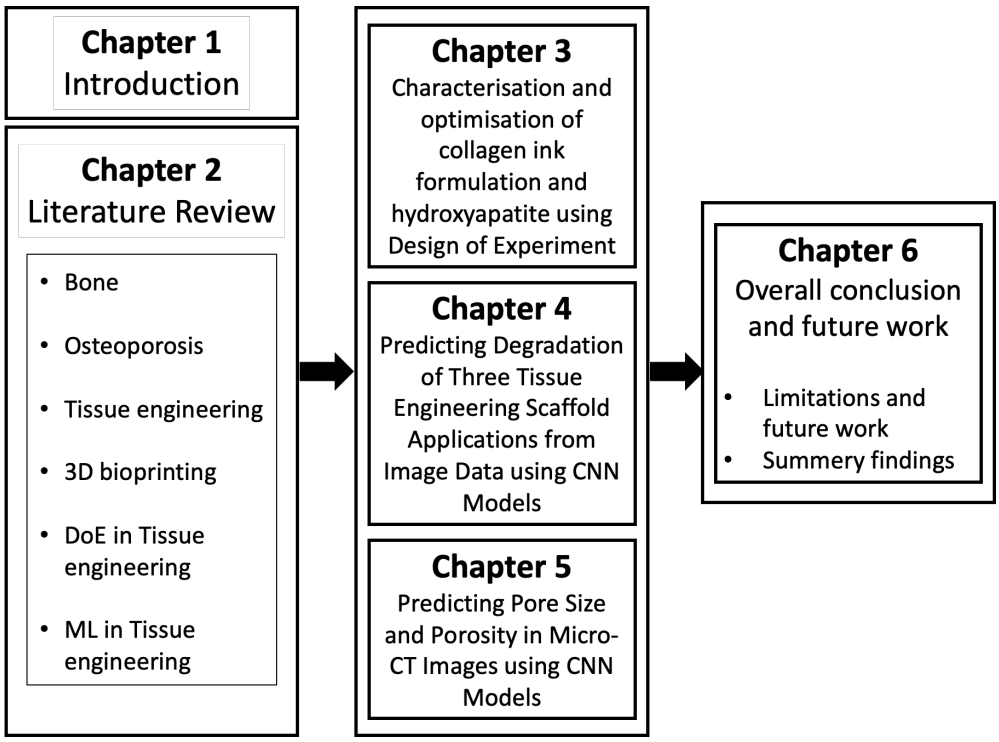



**Figure 1.2**: Outline of this thesis including a more detailed description.

# Chapter 2: Literature review

Sections of this Chapter have previously been presented (with some modification) in a literature review published in MDPI: Bioengineering (2022): **G. Al-Kharusi, N. J. Dunne, S. Little, and T. J. Levingstone "The Role of Machine Learning and Design of Experiments in the Advancement of Biomaterial and Tissue Engineering Research," vol. 9, no. 10**

## 2.1. Bone

An understanding of the multifaceted, continually changing nature of bone is essential in order to develop new treatment for disease, and injuries of the musculoskeletal system. Bones and connective tissue constitute the central framework of the body the skeletal system [31]. They provide support to the body and protect softer tissues such as the heart, lungs, and other soft tissues. In addition, bones of the body are attached to muscle tissues to enable body movement and support [32]. Bone is composed mainly of mineral components, organic matrix, and water. As shown in Figure 2.1, bone composition by weight consists of 65% mineral components such as hydroxyapatite (HA) (85%) and other minerals like calcium carbonate and calcium fluoride. The organic component which is around 20-25%, contains mostly collagen type I at around 90%. The water content present in bones varies between 10-20%. Factors such as age, species, and bone health influence the water content present in bones [33].

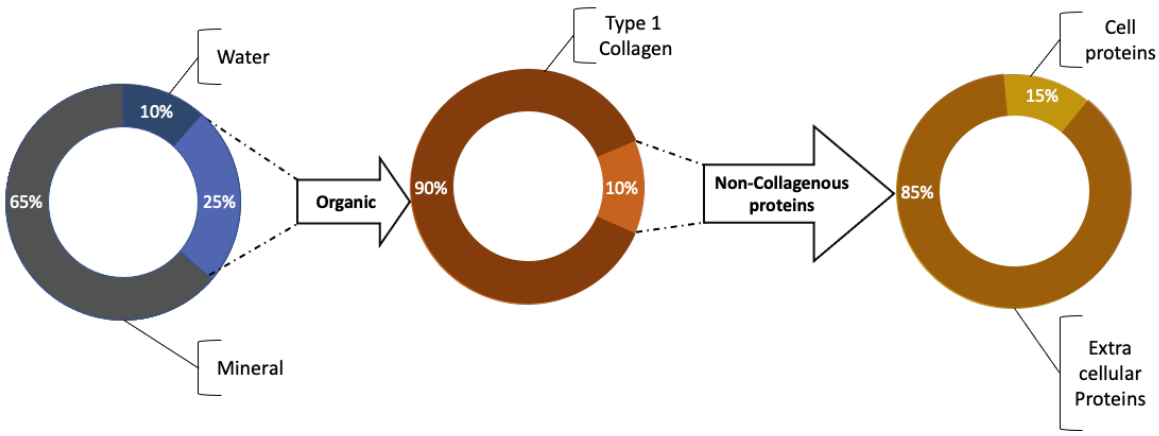



Figure 2.1: Bone composition composed of three parts organic, water and minerals, adapted from [4].

### 2.1.1. Bone structure

Bones can be classified according to the bone shape: irregular, long, flat, or short. **Figure 2.2** illustrates the different parts of the long bone. Specifically, the long bone consists of two major regions: the diaphysis and epiphysis [34]. The diaphysis is the tubular shaft composed of compact bone [34]. The hollow region of the tubular shaft is called the medullary cavity and is filled with marrow [34]. The marrow consists of red and yellow marrow. Red marrow is usually found in the diaphysis region of the long bone, where yellow marrow is an adipose tissue [32]. The region at the end of the bone that is covered by articular cartilage is known as the epiphysis [32]. The epiphysis consists of spongy bone with red bone marrow filling the spaces. The red bone marrow is responsible for the formation of red blood cells. The outer layer of the epiphysis has a gradient structure that

varies from osseous tissue to hyaline cartilage. This region, called the epiphyseal plate, is where bone growth occurs, and it becomes the epiphyseal line when the bones of the human body stop growing approximately at the age of 18-21 years [34].

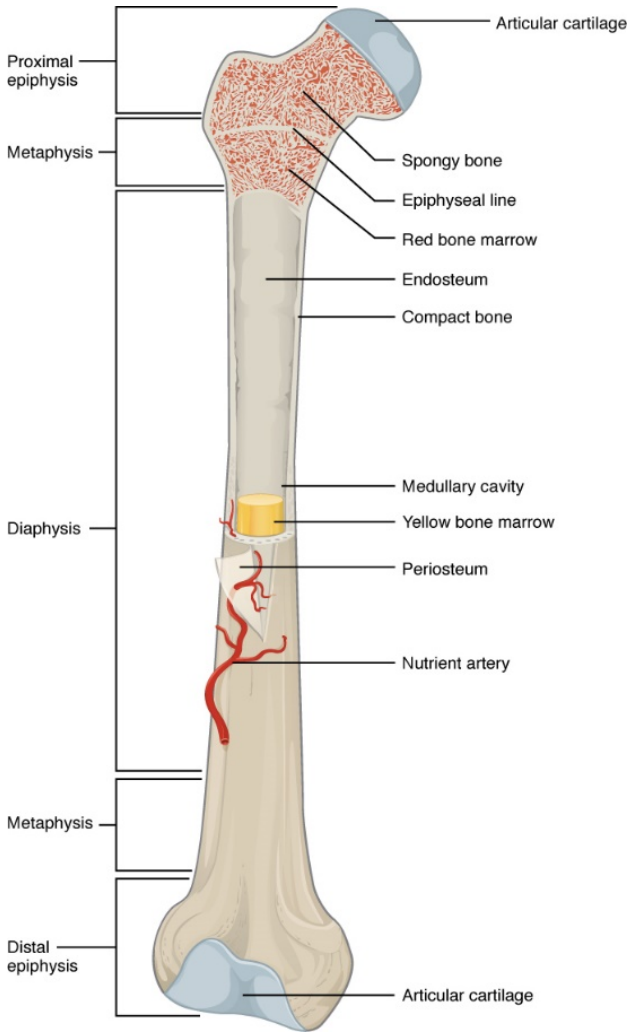



**Figure 2.2:** Long bone anatomy schematic showing diaphysis and epiphysis regions [34].

The endosteum is identified as the connective tissue in the outer lining membrane of the medullary cavity as demonstrated in **Figure 2.3**, this is where bone growth, repair, and remodelling happen. The periosteum is a fibrous membrane periosteum that covers the outer surface of bone and is composed of two layers- an outer and an inner layer [34]. The inner layer is known as the osteogenic layer as it is made up of cells that have osteogenic potential while the outer fibrous layer has more collagen and fewer cells [27].

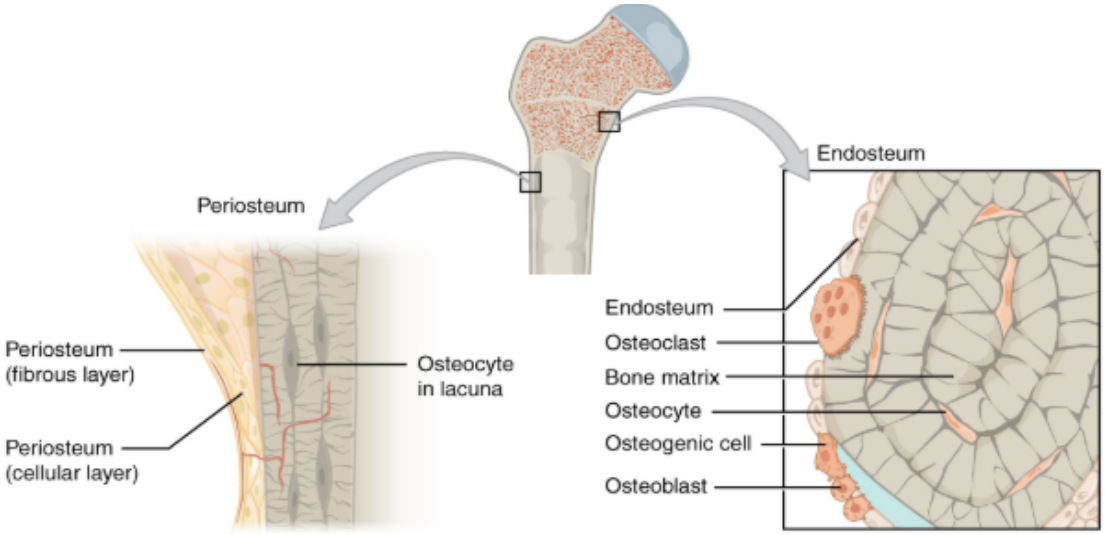



**Figure 2.3**: Overall schematic of the periosteum and endosteum of the bone [34].

Bones contain four different cells osteoblasts, osteocytes, osteoclasts and osteogenic stem cells, as demonstrated **Figure 2.4**. Osteoblast cells are mainly responsible for osteogenesis (bone formation), whereas osteoclasts are responsible for bone resorption. Both osteoblasts and osteocytes form from mesenchymal stem cells; whereas osteoclasts are formed from hematopoietic stem cells where it is relevant to the monocyte/macrophages [32].

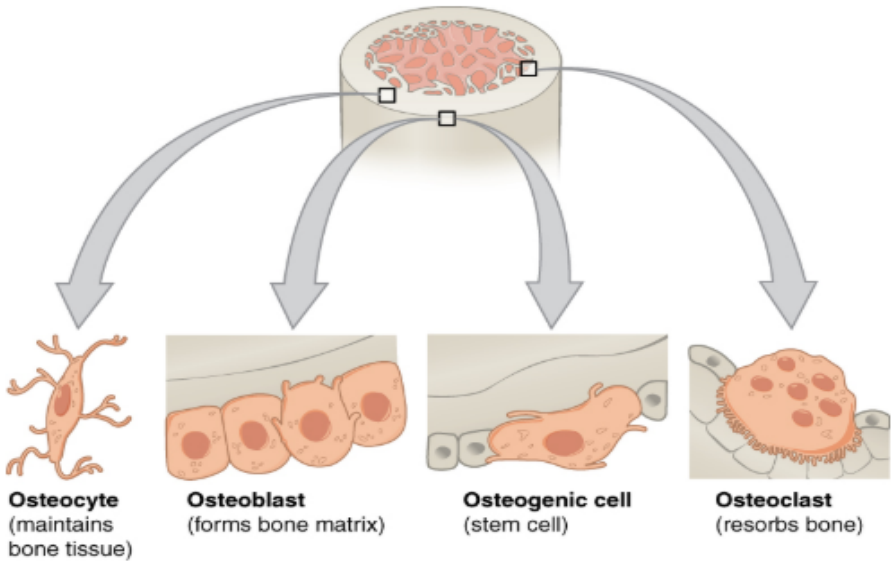



**Figure 2.4:** Four different cell categories can be found within the bones such as osteocyte, osteoblast, osteogenic and osteoclast [34].

### 2.1.2. Natural bone repair

Fracture repair processes aim to re-establish bone tissues to their original physical strength and mechanical properties and are determined by a variety of systemic and local factors. Bone is a living tissue that is constantly undergoing repair and remodelling processes. The bone repair process can be divided into four stages: 1) hematoma formation, 2) cartilaginous callus, 3) bony callus formation, and 4) remodelling (**Figure 2.5**).

When the bone experiences a fracture, blood vessels inside the bone and the surrounding periosteum are damaged, resulting in the creation of a hematoma as shown in **Figure 2.5**. The inflammation stage indicates the start of the bone healing stages usually lasting 1-5 days [35]. Due to the bone injury, the body starts to secrete pro-inflammatory cytokines such as (tumour necrosis factor-alpha, bone morphogenetic proteins, and interleukins. These cytokines help stimulate cellular biology by attracting phagocytic cells like macrophages, lymphocytes and monocytes. This mitogenic activity at the injury site helps to form new small blood vessels [35],[36] and [37].

The next stage of bone healing (cartilaginous callus) commences within 5-11 days of the fracture. In this stage, development of cartilaginous tissue (soft callus) occurs, with the formation of new bone occurring through the process of endochondral ossification [35]. During endochondral ossification the body attempts to improve and stabilise the fractured area, allowing the ossification process to occur. Soft callus expands throughout the fracture gap connecting the bone ends. Then fibroblasts and osteoblasts enter the site and begin to reform bone. Collagen fibres are produced by the fibroblasts to connect broken ends of the bone, conversely osteoblast activity starts to form spongy bone [37].

The next stage of fracture healing involves the formation of a bony callus by the conversion of a fibrocartilaginous callus. The fibrocartilaginous callus is composed of both hyaline and fibrocartilage. This process takes up to 11-28 days [35] for the broken bone ends to be firmly joined together. Finally, osteoclasts and osteoblasts remodel the bony callus, removing the excess material on the exterior and within the medullary cavity of the bone [37]. Bone tissue is formed by the addition of compact bone, this process can take many months to years [35] depending on body health [37].

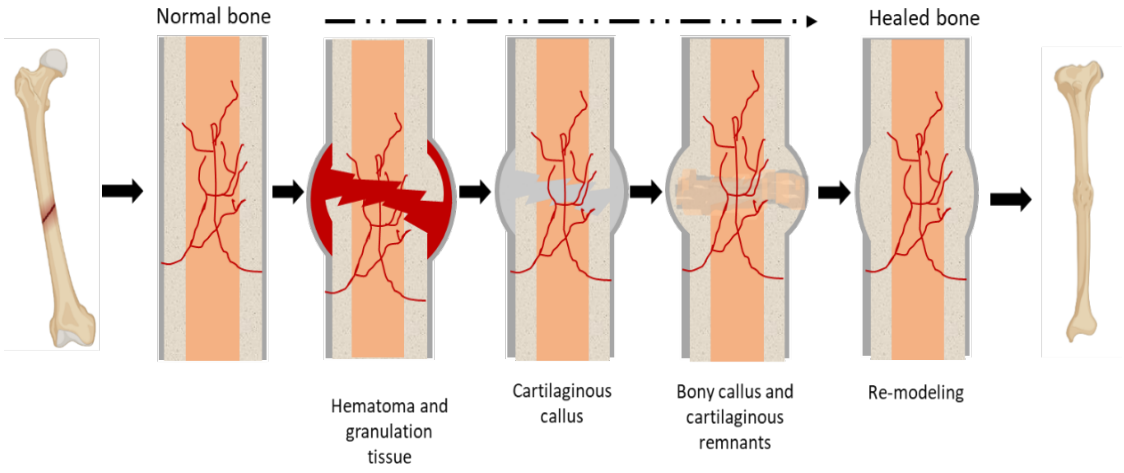



**Figure 2.5:** The four stages of bone repair and remodelling, including the hematoma and granulation process at the fracture site followed by the development of cartilaginous and bony callus leading to the final stage which is the bone remodelling.

### 2.1.3. Bone defects

Bone diseases and fractures are major medical issues that can arise from several reasons, such as acute traumas, congenital abnormalities, or degenerative disorders [38]. Osteoporosis is a prevalent disorder characterised by the gradual reduction of bone mass and density, which increases the risk of fractures [39]. Fractures caused by osteoporosis are especially problematic when they result in non-union, a condition where the bone fails to heal properly, potentially causing long-lasting impairment and suffering [40]. Individuals diagnosed with osteoporosis are at an increased susceptibility to fractures as a result of diminished bone mineral density (BMD), particularly in areas such as the hip, spine, or wrist [41]. The measurement of BMD can be conducted through the utilisation of dual-energy X-ray absorptiometry (DXA). Subsequently, the obtained BMD values are analysed by means of T-scores, which aid in assessing the likelihood of fractures in patients [42]. For instance, individuals with low BMD characterised by highly negative T-scores are indicative of severe osteoporosis, a condition that significantly increases the likelihood of experiencing fractures, as demonstrated in **Table 2.1** [43].

**Table 2.1:** T-score diagnosis for osteoporosis according to World Health Organization [43].

| Interoperation | T-Score |
|---|---|
| Healthy | -1.0 (and higher) |
| Osteopenia | -1.0 to -2.5 |
| Osteoporosis | -2.5 and lower |
| Severe Osteoporosis | -2.5 and lower with one or more fragility fractures |

Osteoporosis is classified into two groups, primary and secondary osteoporosis. Primary osteoporosis often occurs in women after their menopause (postmenopausal osteoporosis) [44]. Primary osteoporosis type 1 usually affects trabecular bone rather than cortical bone, and fractures usually occur in the vertebrae and distal radius. This type can also affect middle-aged men causing vertebral fractures; however, this is less common [33]. Conversely, type 2 is commonly found in patients above the age of 70 of both genders. The main difference between the two types is gender association, however, both result in fractures of the proximal femur, vertebrae, and radii [33]. Secondary osteoporosis can affect both genders. This can be caused due to corticosteroid therapy, as exposure to glucocorticoid treatment increases the fracture risk causing glucocorticoid-induced osteoporosis [33]. Regardless of the improvement in treating osteoporosis over the past few decades, the treatment of osteoporotic fractures in elderly patients still presents a major clinical challenge due to impaired healing in this patient population [33].

TE has the potential to greatly impact the development of new treatments for osteoporotic fractures. Current surgical treatments for osteoporotic fractures involve the fixation of the fractured bone using metal hardware, such as screws and plates. Metal hardware can also be used in conjunction with bone scaffolds to provide stability for the ingrowth of new bone tissues [45]. 3D bioprinting presents an innovative approach in manufacturing 3D scaffolds that can be used to treat osteoporotic fractures. This technology offers advantages for the fabrication of scaffolds with customised shapes, mechanical strength, and porosity/pore sizes [33].

## 2.2. Tissue Engineering (TE)

TE aims to develop new approaches to aid in the regeneration of diseased and damaged tissue. TE can be defined as the combination of the principles of biomaterials and stem cell transplantation to develop and support endogenous cell regeneration [3]. Cell transplantation plays a key role in TE and is used for therapeutic strategies to treat various injuries such as bone fractures. New methods are developed that include direct injection of cells to the affected area, reducing the surgical invasiveness risks [46]. One of the key components in TE is the fabrication of scaffolds, which provide a three-dimensional framework that supports cell attachment, proliferation, and differentiation. Various methods have been employed to create scaffolds specifically designed for bone tissue regeneration, including freeze-drying, electrospinning [47], [48], injectable cements [49], and 3D bioprinting [50], [51], [52], [53], [54].

### 2.2.1. Freeze-drying

Freeze-drying, also known as lyophilization, is a method largely employed to fabricate tissue engineered scaffolds. This process entails initially freezing the scaffold in a controlled manner, followed by the removal of frozen ice crystals through sublimation under low pressure conditions. The removal of ice crystals in this way ensures that a highly porous structure is left behind. The key

element of this technique involves the process of sublimating ice from the frozen solution, while maintaining low pressure. The resultant scaffolds have a low moisture content and highly porous structure. Bioactive molecules, such as platelet-rich plasma (PRP), are frequently incorporated into these scaffolds to enhance their biological effectiveness [55]. The low temperatures involved in the process effectively safeguard the structural and biological integrity of these bioactive agents thus preserving the chemical stability and effectiveness.

### 2.2.2. Electrospinning

Electrospinning is a popular technique in tissue engineering, prominently used in bone tissue engineering [56], [57], [58]. This method involves extruding a polymer solution or melt through a charged nozzle. The resulting formation consists of ultrafine fibres that closely resemble the structure of the extracellular matrix [47], [48]. Electrospun scaffolds can achieve microarchitecture properties that resemble natural bone tissue in terms of their high surface area, interconnected porosity, and mechanical properties [59]. The scaffolds not only promote cell adhesion and proliferation but also facilitate the diffusion of nutrients [60]. They provide a favourable microenvironment for tissue regeneration. Furthermore, electrospinning allows for a high degree of control over the features of the scaffold. Parameters such as fibre diameter, alignment, and composition can be modulated to tailor the scaffolds to closely mimic the architecture of the native bone tissue [60].

### 2.2.3. Injectable cements

Injectable cements, such as calcium phosphate-based cements, provide a minimally invasive approach for scaffold fabrication in bone tissue engineering [61]. These cements can be mixed with cells and bioactive molecules to form a paste-like material that can be injected directly into the defect site [62]. Over time, the cement sets and hardens, providing structural support and promoting bone regeneration [63]. Injectable cements offer advantages, such as ease of handling, adaptability to irregular defect geometries, and the ability to deliver therapeutic agents precisely to the target site [62]. They can also provide initial mechanical stability to the defect site, which is crucial for proper bone healing [63]. Calcium phosphate-based cements, in particular, closely resemble the mineral composition of natural bone, facilitating the integration of newly formed bone tissue around the implant [62]. Injectable cements offer a versatile and minimally invasive strategy for scaffold fabrication in bone tissue engineering, enabling effective repair and regeneration of bone defects [63].

### 2.2.4. 3D Bioprinting

Another emerging technology in bone tissue engineering is 3D bioprinting, which enables the precise deposition of cells, biomaterials, and growth factors in a layer-by-layer manner to create complex three-dimensional structures [64]. 3D bioprinting offers the advantage of fabricating scaffolds with

precise control over their architecture, pore size, and distribution, which are critical factors in promoting cell ingrowth and tissue regeneration [65]. This fabrication technique involves the layer-by-layer deposition of bioinks to produce complex structures designed to generate functional tissue or organs [66], [67], [68], [69]. The process can be divided into three steps: (1) pre-printing, which includes the bioink formulation and pre-processing, (2) printing, where the in-situ printing parameters need to be optimised and corrected, and (3) post-printing, involving the optimisation of the culture conditions to achieve a functional tissue/organ. By using computer-aided design (CAD) models, 3D bioprinting allows for the creation of patient-specific scaffolds tailored to individual anatomical defects [64]. The geometrical data of the 3D tissues used in the CAD design can be obtained using different medical imaging systems, e.g. MRI, X-ray and microcomputed tomography scans [65]. The bioprinting process involves the use of bioinks, which are formulations of cells and biomaterials, to create the desired tissue-like structures [70]. These bioinks can be designed to mimic the composition and mechanical properties of natural bone tissue, facilitating cell attachment, proliferation, and differentiation [70]. 3D bioprinting offers a highly customizable approach for fabricating scaffolds with complex geometries, hierarchical structures, and spatially controlled distribution of cells and bioactive factors [64]. It holds great promise for the development of patient-specific bone TE tissue engineering strategies, enabling precise and personalised treatment for bone fractures and other bone-related conditions [65].

3D bioprinting offers many advantages over other scaffold fabrication techniques. These include high precision, low cost and the ability to create complex 3D tissue structures in high demand within a short period [68], [70]. In addition, the technology enables the use of personalised complex structure designs for a specific patient, thus providing great potential for use in personalised medicine approaches [64].

Each of these strategies makes a distinct and valuable contribution to the area of tissue engineering. Freeze-drying is a highly effective method for the fabrication of porous scaffolds, while 3D bioprinting offers advantages in terms of the tailor ability of scaffold microstructures [71]. Additionally, electrospinning is adept at producing scaffolds with both large surface area and favourable mechanical qualities [72]. The choice of a given approach is contingent upon the precise demands of the tissue engineering application, including the nature of the target tissue, the desired mechanical characteristics, and the necessary level of biological functionality in the scaffold. By combining these approaches, it is possible to create more sophisticated and efficient structures for bone repair and other tissue engineering purposes.

#### *2.2.4.1. Bioprinting techniques*

Inkjet bioprinting

The inkjet (or drop-on-demand) printing method is considered a non-contact procedure based on 2D-desktop inkjet printing technology. This type of printing can be classified into thermal, electrostatic, and piezoelectric inkjet bioprinting [73]. As illustrated in **Figure 2.6**, thermal inkjet bioprinting uses heat energy on the print head to produce pressure pulses that cause the discharge of droplets of bioinks through the nozzle [74]. The temperature involved can reach up to hundreds of degrees for a few microseconds depending on the material being used [75]. In the piezoelectric bioprinting method, droplets are formed due to a pressure transient from a piezoelectric actuator. The piezoelectric bioprinting process uses voltage instead of heat thereby allowing droplets to remain directional and uniform in size [75].

The benefit of inkjet bioprinting is the ability to precisely control droplet size and positioning, which enables the precise arrangement of cells and bioactive compounds. In inkjet bioprinting, the interfacial fluid forces facilitate the self-assembly of these components into structures such as nanofibers and hydrogel scaffolds. The method provides numerous advantages, including high cell viability, rapid printing speed, and the ability to print complex geometries. However, challenges remain, such as the limited availability of suitable bioinks, the requirement for biocompatible and mechanically robust materials, and the optimisation of printing parameters to achieve optimal cell behaviour and tissue functionality [64]. Current research and technological advances in inkjet bioprinting are aimed at overcoming these obstacles and unleashing its full potential for fabricating functional tissue constructs and advancing applications in regenerative medicine [76], [77].

Extrusion- based bioprinting

Extrusion (or pressure-assisted) bioprinting involves the continuous deposition of filaments based on one of two mechanisms: pneumatic force (air pressure) or mechanical force (screw or piston) [73]. This type of printing applies pressure on a syringe that causes material extrusion through a nozzle as shown in **Figure 2.6**. To create 3D structures hydrogels are extruded in two dimensions (x and y-axis) forming a foundation for the subsequent layer, while the printer stage or printhead moves in the z-axis to create a 3D scaffold [78]. To expand the capabilities of extrusion bioprinting, a platform for multi-material extrusion biological printing was created by Liu et.al. This platform allows for the continuous deposition of multiple coded bioinks, enabling the rapid fabrication of complex structures. It employs a digitally controlled extrusion system in which a single print head composed of bundled capillaries coordinates with a motorised table for precise control [79]. Improving the viscosity of the bioink is crucial for attaining greater printability and shape accuracy when creating 3D structures. Nonetheless, increasing viscosity can result in difficulties, such as increased shear

stress, decreased cell compatibility, and increased flow resistance, which can contribute to nozzle clogging [80].

During extrusion bioprinting, factors such as nozzle geometry, printing time and dispensing pressure, influence cell vitality and material consistency. To achieve optimal cell viability, consistent material deposition, and precise printing results using extrusion bioprinting, it is imperative to meticulously regulate these variables and successfully address the corresponding challenges [81], [82]. By addressing these factors and refining the extrusion bioprinting procedure, researchers will be able to realise the maximum potential of this technique for advancing TE and biological manufacturing applications [83].

Laser-assisted bioprinting (LAB)

Laser-assisted bioprinting (LAB) uses a laser as a source of energy to deposit biomaterials [75]. In comparison to other techniques, LAB does not use nozzles and instead uses a laser that can generate a high-pressure bubble [74]. This printing technique consists of a pulsed laser source, a ribbon coated with biomaterials that are deposited onto a metal film, and a collecting substrate, as illustrated in **Figure 2.6**. A droplet is formed when the laser beam is directed onto the ribbon section, causing the biomaterial to evaporate and reach the collector substrate. The technique has been commonly used to print bioinks, proteins and ceramic materials [75].

The ability to print heterogeneous cell populations is one of the many benefits of laser-assisted bioprinting, along with high resolution, minimal cell injury, along with the ability to print with high resolution. It enables the precise positioning of cells and bioactive molecules, thereby facilitating the formation of intricate tissue structures with well-defined spatial organisation. Optimising printing parameters, selecting appropriate biomaterials, and ensuring long-term cell functionality and viability present challenges. Continued research and technological advances in laser-assisted bioprinting seek to expand its applications in TE, regenerative medicine, and drug discovery [73], [74].

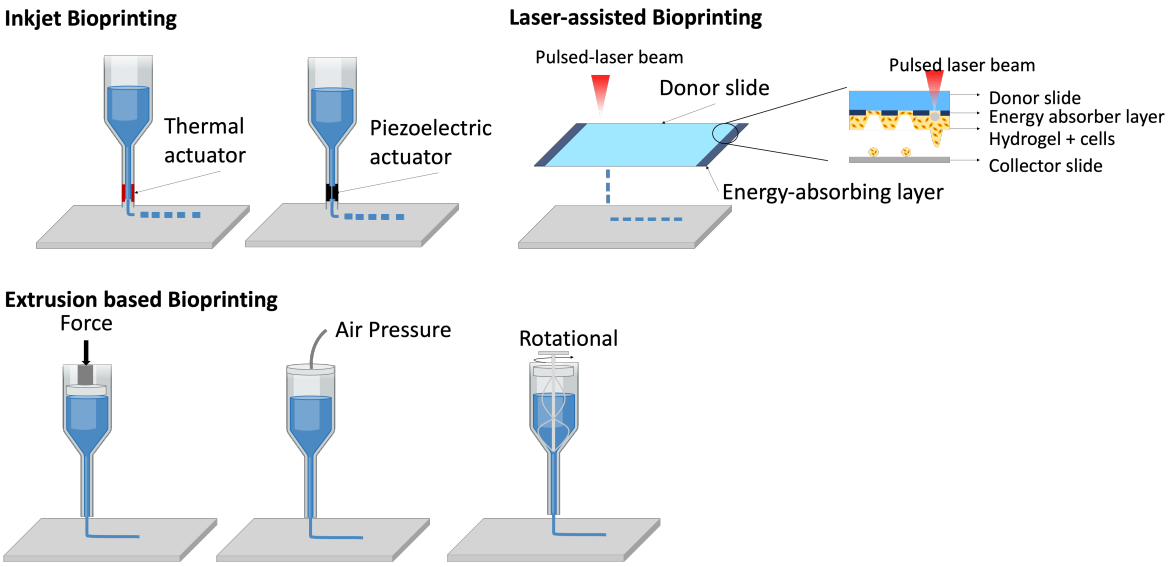



**Figure 2.6:** Bioprinting methods used to build 3D scaffolds., for instance Inkjet bioprinting deposits drop-by-drop method, extrusion- based bioprinting deposits hydrogels via applied force or air pressure, and laser-assisted bioprinting method.

**Table 2.2:** Different bioprinting methods, comparing the printing parameters as well as the advantages and disadvantages of each method.

| Printing method | Speed | Advantages | Disadvantages |
|---|---|---|---|
| **Inkjet bioprinting** | Fast (1-10,000 droplets/s) [78] | High-speed scaffold construction, acceptable cost and high resolution [73], [74]. | Smooth printing is difficult due to regular nozzle blockage [75]. |
| **Extrusion-based bioprinting** | Slow (speed specified depending on material properties) | Ability to deposit bioinks with high cell density [74]. Cells are homogenously distributed [75]. | Low printing resolution, can damage cells due to nozzle shear stress effect and difficulties in fabricating printable bioinks [74]. |
| **Laser-assisted bioprinting** | Medium 200–1600 mm/s [78] | Ability to deposit viscous material either in solid or liquid form [73], high resolution, no clogging and high cell viability [74]. | High temperatures can damage the cells, can be costly, difficult to create 3D structures [74] and time-consuming [73]. |

#### *2.2.4.2. Bioink formulation*

In the field of bioprinting, where numerous biomaterials, including ceramics, hydrogels, composites, and polymers, have been created for use in different bioprinting applications, bioink formulation plays a critical role. These bioinks materials provide unique properties and capabilities that can be customised to fit the needs of the particular bioprinting process and the bioprinted tissues. Here the focus is on bioinks for extrusion-based bioprinting processes for bone tissue engineering applications. This section will discuss the bioprinting requirements needed to optimize bioink and scaffolds properties.

The composition of bioinks is a critical aspect that influences their performance in bioprinting applications. Bioinks must meet various requirements, including mechanical properties, biological compatibility, and printability. Mechanical properties such as stiffness and viscoelasticity should be optimised to provide structural integrity and support for the printed tissue. Biological compatibility is essential to ensure cell viability, proliferation, and functionality within the bioink. Printability refers to the ability of the bioink to be accurately deposited and maintain its shape during the printing process, enabling precise tissue fabrication [84]. Moreover, in the context of bioprinting scaffolds for bone tissue bioprinting applications, specific considerations come into play. Bioinks for bone tissue engineering require additional properties such as osteoconductivity and osteoinductivity to facilitate bone regeneration [9]. Osteoconductive materials provide a scaffold that promotes bone cell attachment and growth, while osteoinductive materials possess the ability to induce stem cells to differentiate into bone-forming cells [9], [85]. Therefore, the ideal bioink formulation for bone tissue bioprinting should incorporate suitable biomaterials with these osteogenic properties to promote successful bone tissue regeneration [86].

#### *2.2.4.3. Biomaterials*

The selection of appropriate biomaterials is pivotal in the fabrication of bone-engineered constructs. A diverse array of both natural and synthetic biomaterials has been employed in the production of bone scaffolds [87]. Natural biomaterials are derived from biological sources and are known for their excellent biocompatibility and bioactivity. Natural biomaterials often mimic the extracellular matrix (ECM), facilitating cell attachment, proliferation, and differentiation. Common natural biomaterials include collagen, alginate, chitosan, gelatin and hyaluronic acid. While they offer the advantage of being more readily accepted by the body, their main limitations are their potential immunogenicity and variability in properties due to their natural origin. On the other hand, synthetic biomaterials are man-made and include polymers, ceramics, and composites. They offer the advantage of having controlled properties, such as degradation rate, mechanical strength, and porosity. Examples of synthetic materials include polylactic acid (PLA), polyglycolic acid (PGA), and polycaprolactone (PCL). These materials can be engineered to meet specific requirements of scaffold design but may

lack the natural signalling cues necessary for optimal cell interaction. It is important to acknowledge that not all materials are suitable for effective cell encapsulation, which is a critical step in scaffold functionality [88], [89].

Hydrogels have become the preferred material for cell encapsulation in the field of bioprinting. Their popularity arises from various inherent characteristics: biocompatibility, biodegradability, similarity to the native extracellular matrix (ECM), and the capacity to sustain a moist environment. The presence of water in this environment is advantageous as it enhances the movement of nutrients and oxygen and assists in the elimination of waste, therefore stimulating the proliferation of cells [90], [91], [92]. In order for a hydrogel to be appropriate for bioprinting, it must meet a specific set of requirements. These include the requirement for suitable rheological properties to maintain the integrity of printed strands, the capability to retain its shape and prevent pore collapse during 3D printing, and ensuring that it is non-toxic to encapsulated cells in order to support their growth and specialisation [90], [93].

Alginate, gelatine, chitosan, collagen, and hyaluronic acid are often used natural hydrogels in the bioprinting of bone scaffolds. Each of these hydrogels provides specific advantages and poses individual difficulties. Alginate is widely recognised for its cost-effectiveness, simplicity in creating 3D structures, and compatibility with living organisms. Nevertheless, bone TE applications face considerable obstacles due to the quick decline in mechanical strength and lack of control over the interior microstructure caused by excessive hydrophilicity [94] Similarly, gelatine is highly regarded for its ability to reduce viscosity under shear stress and its compatibility with living organisms, but its mechanical strength is lacking and it degrades quickly. Chitosan exhibits favourable biocompatibility and biodegradability; however, it is hindered by a slow gelation rate and inadequate mechanical qualities, which pose challenges for its application in cell printing and with pH-sensitive compounds. Collagen, like similar substances, is compatible with living organisms and enhances the attachment of cells. However, it is limited by its weak mechanical capabilities and low thickness. Hyaluronic acid also has limited mechanical strength, despite its biocompatibility and non-toxic degradation [40], [95], [96], [97], [98], [99], [100], [101], [102], [103]. **Table 2.3** provides a brief summary of the advantages and possible drawbacks of the natural hydrogels listed above, particularly in relation to their use in bioprinting bone scaffolds.

**Table 2.3:** Comparative summary of natural hydrogels in bone scaffold bioprinting

| Hydrogel | Benefits | Limitations | Ref |
|---|---|---|---|
| **Alginate** | Affordable, easy 3D fabrication, good biocompatibility, high biodegradability, maintains cell viability | Bioinert, limited long-term stability, rapid loss of mechanical properties in vitro, limited shape-ability | [95], [96], [97], [98], [99], [100], [101], [102] |
| **Gelatin** | Shear-thinning behaviour, accelerates gelation, biocompatible, biodegradable, resembles ECM components | Poor mechanical properties, high degradation rate | [104] |
| **Chitosan** | Biocompatible, biodegradable, regulates cell adhesion and differentiation | Slow gelation rate, poor mechanical properties, conflicts with cell printing and pH-sensitive molecules | [105], [106] |
| **Collagen** | Good biocompatibility, non-toxic degradation, viscoelastic, hydrophilic, antimicrobial properties | Poor mechanical properties, loses shape, low viscosity, slow gelation | [107], [108], [109] |
| **Hyaluronic Acid** | Good biocompatibility, non-toxic degradation, viscoelastic, hydrophilic, antimicrobial properties | Poor mechanical strength | [110], [111], [112], [113] |

The main focus of this study is to produce collagen-based bioinks that mimic the composition of native bone tissue. Collagen has been widely used in regenerative medicine and disease modelling (e.g. bone, cartilage and cornea) and is by far the most prevalent molecule that can be found in the human body making up 30% of protein mass. Collagen has been used previously to fabricate 3D bioprinted scaffolds [114], [115]. To enhance the mechanical and biological properties of collagen, mixing natural and synthetic polymers (e.g. poly(methyl methacrylate) and polyethylene glycol (PEG) [116]) has been used to produce the desired cellular response and an increase in the mechanical stiffness of the scaffolds. HA, beta-tricalcium phosphate (β-TCP) and other calcium phosphate ceramic composites are promising biomaterials that can be used in orthopaedic regeneration owing to their similarity to the mineral component of bone composition. Additionally, bioactive glasses materials enhance the formation of HA layers that can promote chemical bonding with bones, due to their biological performance. These biomaterials substitutes have been previously used in clinical bone defect repair [54].

### Crosslinking methods

Crosslinking methods are often used to modify material mechanical stiffness to provide structural integrity. Three different methods have been reported for crosslinking bioprinted scaffolds, thermal controlled crosslinking by applying a temperature change to the scaffold, chemical crosslinking, such as using tannic acid or, calcium chloride, or physical crosslinking by using UV light [117], [118], [119]. Chemical crosslinking techniques are the most effective for crosslinking collagen scaffolds. The degree of crosslinking can be increased by increasing the crosslinking concentration and treatment time. Using chemical crosslinking agents, unreacted chemicals or residual/ by-products can often be left behind, therefore, to minimise cytotoxicity scaffolds needs to be washed after crosslinking. There are a variety of chemicals that can be used to crosslink collagen scaffolds, such as glutaraldehyde (GA), 1-ethyl-3-(3-dimethylaminopropyl) carbodiimide (EDC), Hexamethylene di-isocyanate (HDI), tannic acid and genipin. While GA is an effective collagen crosslinker, unreacted GA can be cytotoxic and therefore it can only be used at concentrations of 0.0025-2.5 %(w/v) and treatment times of 20 min to 24 h [120]. Other commonly used chemicals with less cytotoxicity are tannic acid and genipin. Both chemicals are extracted from plants. Usually, tannic acid concentration ranges from 0.1-6 %(w/v) at a treatment time of 10 min-120 h [120]. Concentrations of 0.00025-0.6 %(w/v) and treatment times of 1 – 48 h are most frequently used for genipin [120]. As chemical crosslinking can increase the risk of cytotoxicity issues, physical crosslinking methods such as ultraviolet (UV) and dehydrothermal (DHT) treatments can also be used to crosslink collagen scaffolds. Cytotoxic components do not result during physical crosslinking, however; it is less effective in improving scaffolds mechanical properties. The various crosslinking methods used to crosslink collagen scaffolds are summarised in **Table 2.4** [120].

**Table 2.4:** Crosslinking methods, using chemical treatment, changing the percentage of concentration and the treatment time [120]

| Crosslinking method | Concentration %(w/v) | Treatment duration |
|---|---|---|
| Chemical | | |
| Glutaraldehyde (GA) | 0.0025-2.5 | 20 min-24 h |
| 1-ethyl-3-(3-dimethylaminopropyl) carbodiimide (EDC) | 0.01-2.5 | 2-48 h |
| Hexamethylene di-isocyanate (HDI) | 1.5–5 | 5 h-overnight |
| Tannic acid | 0.1-6 | 10 min -120 h |
| Genipin | 0.00025-0.6 | 1h-48 h |
| Physical method | | |
| Dehydrothermal treatment (DHT) | - | 12 h-5 days @>90 C° |
| Ultraviolet (UV) | - | 15 -240 min |
| Gamma irradiation | - | 250-1250 |

#### *2.2.4.4. Bioink characterisation methods properties*

The properties required from bioinks and 3D bioprinted scaffolds fabricated using extrusion-based bioprinting are outlined in **Figure 2.7**. Properties relating to the inherent characteristics of the bioprinting inks, such as their ability to be printed, their viscoelasticity, storage modulus, gelation properties, and their compatibility with living organisms. The ink's behaviour during the printing process and its interaction with the bioprinter's mechanics are heavily influenced by these qualities, making them essential factors. Assessment of bioprinted scaffolds includes the evaluation of porosity, degradation rates, mechanical strength, printing quality, and cell-friendliness. Each of these factors is crucial in determining the scaffold's capacity to support cellular activities and tissue regeneration.

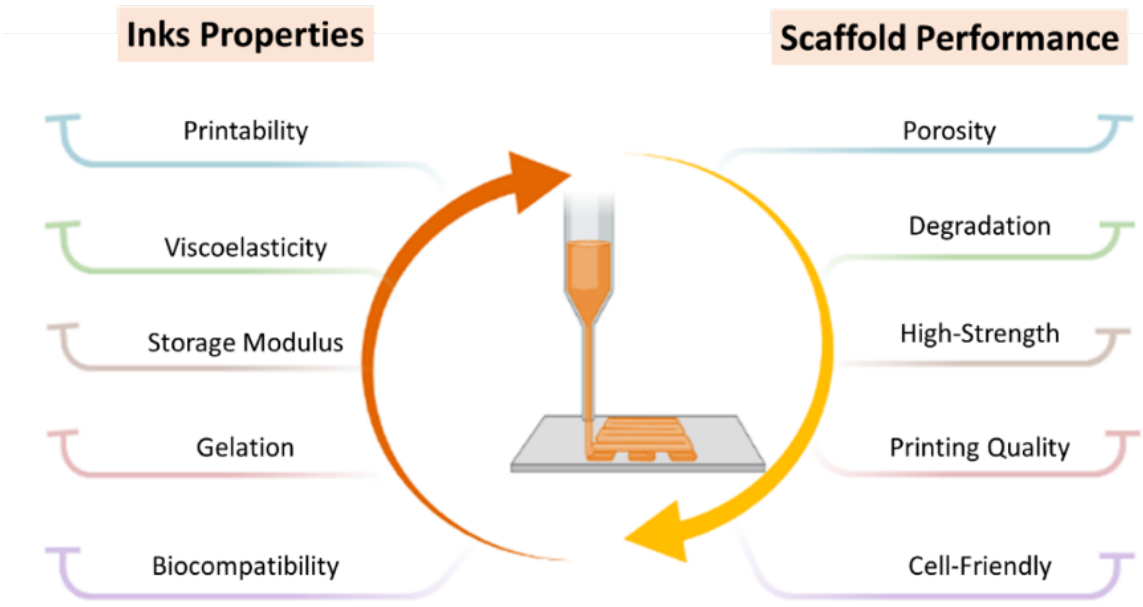



**Figure 2.7:** A framework for sequentially characterising 3D bioprinting, from assessing ink properties to evaluating scaffold performance.

## Rheological behaviour

The rheological properties of inks are important parameters as the material needs to be extruded through a nozzle and to resist deformation after printing. Appropriate rheological properties of bioinks are also required to ensure the maintenance and encapsulation of viable cells during printing. Higher viscosity materials provide greater structural stability; however, they also require greater printing forces. Ideally for extrusion-based bioprinting bioinks should display shear-thinning behaviour, or a drop in viscosity under shear stress, to permit smooth extrusion through the printer nozzle, and then quickly regain its viscosity post-extrusion to retain the scaffold's structure [121][64], [65], [122]. To better understand the viscoelastic characteristics and flow behaviour of bioinks, rheological characterization is a key step in 3D bioprinting for bone regeneration [121]. The bioinks printability, the printed scaffold's structural integrity, and the scaffold's efficacy in encouraging bone regeneration are all greatly impacted by the bioink's rheological properties [121]. Bioinks are commonly characterised rheologically by measuring their viscosity, yield stress, storage and loss moduli (G' and G") with a rheometer [121]. One of the ongoing rheological limitations relating to bioinks is the lack of standardisation in parameters reported between labs. Therefore, Townsend et al. suggested the use of the Herschel-Buckley model to evaluate the shear stress to yield stress, shear rate, flow and consistency index, resulting in standardising the reporting of rheological parameters for bioinks [123]. Printability of bioinks can be assessed by quantifying extrudability, filament fusion, filament collapse [124] .

A range of studies have focused on achieving bioinks with the optimal rheological properties. By adjusting the polymer concentration and the level of methacrylation, Ouyang et al. demonstrated that the rheological characteristics of gelatin methacryloyl (GelMA)-based bioinks could be precisely tuned, enabling the creation of 3D constructs with controlled mechanical properties that could support osteogenic differentiation of human adipose-derived stem cells (hASCs) [125]. In a different study, Duarte Campos *et al.* discovered that the bioink formulation made of methylcellulose, hyaluronic acid, and gelatin had the best rheological properties for printing and supported the osteogenic differentiation of 3D bioprinted mesenchymal stem cells derived from bone marrow [126]. Additionally, Gao *et al.* showed that a composite bioink made of gelatin, fibrinogen, hyaluronic acid, and glycerol had favourable rheological characteristics that made it easier to enable the 3D bioprinting of constructs that could support osteoblast growth and the deposition of minerals that resemble bone [127].

### Extrudability

One of the basic printability requirements is to achieve extrusion of the bioinks from the printing system. The amount of pressure required to achieve extrusion, or extrudability, can affect the cell viability and printing time. The more pressure added to the material to be extruded the greater the shear stress applied to cells, meaning that damage may be inflicted upon the cells during extrusion [128], [129]. Therefore, minimising pressure provides higher cellular viability. Additionally, materials that extrude easily out of the nozzle may print the structure at a faster rate. According to literature, extrudability has been linked to several factors such as: printing parameters, ink viscosity and shear thinning ability. Hölzl *et al.* stated that bioinks are easily extruded when nozzles diameter is increased, length is decreased and using conical shaped nozzles [130].

### Printing fidelity

Printing fidelity is an important parameter that has been used previously to describe the bioprintability of inks. Fidelity determines the level of difference between the designed structure and the actual printed structure [131]. Therefore, the structure with higher fidelity indicates a closer match between the actual and printed structure, on the other hand, low fidelity indicates a higher difference between the designed and printed scaffold. The rheological properties and the bioink's composition have an influence on the injectability of the inks through the nozzle, which affect the filament morphology, printing quality and post-printing stability as shown in **Figure 2.8**. Bioinks with lower viscosity generally have better cell viability, however they have the issue of low fidelity and low printing resolution as shown in **Figure 2.8** (B-D). Higher viscosity does not necessarily increase printing fidelity. The rheological properties of a bioinks can be defined in terms of their storage (G') and loss (G") moduli. G'' represents the liquid state, on the other hand, G' represents the elastic state of the bioinks. Bioinks with higher G' values than the G'' result in higher printing

fidelity as the mechanical stiffness of the ink is higher as shown in **Figure 2.8** (A). By getting the ratio between G' and G'', known as the loss tangent (δ), which can determine the bioprintability of the ink as illustrated in **Figure 2.8** [132],[133].

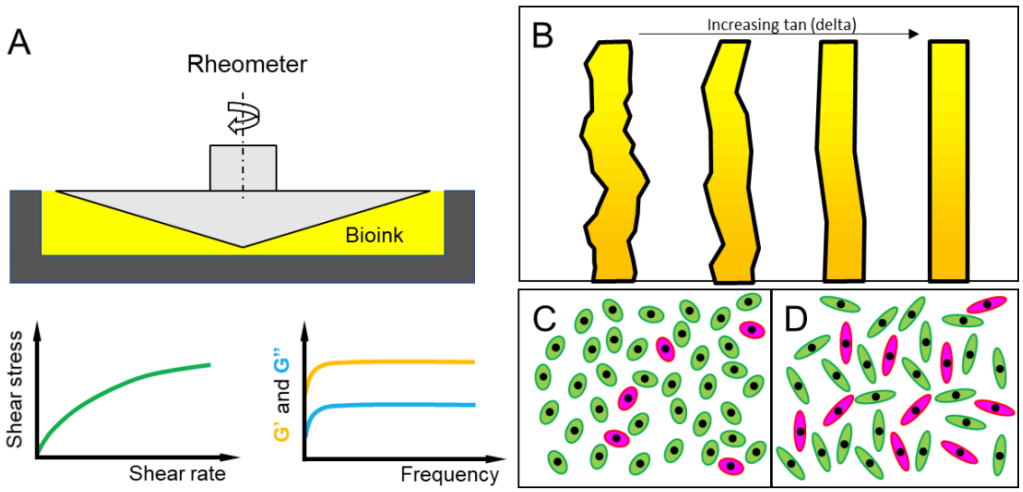



**Figure 2.8:** Rheological behaviour that affects the bioinks fidelity. A) The evaluation of the bioinks shear stress and viscosity using cone-and-plate rheometer. B) The effect of loss tangent parameter on the filament uniformity. C-D) The effect of bioinks viscosity on cell viability where the pink represents the dead cells and green illustrates the live cells (C) shows bioinks with low viscosity and (D) high viscosity bioinks [131].

It has been examined previously by some studies that adjusting the print speed parameter can improve the printed structure fidelity where the velocities should be matched to produce a desired printed pattern when printing on a flat surface. When ink velocity ($v_{ink}$) was lower or higher than nozzle velocity ($v_{noz}$) shorter or longer filaments than intended were generated due to different deposition forces (**Figure 2.9**) [134].

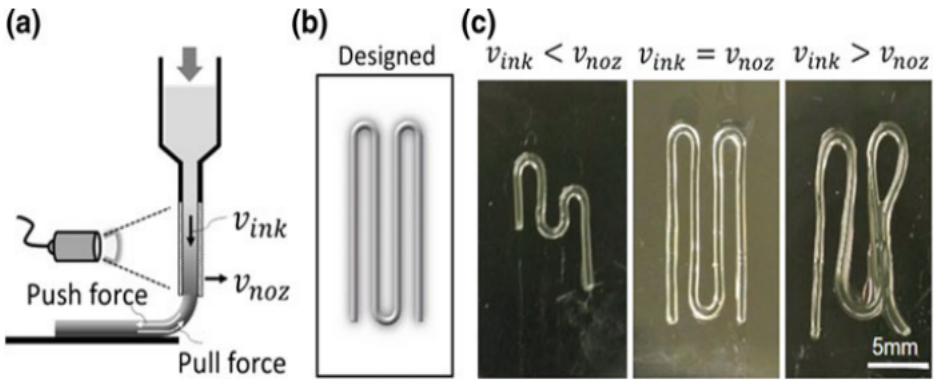



**Figure 2.9:** The influence of print speed on the scaffold printing quality. a) Schematic illustrating standard printing on a flat surface, showing the push and pull forces between the deposited ink and the ink yet to be deposited. b) Diagram of a proposed parallel line model. c) Example images of printed structures with various configurations of $v_{ink}$ and $v_{noz}$. [134].

#### *2.2.4.5. Bioprinted scaffold characterisation properties*

Morphological properties

Morphological characterisation plays a crucial role in understanding the structure and architecture of the printed scaffolds. It mostly involves looking at important properties such as surface morphology, internal structure, pore size, porosity, and pore interconnectivity, which can be studied in depth with tools like scanning electron microscopy (SEM), confocal microscopy, and micro-computed tomography (micro-CT) [135]. Due of its high-resolution imaging capabilities, SEM is a commonly used technique that offers in-depth insights into the scaffold's surface and interior structure [136]. Researchers may examine a variety of micro-architectural characteristics using SEM, including pore size, surface roughness, strut thickness, and overall scaffold morphology [137]. These characteristics are essential for effective tissue ingrowth. Confocal microscopy is a helpful alternative to SEM for characterising scaffolds due to its own set of benefits. It can offer real-time information on the distribution of cells and biomolecules within the scaffold and allow for the visualisation of specific cell-scaffold interactions in a three-dimensional setting [138]. The scaffold's bioactivity and biocompatibility can be evaluated by directly observing cell morphology, dispersion, and proliferation within the collagen [139]. On the other hand, micro-CT images shows the 3D printed scaffold in its entirety enabling quantitative examination of complicated scaffold morphologies and pore interconnectivity to be examined and quantified., This non-destructive imaging technology delivers high-resolution volumetric data that can be reconstructed to produce a full 3D picture of the complete scaffold structure [140]. Analysis of porosity, pore size, and pore distribution with micro-CT is necessary for determining a scaffold's performance, particularly its potential for nutrition diffusion and cellular invasion, all of which are essential to tissue regeneration [141].

Degradation properties

Bone scaffold materials' degradation characteristics play an important role because of their effect on tissue regeneration. For optimal conditions for cell proliferation and differentiation, the breakdown rate of the scaffold should parallel that of new bone tissue creation. Degradation is often measured by observing in vitro or in vivo dimensions and gravimetric (weight) changes over time. Gravimetric study, for instance, entails frequently weighing the degraded scaffold after submerging it in a simulated bodily fluid. Degradation of 3D printed PCL/HA scaffolds was studied using this technique by Li *et al.* [142]. They discovered that scaffolds with a higher HA content degraded at a slower rate, thus the degradation rate could be adjusted by changing the PCL/HA ratio.

SEM and micro-CT are two examples of imaging techniques that can be used to measure dimensional changes, such as those in scaffold volume or thickness. Degradation of 3D printed polycaprolactone scaffolds was evaluated by Hollister *et al.* by carrying out SEM measurements of decreasing scaffold thickness over time, revealing a direct correlation between degradation rate and starting pore size

[143]. The scaffold's performance and appropriateness for bone regeneration can be assessed by combining the results of these degradation characterisation methods with those from other parameters, such as mechanical strength and pore size. However, these techniques come with limitations; they can be time-consuming and carry a risk of damaging the scaffolds during measurement. The introduction to the scaffold degradation chapter will delve deeper into these conventional methods, addressing the challenges they present in more detail and setting the stage for the need for more efficient characterisation approaches.

Mechanical properties

Producing bioprinted scaffolds with the adequate mechanical properties of scaffold is an ongoing challenge in TE. The mechanical properties of a bioprinted scaffold should ideally match those of the host implantation site for optimum tissue regeneration [144]. The ideal scaffold must be strong enough to endure surgical handling during implantation and retain its mechanical strength post-implantation until completion of the tissue regeneration process. Implanted scaffolds are intended to be subjected to continuous load-bearing due to the host body weight and movements. Fractures normally heal to the point of weight-bearing after six weeks in young healthy individuals [145], however, this process can be slower in elderly people and those with osteoporosis. The mechanical strength of a scaffold is influenced by the structural design of the scaffold and its post-printing conditions. Furthermore, composite materials can increase viscosity and the mechanical strength of 3D bioprinted scaffolds. For example, synthetic polymers such as poly(caprolactone) (PCL), polylactic acid (PLA), and calcium phosphate ceramics such as HA and beta-tricalcium phosphate (β-TCP) are commonly used to fabricate bone tissues combined with natural polymers when bioprinting scaffolds for bone TE applications [131].

## 2.3. Design of Experiments (DoE)

DoE can be defined as a mathematical approach that is used for planning and performing experiments, data analysis, and interpretation of the conducted experiments [12]. A DoE approach uses a controlled set of tests to model the relationships between factors and observed responses to plan experiments and analyse data [146]. Using this method, researchers can make evidence-based decisions with the minimum number of experiments. Once the effective factors have been identified, DoE methods can be employed to optimise the experimental response variables [146]. To determine the relationship between the factors and the response variables, the DoE variables must be selected carefully, including their ranges and the number of experiments run [146]. DoE can be applied in several types of systems and processes, such as during product design and development, for statistical quality control, to assess the systematic randomisation used for experiment planning, for results of model fitting and optimisation to conduct systematic research of a system [146]. DoE studies should be designed using as few experimental runs as possible when constructing predictive models and

making a design or technology decision because each experimental run requires costly and time-consuming experimental analysis [147].

The typical approach of a DoE workflow for process optimisation, is illustrated in **Figure 2.10**. In general, the process involves nine steps that can be described as follows: (1) identifying the main project problem, by asking what are the main outcomes of the project; (2) structuring the DoE, which involves planning the experiment and outlining the main objectives of the project; (3) determining the factors, levels, and responses to be investigated in the study, identifying the response assumptions, and defining the methods to be used; (4) the experiment is then completed according to the experimental plan and outputs measured; (5) using output data, mathematical models of the studied process are produced, to meet the study objectives; (6) the built model is evaluated by using the response data and demonstrated visually using plots; (7) the measured responses are then used to identify the significant factors; (8) the final stages of the optimisation involve conducting additional experiments to verify the model's optimal responses; and finally, (9) additional testing is conducted where there is missing data or where further data analysis is required with altered ranges of factors and responses [148].

Generally, a DoE approach is applied in a phased way where a screening study is firstly completed. This allows the number of factors to be reduced and the appropriate levels for each factor to be determined before the optimisation. A range of DoE methods has been used for materials sciences and engineering applications, including factorial experiments, Taguchi and response surface methodologies (RSM) [149], [150], [151]. The following section elaborates on the differences between these methods and how they have been applied to biomaterials and TE applications.

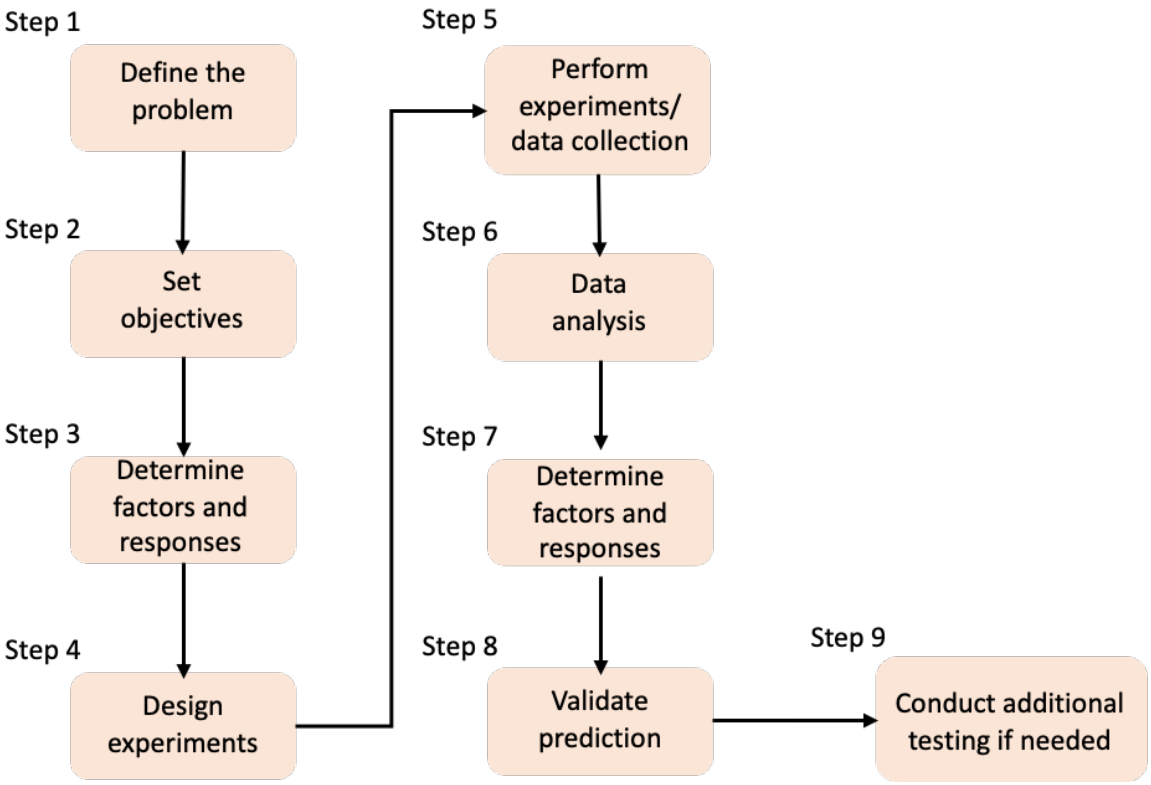



**Figure 2.10:** DoE workflow for the process optimisation.

### 2.3.1. Factorial experiments

Factorial experiments consist of two or more factors, each with discrete possible levels. For two-level factorial designs, the input factors are set at two levels, a 'low' level and a 'high' level, defined as '−1' and '+1', respectively. Full factorial designs contain all possible combinations of low and high levels for all input factors. Therefore, if there are k factors, a full factorial design will consist of 2k experimental runs [12]. This type of design is useful when the number of factors to be explored is low. When there are larger numbers of factors, the design becomes inefficient as a large number of experimental runs are necessary e.g., for a two-level design with four factors (24), 16 runs are required, whereas for seven factors (27), 128 runs are required. In these cases, a fractional factorial design can be employed, whereby a fraction i.e., ½ or ¼, etc., of the runs specified in the full factorial design are carried out. For example, a full factorial design with three factors at two levels, will result in 23 = eight experimental runs, whereas a ½ fraction design, written as 23−1, requires four experimental runs. Fractional factorial designs are only appropriate if the expected interactions between the factors are negligible in comparison to the main effects. The factorial designs are best suited for screening experiments completed to select the main effects within an experiment. Three-level factorial designs examine the factors at three levels, 'low', 'intermediate' and 'high' or '-1', '0' and '1' [152]. Three-level designs enable quadratic responses to be investigated, however, these quickly become prohibitive in terms of the number of runs required.

### 2.3.2. Taguchi Designs

Taguchi designs are types of fractional factorial designs that involve a subset of combinations of multiple factors at multiple levels. The factors are divided into two sets: (1) control factors, which are under our control, and (2) noise factors, which vary due to the experimental environment and are not controlled. The noise factors can vary during the experimental environment even though they have no direct control [153]. Taguchi designs involve the optimisation of a process that has several control factors which directly affect the output target or desired value. These variables can be classified into inputs (M), noise factors (Z), design parameters (X) and outputs (Y), as illustrated in the P-diagram in **Figure 2.11** [154]. The Taguchi design employed will depend on the objectives of the experiment, e.g., two-level Taguchi designs can be used for screening, and other methods can be used for a more detailed investigation of a process [155].

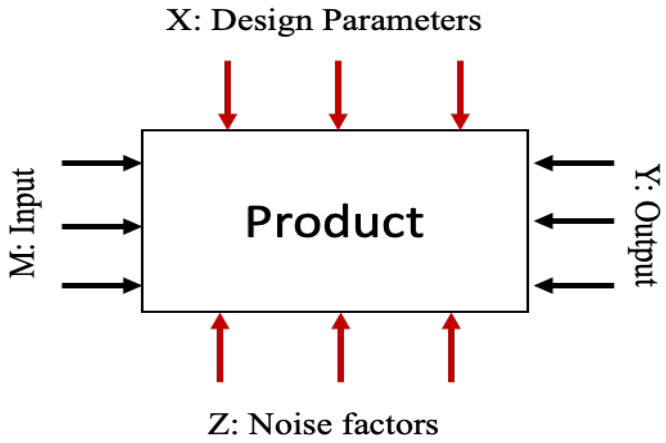
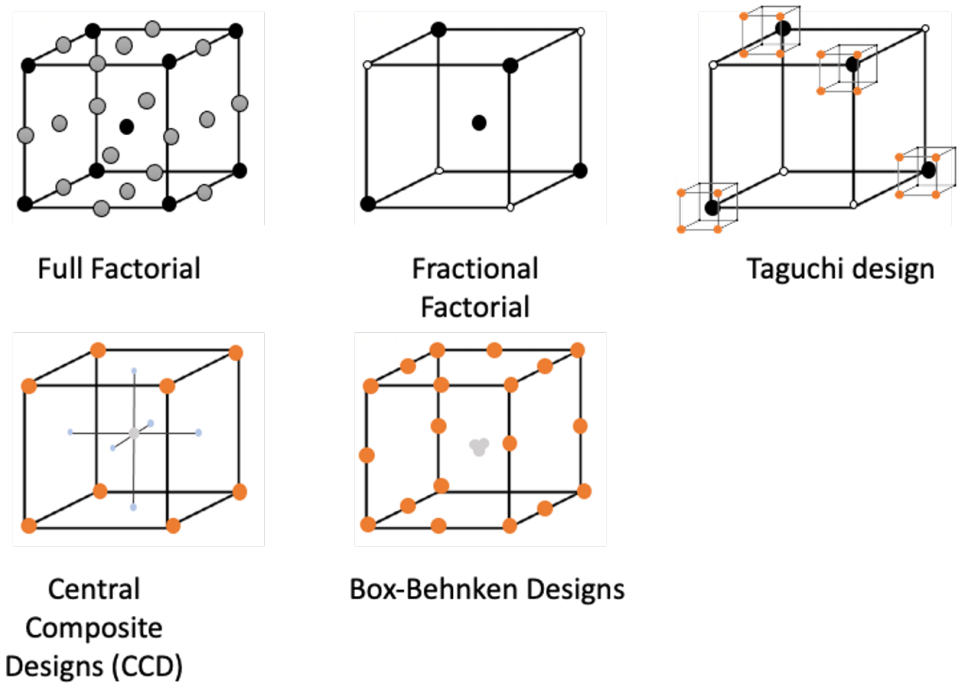



**Figure 2.11:** P-diagram. A P-diagram is used to classify the variables associated with the product into input energy, signal or user intent (M), noise factors (Z), design parameters (X) and output/key product characteristics, functions, performance, etc. (Y).

### 2.3.3. Response Surface Methodology (RSM)

RSM is a collection of statistical and mathematical methods that can be applied in modelling and analysing problems where several input variables affect the response of interest, and the main objective is to optimise this response [12]. The two main groups of RSM designs are (1) central composite designs (CCDs) and (2) Box-Behnken designs (BBDs). Both designs provide an understanding of the behaviour of a system (i.e., reveal the connection between factors and responses) and enable its optimisation. CCDs are usually applied after a process of screening has narrowed down the important factors. It contains central and axial points in addition to cube points, which allow the estimation of higher-order effects, based on a curvature of the response [156]. BBDs

have fewer experimental runs than CCDs and do not have points at the vertices of the cube (i.e., low and high points). As a result, the prediction quality of BBDs, the quality is lower than the standard CCDs, however, they offer advantages for physical experimentation because extreme points are time-consuming and costly to investigate [156]. RSM is primarily aimed at optimising a system and can also be used to assess interactions and higher-order terms (e.g., quadratic or cubic), which is not feasible with other experimental design methods. The choice of the DoE methodological approach depends on the problem that needs to be investigated and the main experimental objectives [157]. The data points required for each DoE method, are summarised in **Figure 2.12**.




| | Required Experiment Data points |
|---|---|
| Full Factorial Design | 27 |
| Fractional Factorial Design | 5 (82%-time reduction) |
| Taguchi Design | 16 (41%-time reduction) |
| Central Composite Design | 15 (44%-time reduction) |
| Box Behnken Design | 13 (52%- time reduction) |

**Figure 2.12:** Number of experimental runs required for each design for 3 factors investigated at 3 levels.

### 2.3.4. Statistical Tools

In addition to selecting representative runs that successfully sample the domain of research, dedicated procedures for post-processing the experimental results need to be used. These methods yield both qualitative and quantitative data relating to the impact of the many independent variables on the dependent variables. The analysis of variance (ANOVA) method is a mathematical and statistical process for determining whether there are differences between the means of groups within a sample and whether these differences are random or can be related to a particular cause [158]. In DoE, the sample represents a set of experiments completed in accordance with a predetermined plan while groups within a sample are a collection of data connected to a specific factor, level or response. ANOVA breaks down the total variance and allocates it to all the distinct causes by comparing the group means of a sample. As a result, it may be used to quantify the effect of factors and responses on the independent variables [158].

### 2.3.5. Comparison of the DoE Techniques

The DoE techniques described have various advantages and disadvantages and the choice of design will depend on the objectives of the experiment and the number of factors that need to be investigated. Two-level factorial experiments are best suited for the investigation of main effects or as screening designs [12]. Taguchi designs are also best suited for screening experiments. Taguchi designs are often utilised for very large screening experiments [159]. Three-level factorial designs and RSM techniques are more suited for studying interactions between factors, for process optimisation, troubleshooting process problems and the assessment of the overall robustness of a process [160]. Generally, it is recommended to complete a screening design to determine the main effects before optimisation to reduce the numbers of factors required and to ensure the suitability of the levels selected for each factor. In the selection of the most suitable RSM technique, it is useful to consider the number of experimental runs required for each design. Considering an experimental design, consisting of three factors at three levels, a full factorial design will require 27 experimental runs, a BBD will require 13 experimental runs and a CCD will require 15 experimental runs. Although the CCD approach requires a greater number of experimental runs, it has advantages in that it can include up to five levels per factor and they allow for the inclusion of runs where all factors are at their extreme settings, e.g., all at the high settings.

## 2.4. Application of DoE Methods in Biomaterials and TE Research

There have been many studies applying DoE methods in biomaterials and TE research which include the optimisation scaffold fabrication methods [157], [161], [162], [163], [164], [165], hydrogels [166] , bioactive extraction methods [167], electrospun materials [168] and 3D bioprinting. In particular, 3D bioprinting [169] has been the focus of a number of studies [170], [171], [172].

DoE has been employed to explore the influence of the bioink's properties, printing parameters and scaffold design on the properties of the resultant construct [170], [171], [172]. For instance, Trachtenberg *et al.* applied a full-factorial design to investigate the influence of poly (propylene fumarate) (PPF) concentration, printing pressure, printing speed and fibre spacing on the bioinks viscosity, fibre diameter and pore size of 3D printed polymer PCL scaffolds [172]. The study generated linear models relating the PPF concentration to the shear-thinning behaviour of the bioinks, and fibre-spacing and the pressure to the pore size and fibre diameter. Overall, the work provided statistical models with the potential for evaluating the 3D printing compatibility of novel biomaterials and for optimising the extrusion of these materials for fabricating 3D scaffolds with predictable architectures.

Bhargav *et al.* optimised the surface morphology and structure of e-jetted (Electro-hydro dynamic jetting) 3D printed scaffolds using a Taguchi design [170]. This study optimised the scaffold surface morphology by altering the following morphological parameters: (1) pore size, (2) fibre diameter, (3) fibre orientation and (4) the number of layers [170]. Taguchi design was used to understand the relationship between these input parameters and their effect on the mechanical and morphological properties of the resultant construct. These structural parameters play a key role in cell attachment to the construct. In this study, the construct was designed as a square mesh. A Taguchi design was applied, using an orthogonal array, where four factors (i.e., pore size, fibre diameter, fibre orientation and number of layers) were evaluated at three levels. The results showed the effect of the four factors on the mechanical properties of the construct [170].

RSM has also been applied for the optimisation of tissue-engineered constructs. Shizard *et al.* investigated the relationship between the architecture and mechanical performance of the constructs fabricated using 3D printing, using the RSM technique [171]. The study showed the influence of the pore size, architecture and porosity, on the mechanical properties of both uniform and gradient constructs designed for the TE applications relating to hard tissue repair. Specifically, the study aimed to simultaneously optimise the physical, mechanical and biological properties of the construct using the CCD method. The study investigated two factors, based on the geometric parameters of the scaffold, i.e., (1) strut length and (2) strut radius. The porosity and Young's modulus of the construct was determined using the experimental methods and finite element analysis (FEA) modelling. FEA is a widely used computational approach for the analysis of stress distribution within complex geometries and the optimisation of the mechanical properties of a designed element [173]. The use of simulation models, such as the FEA, can be expensive and time-consuming, and requires expensive software and significant processing power, therefore, their utility is limited. Applying DoE methods to simulations allows for the creation of surrogate models that have a sufficient predictive performance and can be utilised to explore the broad domains in a quick and straightforward manner [174], [175].

Jankovic *et al.* also highlighted that during the selection of the optimal design, the physical limitations of the experiment, such as time and material resources and the ability to perform experiments under extreme conditions must be carefully considered and the selected design should secure a comprehensive picture of interactions, using as few resources as possible during the physical experiment. Large data sets and certain types of data cause significant challenges for the DoE methodologies. Correlational or ML methods are better suited for the analysis of big data sets [147]. The next section of this thesis discusses the potential benefits of introducing ML into biomaterials and TE research.

## 2.5. Machine Learning

ML has the potential for application in a range of biomaterials and TE applications, such as materials development, the optimisation of scaffolds, cells, and drug delivery [176]. While the DoE is a powerful tool for identifying the relationships between input parameters and reducing the need for costly and time-consuming experiments, the limitations relating to the application of these techniques in biomaterials and TE research remain. The application of ML techniques to these research fields presents new opportunities to utilise data to better customise TE processes. Harnessing the power of ML has the potential to bring about rapid advances within the fields of biomaterials and TE. ML can utilise larger quantities and a wider variety of data, including experimental parameters, sensor observations and images or scans, to extend the potential for identifying key relationships between the properties of tissue-engineered constructs.

In this section, a brief overview of ML is presented, identifying the key types relevant to biomedical applications, followed by a review of the current state of the art in applying ML in biomaterials and tissue engineering.

There are different ways to define ML, e.g., according to Alpaydin [177], ML is considered part of artificial intelligence (AI) where the system can learn from given data to produce predictions and to optimise the model parameters using training data. Similarly, Park *et al.* state that ML can be defined as a field in computer science that can create algorithms that can learn from a big set of data and produces predictions on the data [178]. ML models have shown great improvements in learning complex patterns that enable a model to predict unobserved results and allow computers to train on imported data and use statistical approaches to output results within a certain range [179]. In general, ML techniques can be grouped into three types: (1) supervised [180], (2) unsupervised [181] and (3) reinforcement learning [182], according to how they use labelled data. An overview of these techniques is provided in **Figure 2.13**.

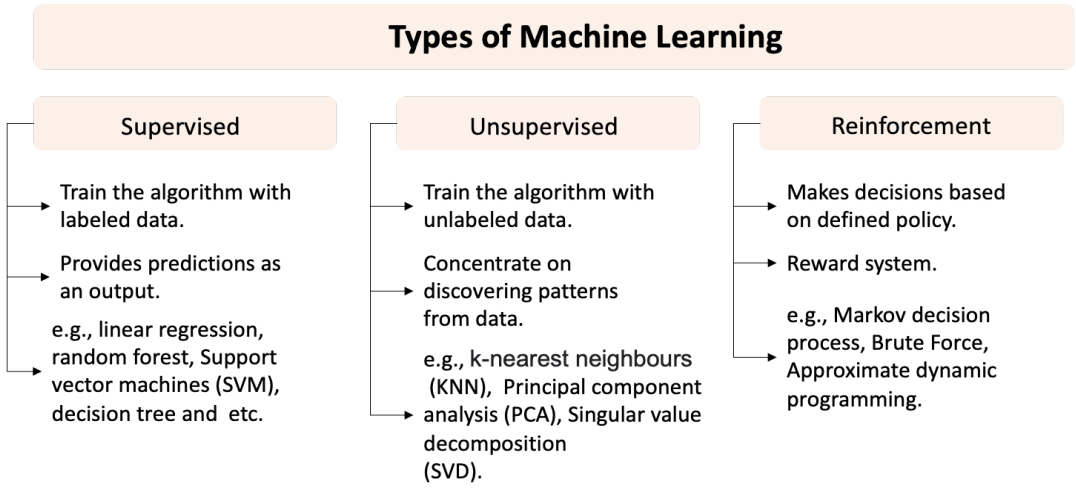



**Figure 2.13:** Overview of the ML types that can be used for different applications, supervised, unsupervised and reinforcement learning.

### 2.5.1. Supervised Learning

Supervised learning is an ML approach that aims to predict unknown outputs using labelled training data, based on prior observations. Supervised learning works by receiving datasets and then training a regression/classification model [183], [184], [185]. Subsequently, the model can generate predictions to respond to new, unseen input data. There are several types of classification techniques that focus on providing categorisation, data analysis and pattern recognition [185], [186]. The benefits and limitations relating to supervised ML techniques that have been previously applied and have potential for greater use in biomaterials and TE applications are summarised in **Table 2.5**.

**Table 2.5:** ML approaches that can be used in Biomaterials and TE applications.

| Algorithms | Category | Assumptions | Benefits | Limitations | Ref |
|---|---|---|---|---|---|
| Linear regression | Regression | Linearity, fixed features, independence, normality;<br>Error variance is assumed to be constant. | Simple application;<br>Guaranteed to find the optimal solution. | Only works for linear relationship data. | [186], [18 |
| Random forest | Classification | Assume model errors are uncorrelated and uniform. | Provides fast learning and highly accurate predictions;<br>Can intake large set of data without variable deletion;<br>Can work with unbalanced data sets. | Time-consuming to form predictions. | [188], [18 |

| | | | | | |
|---|---|---|---|---|---|
| Decision tree | Classification, Regression | The classes must be mutually exclusive. | Easy to use and to understand, efficient algorithm (especially for predictions). | Depending on the selection order, missing factors from the characteristic overfitting. | [188] |
| Neural networks | Classification, Regression | Variable independence, linearity. | Can be used for classification and regression, able to use the Boolean functions; Allows inputs with noise. | Overfitting due to too many attributes; Hard to understand the algorithm structure. | [188] |
| Support vector machines (SVM) | Classification, Regression | Model assumptions depend on the probability of default (PD). | Complexity of the model can be easily controlled; The models use non-linear boundaries. | Hard to understand the algorithm structure; Data training is slow. | [186], [18 |
| Kernel ridge regression (KRR) | Regression | Linear or nonlinear function. | Computational simplicity; Prevents overfitting. | Computationally expensive. | [190], [19 |
| Bayesian optimisation (OP) | Optimisation | A non-convex problem; No access to derivative. | Hyperparameter tuning; Cost-efficient. | The objective function can't be modelled; High dimension problem. | [192], [19 |

#### 2.5.1.1. *Linear Regression*

Regression analysis can be described as the function used to make predictions on real value outputs, where this function can signify the dependent variable by identifying the independent variables [187]. Linear regression analysis is an approach whereby a linear relationship is modelled to predict or explain the relationship between variables [194]. This linear relationship between two variables can be illustrated as a straight line. A linear regression model, therefore, aims to optimise the fitting of a straight line to a given dataset [186]. However, the use of a straight-line approach can provide an imperfect summary of the complex relationships and can be influenced by randomness in the experimental data.

#### *2.5.1.2. Decision Tree and Random Forest*

A decision tree is a supervised learning algorithm that can be used for classification and regression problems. The approach involves a series of sequential decisions that enable a specific result to be reached. For classification problems, decision trees can be used to segregate a data set into classes that correspond to the response variable. The most basic decision trees involve splitting the response variable into two categories: (1) yes/no or (2) 0/1. Alternative decision tree algorithms can be used if the response variable contains more than two categories. A regression tree is a type of decision tree in which the target variable can take continuous values. They are frequently used to predict numerical problems. The type of decision tree that needs to be applied depends on the desired variable [195].

Decision trees are extremely quick and can handle high-dimensional datasets and larger input datasets compared to other approaches [196]. One challenge in applying decision trees is that they can be prone to overfitting issues, where the system tightly fits the training data to the extent that it is inaccurate in predicting the outcomes of new data [197]. While such systems have a very low training error, the test error may be bigger. This problem can be addressed by using random forests, which combine [198] several decision trees, and uses bootstrapping and aggregation to train numerous decision trees, simultaneously [199]. Data and characteristics are randomly selected for each decision tree and an average of the individual decision tree predictions yields the result. Each tree receives data from the original dataset and at each node, a subset of the optional attributes is chosen at random. This approach combines many weak or poorly connected classifiers into one strong classifier [200]. As a result, random forests maintain their speed while also being extremely resistant to overfitting [201].

#### *2.5.1.3. Neural Networks*

Neural networks, also known as artificial neural networks (ANNs), are defined as computational models that attempt to imitate the human brain using neuron nodes interconnected in a web. In the

human brain, billions of cells called neurons can be found where they are responsible for processing information (i.e., input data) and generating responses (i.e., output data). Similarly, ANNs have hundreds of thousands of artificial neurons, called processing units, as interconnected nodes [187]. More recent models, called deep neural networks or deep learning, have been used extensively for natural language processing and computer vision and can contain billions of neurons [187]. ANNs work by arranging processing units into layers of inputs and outputs [187]. The input layer collects data, then the neural network model uses hidden layers and nodes to learn through many iterative phases and to optimise the predicted results as an output [187].

Knowledge-based ANNs utilise a hybrid learning approach, combining theoretical knowledge with the knowledge learnt from a set of classified examples, thus enabling them to learn more effectively than the classical ANN approach. In the knowledge based ANNs, the output of one sub-ANN is used as an input to another sub-ANN in the chain. This allows the hidden layers of the knowledge based ANNs to work in a more dimensionally uniform environment than the classical ANNs, resulting in a reduction of 12 neurons. This approach has improved the accuracy in training ANNs, while also minimising the prediction error [202]. Nagerejan *et al.* applied knowledge-based ANNs to develop a metamodel capable of dynamically predicting control factors of a fused deposition modelling additive manufacturing process training time [202]. The study demonstrated the potential of this approach to reduce the dimensionality of the complex additive manufacturing problems.

A further class of ANNs is the convolutional neural networks (CNNs) that apply a convolution function to further refine the outputs. CNNs have been widely used in the material manufacturing sector, mainly using computer vision for detecting defects [155], [203], [204], [205]. CNNs learn using images as inputs to the model and internal layers that can detect certain features, such as edges and lines in an object. The classifier is trained by using labelled images and can output a class label or labels, localisation of objects or a full segmentation of the image.

#### *2.5.1.4. Support Vector Machines (SVMs)*

A classical and widely used ML technique, support vector machines (SVMs) are linear classifiers that predict the class of each input's members from a set of two possible classes. To classify all inputs in a high-dimensional or even infinite space, SVMs generate hyperplanes or groups of hyperplanes. The closest points of categorisation are known as support vectors. SVMs are most concerned with the hyperplane-to-support-vector margin [206]. The success of SVMs in producing accurate findings is due to their ability to train well with only a few features, robustness against model error and computational efficiency when compared to other ML methods, such as ANNs [197].

#### *2.5.1.5. Kernel Ridge Regression (KRR)*

A refinement of SVMs, the Kernel ridge regression (KRR), also known as least-square support-vector machines (LS-SVMs), is a non-parametric technique that calculates the target by

computing the inputs directly [190]. It is a nonlinear regression method that incorporates regularisation to avoid overfitting. Hyperparameters, i.e., parameters used to control the learning process, and training data size have a significant impact on the performance of the KRR learning model [191]. The approach can be used for classification and regression analysis [207].

#### *2.5.1.6. Bayesian Optimisation (BO)*

Hyperparameters and their optimisation are a key part of ML engineering and can have a significant impact on the performance of the model. Bayesian optimisation (BO) is commonly used in ML for hyperparameter optimisation [208] and is very useful in situations where evaluations of a function are costly[209]. Bayesian optimisation is a sequential model-based approach designed to deal with the problem of finding a global minimiser (or maximiser) of an unknown objective function *f*:

$$x^* = \arg\min_{x \in X} f(x)$$

Where $x$ is some design space of interest. Furthermore, the Bayesian optimisation is about maintaining a probabilistic surrogate model over likely functions given in the observed data, and sequentially selecting the future query points according to a selection policy, which leverages the uncertainty in the surrogate to negotiate the exploration of the search space and the exploitation of currently suspected modes [205], [206]. This has a particular use for complex scenarios, such as those found in biomaterials and TE, where the model must incorporate the input from several complex systems.

#### *2.5.1.7. Hierarchical Machine Learning (HML)*

One of the major challenges in applying ML to the fields of biomaterials and TE research, is the limited availability of labelled experimental datasets. This can result in highly imbalanced data where there are higher volumes of data from typical or "normal" scenarios and relatively low volumes of input data for the disease, treatment or syndrome cases. Statistical ML methods then tend to default to see everything as the typical or majority case. Hierarchical (HML) is used to handle class imbalance with smaller labelled datasets and can be considered a supervised method. HML involves adapting the human learning strategy using multi-level learning [210] and works by compartmentalising and separating the classifications, e.g., between individuals and the diagnosis [211].

## 2.6. Applications of ML in Biomaterials and TE Research

In the years to come, ML will continue to be a crucial part of how science and understanding move forward. As increasingly massive datasets are generated and captured, these technologies have the potential to enhance engineering design and act as more accurate experimental outcome predictors. Numerous other engineering fields have acknowledged the value of these technologies and have

already started to adopt them [212], [213]. The development of biomaterials and medical device technologies for TE applications has lagged this trend. The use of ML in biomaterials and TE research has the potential to provide researchers with the ability to discover patterns in data, enabling the accelerated development and specialisation of outputs for individualised or personalised solutions. The application of ML in biomaterials and TE is a nascent field and, to date, relatively few studies have explored the use of ML techniques. At this stage, supervised learning methods have been most used in TE. A key requirement for the development of most supervised ML models is the labelled data, and even the unsupervised methods that generally require some labelled data to evaluate the performance of the generated models. In TE, these data typically take the form of biomaterial or tissue-engineered construct characteristics, which can be analysed to produce predictions, based on extracted features [19]. Currently, there is a lack of suitable labelled publicly available datasets for the evaluation of ML applications in these areas.

Recent advances have involved the application of ML for material optimisation, classification and image segmentation [18], [24], [27], [183]. In particular, there has been recent interest in bringing ML approaches to optimise and automate the fabrication processes and provide predictions relating to the material behaviour under certain parameters [14], [28], [176]. Entekhabi *et al.* applied the ML approaches to explore the rate of degradation of a freeze-dried gelatin scaffold crosslinked with genipin [24]. In this study, the scaffolds were fabricated using different concentrations of gelatin (2.5%, 5% and 10%(w/v)) and genipin (0%, 0.125%, 0.25%, 0.5% and 1% (w/w)) using freeze-drying to create the porous 3D constructs. The rate of construct degradation was measured experimentally by determining the weight change of the scaffold over a 28-day timeframe and collated for mathematical modelling using the data-driven ML approaches. The collected data served as the input for two different supervised learning algorithms, neural networks (i.e., ANN) and KRR. For developing an accurate and vigorous prediction, different experimental measurements were selected, according to their correlation with the degradation rate, generating the following variables: porosity, pore size, swelling behaviour, mechanical properties, the extent of crosslinking, and degradation behaviour (**Figure 2.14**). The predictions obtained from the different algorithms were compared to the experimental data, showing that ANNs topped the ranking with a mean squared error of 2.68%. Although, in other studies, the KRR has been found to provide a better accuracy than the ANNs, while also having the advantage of not being computationally expensive in training big data [214]. Overall, this study demonstrated the role of ML in saving time and reducing the cost of experimental studies. Further studies can be carried out to explore the different parameters that could be optimised to improve the degradation rate prediction, as well as various other types of data [24].

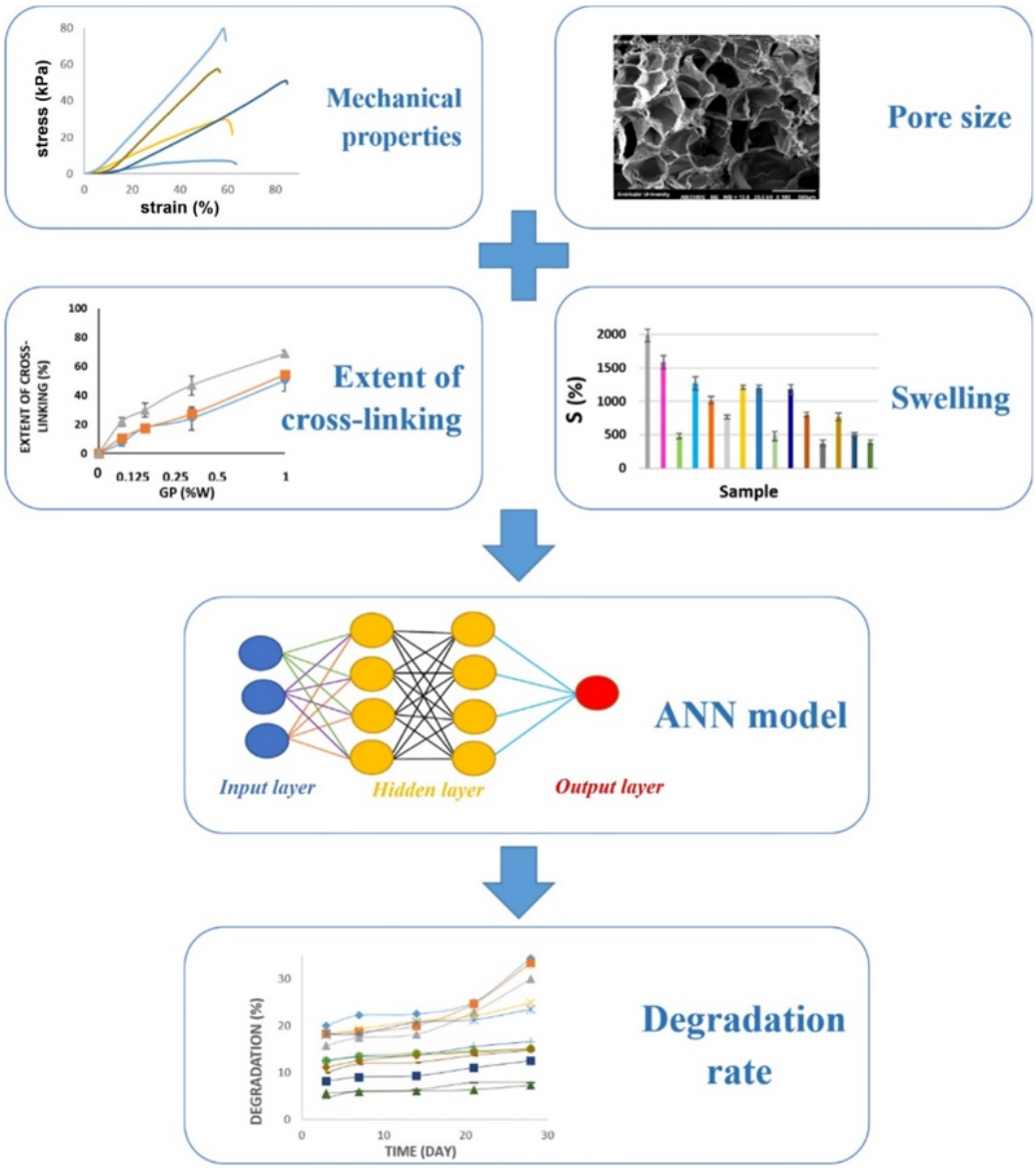



**Figure 2.14:** Schematic diagram of the input data (from the material characterisation results) and the output prediction using ML methods [24].

ML has also been recently applied to optimise the various steps of the 3D bioprinting process for the fabrication of tissue-engineered constructs [18], [19], [20], [21], [22]. Lee *et al.* developed a ML-based method for the design of 3D-printable bioinks composed of naturally derived biomaterials. In this study, the relationships between the rheological properties and printability were analysed using ML. The analysis process employed the relative least general generalisation algorithm, an ILP methodology that is useful for classification problems. A multiple regression was used to support the ML results and the prediction of the printability by the ink composition. In this study, 19 samples were used for modelling and six samples for the validation of the prediction algorithm. The study demonstrated a universal relationship between the mechanical properties of the bioinks and the printability, showing that a high elastic modulus improves the shape fidelity, and that extrusion is

possible below the critical yield stress. Based on this relationship, various formulations of naturally derived bioinks that provide high shape fidelity were derived using the multiple regression analysis [16].

A recent study by Ng *et al*. highlighted the potential of applying computer vision and ML to optimise three different bioprinting methods: (1) extrusion, (2) jetting-inject and (3) vat polymerisation-stereolithography [18]. Within their study, they proposed mathematical equations that can be used to identify the correlations between the bioprinting parameters for each process [18]. Each bioprinting process has different parameters of interest and different bioinks require unique bioprinting parameters depending on the material behaviour. For the extrusion-based bioprinting techniques, the important parameters that could be investigated using ML techniques, include the printing resolution, the nozzle diameter, the material viscosity, the nozzle length, the stage speed and the change in pressure (**Figure 2.15**(A)). The relationships between these parameters can be modelled using deep learning that can be trained by taking the main printing parameters as inputs and error minimising between the predicted and actual outcomes. By selecting the optimal parameters of the key outputs, e.g., printing resolution, cell viability and fabrication, speed may be influenced [18].

Furthermore, Ng *et al.* recommended the use of a reinforcement learning agent to automatically select the values for the pressure drop and plate speed. It will assist reinforcement learning in learning and selecting the ideal values for printing parameter variables so that poor outcomes, such as a low cell viability, will not occur. This will enable the production of improved bioprinted scaffolds with the desired fabrication speed, higher cell viability and better printing resolution [18]. Finally, the use of in-situ monitoring in bioprinting can help reduce possible errors, such as excess or missing layers of material, to guarantee consistency in the fabrication of 3D bioprinted constructs (**Figure 2.15**(B)). In this study, a CNN classifier was trained by using images labelled as ‘under extrusion’, ‘good quality’ and ‘over extrusion’ (**Figure 2.15**(B)). The schematic diagram represents a feedback loop that adjusts the 3D printing parameters, such as the material flow rate. This is accomplished by using real-time in-situ monitoring (recording images) and the CNN model. This ML approach enables the production of constructs with a higher repeatability and accuracy. This approach can also be used to predict the material properties of a diverse range of bioinks compositions and for the development of novel scaffold designs for specific purposes by learning from a huge database of materials and designs [19].

Conev *et al.* also applied ML for the optimisation of the 3D printing parameters. The study distinguished between low-quality and high-quality printing configurations as a first step toward developing a recommendation system for identifying the optimal printing circumstances. The ML-based framework took the composition of the material and the printing parameters as inputs and predicted whether the quality of the print would be “low” or “high”. They applied two ML-based

strategies: (1) a direct classification-based method that used a regression ML model to approximately predict the values of a printing quality metric and (2) an indirect approach that used a ML model to train a classifier to distinguish between "low" and "high" quality prints. The random forests method is the foundation of both models. One of the main issues faced within this study was the lack of data. Their analysis had revealed that a complete factorial design for data collecting can result in data redundancy in the context of ML [183].

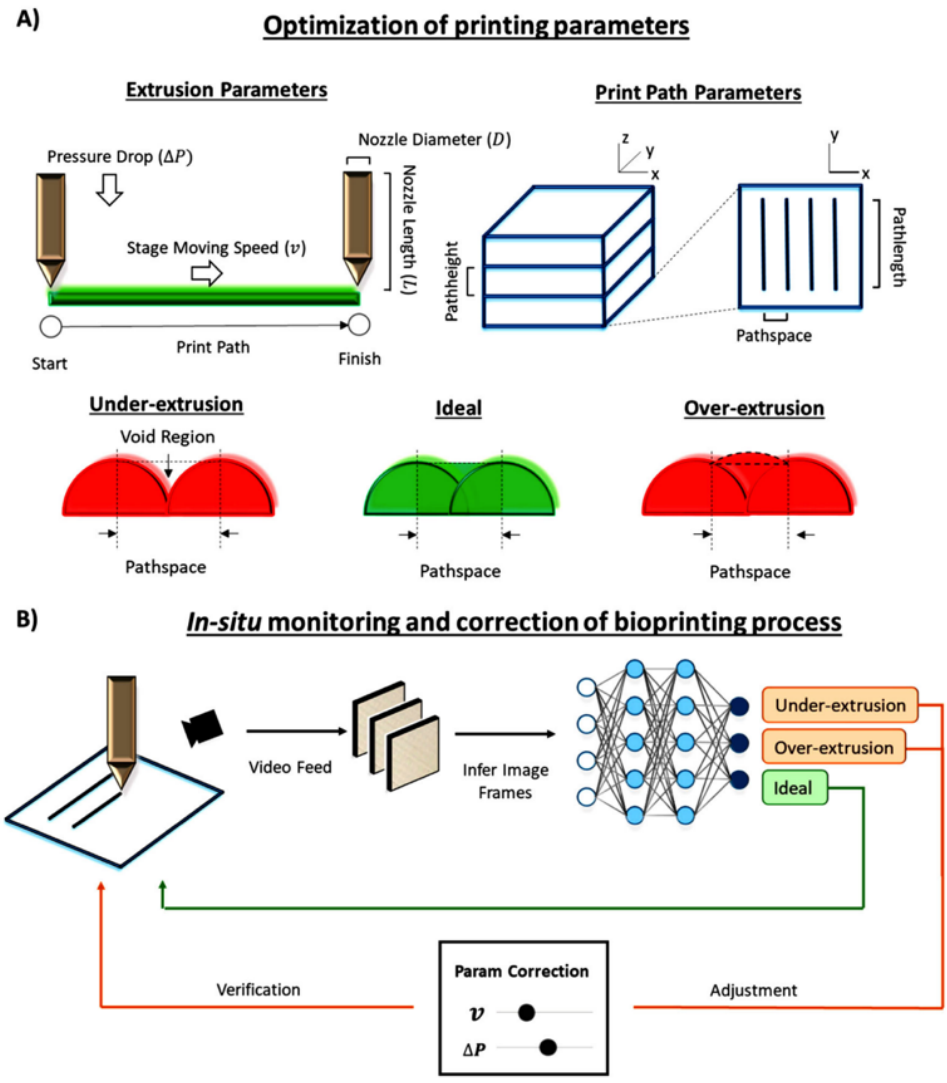



**Figure 2.15:** (A) Three-dimensional bioprinting optimisation processes. (B) Computer vision method used for the optimisation and correction of 3D bioprinting using ML approaches [18].

One challenge in the application of ML to biomaterial and TE applications is the limited data available for the model generation. Bone *et al.* addressed the problem of a small dataset by constructing a HML algorithm, wherein the structure of the middle layer leverages the known

physical relationships relating to the alginate's gelation process [21]. This approach was applied to optimise the alginate hydrogel scaffolds fabricated by 3D bioprinting, using the freeform reversible embedding of the suspended hydrogel (FRESH) method. Within the study, the material selection, material formulation and the process parameters were explored to achieve the optimal print fidelity of the printed scaffolds, in terms of linewidth and shape fidelity. The process firstly involved generating a dataset of both high- and low-fidelity alginate prints by systematically varying the print input parameters and assessing the resulting prints in terms of dimensional similarity to the original CAD designs. The model fit was assessed by cross-validation and then optimised to minimize the print error, generating a new set of optimised input variables predicted to generate the high-fidelity prints with an error of less than 10% in dimensionality from the original CAD specification.

An alternative approach to overcome the challenge relating to the small dataset was employed by Ruberu *et al.*, where they utilised the Bayesian optimisation (BO), a sample efficient optimisation algorithm, for the optimisation of the 3D bioprinting of GelMA and hyaluronic acid methacrylate (HAMA) bioinks [20]. The performance was assessed based on two fundamental criteria in the printing process: (1) the filament formation of the bioinks and (2) the layer stacking of the 3D scaffold, were incorporated into a scoring system established to assess the printability. The process involved adding the bioink's concentration and printer parameter settings to the optimiser search space and the output recommendations predicted by a 'black-box' model were provided to the experimenter where they were scored, based on a visual assessment of the filament morphology and pore architecture.

For numerical simulations, data-driven methods using ML have also been shown to outperform traditional methods grounded in mathematics and physics. Koeppe *et al.* applied neural networks and deep learning to forecast the stress in a 3D printed lattice structure [25]. The approach involved manufacturing and mechanically testing the lattice specimens. The experimental results were used to validate a parameterised FEA model designed to calculate the stresses in the structures with different design parameters during deformation. Finally, these deformations and design parameters were used to train a neural network. They reported that a ML model takes roughly 0.47 s to predict the stresses, instead of 5–10 h for an FEA simulation [25]. Similarly, Khadilkar *et al.* used the data-driven CNN to make stress predictions in milliseconds, compared to an FEA method which took a 2–3 min to give stress predictions [215].

## 2.7. Classical ML Techniques Compared with DoE Methods

The selection of a ML approach over a DoE approach requires a clear understanding of the differences between the two methodologies. Nowadays, DoE is used widely to help optimise processes by reducing the running time and cost of experiments [216]. The process is a human-centred method using a relatively small volume of data, where the researcher is required to

select the necessary input factors that need to be included within an experiment, depending on their existing knowledge of the process. By comparison, ML is an automated process, where the data patterns are detected, based on both the input and the output data [217]. According to Freiesleben *et al.,* ML supervised algorithms may be slightly human biased because of the data labelling compared to the unsupervised algorithms but still give better and faster results once trained [216]. In some cases, dealing with a high volume of data, i.e., "big data", or data with a high dimensionality (p>>n) can have a great effect on the performance of the statistical methods. Typically, DoE methods may encounter problems when data are not in numerical format [218], whereas some ML approaches can incorporate different input and output data types. Therefore, the size and type of the data to be used can have a greater influence on the performance of the DoE studies, compared to ML-based studies.

Comparing the two approaches for application in biomaterials and TE research, it is noted that the use of the DoE methodologies is more effective in terms of experiment reduction, by detecting the most relevant factors, while ML can be used for the high accuracy prediction or classification on a large amount of data. In terms of TE, ML can play an important role in simplifying the modelling of complex interactions involved in multiple biological, chemical, and physical processes in TE. Understanding and defining the principles underlying these processes is considered highly challenging. While standard statistical optimisation, e.g., DoE, has been used in numerous studies in recent years to produce optimal design/fabrication parameters [24], ML has, more recently, shown the potential to produce prediction in terms of scaffold fabrication. The main objective for both ML and the more specific statistical optimisation is to use data to learn and develop mathematical models. The main differences are that statistical optimisation requires a connection between the selected variables to make predictions for the new variables. However, ML can predict data without having to make a new assumption about the actual relationship between the variables. This means that ML treats algorithms, such as a black box [24]. In summary, the two methodologies have two different aims; a DoE primarily focusses on identifying the optimal input factors for the relevant process parameters while ML focuses on identifying patterns in unstructured raw data [216].

One challenge in developing ML models is that using large datasets to train a model can be time consuming and expensive. Therefore, the combination of DoE methods with ML holds the potential to further enhance the optimisation within the field of TE. This approach has been successfully applied in product innovation [218], and the chemical [219] and energy consumption industries [220]. DoE data has been used previously in ML algorithms to optimise the initial parameter settings (**Figure 2.16**) [218]. In addition, the use of ML has also helped the aim of DoE by detecting the optimal factors and interactions [216] (**Figure 2.16**), where the final ML algorithm proposes the next experimental configuration. Therefore, this strategy is often referred to as "active learning" [221] since it puts the learner in control of the data and from that, the machine [222], [215], [219]

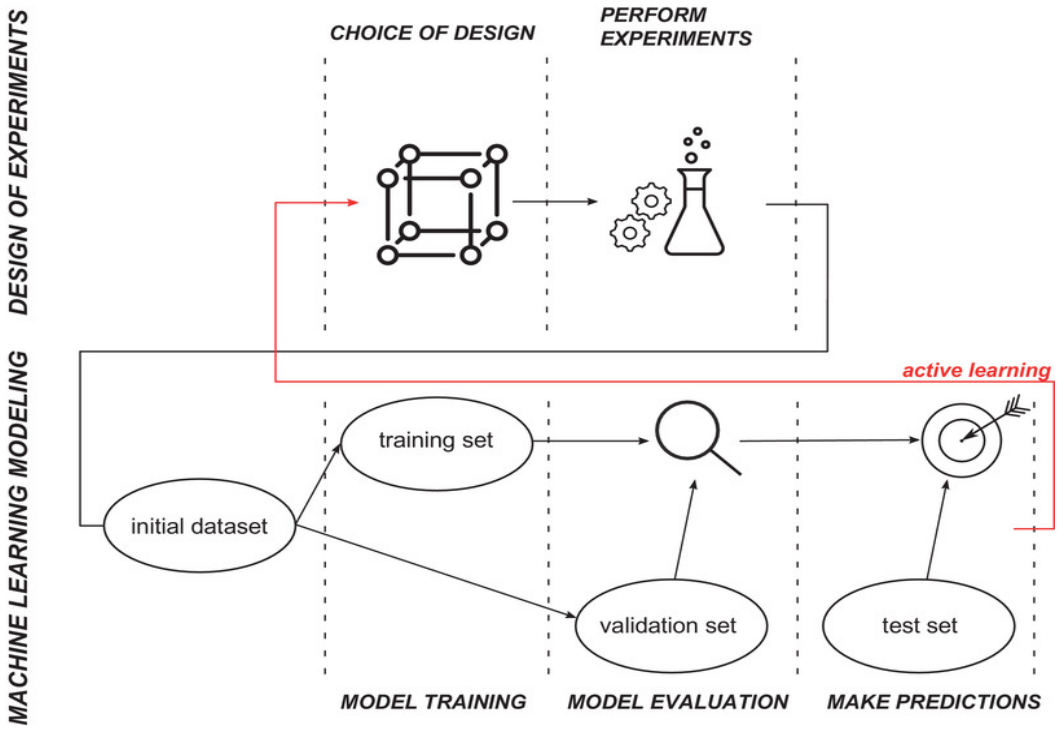



**Figure 2.16:** Summarised workflow, describing the link between ML and the DoE, where the DoE data is being used as an input for the ML model. Active learning can occur when the ML result is used as an input suggestion to design a new experiment [218].

**Figure 2.17** illustrates the core processes for the two methodologies—emphasising the human-based and the software-based parts. This schematic shows how the potential support can be provided to the DoE core process by using ML, and the possibility of replacing the human-based part with a fully software-based core [216]. While DoE and ML are often regarded as if they are independent the quality of final results is dependent on both. The initial DoE design decision must be made with the ML algorithm in mind and the ML models should be picked based on the unique characteristics of the dataset collected by the DoE. However, to date, the combined application of DoE and ML approaches has yet to be used to its full potential.

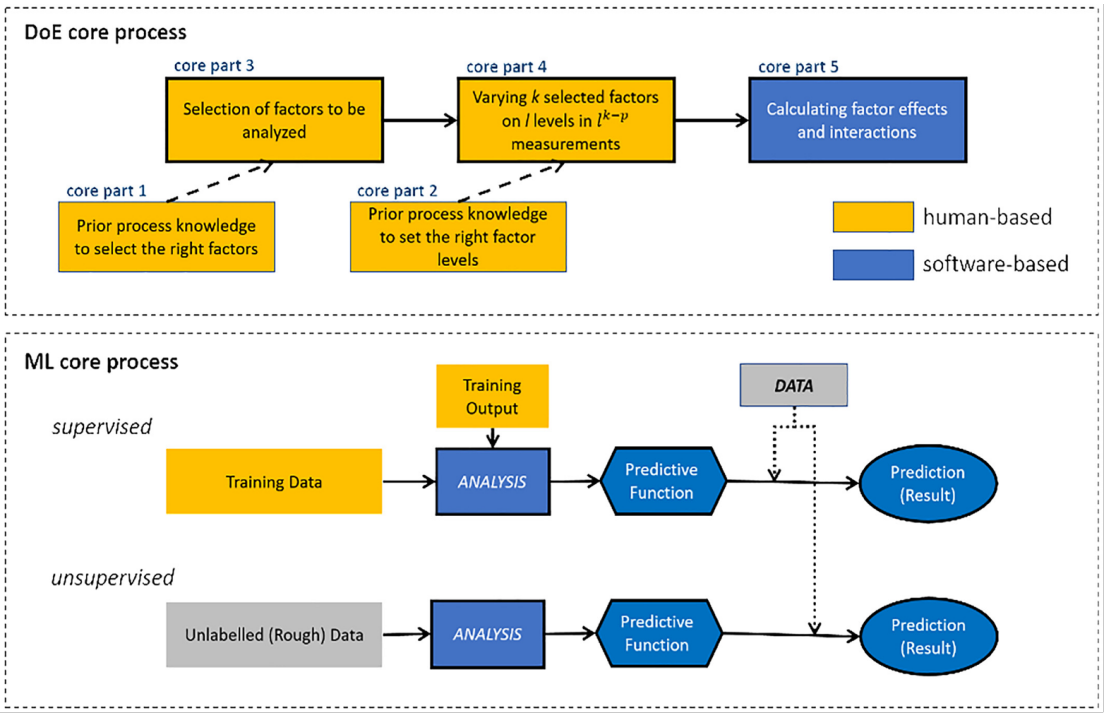



**Figure 2.17:** Core processes for the Design of DoE and ML, including human and software-based parts [216].

## 2.8. Research Gap

The literature review highlights the need for the development of bioinks that meet the challenging requirements related to the bioprinting of scaffolds for bone tissue engineering applications. Specifically, these bioinks should combine the biological properties required to promote cell viability, proliferation and osteogenic differentiation and the physical properties, e.g. rheological properties, required for the bioprinting process. Furthermore, the printed scaffolds require the mechanical properties and degradation properties required for bone tissue engineering applications.

The literature review also highlights the underutilisation of mathematical modelling methodologies in the field of tissue engineering and more specifically in addressing the goal of optimising collagen-based scaffolds for bone tissue engineering applications. Previous studies have not extensively exploited DoE to optimise the bioprinting process or improve scaffold properties and no previous study has focussed on using the DoE approach to optimise collagen HA scaffolds. Additionally, the characterisation of tissue engineering scaffolds remains largely dominated by manual processes.

ML approaches show great potential in the enhancement of data-driven decision making but it has yet to be widely applied in tissue engineering applications. While traditional DoE approaches are limited to numerical inputs, ML offers the ability to analyse large datasets, including images, to predict scaffold behaviour a technique that could significantly advance scaffold design and

performance evaluation. The application of these approaches to predict the degradation properties and structural integrity of 3D bioprinted scaffolds is not fully explored within the tissue engineering field. As highlighted within the thesis objectives in Section 1.2, this project, therefore, proposes to address these gaps by developing a combined DoE and ML approach to systematically optimise scaffold printability and to predict scaffold degradation, pore size and porosity information, ultimately contributing to more effective tissue engineering solutions.

# Chapter 3: Development and Optimisation of a 3D bioprinted collagen- hydroxyapatite scaffold using Design of Experiments

## 3.1. Introduction

Tissue engineering offers a promising solution for the treatment of challenging bone injuries and defects [223], [224]. The main constituents of bone tissue are collagen and hydroxyapatite (HA), with other protein components including laminin and fibronectin also present within bone ECM [225]. HA is a promising bone substitute material due to its outstanding biocompatibility and osteoconductivity [226], [227].The bone extracellular matrix contains collagen, specifically type I collagen the most prevalent structural protein in the human body, which contributes to the strength and toughness of this mineralised tissue. There is evidence that adding collagen to mineralised bone cement improves biomechanical qualities. Additionally, bone scaffolds containing collagen and HA have been shown to effectively mineralise following implantation [228].

3D bioprinting offers a new frontier in the fabrication of complex structures for applications in tissue engineering. This method combines biomaterials and bioactive macromolecules to fabricate scaffolds for the treatment of bone defects and injuries. From the different bioprinting techniques, extrusion-based printing techniques have been most widely applied to produce scaffolds for bone tissue engineering applications. While numerous collagen-based bioinks have been reported on in the literature [229], [230], [231], the influence of process parameters on the properties of the printed scaffolds has yet to be systematically investigated. Furthermore, while the biomechanical enhancement provided by HA is well-documented, its integration into collagen bioinks has not been extensively explored. This chapter aims to optimise collagen scaffolds properties and printing parameters using Design of Experiments (DoE) methods. DoE is a powerful tool for analysing the influence of process factors on specific properties, utilising systematic randomisation to produce experiment planning, as well as model fitting to results. The Response Surface Methodology (RSM) method was performed to analyse the relationship between the ink/scaffold formulation and response to determine the optimal ink combination and printing parameters for bioinks containing various combinations of collagen and HA. The study also explored the repeatability of the bioprinting process. The first step, printing procedures were developed by assessing the effectiveness of various nozzle sizes, crosslinking concentrations, and duration. The second step is to evaluate the impact of print quality variables, including layer count and printhead speed, and evaluate the addition of HA to optimal collagen concentration. This research aims to formulate an optimal procedure to produce collagen and collagen/HA inks and scaffolds.

Moreover, the analysis of scaffold degradation, a vital factor for tissue regeneration typically lacks the integration of image data, which could offer valuable insights into temporal changes. This gap signifies the need for a comprehensive approach that applies DoE not only to refine bioprinting parameters but also to incorporate advanced analytical techniques for a thorough assessment of scaffold performance over time.

### 3.1.1. Chapter Aims

This chapter focuses on the development and characterisation of 3D bioprinted collagen and collagen/HA scaffolds for use in bone tissue engineering applications. The scaffolds were fabricated using an extrusion-based 3D bioprinting method. This chapter addresses Objective 1 of the thesis: To develop a collagen/HA bioprinted scaffold for bone tissue engineering applications and systematically evaluate and optimise the various parameters affecting printability, degradation, mechanical, and rheological properties using DoE. This objective was achieved using a two-stage approach, firstly a preliminary study to identify the optimal collagen concentration and cross-linking conditions for the bioink and following this a more comprehensive assessment was carried out to assess the incorporation of HA into the bioprinted scaffolds.

To accomplish this goal, the specific objectives were as follows:

(1) to fabricate a collagen-based ink suitable for bioprinting,

(2) to design a scaffold structure for printing,

(3) to apply DoE methodology to assess the influence of needle size, varying collagen concentrations, tannic acid crosslinking concentration, and post-printing crosslinking time on the printability and mechanical strength of 3D bioprinted collagen (COL) scaffolds and to identify the optimal parameters (DOE Study 1),

(4) to apply DoE methodology to assess the influence of the addition of HA to the optimal collagen scaffold and the effect of number of layers and printing speed on the properties of COL/HA scaffolds and identify the optimal collagen/HA scaffold for bone tissue engineering applications (DOE Study 2).

## 3.2. Materials and methods

### 3.2.1. Ink preparation

Two types of ink were fabricated, collagen and collagen/HA. The collagen ink was fabricated by adapting a previously published protocol by Lee *et al.* [232]. The fabricate this ink, collagen type I (milled bovine tendon long fibre powder, Collagen Solutions, United Kingdom) was dispersed in 0.5 M acetic acid (Sigma-Aldrich, Wicklow, Ireland) at concentrations of 4, 5 and 6 %(w/v), then refrigerated for 24 h. The collagen solution was homogenised using an overhead blender (IKA, Ultra-Turrax, T-25) for 30 min to 1 h at 4 ºC, to prevent collagen denature. Then the collagen solution was passed through two stainless steel meshes with sizes of 30 and 50 mesh to achieve a homogenous hydrogel that could be printed through small nozzles sizes of the bioprinter (Figure 3.1). For the COL/HA inks, micro-particles of HA (particle size 3.6 μm, Plasma Biotal Limited, UK) were initially added to acetic acid at concentrations of 0, 0.05, 0.5 and 1 %(w/v). The HA micro-particles were then sonicated (BRANSON digital sonicator, USA) for 10 min. Then, collagen type I was added

to this HA solution at concentration of 4 %(w/v), the optimal collagen bioink composition as determined from Study 1, and placed in a fridge for 24 h, to aid in the solubilisation of the collagen fibres. After 24 h the overhead blender was used to homogenise, the hydrogel as shown in Figure 3.1. The inks investigated in the study are summarised in Table 3.1.

**Table 3.1:** Inks compositions for Study 1 and 2.

| **Material** | Collagen (w/v) | HA (w/v) |
|---|---|---|
| **Study 1** | | |
| COL_4% | 4 % | - |
| COL_5% | 5 % | - |
| COL_6% | 6 % | - |
| **Study 2** | | |
| COL (Ink 1) | 4 % | 0 % |
| COLHA_0.05% (Ink 2) | 4 % | 0.05 % |
| COLHA_0.5% (Ink 3) | 4 % | 0.5 % |
| COLHA_1% (Ink 4) | 4 % | 1 % |

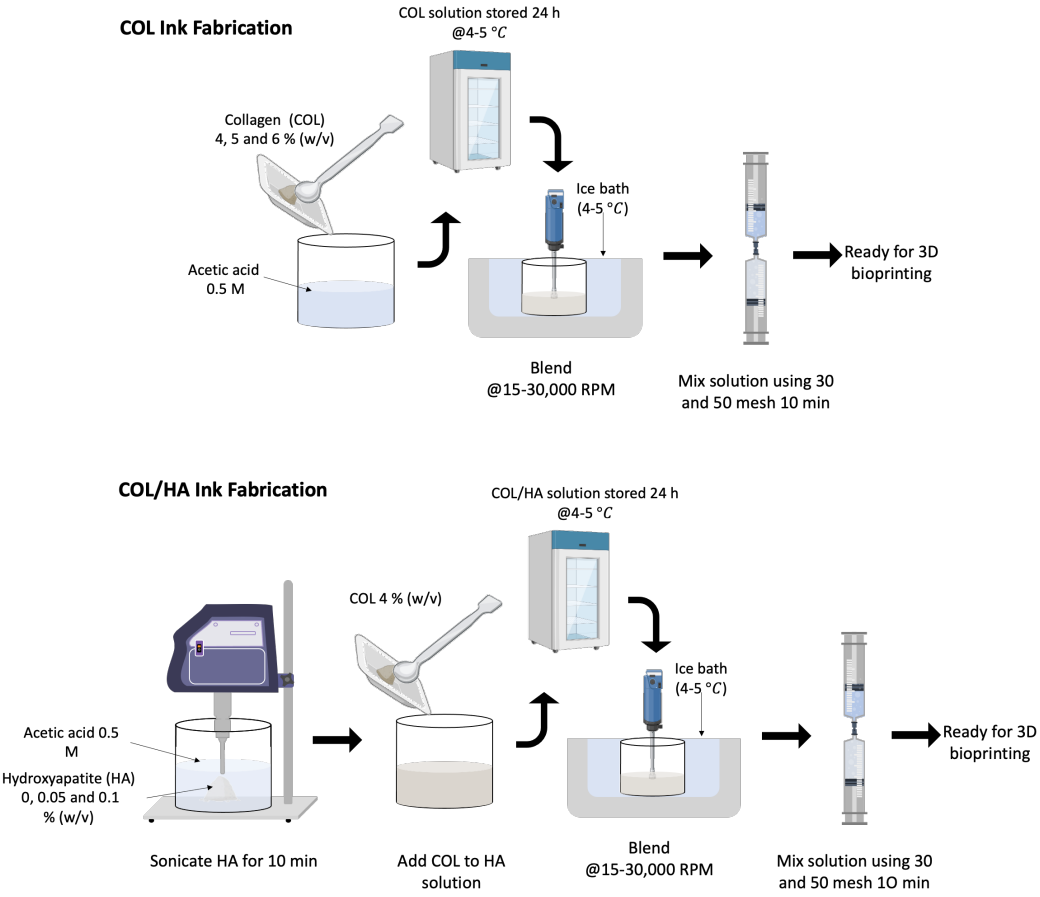



**Figure 3.1:** COL and COL/HA inks protocol. First COL was combined with acetic acid. The slurry was then blended at high speed before being passed through a custom dual syringe system fitted with meshes to homogenize the ink.

### 3.2.2. 3D Bioprinting

The Incredible$^{+}$ Bioprinter (Cellink, Sweden) was used to print collagen and collagen/HA inks. This printer uses the extrusion-based bioprinting method where the material is loaded into a syringe and printed as filament onto a petri dish. The printer method uses a pneumatically controlled dispensing system where the pressure applied to the hydrogel is controlled using compressed air.

#### *3.2.2.1. Scaffold design*

Scaffolds initially were designed to obtain cubic and cylindrical shapes with dimensions $15\ X\ 15\ X\ 3\ mm$ (height x width x length) and $15\ X\ 15\ mm$ (height x diameter) using SolidWorks software (version 2020) to create STL format design. This STL file was then converted to a G-code using Slic3r software (Slic3r 1.3.0, AGPLv3). The G-code specifies the object printing parameters in terms of infill pattern, infill density, print speed and the number of layers (**Figure 3.2**). The microstructural properties such as porosity and pore sizes of the scaffold can be altered by changing the infill pattern and density. In this case for both studies, a rectilinear pattern with an infill density

of 15% was chosen according to the literature [115] to give a simple scaffold structure. **Figure 3.2** shows how changing the infill density can affect the scaffold porosity and pore sizes.

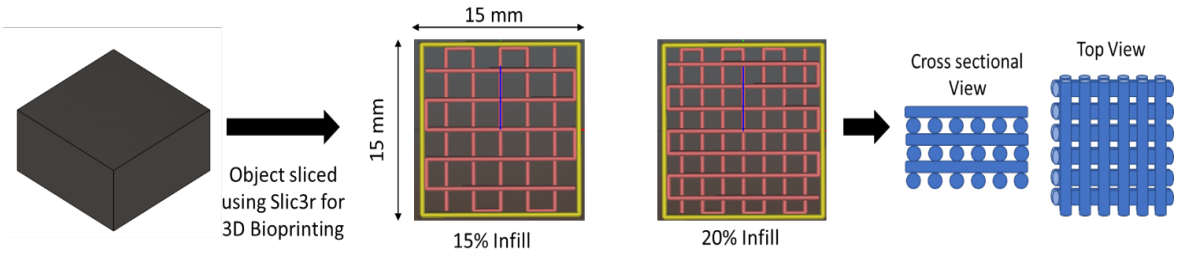



**Figure 3.2:** Scaffold designing process illustrating the conversion of STL 3D object and sliced using the Slic3r software that can be read by the bioprinter specifying the infill density of the object.

#### *3.2.2.2. Printing parameters*

The bioprinting parameters that can be controlled during the printing process including pressure, printing speed and needle gauge size. The ideal bioprinting parameters for a particular ink depend on the viscosity (i.e. the shear-thinning property), crosslinking method, and the planned print geometry [233]. For this case, a collagen hydrogel was used as the main ink material. Printing was carried out at room temperature (20 °C). The needles selected for printing were 23G (internal diameter = 0.337 mm), 22G (internal diameter = 0.413 mm) and 21G (internal diameter = 0.514 mm). The pressure was manually adjusted depending on collagen and HA concentration (viscosity) and needle gauge size to give a consistent flow of ink from the needle during the printing process. The pressure values required ranged between 50-450 kPa. In the DoE studies detailed in Section 3.3.3, pressure value became an essential response metric for each printing run. This measure was critical because it directly correlates with the printability and quality of the scaffold. Higher material concentration and smaller needle diameters typically necessitate increased pressure for extrusion. By recording this pressure, the study can determine the optimal conditions for scaffold printing. Higher pressure may indicate a more challenging extrusion process, potentially affecting the precision and uniformity of the scaffold's pores and walls. Monitoring this parameter is key to achieving the desired scaffold structure, particularly when dealing with varying material consistencies and 3D printer. Printing speed was constant 10 mm/s for COL study, however for COL/HA was varied between 1 mm/s - 6 mm/s. Printing speed affects the print fidelity of the printed scaffold as it influences the deposition of the filament during the printing process.

### 3.2.3. Crosslinking

The crosslinking of scaffolds, a process usually conducted post-printing, enhances the structural integrity of printed hydrogels. This process bolsters scaffold stiffness and moderates its degradation rate. In this study, the COL scaffold was crosslinked using tannic acid (Sigma-Aldrich, Ireland) at concentrations of 4, 5, and 6 %(w/v). This process involves the creation of bonds—covalent, ionic,

and hydrogen—between tannic acid and collagen, improving the scaffold's physical and mechanical properties. The crosslinking process took place in an incubator for durations ranging from 15 to 60 min. The temperature of 37 °C and pH of 4.2 within the incubator were maintained at specific levels to optimise crosslinking. TA concentration ranges from 0.1-6 %(w/v) at a treatment time of 10 min- 120 h [120]. After crosslinking, the scaffolds were washed with deionized water for approximately 1 h to eliminate any excess tannic acid. This washing step is critical to prevent any toxicity that might occur if surplus tannic acid is left within the scaffold [234].

## 3.3. Characterisation Methods

### 3.3.1. Ink characterisation methods

#### *3.3.1.1. Fourier transform infrared (FT-IR) spectroscopy*

FT-IR spectroscopy, a powerful tool for characterising the molecular composition of materials, was used to examine the chemical composition of the COL and COL/HA inks. Specifically, it was used to identify the characteristic absorption peaks of COL and HA, which indicate their presence and potential interactions in the inks.

The inks were first prepared for FT-IR analysis by freeze-drying to remove any residual moisture which could interfere with the spectroscopy readings. The dried scaffolds were then carefully ground into a fine powder to ensure a homogenous sample and enhance the accuracy of the subsequent spectral analysis. The Spectrum Two FT-IR instrument (PerkinElmer, UK) was used for this purpose, utilising the Attenuated Total Reflectance (ATR) technique. ATR-FTIR allows for the direct examination of solid and liquid samples without extensive preparation and enhances the surface sensitivity of the FTIR analysis, making it particularly useful for studying the surface interactions between collagen and hydroxyapatite. Measurements were carried out at room temperature to minimise potential thermal effects on the spectra. The analysis was carried out over the wavelength range from 400 to 4,000 $cm^{-1}$, offering a comprehensive overview of the material's spectral features. The instrument's resolution was set at 4 $cm^{-1}$, striking a balance between detail and signal-to-noise ratio. FT-IR spectra are rich in information, as each peak corresponds to a particular chemical bond vibration. Therefore, by examining the changes in peak intensity, position, and width, one can gain insights into the COL and HA concentrations, their potential interactions, and the effectiveness of the crosslinking process. This step was essential for the validation of the ink's composition and scaffold crosslinking efficiency, which are critical parameters for its performance in bone tissue engineering applications.

#### *3.3.1.2. Injectability test*

Injectability testing assesses the force required to achieve a consistent flow of ink from a needle using a lab-based method that mimics the extrusion-based bioprinting process. This test was used for

screening all bioinks produced in this study to ensure that excessive forces were not required for extrusion of the bioink and the freedom from clogging (needle blockage) during printing. Injectability testing was conducted using the Zwick/Roell (Zwick GmbH & Co., Ulm, Germany) Mechanical Testing Machine fitted with a 500 N cell load (**Figure 3.3**) at a speed of 0.1 mm/s up to 80% strain and a pre-load of 0.1 N. COL hydrogels (4, 5 and 6 %(w/v)), and COL/HA (4:0, 4:0.05, 4:0.1 %(w/v) were placed into a 3 mL syringe and secured in a custom-designed rig. Each hydrogel concentration was examined with three different needle sizes, 23G (0.337 mm), 22G (0.413 mm) and 21G (0.514 mm). This test method aimed to determine the force required to inject hydrogels by determining the maximum force when hydrogels start to flow through the needle.

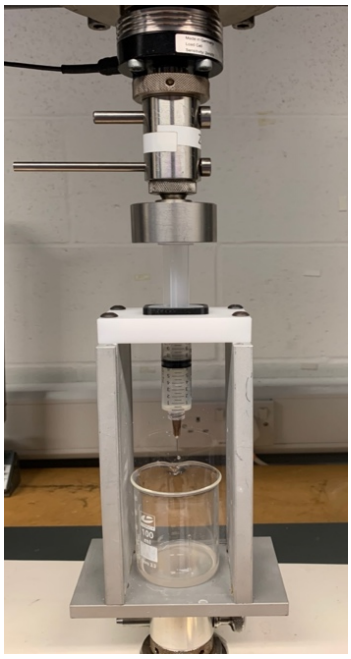


**Figure 3.3:** Test apparatus and necessary set up to determine the extent of injectability using Zwick equipment.

A typical force versus extrusion curve for the ink consists of three regions **Figure 3.4**-A). These regions are: 1) initial gradient where the plunger overcomes the friction between barrel and material extruded, 2) maximum force to be reached for material to start coming out of the needle and 3) plateau region when material is extruded at a steady state. Conversely, some material causes needle clogging due to blockage that may be produced due to the presence of bubbles or collagen fibres. In these cases where there was no steady flow of the ink/ plateau region was observed after the initial gradient (**Figure 3.4**-B).

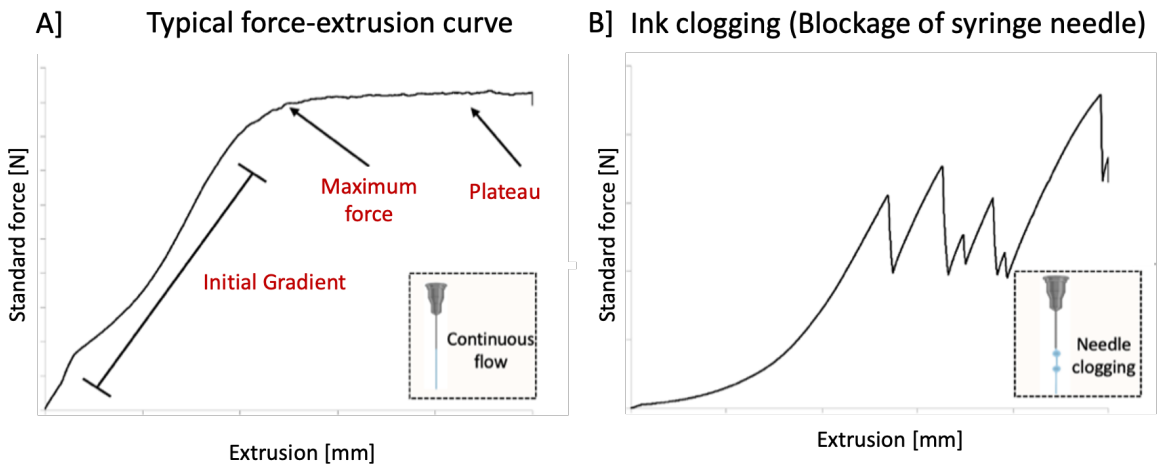



**Figure 3.4:** A) Plot of ink ejection of a continuous flow, B) Plot force vs displacement presenting ink clogging.

### *3.3.1.3. Rheological analysis*

As the addition of HA particles to the COL ink increased the complexity of their rheological profiles and thus a more comprehensive rheological assessment was carried out on COL/HA study 2. Rheological analysis was conducted with a cone-plate geometry rheometer (Anton Paar, MCR 302, United States) fitted with a 40 mm diameter 1º cone plate geometry (CP40-1) was utilised for these tests. A quantity of 5 mL of each ink was placed into the gap between the cone and plate, providing ample material for accurate measurement. Each test evaluated key rheological parameters, namely the storage modulus (G′ [Pa]), loss modulus (G″ [Pa]), and complex viscosity ($\eta^*$ [Pa.s]). These values offer insightful information about the ink's elastic and viscous characteristics, which greatly influence its handling, extrusion, and eventual solidification within the printing process. To ensure repeatability and robustness of the data, each test was performed three times per ink. Two main sweeps were conducted. The first was a frequency sweep, ranging from 0.1-10 Hz with a constant strain of 1 %, conducted at a stable temperature of 25 °C. This step provided crucial information about the ink's viscoelastic behaviour under varying deformation rates, simulating the changing forces experienced during the printing process. The second sweep was a temperature sweep, conducted between 10-50 °C at a ramping rate of 5 $°C\ min^{-1}$. During this sweep, a constant frequency of 1 Hz and a strain of 1 % were maintained. This sweep gave insights into the ink's gelation temperature, a critical parameter that influences the ink's transformation from a liquid to a semi-solid state. This temperature sensitivity information aids in fine-tuning the printing process and subsequent scaffold cross-linking for optimised scaffold properties. Altogether, these comprehensive rheological assessments ensured a deeper understanding of the ink's behaviour under different conditions, enabling informed adjustments to the bio-printing parameters and the resulting scaffold's performance.

The Sequential Least Squares Programming (SLSQP) algorithm was implemented to optimise the accuracy of the estimates for k and n. This approach ensures that the model predictions correspond closely with the empirical data of shear stress and shear rate. By minimising the differences between the predicted and observed values of the shear stress and rate, the SLSQP method facilitates precise rheological characterisation of the bioinks.

To assess the rheological properties of printing inks, the power-law model was used, expressed as

$$\tau = k.\gamma^n$$

**Equation 3.1**: Power-law model

where τ signifies shear stress, γ is the shear rate, k is the consistency coefficient, and n is the flow behaviour index. These parameters describe the ink's behaviour across different shear conditions.

Using the power-law model, the values of k and n were calculated to theoretically predict the pressure required for bioprinting. These theoretical values were then compared with the experimental pressure values obtained from the Incredible$^+$ 3D bioprinter. By conducting this comparison, it was possible to validate the accuracy of the theoretical model and ensure that the bioink formulations were optimised for consistent and reliable bioprinting performance.

### *Pressure calculation*

The extrusion pressure requisite for the 3D bioprinting process was calculated using the equation relating to pipe flow for power-law fluids (**Equation 3.1**), which is paramount for predicting the flow of non-Newtonian fluids through a cylindrical conduit [235]. The pressure ($P$) necessary for extrusion through a needle is shown schematically in (**Figure 3.5**). The pressure drop for the flow of power-law fluids in pipes is expressed as:

$$\Delta P = \frac{2kL}{R}\left[Q.\frac{3+\frac{1}{n}}{\pi R^2}\right]^n$$

**Equation 3.2:** Pressure drop in pipe flow.

Where ΔP ($P_L$ – $P_0$ in Figure 3.3) is the pressure difference required to drive the flow, k is the consistency coefficient, n is the flow behaviour index, L is the length over which the pressure is applied (the length of the needle), Q is the volumetric flow rate, and r is the internal radius of the needle. The volumetric flow rate (Q) was set according to the desired deposition rate, which directly depends on the printing speed and the cross-sectional area of the extruded filament. The pressure determined from this calculation was used to adjust the printing pressure required for each bioink to ensure stable and consistent extrusion, which is critical for the fidelity and structural integrity of the printed scaffolds.

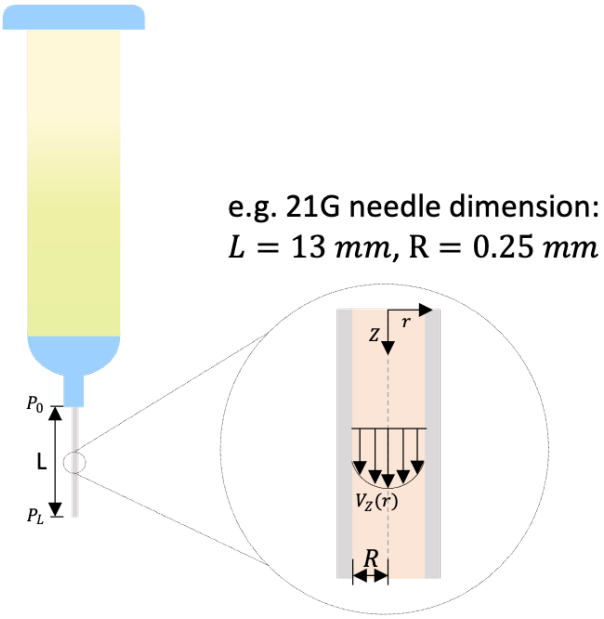



**Figure 3.5:** Schematic representation of the extrusion process through a syringe and nozzle setup. The diagram shows the velocity profile in the needle where L = needle length, $P_0$= initial pressure, $P_L$ = outlet pressure (at the tip of the needle) and R= inner needle radius.

### *3.3.1.4. Ink shape fidelity/printability assessments*

String/filament test

The filament test is one of the printability screening procedures that has been used to check the printing quality. Initially, ink was loaded into a 3 mL pneumatic cartridge, and a Luer lock female-female connector was used to transfer the viscous ink between the syringes. The filament test was carried out for the COL/HA study. The needles that were used in the testing were 23G, 22G and 21G. Then the cartridge was attached to the bioprinter with a microscopic camera (RS Pro Wi-Fi Digital Microscope) focused on the needle tip to observe the filament extrusion. The air pressure was slowly increased in increments of 5 kPa until the ink started to be extruded at a steady rate. Finally, the ink is either classified as failing or passing the test, depending on the filament formation (**Figure 3.6**). A test failure is indicated by the formation of a liquid droplet that falls from the needle. A test is considered successful when a thin filament forms and hangs more than 5 mm from the needle tip. The length of a filament before it breaks can be used as a relative gauge of the printability of an ink [236].

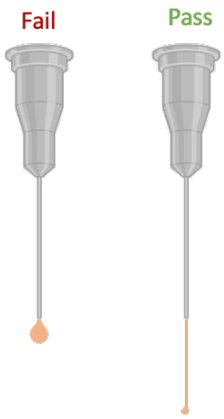


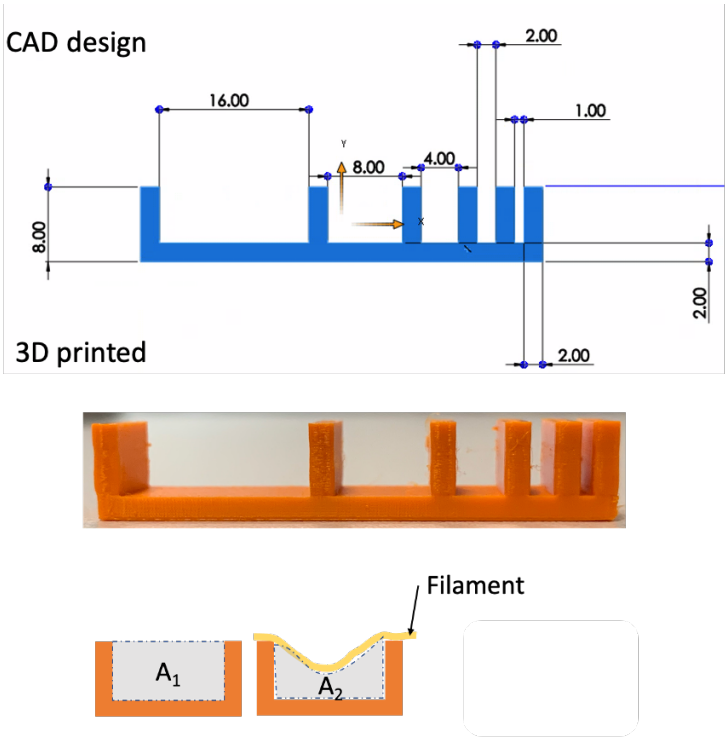

**Figure 3.6:** At the needle's tip, the bioink on the left created a liquid drop. When extruded, the bioink on the right showed the potential of a material for 3D bioprinting by forming a filament.

## Filament collapse test

To determine printing quality, further tests were used to examine filament collapse, initially on a platform designed on CAD with six pillars of known distance of 1, 2, 4, 8 & 16 mm [237] and 3D printed using a PRUSA MINI+ (PRUSA, Czech Republic) as shown in **Figure 3.7**. Using an Incredible$^{+}$ bioprinter (Cellink, Sweden), a single ink filament was placed across these gaps, and the process was captured using a USB microscopic camera (RS Pro Wi-Fi Digital Microscope) at a frame rate of 60 fps, and a resolution of 1080 x 1024 pixels. COL/HA inks were placed in 3 mL pneumatic cartridge. A 23G, 22G and 21G were then used to extrude the inks. The deposition speed was set at 1-10 mm/s and the air pressure was changed in accordance with each different concentration. The print path continued for 10 mm after the last pillar, and the needle-tip was positioned at 0.3, 0.4 and 0.5 mm (inner diameter of needle sizes) above the top surface of the pillars. The images produced were quantified with ImageJ software (version: 2.0.0-rc-43/1.50e, National Institutes of Health (NIH), United States)). The area of the deflection ($A_2$) and un-deflected ($A_1$) filament are shown in **Figure 3.7**. The collapse % was measured using **Equation 3.3** [237]:

$$C_f = \frac{A_1}{A_2} \times 100$$

**Equation 3.3:** Filament collapsing rate [%]




**G-code (straight line)**

```
G90
G0 Z30
G0 X0 Y0
G0 Z0.40

T0

G1 Z0.4 F800
G0 X10 Y10

M760;
G1 X-5 E1

M761;
G0 X0 Y0
G1 Z30

M84 ;disable motors
;END
```

**Figure 3.7:** Filament Collapse Test: CAD design for testing rig and manufactured using 3D printer, deflection measurement schematic.

Layer stacking test

To evaluate object stability after printing layer stacking was tested as one of the printing fidelity procedures. COL/HA inks were placed in 3 mL pneumatic cartridge. A 21G was used to extrude the ink. The deposition speed was set at 1 mm/s and the air pressure was changed in accordance with each different ink concentration. A "+" symbol was created by crossing the first line with a second line that is extruded at an angle to it. A USB microscopic camera (RS Pro Wi-Fi Digital Microscope) was used to classify whether two lines merges together (indicating test fail) or stack on top each other (indicating test pass) [236].

### 3.3.2. Scaffold characterisation method

#### *3.3.2.1. Porosity*

The ability to print a porous scaffold was also an important consideration when assessing the printability of the COL/HA bioinks study. This characteristic was examined by printing scaffolds at various speeds, ranging from 1 to 6 mm/s, and altering the number of layers from 5 to 15.

The determination of scaffold porosity was carried out through a gravimetric method [238]. This method uses straightforward measurements of the dimensions and mass of the scaffolds. To ensure accuracy, an analytical balance (METTLER AT261, Mettler Toledo, Belgium) was used to determine the scaffold's mass, while a vernier calliper was employed to gauge the volume of each scaffold. Scaffold density was calculated as follows:

$$\rho = \frac{Mass\ [g]}{Volume\ [m^3]} = \frac{m}{V}$$

**Equation 3.4:** Density formula for the scaffold density calculation.

Porosity measures the relative density of the scaffold with the theoretical density of COL taken as 1.3 g $cm^{-3}$ [239] and for HA taken as 3.6 g $cm^{-3}$[240]. 3D printed samples were crosslinked and freeze-dried before porosity analysis was completed. Scaffold porosity was calculated as follows:

$$Porosity\% = 100 - \left[\left(\frac{\rho_s}{\rho_m}\right) \times\ 100\right]$$

**Equation 3.5:** Formula for the calculation of the scaffold porosity (%), using the ratio between the density of scaffold and the solid density of the material.

Where $\rho_s$ indicates to scaffold density and $\rho_m$ material solid density.

The porosity analysis provides critical insights into the scaffolds' structural properties, influencing cell infiltration, nutrient diffusion, and overall tissue regeneration capabilities. Understanding these parameters enables the fine-tuning of the 3D printing and crosslinking processes for optimised scaffold design for bone tissue engineering applications.

#### *3.3.2.2. Mechanical testing*

Mechanical testing was performed to determine the compressive properties of the bioprinted scaffold (i.e., compressive strength and elastic modulus) for the COL from DoE Study 1 and COL/HA scaffolds fabricated in DoE Study 2. Unconfined compression testing was completed for 3D bioprinted scaffolds (n = 3). Scaffolds were immersed in a water bath containing phosphate buffered saline (PBS) solution (pH 7.4) (Sigma-Aldrich, Wicklow, Ireland) throughout testing and maintained temperature 37 °C (to mimic the body environment conditions). Tests were conducted using the Zwick machine fitted with a 500 N cell load at a speed of 1 mm/min up to 10 % strain/mm and a pre-load of 0.5 N. Elastic modulus was calculated from the slope of the linear region of the stress-strain curve for each sample.

#### *3.3.2.3. Pore size*

The analysis of scaffold pore size is crucial for understanding the potential for cell infiltration and nutrient diffusion. Pore size measurements were performed for all COL and COL/HA scaffolds in DoE Study 1 and Study 2 using ImageJ software. This is a powerful tool for image processing and analysis, capable of quantitatively evaluating features in images, including pore size in our scaffold

samples. Three separate scaffold samples (n = 3) were analysed to ensure the data captured represented the average properties of the scaffold. Images were captured using a microscopic camera (RS Pro Wi-Fi Digital Microscope). Images of the scaffolds were loaded into ImageJ, and a relevant scale was established based on the image's pixels and dimensions.

This essential step ensures the accurate measurement of pore sizes by calibrating the pixel distance to the known scale bar provided in the images. Next, images were converted into a binary format to provide a clear distinction between the pore spaces (representing the 'void' or empty spaces) and the scaffold walls (the 'solid' part) **Figure 3.8**). This conversion simplifies the images, enabling precise delineation of the pores for accurate measurement. Upon conversion, the software was able to detect and outline each individual pore in the image, a powerful visual tool for understanding pore distribution and size variability across the scaffold. Furthermore, ImageJ generated a table containing the number of pores identified in each image, along with their respective areas, measured in $mm^2$. Furthermore, for the optimal scaffold, pore diameter was also quantified [mm]. This data was exported to a spreadsheet in MS Excel (Microsoft Excel, version 16.55) for further analysis and graphing.

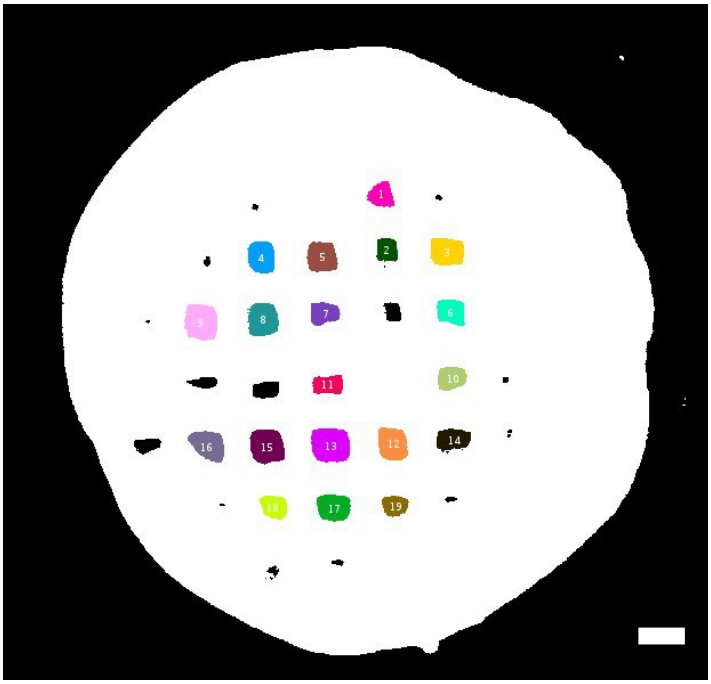



**Figure 3.8:** Pores size distribution of the 3D printed scaffolds analysing the microscopic images using ImageJ.

### *3.3.2.4. Degradation Properties*

Degradation analysis were performed COL/HA scaffolds in DoE Study 2. Material degradation relates to a change in properties (e.g., physical, chemical or mechanical) due to the influence of one or more environmental factors (e.g., temperature, chemicals, light or applied force). Degradation

properties were measured as a function of mass loss, change in morphology and mechanical properties at 3, 7, 14, 21 and 28 days. 3D printed scaffolds were placed in 5 mL simulated body fluid (pH 7.4) at 37 °C for up to 28 days. For each timepoint, each scaffold was removed from the fluid and washed with DI water. The scaffold was then dried using filter paper to remove excess liquid and weighed using an analytical balance (METTLER AT261, Mettler Toledo, Belgium) and vernier calliper (**Figure 3.9**). The extent of scaffold degradation as a function of mass loss and dimensional change (measuring the scaffold diameter and thickness) were determined **Equation 3.6** and **Equation 3.7**).

$$Degradation\% = \left(\frac{W_0 - W_f}{W_0}\right) x\ 100$$

**Equation 3.6:** Mass loss, $W_0$ = Initial weight/dimensions (Day 1 post-crosslinking), $W_f$ = Final weight/ dimensions.

$$Degradation\% = \left(\frac{D_0 - D_f}{D_0}\right) x\ 100$$

**Equation 3.7:** Dimension loss, $D_0$ = Initial weight/dimensions (Day 1 post-crosslinking), $D_f$ = Final weight/ dimensions.

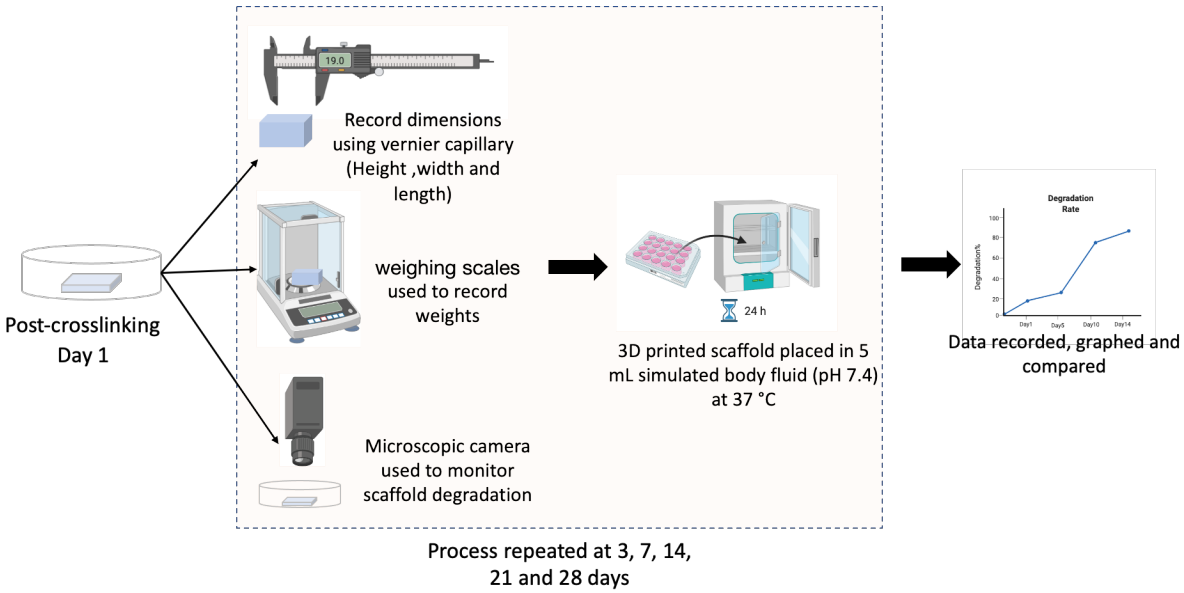



**Figure 3.9:** Degradation analysis procedure.

### 3.3.3. Statistical analysis

Numerical data is displayed as mean ± standard deviation (S.D). Two-way Analyses of Variance (ANOVA) were undertaken for comparing several samples. The statistical significance criterion was established at $p < 0.05$. Statistical analysis in this study was conducted using GraphPad Prism 8.0.2 (Dotmatics, USA).

### 3.3.4. DoE Methodology

The DoE software Design-Expert V12 (Stat-Ease Inc, USA) was utilised for the analysis and optimisation of the experimental factors relating to the bioprinting process. Two studies were carried out, firstly a preliminary study was conducted to determine the optimal collagen concentration and crosslinking conditions (Study 1). This study also explored the effect of the bioprinter needle size on bioink injectability. Following identification of the optimal COL bioink, the incorporation of HA into the bioink was then explored and a second DoE study was conducted to optimise the COL/HA ink formulation and printing parameters (Study 2).

#### *3.3.4.1. DoE Study 1: Collagen ink*

The Box–Behnken design (BBD) was utilised to generate the design space. Four numerical factors were included in Study 1: a) collagen concentration, b) tannic acid concentration, c) crosslinking time and d) needle size (Table 3.2). The upper and lower limit for the factors investigated in each study were selected based on a review of the literature and preliminary testing in the laboratory. For Study 1 a three-level factorial BBD was implemented, yielding 29 experimental runs (detailed in Appendix B, Table 1.B). The principal response variables measured to ascertain the characteristics of the bioink and scaffolds were printing pressure (evaluated via 3D bioprinter) (referred as R1), Young's modulus (determined through compression tests) (referred as R2), and average pore size quantified through image analysis (referred as R3).

**Table 3.2:** Numerical factors and their lower and upper levels for DoE study 1.

| Factors | Units | Lower limit | Higher limit |
|---|---|---|---|
| A-Collagen concentration | %(w/v) | 4 | 6 |
| B-Tannic Acid concentration | %(w/v) | 4 | 6 |
| C-Crosslinking Time | min | 15 | 60 |
| D-Needle Size | G | 21 | 23 |

Upon completion of the experimental testing, the Design-Expert software was used to analyse the data and develop regression equations relating the study inputs and outputs. The significance of each

factor within each equation was determined by employing lack of fit evaluations, and ANOVA using the Design-Expert software. Statistical significance was established for p–value below 0.05. The regression models were then used to optimise each process.

#### *3.3.4.2. DoE Study 2: Collagen/HA ink*

For Study 2, three numerical factors were included: a) HA concentration, b) number of layers and c) printing speed **(**

**Table 3.3**). A total of 17 runs were included in Study 2 as detailed in **Appendix B, Table 2.B.** The responses investigated were printing pressure (evaluated via 3D bioprinter) (referred as R1), Young's modulus (determined through compression tests) (referred as R2), average pore size (referred as R3), and scaffold degradation rate (referred as R4). As per Study 1, the Design-Expert software was used to analyse the data and develop regression equations relating the study inputs and outputs which were then used to optimise each process.

**Table 3.3:** Numerical factors and their lower and upper levels for DoE study 2.

| Factors | Units | Lower limit | Higher limit |
|---|---|---|---|
| A-HA concentration | %(w/v) | 0 | 0.1 |
| B-Number of layers | - | 5 | 15 |
| C-Printing speed | mm/s | 1 | 6 |

## 3.4. Study 1 Results and Discussion

### 3.4.1. Study 1: Ink characterisation

#### *3.4.1.1. FTIR analysis*

Chemical analysis of the COL 4, 5, and 6 % (w/v) inks was carried out using FT-IR spectroscopic analysis. The results illustrated in **Figure 3.10** provide a definitive confirmation of collagen presence within the scaffolds at various concentrations. Characteristic absorption bands corresponding to collagen's distinct amide groups are clearly evident. The amide A band, primarily associated with N-H stretching vibrations, is visible at approximately 3,200 $cm^{-1}$. The amide I band, found at 1,628 $cm^{-1}$, is typically attributed to C=O stretching vibrations and is a reliable marker for the presence of collagen's protein backbone. The amide II band, observed at 1,529 $cm^{-1}$, arises from coupled N-H bending and C-N stretching motions. Lastly, the amide III band, which occurs near 1,189 $cm^{-1}$, can be linked to the C-N stretching and N-H bending vibrations from the collagen's amino acid side chains. These peaks collectively validate the structural integrity of collagen across the different concentrations analysed and are indicative of the successful incorporation of tannic acid crosslinking within the scaffold structure. These findings are consistent with previous studies that have characterised collagen using FTIR spectroscopy[241].

FT-IR spectroscopy analysis confirms the presence of collagen and tannic acid crosslinking within scaffolds fabricated using each concentration of collagen **Figure 3.11** illustrates the FTIR spectrum for the crosslinked collagen scaffold and pure COL 4%(w/v) scaffold. For the collagen scaffold crosslinked with 5 %(w/v) tannic acid absorption peaks were observed at the frequencies of 3,233, 2,916, 1,233 and 1,022 $cm^{-1}$. There is a minor shift and broadening at the peak of 3,233 $cm^{-1}$ **Figure 3.11**, which indicates the stretching of both phenolic hydroxy of tannic acid and aliphatic hydroxy of collagen. This may be due to the formation of a hydrogen bond between the OH group of tannic acid and the free NH group of collagens. These findings are consistent with similar studies from the literature [242].

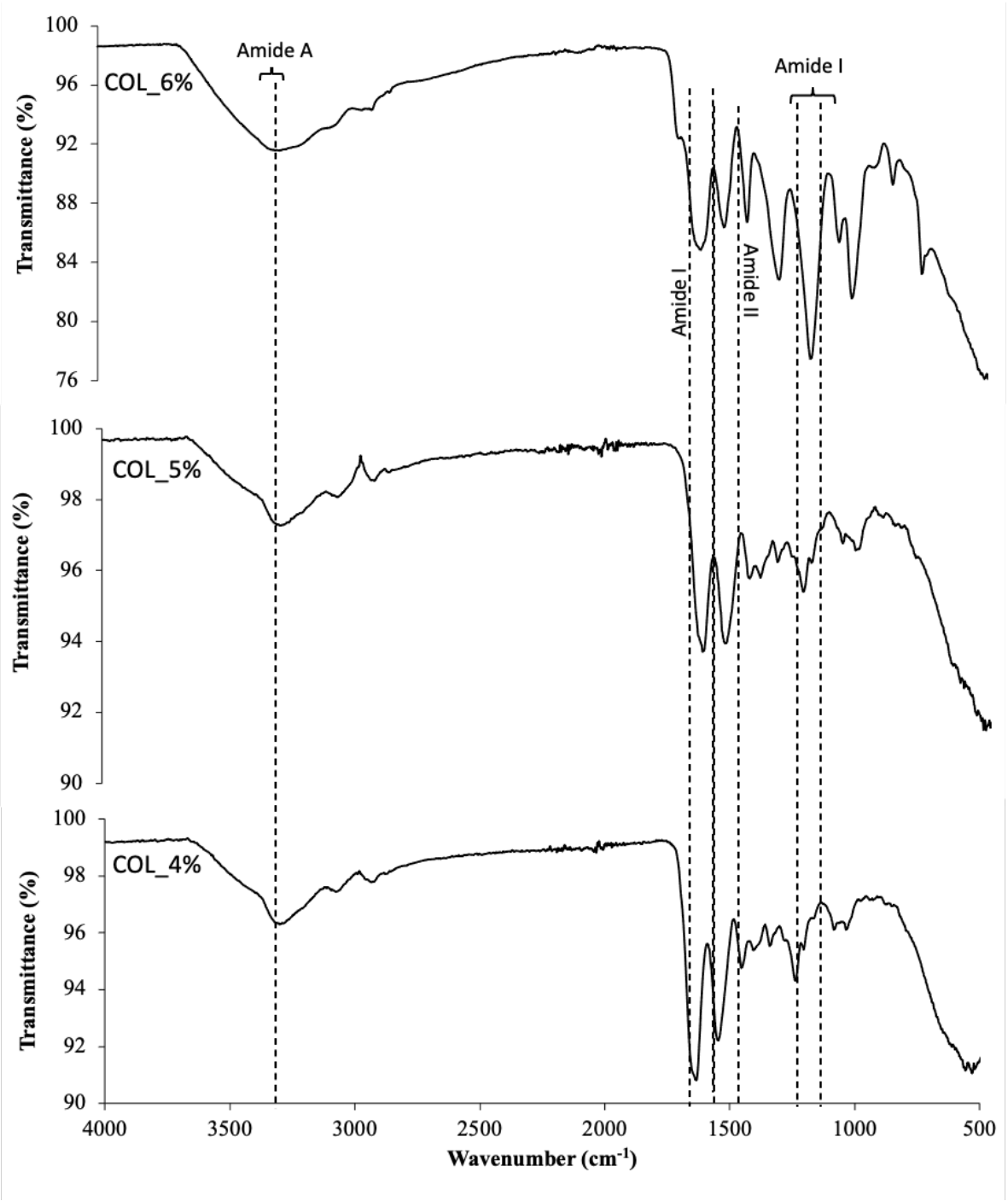



**Figure 3.10:** FTIR Spectra of collagen at various concentrations, indicating the interaction between the components.

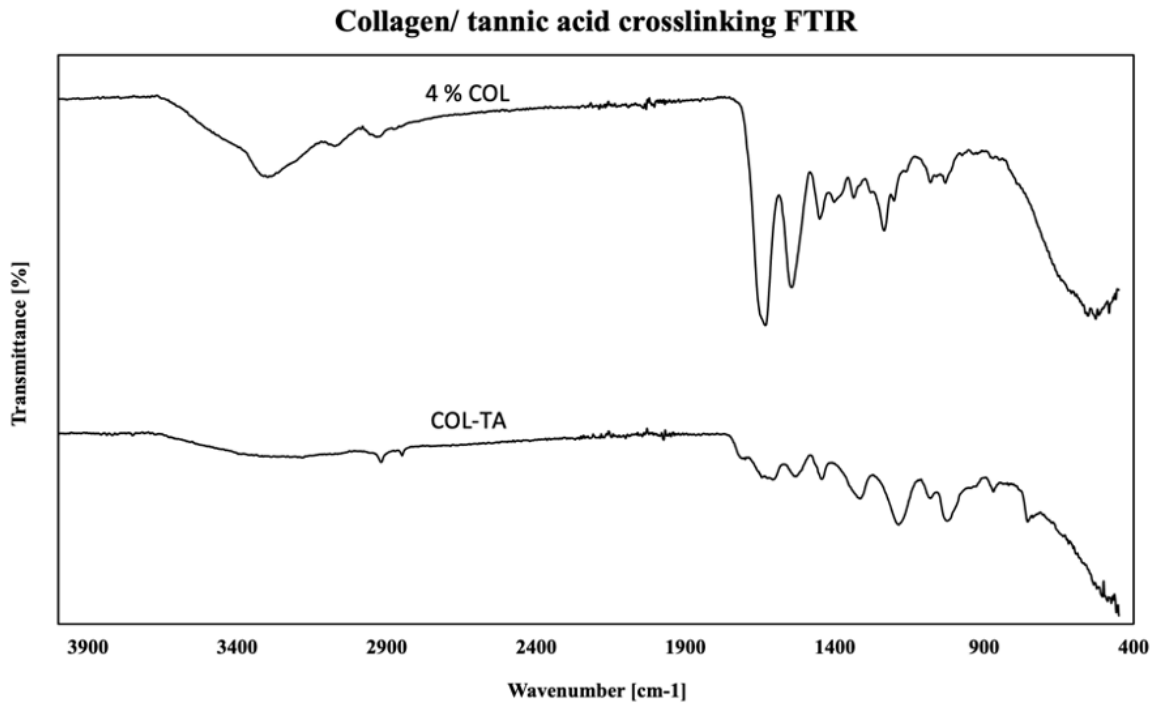



**Figure 3.11:** Spectra demonstrating collagen crosslinking, with changes in amide bands reflecting the crosslinking degree.

### *3.4.1.2. Injectability test*

The injectability studies conducted on collagen inks, using different needle sizes (23G, 22G and 21G) and variable concentrations, provide valuable insights into the flow dynamics of these materials. In the context of the tests for the needle with the largest internal diameter (21G) (**Figure 3.12**-A), a clear correlation between the concentration of collagen and the force required for extrusion was detected. In particular, the collagen ink with a concentration of 4 %(w/v) exhibited a force profile that followed a straight line, suggesting that it is a uniform material with consistent extrusion characteristics. In contrast, the formulations with 5 and 6 %(w/v) concentrations showed progressively greater resistance, predicted due to the increasing viscosity resulting from increased polymer levels. Significantly, the gradual increase in force indicates a viscous but regulated extrusion process. The significant force peak observed for the 6 %(w/v) collagen ink during the transition to the 22G needle indicated an increased resistance to extrusion (**Figure 3.12**-B). This temporary increase, which is probably caused by a brief blockage, highlights the difficulties presented by smaller needle sizes. The inks with concentrations of 4 and 5 %(w/v) demonstrated higher extrusion forces and showed more consistent profiles, indicating a lower possibility of blockages and a more consistent extrusion process.

The tests for the needle with the smaller internal diameter (23G) further highlighted the complex nature of extruding inks with high viscosity through smaller needle (**Figure 3.12**-C). The force profile of the 6 %(w/v) collagen ink exhibited significant fluctuations, suggesting irregular suspension in flow and the possibility of clogging events (**Figure 3.12**-C). The collagen variation with a concentration of 5 %(w/v) displayed comparable patterns, although to a lesser degree. On the other hand, the collagen ink with a concentration of 4 %(w/v) consistently exhibited the lowest and most consistent extrusion force. This indicates that it has a more desirable flow characteristic for bioprinting purposes.

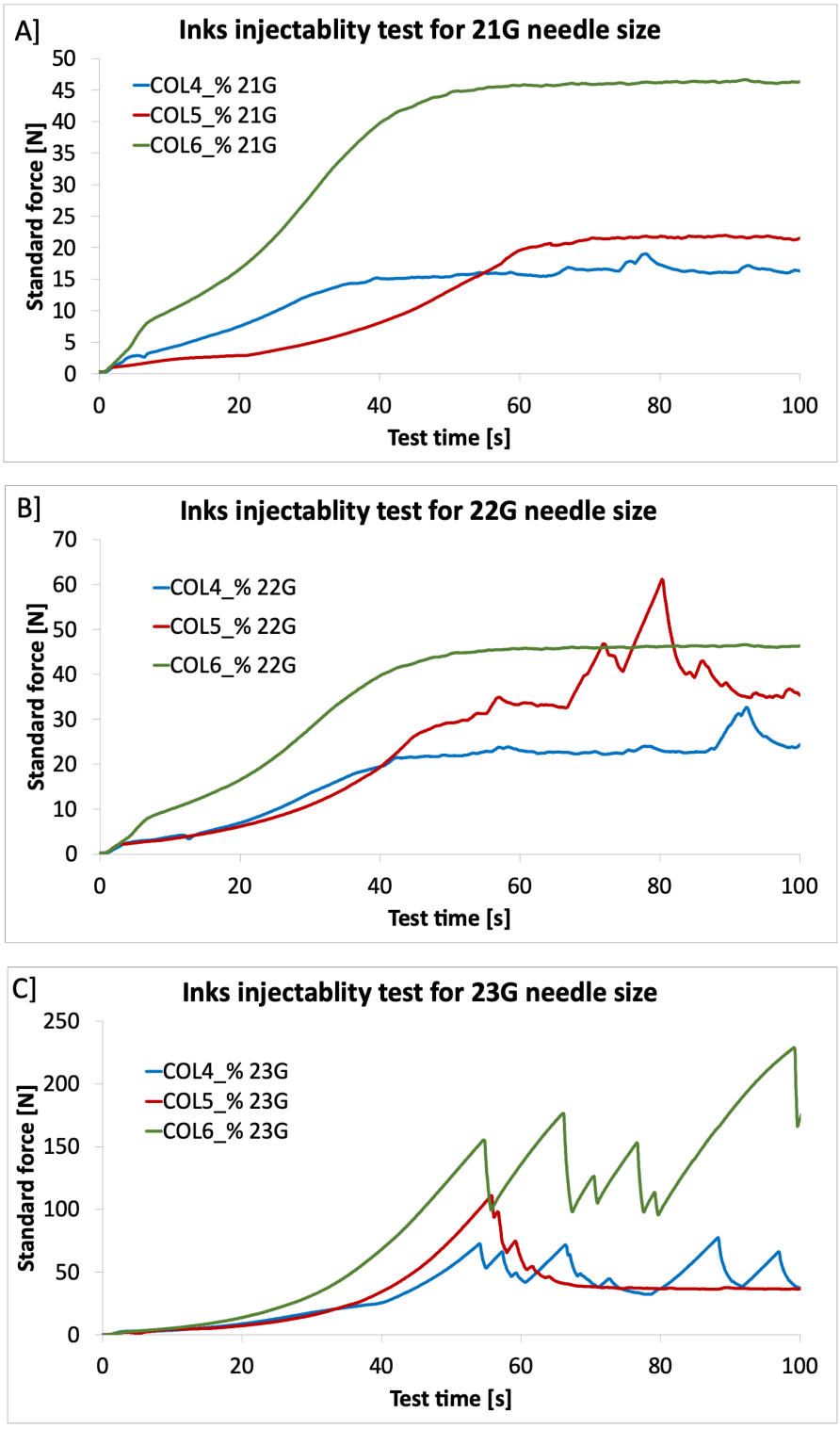



**Figure 3.12:** Standard force vs extrusion of collagen injectability test for three concentration 4, 5 and 6% collagen tested with three needle sizes 21G, 22G and 23G.

### 3.4.2. DoE Study 1 Optimisation of COL ink formulation and scaffold properties

Following the assessment of chemical composition and injectability of the COL-4%, COL_5% and COL_6% inks, DOE Study 1 sought to identify the optimal collagen ink formulation and crosslinking conditions. The full results dataset for Study 1 can be found in Table 1.B of **Appendix- B** showing the 29 runs and the corresponding responses for each run. Employing RSM with a quadratic model, the general form of the second-order polynomial equation used to describe the relationship between the independent variables and the response variable is as follows:

$$y = \beta_0 + \sum(\beta_i X_i) + \sum(\beta_{ii} X_{ii}^2) + \sum(\beta_{ij} X_i X_j) + \in$$

**Equation 3.8:** Second-order polynomial equation, where Y is the predicted response, $\boldsymbol{\beta_0}$ is the intercept term, $\boldsymbol{\beta_i}$ are the linear coefficients for the factors, $\boldsymbol{\beta_{ii}}$ are the quadratic coefficients for the square of the factors, $\boldsymbol{\beta_{ij}}$ are the interaction coefficients for the product of factors $\boldsymbol{X_i}$ and $\boldsymbol{X_j}$, $\boldsymbol{X_i}$ and $\boldsymbol{X_j}$ are the coded levels of the independent variables, and $\in$ is the random error term.

In the context of Study 1, four independent variables, A (Collagen concentration), B (Tannic acid concentration), C (Crosslinking time), and D (Needle size), the specific quadratic model is presented as follows:

$$y = \beta_0 + \beta_1 A + \beta_2 B + \beta_3 C + \beta_4 D + \beta_{11} A^2 + \beta_{22} B^2 + \beta_{33} C^2 + \beta_{44} D^2 + \beta_{12} AB + \beta_{13} AC + \beta_{14} AD + \beta_{21} BA + \beta_{23} BC + \beta_{24} BD + \beta_{34} CD + \in$$

Each term in the equation represents a different type of effect:

- The $\beta_i$ terms represent the main effects of each factor.
- The $\beta_{ii}$ terms represent the pure quadratic effects, showing non-linearity.
- The $\beta_{ij}$ terms represent the interaction effects between different factors, which capture how the response changes when two factors are simultaneously varied.

#### *3.4.2.1. Response Models*

The summary of the variance analysis for the measured responses is presented in **Table 3.4**. Model terms with p-values below 0.05 are considered statistically significant, while those with p-values above this threshold do not reach significance at the 95% confidence level. Additionally, the lack of fit p-values exceeding 0.05 for all responses indicates a satisfactory correlation between the experimental data and the predictive models, confirming that the models are adequately fitted to the

data. $R^2$ serves as a measure of the model's fit quality, reflecting the portion of total variation that is explained by the model. The adjusted $R^2$ provides a more accurate assessment of fit quality, especially as the model incorporates extra terms due to the three-level independent variables and is less influenced by the number of degrees of freedom. The ANOVA table provided outlines the statistical analysis for three different responses (**Table 3.4**): printing pressure, Young's modulus, and pore size, as part of an experiment to understand the effects of different factors on the quality of 3D bioprinted collagen.

Printing pressure (R1)

The printing pressure varied between 185 and 399 kPa. Needle size (D) is the most influential factor with an F-value of 67.31, followed by the squared terms of collagen concentration ($A^2$), and needle size ($D^2$), all showing significant effects on printing pressure. The ANOVA for printing pressure reveals a significant quadratic model with a p-value less than 0.0001, indicating that the lack of fit is not significant ($p = 0.6956$), suggesting the model fits the actual data well. The model explains 82.08% of the variability ($R^2 = 0.8208$), with adjusted $R^2$ of 0.772, indicating a good fit with some room for improvement, and predicted $R^2$ of 0.6945, suggesting reasonable predictability.

Young's Modulus (R2)

The Young's modulus ranged between 0.0218 - 0.1508 MPa. The factors influencing the Young's modulus are tannic acid (B) and crosslinking time (C), both of which are significant, with crosslinking time showing a more substantial effect (F-value = 29.51). For Young's modulus, the model is also significant with a p-value less than 0.0001, but with a lower $R^2$ value of 0.581, indicating that approximately 58.1% of the variability in Young's modulus can be explained by the model. The lack of fit is not significant ($p = 0.1735$), suggesting the model's adequacy.

Pore Size (R3)

Scaffold pore size for the scaffolds fabricated in Study 1 ranged between 0.142and 0.833 $mm^2$. For pore size (R3), the model is highly significant ($p < 0.0001$) with an $R^2$ value of 0.9298, indicating that it explains 92.98% of the variance in pore size within the design space. The individual effects of tannic acid (B) and needle size (D) on pore size are not significant, with p-values of 0.7956 and $< 0.0001$, respectively. On the other hand, crosslinking time (C) shows a highly significant effect ($p < 0.0001$), suggesting it is a critical factor in controlling pore size. The lack of fit is non-significant ($p = 0.2417$), which suggests that the model predictions are reliable. This indicates that while some factors do not individually influence the pore size significantly, crosslinking time is a key parameter. The model's suitability for prediction within the explored design space is affirmed by the non-significant lack of fit for all responses. Further investigation could focus on the interactions between these factors to refine the model and enhance its predictability.

**Table 3.4:** ANOVA for response surface quadratic model for printing pressure, Young's modulus and pore size.

| **R1- Printing pressure** | **Sum of Squares** | **F-value** | **p-value** | **Comment** | **$R^2$** | **Adjusted $R^2$** | **Predicted R** |
|---|---|---|---|---|---|---|---|
| **Model** | 58110.34 | 16.8 | < 0.0001 | significant | 0.8208 | 0.772 | 0.6945 |
| A-Collagen | 1141.73 | 1.98 | 0.1733 | | | | |
| D-Needle Size | 38807.71 | 67.31 | < 0.0001 | | | | |
| $A^2$ | 5899.62 | 10.23 | 0.0041 | | | | |
| $D^2$ | 13808.23 | 23.95 | < 0.0001 | | | | |
| **Residual** | 12685.08 | | | | | | |
| Lack of Fit | 9827.56 | 0.7643 | 0.6956 | not significant | | | |
| **R2- Young's modulus** | | | | | | | |
| **Model** | 0.0133 | 18.02 | < 0.0001 | significant | 0.581 | 0.5487 | 0.4733 |
| B-Tannic Acid | 0.0024 | 6.54 | 0.0167 | | | | |
| C-Crosslinking Time | 0.0109 | 29.51 | < 0.0001 | | | | |
| **Residual** | 0.0096 | | | | | | |
| Lack of Fit | 0.009 | 2.69 | 0.1735 | not significant | | | |
| **R3-Pore size** | | | | | | | |
| **Model** | 1.16 | 129.99 | < 0.0001 | significant | 0.9298 | 0.9325 | 0.9184 |
| B-Tannic Acid | 0.0002 | 0.0685 | 0.7956 | | | | |
| C-Crosslinking Time | 0.2897 | 324.42 | < 0.0001 | | | | |
| D-Needle Size | 0.0034 | 65.49 | < 0.0001 | | | | |
| **Residual** | 0.07545 | | | | | | |
| Lack of Fit | 0.0061 | 2.13 | 0.2417 | not significant | | | |

#### *3.4.2.2. Validation and verification of the response models*

Normal probability plots of residuals are crucial for assessing whether the residuals from the models deviate from a normal distribution. For a model to be considered adequate, the residuals should ideally lie close to a straight line on these plots. The plots for printing pressure, Young's modulus and pore size (**Figure 3.13** A, B and C respectively) show that the points closely following the diagonal line without systematic deviations, suggesting that the residuals are normally distributed, satisfying one of the critical assumptions of the ANOVA. In cases where a clear pattern or systematic deviation from the line is observed, this would indicate potential issues with normality, which might necessitate a transformation of data or a revision of the model.

The plot of studentised residuals against predicted values (**Figure 3.14**) is used to detect homoscedasticity the assumption that the residuals have the same variance across all levels of the independent variables. These plots show a random spread of residuals across the range of predicted values, indicating that the variance is constant (homoscedasticity). If, in contrast, the residuals fan

out or in (forming a cone shape), this would suggest heteroscedasticity, indicating that the model's assumption of equal variance is violated.

The correlation between predicted and actual values provides a direct measure of the model's predictive accuracy. **Figure 3.15** Displays the externally studentised residuals plotted against the anticipated values. No megaphone pattern were observed in any of the responses, indicating a lack of increased variation and thus no requirement for a model modification. The data points are distributed randomly and positioned within specified limitations, with the majority of responses falling between the range of -2 to +2.

The independence of residuals is another fundamental assumption in regression analysis. The plot of studentised residuals versus run number checks for any pattern related to the order of the experimental runs. For study 1, the random distribution of residuals with respect to the run number was observed for all responses implying that the residuals are independent of each other, and that no time related or order effects are influencing the results (**Figure 3.16**). The absence of any patterns, trends, or cycles in this data suggests the lack of bias on the model's results.

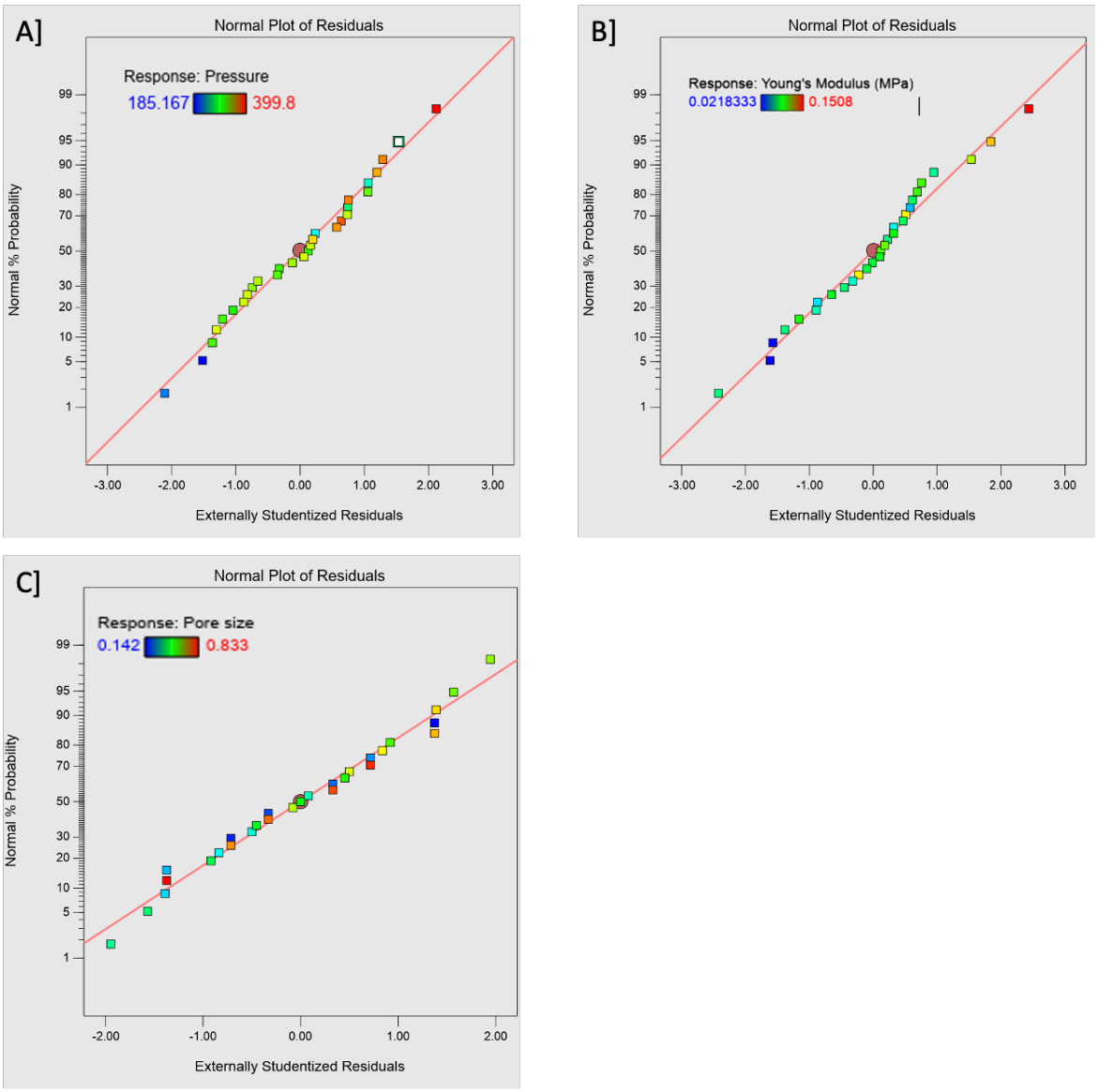



**Figure 3.13**: Normal probability plots for A] printing pressure, B] Young's modulus and C] pore sizes for 3D bioprinted pure collagen scaffold.

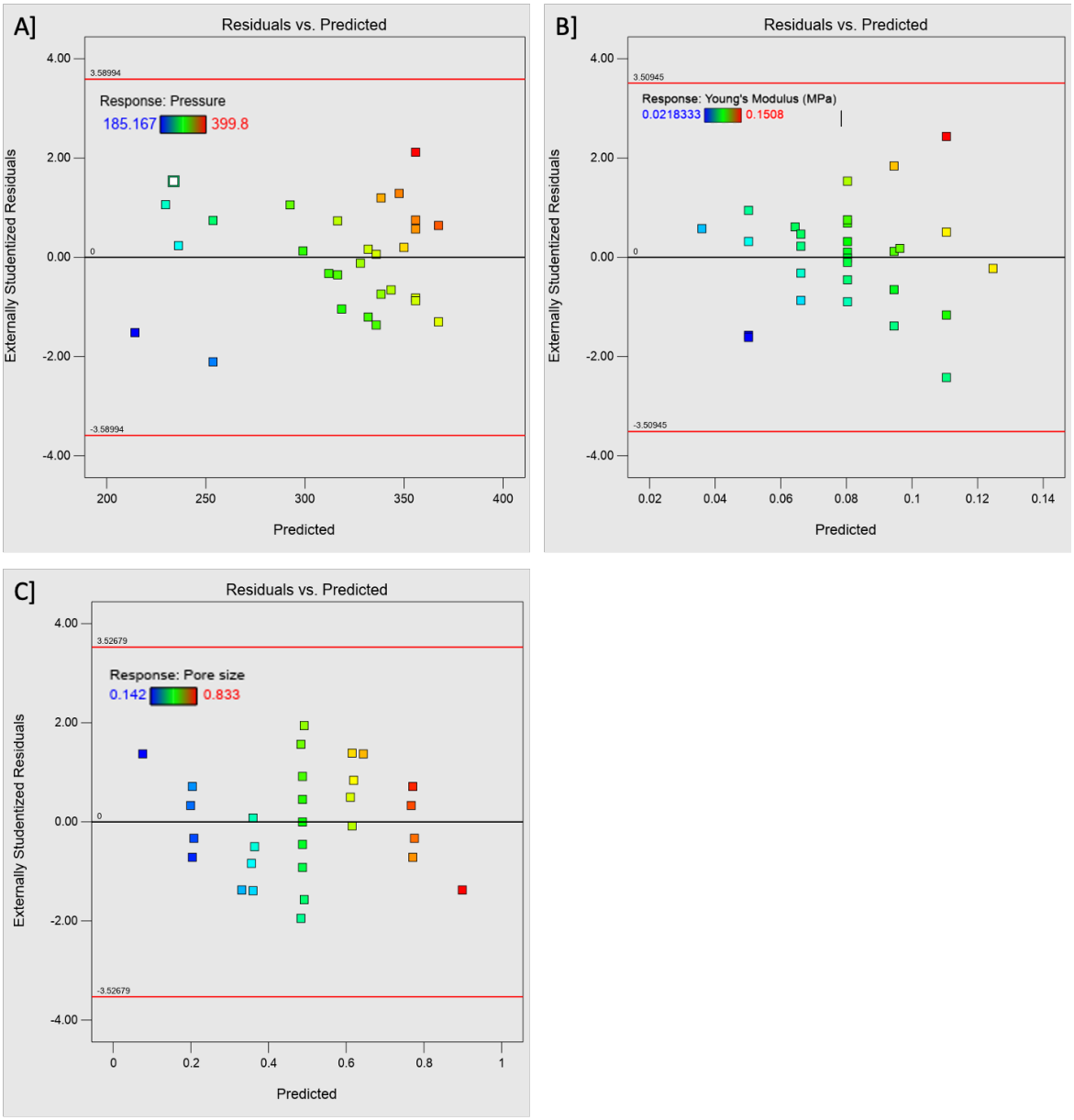



**Figure 3.14:** Studentised residuals versus predicted values plots for A] printing pressure, B] Young's modulus and C] pore sizes for 3D bioprinted pure collagen scaffold.

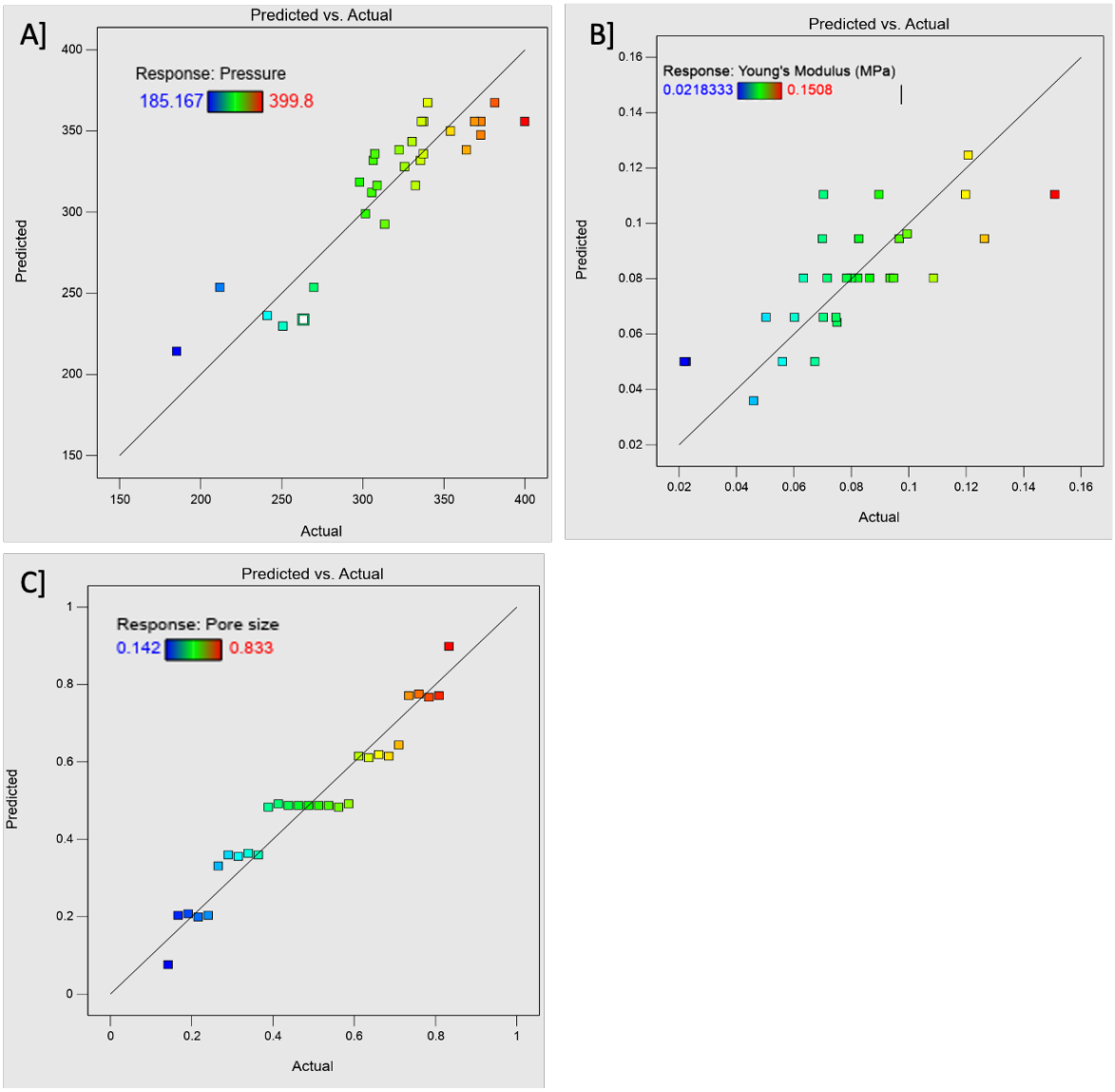



**Figure 3.15:** Predicted versus actual values plots for A] printing pressure, B] Young's modulus and C] pore sizes for 3D bioprinted pure collagen scaffold.

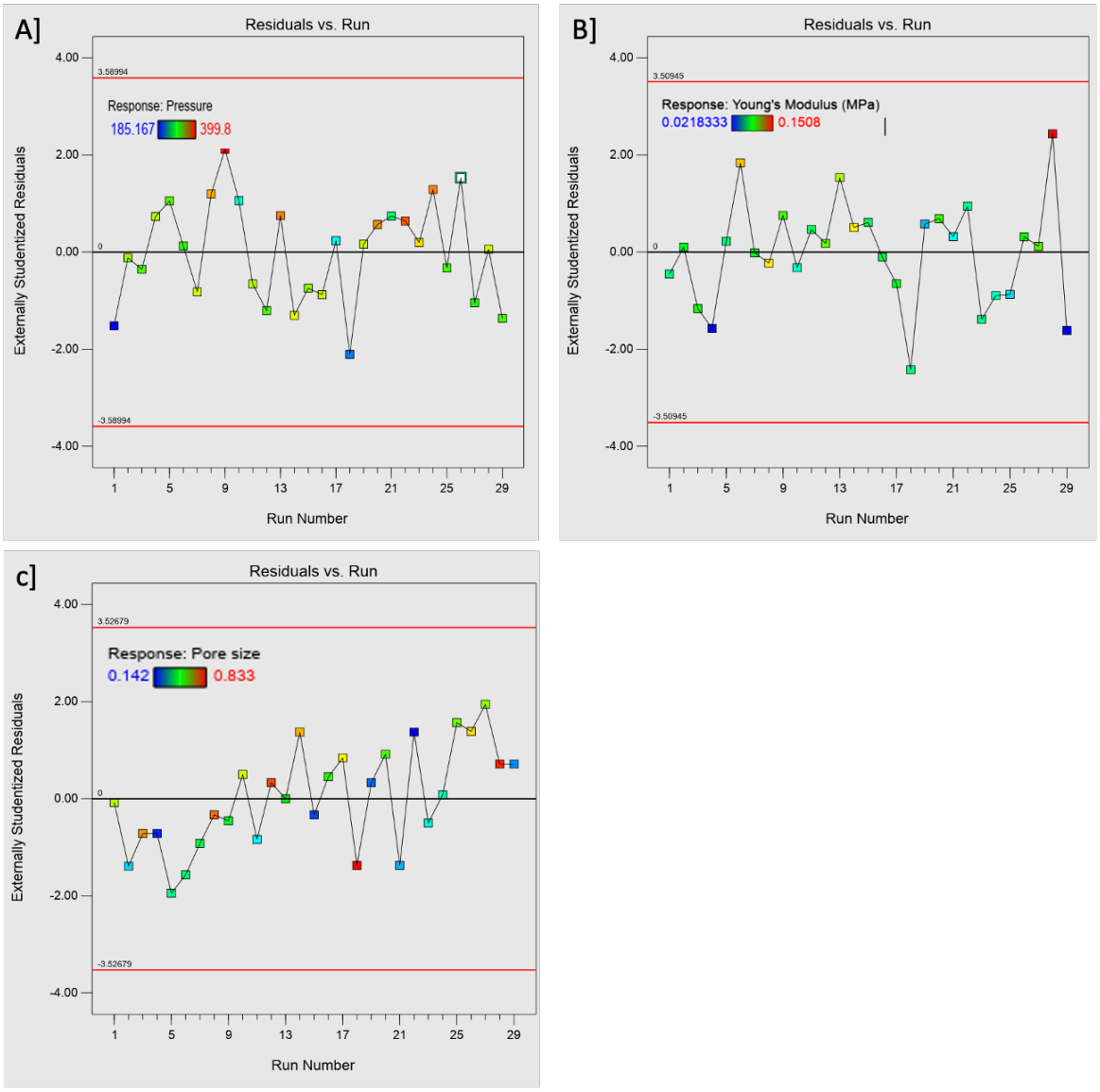



**Figure 3.16:** Studentised residuals versus run number plots for A] printing pressure, B] Young's modulus and C] pore sizes for 3D bioprinted pure collagen scaffold.

### *3.4.2.3. Responses analysis study 1*

Printing pressure response

The printing pressure of 3D bioprinted collagen is affected by collagen concentration (A) and Needle size (D) with increased printing pressure observed for increased collagen concentration and increased needle gauge size, (**Figure 3.17**). The plot indicates that collagen concentration (A) has a significant effect on the printing pressure, as seen by the pronounced steepness of its response curve. The sensitivity of the printing pressure to collagen concentration underscores the critical nature of collagen concentration in the bioprinting process, suggesting it as a primary optimisation target.

An increase in either collagen concentration (A) or needle gauge size (D) correlates with an increase in printing pressure (**Figure 3.17**-B). The interaction between these two factors is evident from the curvature of the plot, which implies that the effect of one factor on the printing pressure may depend on the level of the other factor. It is crucial to note the presence of error bars, indicating the standard deviation of the results, which becomes more pronounced at higher levels of both factors. This variation underscores the need for precise control over these parameters to ensure reproducibility and reliability in the bioprinting process. The perturbation and interaction plots, **Figure 3.17**-A and **Figure 3.17**-B, demonstrate the relationship between the bioprinting parameters and the printing pressure required for the bioprinting of collagen scaffolds. The perturbation plot (**Figure 3.17**-A) identifies collagen concentration as a key factor of printing pressure. The interaction plot (**Figure 3.17**-B) provides further insight into the compounded effect of collagen concentration and needle size, highlighting an area of parameter space where the printing pressure reaches its desired level. The results show that smaller needle sizes (23 G) and increased material concentration increase the extrusion pressure. Similar findings have been reported in the literature [243], [244]. Kyle *et al.* and Ouyang *et al.* reported that printing parameters, including material viscosity and needle gauge size, are key factors in achieving optimal printing performance [243], [244].

The contour plot in **Figure 3.18**-A demonstrates the relationship between collagen concentration (Factor A) and needle size (Factor D) with regard to the printing pressure. The contour lines delineate regions of constant printing pressure, with the colour gradient indicating increasing pressure from blue (low pressure) to red (high pressure). The plot suggests an optimal region (shown in green) where the printing pressure is at its lowest. This region is crucial for ensuring a smooth extrusion process without compromising the structural integrity of the bioprinted collagen. The plot indicates that lower needle gauge sizes and mid-range collagen concentrations might provide the most favourable conditions for printing quality and cell viability. **Figure 3.18**-B expands upon the contour plot by providing a three-dimensional response surface of the same variables. This visualisation helps in understanding the nature of the relationship between needle size and collagen concentration. The surface rises with increased collagen concentration and needle gauge size (23 G), which implies

higher printing pressures are required under these conditions compared to lower collagen concentration and larger diameter needles (21G). The 'valley' or the lowest point on the surface represents the optimal combination of both factors for the lowest printing pressure, which aligns with the green region in the contour plot. This 3D perspective is particularly useful for identifying the direction of change required to reach the optimal print conditions.

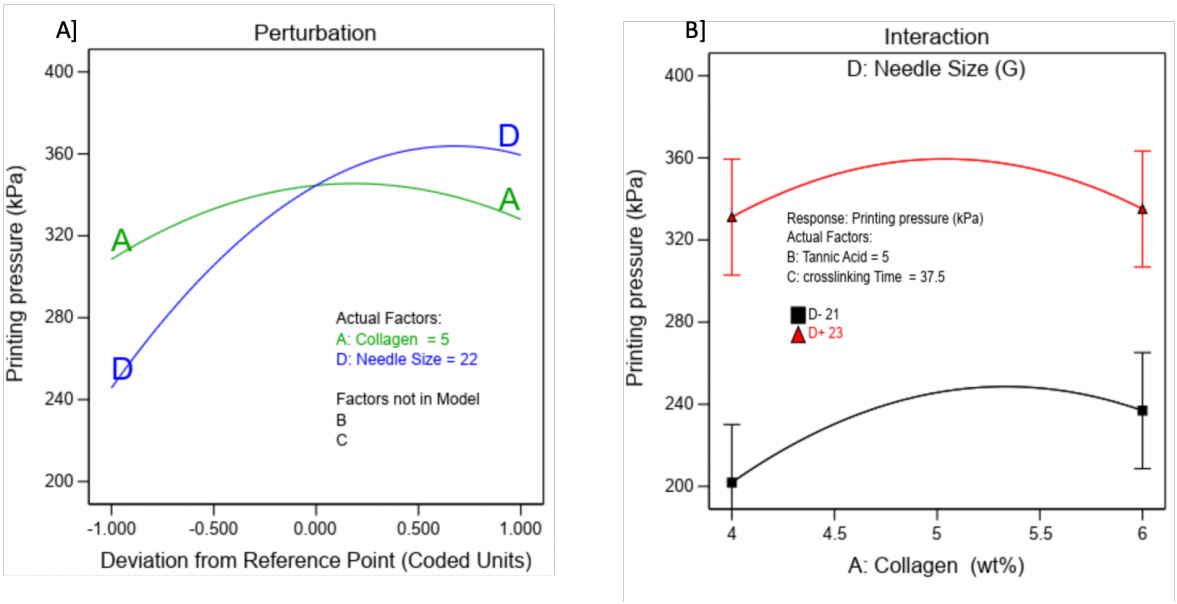



**Figure 3.17:**A] Perturbation plot displaying the sensitivity of Factor A (collagen concentration ) and Factor D (needle size) to pressure parameter. B] Interaction effects of collagen concentration and needle size on printing pressure.

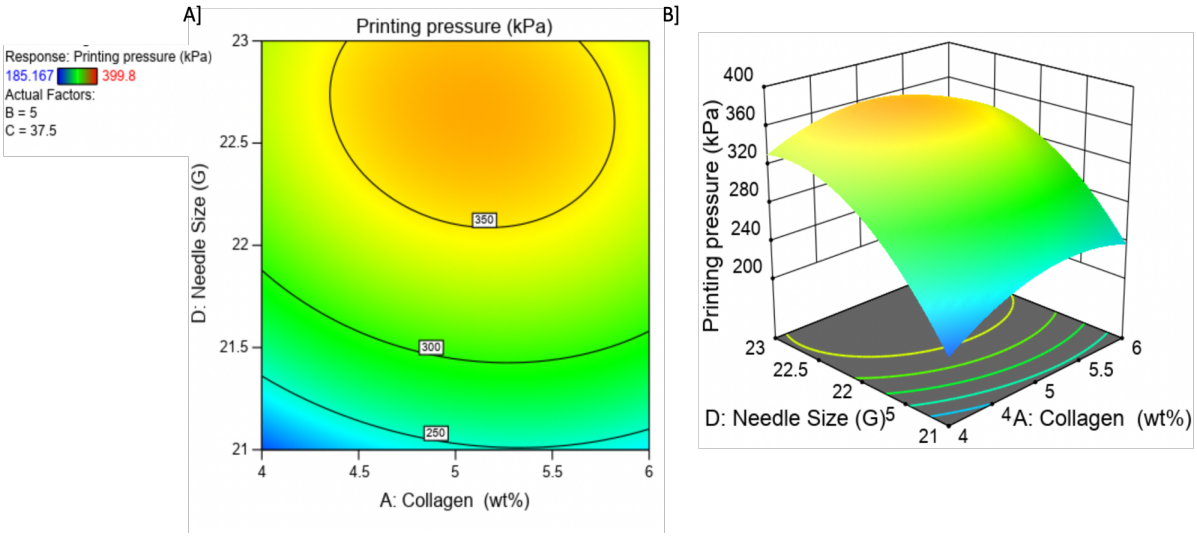



**Figure 3.18:** A] Contour plot of printing pressure as influenced by collagen concentration and needle size. B] 3D response surface showing the effect of needle size and collagen concentration on printing pressure.

Young's modulus response

**Figure 3.19**-A provides a perturbation plot, which reveals the sensitivity of Young's modulus to changes in three different scaffold fabrication parameters: collagen concentration (A), crosslinking agent concentration (B), and crosslinking time (C). The plot indicates that crosslinking agent concentration and crosslinking time have a more pronounced effect on Young's modulus compared to parameter collagen concentration Notably, an increase in crosslinking agent concentration and crosslinking time corresponds to an increase in Young's modulus, indicating that these parameters are critical for enhancing scaffold stiffness. The perturbation plot, however, also reveals the limited model fit, indicated by an $R^2$ value of 0.581, which suggests that additional factors may influence the response and should be investigated.

**Figure 3.19**-B and show interaction plots for the effect of collagen concentration with crosslinking agent concentration and crosslinking time, respectively. The plots demonstrate a trend of increasing Young's modulus with higher levels of both crosslinking concentration and crosslinking time. This linear relationship aligns with the hypothesis that an increase in crosslinking density within the scaffold structure results in greater stiffness. These results are consistent with the findings of Lee *et al.* [245], who reported an increase in scaffold stiffness with an increase in tannic acid concentration.

The collagen concentration and needle size parameters did not significantly influence the Young's modulus within the tested ranges, indicated by p-values higher than the 0.05 threshold. These findings have important implications for the design and fabrication of scaffolds for tissue engineering applications, where mechanical properties need to be tailored to mimic the native tissue properties.

**Figure 3.20**-A shows a contour plot illustrating the influence of collagen concentration (A) and tannic acid concentration (B) on the Young's modulus of the scaffold. The contour lines represent levels of Young's modulus, with the green areas denoting regions of higher stiffness. As the concentration of tannic acid increases, so does the Young's modulus, suggesting that tannic acid plays a significant role in enhancing the stiffness of the scaffold. Complementing the contour plot, **Figure 3.20**-B is a 3D response surface plot that further visualises the relationship between collagen concentration , tannic acid concentration , and Young's modulus. The surface plot highlights a region where the modulus reaches its peak, corresponding to the optimal concentrations of both collagen and tannic acid for maximal scaffold stiffness. **Figure 3.20**-C, the effect of collagen concentration and crosslinking time on Young's modulus is shown. This plot reveals that crosslinking time has a more pronounced effect on stiffness than collagen concentration. The accompanying 3D response surface plot, **Figure 3.20**-D maps Young's modulus against collagen concentration and crosslinking time, showing the optimal conditions for maximum scaffold stiffness.

The analysis of the experimental plots indicates that the concentration of tannic acid and the duration of crosslinking are critical factors influencing the Young's modulus of the bioprinted scaffold. The

data suggest that while both parameters significantly impact the mechanical properties, tannic acid concentration exerts a slightly greater influence on Young's modulus. This finding highlights the importance of precise control over chemical composition and processing time to tailor the mechanical characteristics of the scaffold, ensuring its suitability for intended biomedical applications. This is consistent with the understanding that crosslinking agents like tannic acid can create more rigid structures by forming additional bonds within the scaffold matrix. The results support the concept that a carefully controlled crosslinking process is essential for fabricating scaffolds with desired mechanical properties.

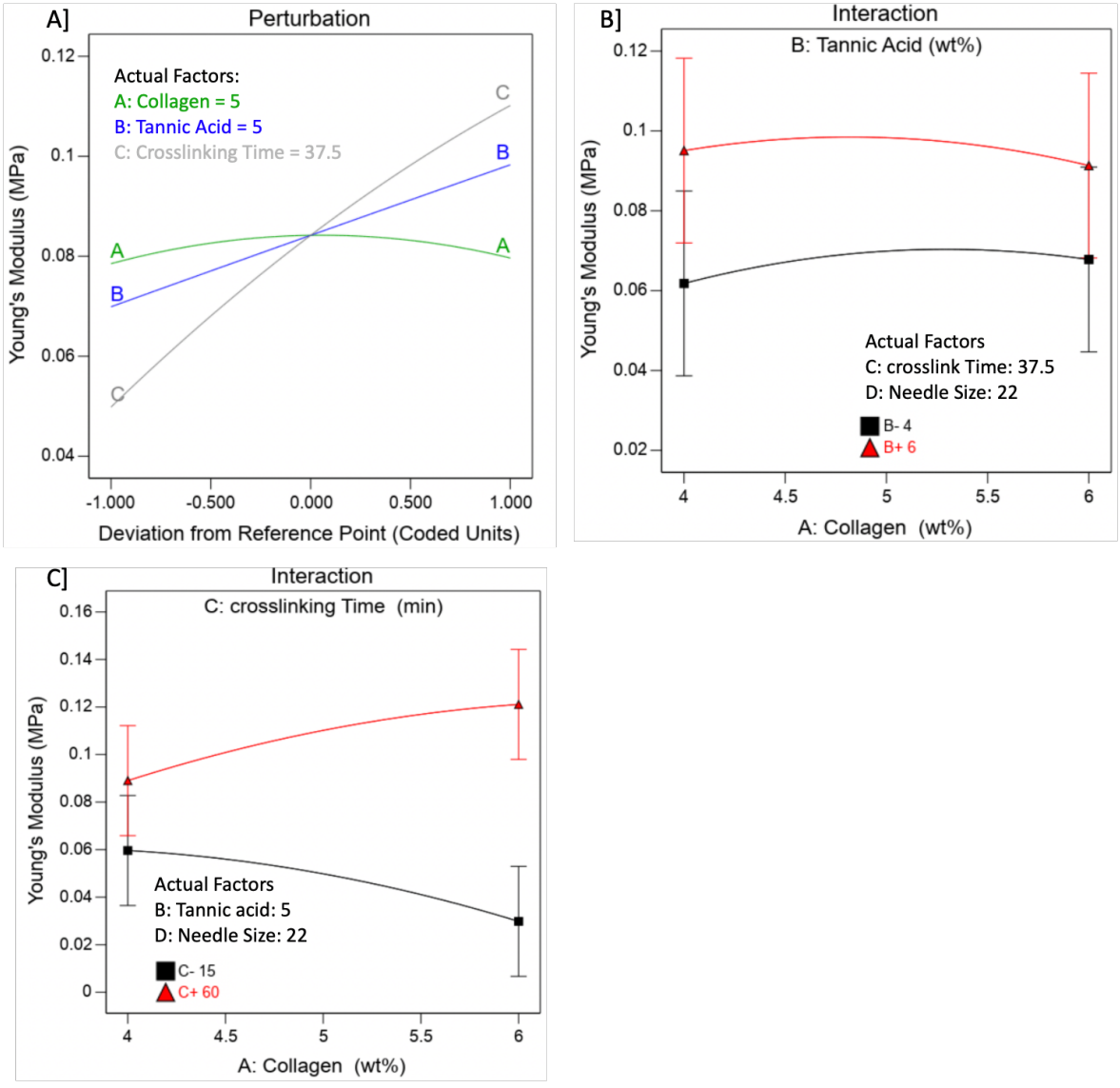



**Figure 3.19:** A] Perturbation plot illustrating the effects of fabrication parameters on Young's modulus. B]-C] Interaction plots demonstrating the effect of collagen concentration and crosslinking concentration and time on Young's modulus.

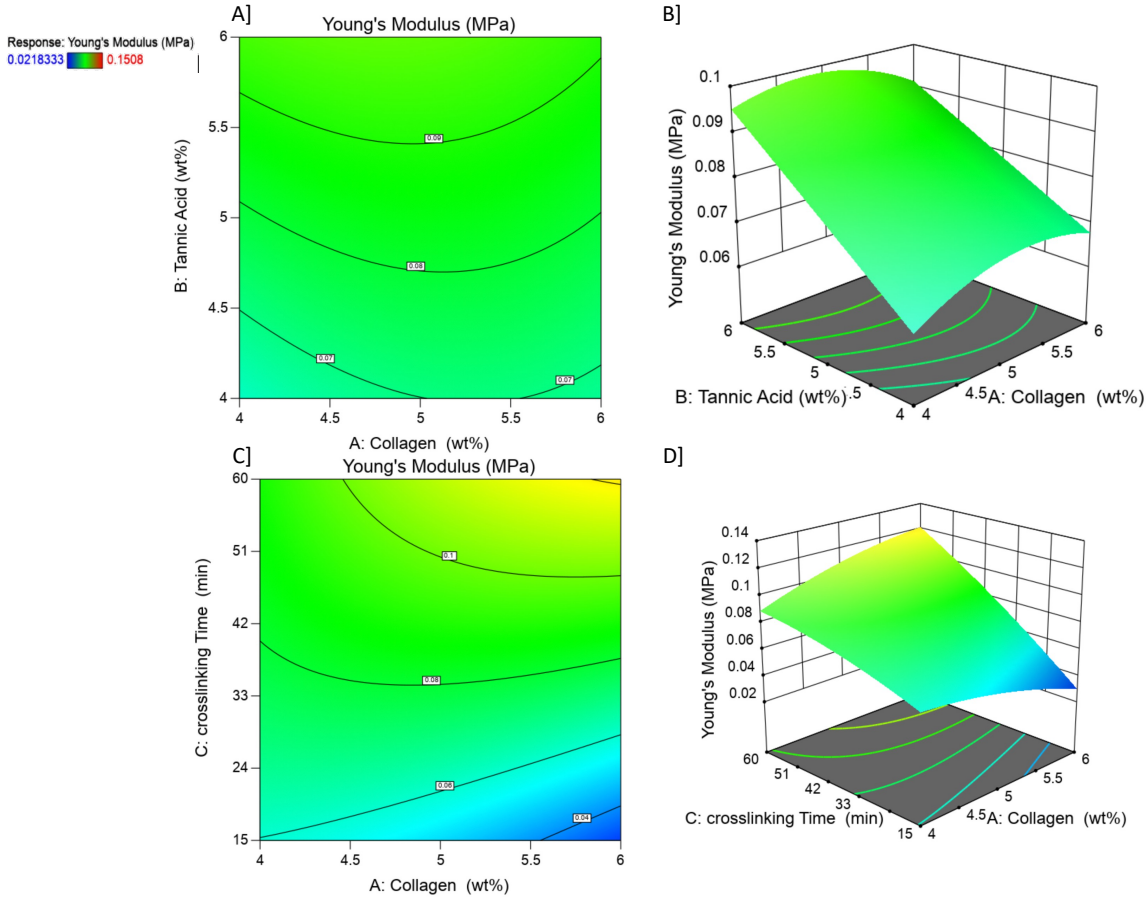



**Figure 3.20:** A] Contour plot of Young's modulus against Collagen and tannic acid concentration. B] 3D Response Surface of Young's modulus against collagen and tannic acid concentration. C] Contour plot of Young's Modulus against collagen concentration and crosslinking time. D] 3D Response Surface of Young's modulus against collagen concentration and crosslinking time.

Pore size response

The perturbation plot (**Figure 3.21**-A) demonstrates that pore size was influenced by three factors: collagen concentration (A), tannic acid concentration (B), and crosslinking time (C). The plot reveals a marked effect of crosslinking time on pore size, with the line for crosslinking time (C) showing a steep incline, indicating that longer crosslinking times are associated with increased pore size. Collagen concentration also influences pore size but to a lesser extent, as shown by the gentler slope of factor A. In contrast, tannic acid concentration shows a minimal effect within the explored range, suggesting that, under these conditions, it does not significantly alter the pore structure.

Increasing both collagen concentration (A) and tannic acid concentration (B) led to an increase in pore size (**Figure 3.21**-B). The plot illustrates a more pronounced effect of crosslinking time on pore size compared to collagen concentration. As crosslinking time increases, pore size tends to increase, which may be attributable to the longer period allowing for the formation of a more porous structure, possibly due to changes in the collagen matrix as it undergoes crosslinking. Finally, **Figure 3.21**-D demonstrates the relationship between crosslinking time and needle size on pore size. This interaction plot indicates that larger needle sizes (21G) and longer crosslinking times contribute to larger pore sizes.

Analysing these plots together offers useful insights relating to the influence of process parameters on the pore size of collagen scaffolds. The duration of crosslinking is crucial in determining pore size, indicating that precise management of the crosslinking process is necessary to obtain the intended pore structure. Collagen concentration and needle size have an impact, but the crosslinking time shows to be more influential within the parameters evaluated. Considering the influence of the crosslinking parameters on scaffold stiffness, it is likely that the stiffer scaffolds can better maintain the open scaffold structure and thus display larger pore sizes than the less stiff scaffolds. These findings are consistent with recent studies that have shown similar results. For instance, Abdollahiyan *et al.* [246] reported that extended crosslinking times significantly increased pore sizes, attributing this to the more extensive crosslinking network formation which enhances the structural integrity and porosity. Similarly, Gao *et al.* and Koo *et al.* [246], [247] observed that higher collagen concentrations and prolonged crosslinking times contributed to larger pore sizes in 3D bioprinted scaffolds, supporting the study observations. These studies collectively underscore the importance of optimising crosslinking time and collagen concentration to control the pore architecture of bioprinted scaffolds effectively.

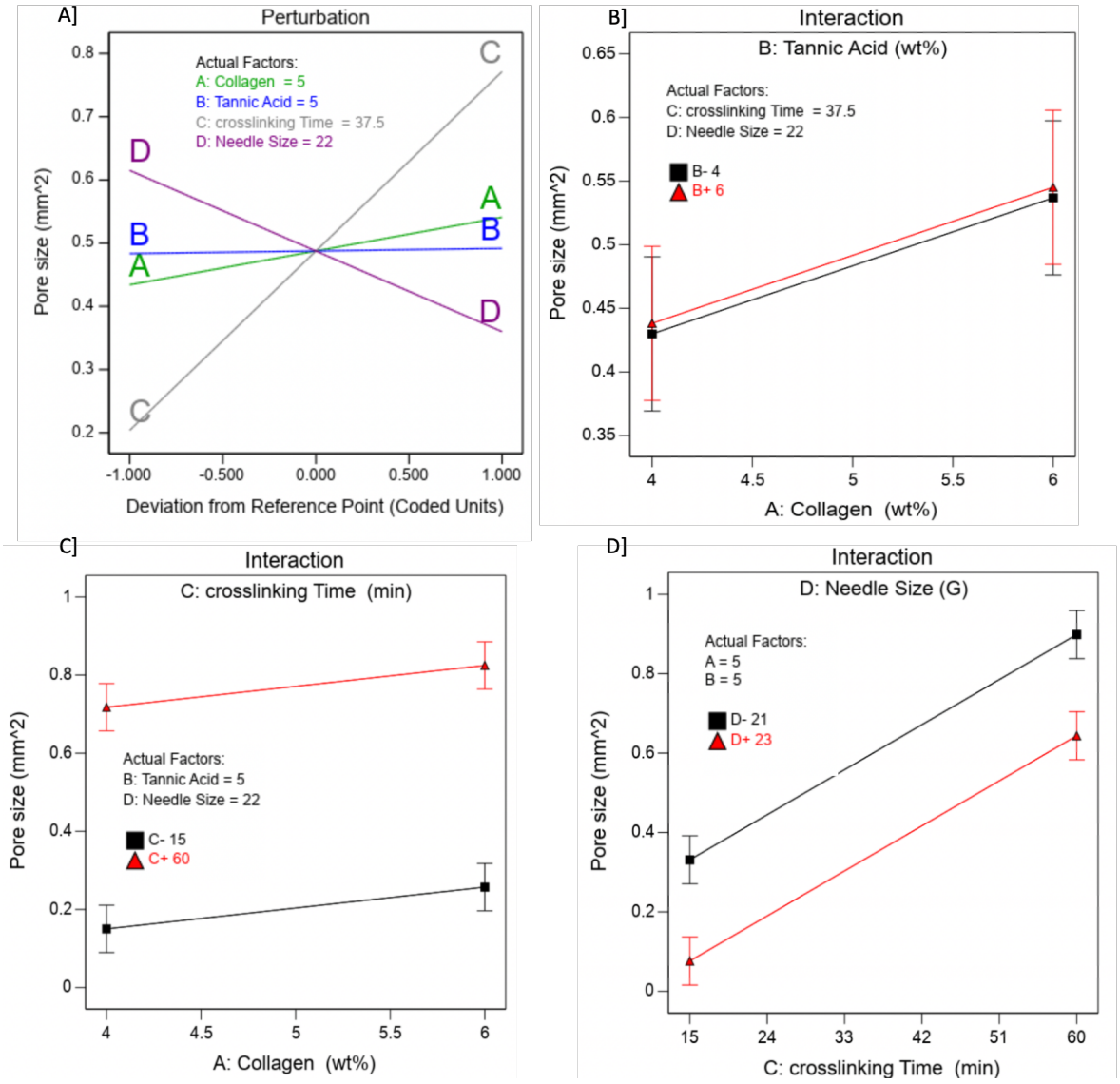



**Figure 3.21:** A] Perturbation Plot for Pore Size Response. B] Interaction Effect of collagen and tannic acid concentration on pore size. C] Effect of Collagen concentration and crosslinking time on pore size. D] Effect of crosslinking time and needle size on pore size.

**Figure 3.22**-A illustrates a two-dimensional contour plot indicating the effect of collagen concentration (A) and crosslinking time (C) on pore size. The plot displays a gradient of pore sizes, with larger pore sizes correlating with higher crosslinking times. Collagen concentration also affects pore size, although the impact is less pronounced than that of crosslinking time. The contour lines that are far apart in the central region indicate that within this area, changes in the parameters do not result in significant alterations in pore size. The corresponding 3D surface plot in **Figure 3.22**-B provides a more tangible view of the same interactions, with the z-axis representing pore size. This visualization reinforces the findings from the contour plot, where higher crosslinking times and, to a lesser degree, increased collagen concentrations lead to larger pore sizes. The plot's peak suggests the optimal parameter setting for maximizing pore size under the tested conditions.

**Figure 3.22**-C shows the impact of needle size and crosslinking time on the pore size. A clear trend is visible; larger needle sizes and longer crosslinking times are associated with increased pore size. This again may relate to the how the stiffness properties of the scaffold influence the ability of pores to maintain their shape as the larger needle sizes lead to the formation of thicker struts. The 3D surface plot in Figure 3.22-D complements the contour plot, providing a visual representation of how pore size increases with larger needle sizes and longer crosslinking times. The rising plane of the surface plot towards the higher values of both factors emphasizes their significance in determining pore size.

In **Figure 3.22**-E, we observe the influence of tannic acid concentration and crosslinking time on pore size. The contour plot suggests that pore size increases with longer crosslinking times, while the impact of tannic acid concentration is less evident. It can be inferred that crosslinking time is a more dominant factor in manipulating pore size compared to the concentration of tannic acid within the examined range. Lastly, **Figure 3.22**-F presents a 3D surface plot showing the combined effect of tannic acid concentration and crosslinking time on pore size. Similar to the contour plot, the 3D plot suggests that an increase in crosslinking time leads to a more pronounced increase in pore size compared to changes in tannic acid concentration.

The collection of graphs shows that the duration of crosslinking is a crucial component that affects the size of pores in 3D bioprinted scaffolds. This knowledge is crucial for scaffold design, especially in situations where pore size is essential for material performance. The permeability of scaffolds can greatly impact characteristics like cell motility, nutrient diffusion, waste clearance mechanical integrity, and overall bioactivity. By changing the crosslinking time, collagen concentration, needle size, and tannic acid concentration, it is possible to customise the pore size of scaffolds to meet specific needs for different tissue engineering purposes. Thus, adjusting fabrication settings to control pore size can significantly influence the effectiveness of tissue-engineered constructs.

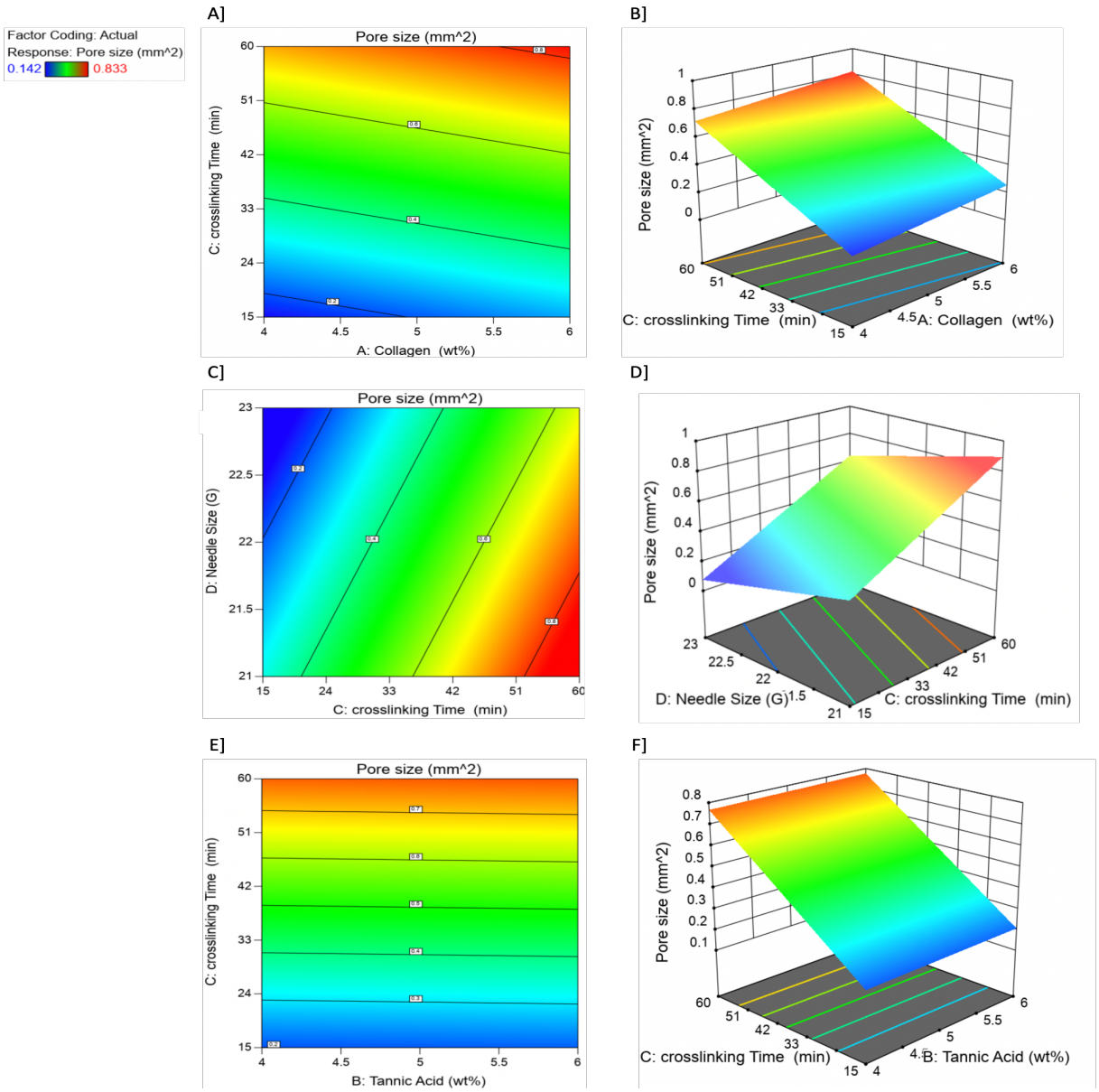



**Figure 3.22:** A] Contour plot for pore size response with factor A and factor C. B] 3D surface plot for pore size response with factor A and factor C. C] Contour plot for pore size response with factor d and factor c. D] Surface plot for pore size response with factor D and factor C. E] Contour plot for pore size response with factor B and factor C. F] 3D surface plot for pore size response with factor B and factor C.

### *3.4.2.4. Study 1 Optimisation*

Optimising the properties of 3D bioprinted collagen scaffolds is essential to achieve the desired functionality and structural integrity for tissue engineering applications. As indicated by the RSM results, the optimisation process involves adjusting multiple parameters to influence scaffold characteristics, such as printing pressure, Young's modulus, and pore size. In this study, a numerical optimisation strategy was employed, assigning specific goals to each response while allowing the parameters to vary within pre-defined limits (**Table 3.5:** Optimisation criteria for the scaffold properties**Error! Reference source not found.**. The aim of optimisation was to maximise the scaffold's Young's modulus whilst concurrently minimising the ink printing pressure and pore size. The optimisation utilised a desirability function approach, transforming each response into a dimensionless measure of performance, with a desirability index (di) ranging from 0 to 1 the closer the di is to 1, the more desirable the outcome. Collagen concentration and printing pressure were given the highest importance, indicating a priority to achieve a scaffold with sufficient structural integrity and ease of extrusion. Young's modulus was also of high importance, aligning with the goal to maximise the stiffness of the scaffold to provide sufficient support to repair tissue during the healing process. Pore size was minimised, which is essential to control the scaffold's porosity for potential cell attachment, ingrowth and nutrient diffusion, should cell seeding be considered in future applications.

**Table 3.5:** Optimisation criteria for the scaffold properties

| Name | Goal | Lower Limit | Upper Limit | Importance |
|---|---|---|---|---|
| A: Collagen [%(w/v)] | in range | 4 | 6 | 5 |
| B: Tannic Acid [%(w/v)] | in range | 4 | 6 | 3 |
| C: Crosslinking Time [min] | in range | 15 | 60 | 3 |
| D: Needle Size [G] | in range | 21 | 23 | 3 |
| Printing pressure [kPa] | minimise | 185.2 | 399.8 | 4 |
| Young's Modulus [MPa] | maximise | 0.022 | 0.151 | 4 |
| Pore size [$mm^2$] | minimise | 0.142 | 0.833 | 3 |

The optimisation results (**Table 3.6**) reveal that a collagen concentration at the lower limit of the range (4 %(w/v), combined with the highest concentration of tannic acid (6 %(w/v) ), an intermediate crosslinking time (~37 min), and the largest needle size (21G), leads to a desirable balance of scaffold properties. These conditions yield a scaffold with lower printing pressure, suggesting easier extrusion, a moderate Young's modulus indicative of necessary stiffness, and a controlled pore size. The desirability function for the top five solutions suggested by the optimisation

is 0.704, indicating a relatively high overall desirability for the optimisation goals set. This balanced optimisation approach prioritises the printing pressure and mechanical stiffness of the scaffold while maintaining a controlled pore size, even though individual desirability for pore size might not be at its theoretical optimum.

**Table 3.6:** Optimal solutions as obtained by Design-Expert

| Number | Collagen %(w/v) | Tannic Acid %(w/v) | crosslinking Time (min) | Needle Size (G) | Printing pressure (kPa) | Young's Modulus (MPa) | Pore size ($mm^{\wedge 2}$) | Desirability |
|---|---|---|---|---|---|---|---|---|
| **1** | **4** | **6** | **37** | **21** | **106** | **0.094** | **0.614** | **0.704** |
| 2 | 4 | 6 | 37 | 21 | 106 | 0.095 | 0.62 | 0.704 |
| 3 | 4 | 6 | 36 | 21 | 106 | 0.093 | 0.608 | 0.704 |
| 4 | 4 | 5.995 | 37 | 21 | 107 | 0.094 | 0.616 | 0.704 |
| 5 | 4.002 | 5.999 | 36 | 21 | 107 | 0.094 | 0.61 | 0.704 |

### *3.4.2.5. Study 1 Confirmation*

The confirmation results of the optimised parameters reveal a scaffold with a heterogeneous pore distribution and a Young's modulus reflecting of the required stiffness appropriate for handling and initial structural support. The mean pore size aligns with the targeted range, taking into consideration the lower and upper limits for the pore size set during the optimisation process. The variability in pore sizes is evident and should be considered when predicting how the scaffold will interact with the intended biological environment. The mechanical testing results, represented by the stress-strain curve, confirm that the scaffold exhibits a degree of elasticity indicated by a consistent slope in the elastic region. This characteristic is essential for scaffolds that need to mimic the mechanical behaviour of the native extracellular matrix to support tissue formation and integration.

The printing pressure of 4 %(w/v) collagen ranged between 102-110 kPa, The experimental results show a variation of 3.92% compared to the printing pressure predicted by the DoE (**Table 3.7**.). Figure 3.23-A illustrates a stress vs. strain curve for a scaffold composed of 4 %(w/v) collagen concentration . The curve shows the material's response to tensile loading up to a strain of 0.12. The Young's modulus is $0.1191 \pm 0.042$ MPa, indicating the stiffness of the material under small deformations. The positive slope demonstrates an increase in stress with strain, suggesting that the scaffold material exhibits elastic behaviour in the tested strain range. This mechanical property is important for ensuring the scaffold can withstand the stresses of handling and implantation without permanent deformation. The observed difference of 21.07% between the predicted and actual values of Young's Modulus as illustrated in **Table 3.7**.

These findings are consistent with previous studies that emphasize the importance of mechanical properties in scaffolds for bone repair. For instance, Kim *et al.* reported that collagen-coated α-TCP/collagen scaffolds demonstrated a lower elastic modulus (0.55 MPa) relative to trabecular bone

but significantly higher than pure cell-laden collagen, indicating enhanced mechanical stability with added bioceramic components [248]. Moreover, a review by Perez and Mestres discussed that optimising the pore size and Young's modulus of scaffolds is critical for balancing mechanical strength and biological functionality [249], which aligns with study observation of the scaffold's elastic behaviour and suitability for bone repair applications. Jianghui Dong *et al.* also highlighted that 3D-printed scaffolds with optimized mechanical properties, including appropriate Young's modulus, are essential for successful bone defect repairs [250].

Figure 3.23-C and D shows the pore size distribution of the scaffold with a mean pore size of $0.638 \pm 0.263$ mm². In addition to measuring the mean pore diameter of the printed optimised scaffolds, the pore area was also assessed. The histogram illustrates the frequency of pores with various areas within the scaffold, indicating that the most common pore area falls between 0.6 to 0.65 mm² and average pore diameter of 350-435 μm. A marginal 2.23% increase in the experimental pore size (0.638 mm²) compared to the prediction (0.614 mm²) as shown in **Table 3.7**. The relatively wide distribution, as indicated by the standard deviation, suggests there is variability in the pore sizes across the scaffold. The broader range of pore sizes could be beneficial for certain tissue engineering applications, where a heterogeneous pore structure may support various cellular processes such as infiltration, nutrient diffusion, and waste removal [251].

Building on the preliminary findings from Study 1, Study 2 improved the identified optimal parameters for the collagen bioprinted scaffold: a collagen concentration of 4 %(w/v), the highest concentration of tannic acid at 6 %(w/v), a crosslinking time of approximately 37 min, and the use of a 21G needle size. These parameters were determined to achieve an optimal equilibrium between the ease of extrusion, mechanical rigidity, and control over pore size in collagen scaffolds created through bioprinting. The next phase, Study 2, employed these optimal conditions as a baseline for HA addition to achieve the optimal collagen/HA scaffold. The focus of Study 2 is on understanding how varying HA concentrations influences the 3D bioprinted scaffolds' mechanical properties, such as the Young's modulus, scaffold degradation. Additionally, the study examines the influence of printing speed and the number of layers on the scaffolds' structural and mechanical integrity.

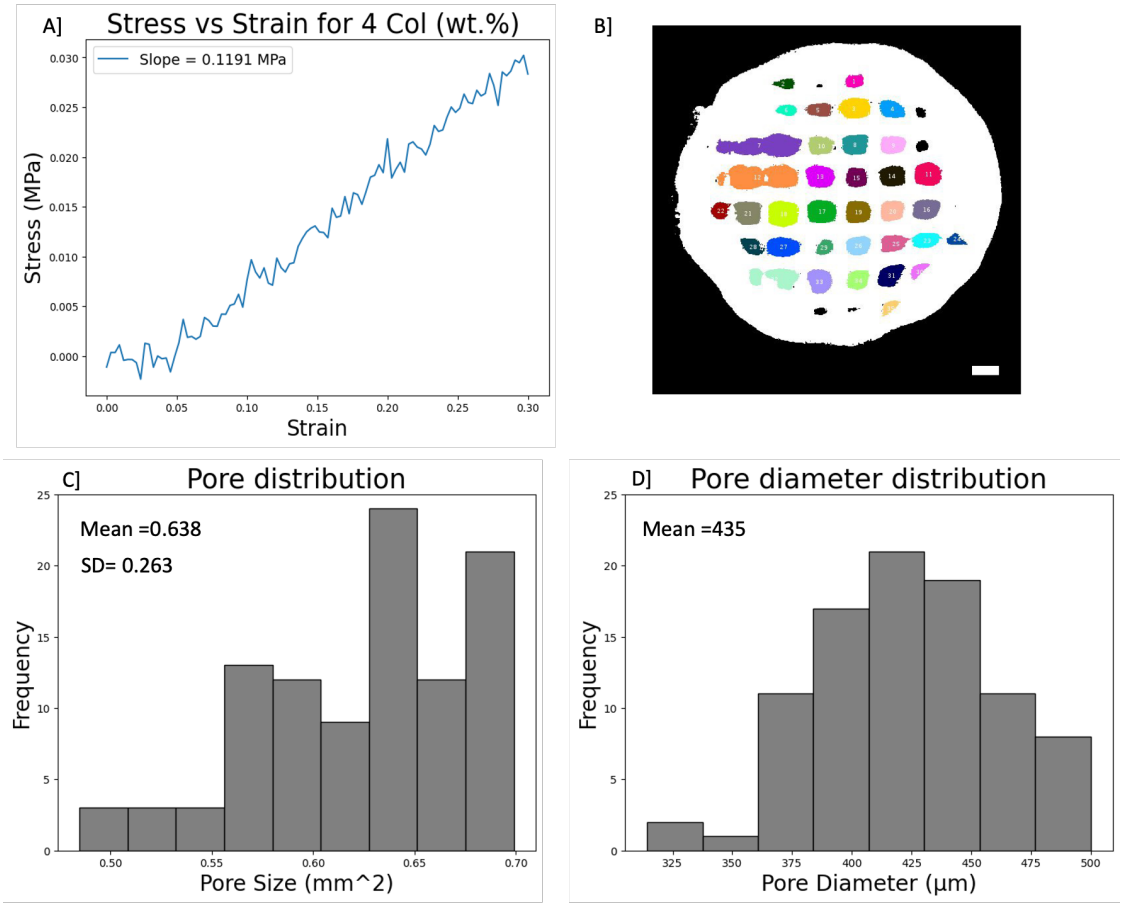



**Figure 3.23:** RSM confirmation experiment A] Stress vs. strain curve for a scaffold with 4 %(w/v) collagen concentration. B] Binary image of 3D printed scaffold (scale bar= 1mm) C] Average pore area of 4 %(w/v) collagen. D]Average pore diameter of 4 %(w/v) collagen. With each test conducted in triplicate (n=3) for reliability and statistical significance

**Table 3.7:** Results of the DoE optimisation of the COL bioink composition demonstrate. The models were validated by comparing the difference between the expected responses for the optimal COL composition and crosslinking conditions and the actual values obtained from experimental data.

| Response | DoE Prediction | Experimental values | Difference (%) |
|---|---|---|---|
| **Printing pressure (kPa)** | 106 | 102 | 3.92 |
| **Young's Modulus (MPa)** | 0.094 | 0.1191 | 21.07 |
| **Pore sizes ($mm^2$)** | 0.614 | 0.628 | 2.23 |

## 3.5. Study 2 Results and Discussion

### 3.5.1. Study 2: Ink characterisation

#### *3.5.1.1. FTIR analysis*

In **Figure 3.24**, the FTIR spectroscopy results for COL and COL/HA composites at various concentrations are presented. The spectrum for pure collagen at 4 %(w/v) concentration serves as a baseline, displaying characteristic amide bands. The amide I band, typically found near 1650 $cm^{-1}$, is associated with C=O stretching vibrations, and the amide II band, near 1550 $cm^{-1}$, results from N-H bending and C-N stretching vibrations, both indicative of the protein's secondary structure. With the introduction of 0.05 %(w/v) HA, slight shifts in the peak positions and intensities are noticeable. These changes can be attributed to interactions between collagen and the HA, which could be indicative of binding or complexation between the two materials. As HA is known for its strong affinity to protein surfaces due to ionic and hydrogen bonding, these spectral changes may reflect the initial stages of this interaction. Increasing the HA concentration to 0.5 %(w/v) shows more pronounced spectral differences. There could be a reduction in the intensity of the amide bands and the appearance of new peaks associated with phosphate groups from HA, typically observed near 1000 $cm^{-1}$ and below, representing the vibrational modes of the phosphate ions. This suggests a higher degree of interaction between collagen and HA, possibly indicating a more significant incorporation of HA into the collagen matrix. At the highest HA concentration of 1 %(w/v), the FTIR spectrum likely exhibits further peak shifts and intensity changes. This level of HA incorporation might result in more extensive hydrogen bonding and ionic interactions, which could lead to alterations in the collagen secondary structure, as evidenced by the changes in the amide I and II bands.

These findings are consistent with previous studies. For example, a study on chitosan-collagen-hydroxyapatite membranes observed similar characteristic absorption bands for collagen (amide I at 1600–1700 $cm^{-1}$ and amide II at 1500–1550 $cm^{-1}$) and noted changes in the spectra with the incorporation of HA, indicating interactions between the collagen and HA components . Another study on the synthesis and characterisation of hydroxyapatite-collagen composites also reported FTIR spectra showing shifts and new peaks due to HA incorporation, which is consistent with our observations [252].

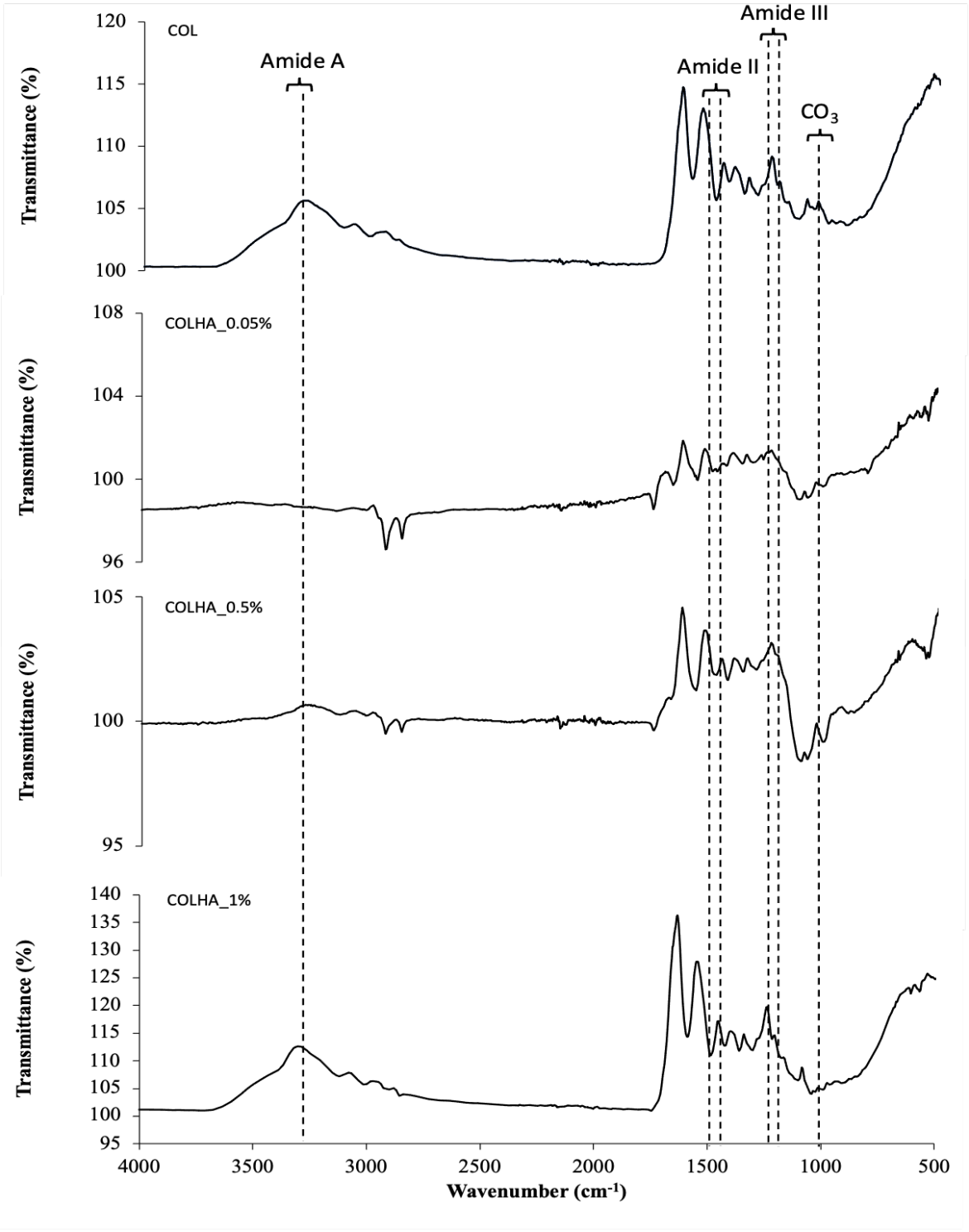



**Figure 3.24:** FTIR Spectra of Collagen Composites. Spectra of collagen with varying levels of HA, indicating the interaction between the components.

#### *3.5.1.2. Injectability test*

The injectability test was next carried out to assess the influence of the addition of HA to the collagen inks on the force required for extrusion. The given graphs in **Figure 3.25** Demonstrate the results of the injectability test, which assesses the four different ink formulations across a range of needle gauges. This assessment is essential for determining their suitability for use in 3D bioprinting. The performance of each ink when subjected to the mechanical stresses of the Zwick machine provides insight into its rheological behaviour in a simulated bioprinting setting. The test shows that Inks 1(COL) and 2 (COLHA_0.05%) have a consistent force profile during the extrusion process, using a 21G needle. The stability of measured force values for these inks indicates that they have a well-balanced rheological composition, enabling a smooth and consistent flow with controllable resistance. This is crucial for preserving the structural integrity after the extrusion process. Equally, Ink 3 (COLHA_0.5%) exhibits notable fluctuations in shear force, suggesting the presence of intermittent blockages or irregular flow. Ink 4 (COLHA_1%) exhibits minimal shear forces, suggesting a reduced viscosity that promotes fluidity but may affect the structural integrity of the printed objects. Transitioning to the 22G needle, Ink 1 (COL) exhibits a progressive rise in shear force as time progresses, indicating a consistent accumulation of pressure that facilitates a regulated extrusion procedure. Ink 2 (COLHA_0.05% ) exhibits a somewhat consistent and lower shear force profile, indicating a smooth flow that is advantageous for creating more intricate designs. Nevertheless, the pronounced spike in the force profile of Ink 3 (COLHA_0.5% ) indicates a momentary obstruction occurrence, perhaps causing an interruption in the printing process.

The 23G needle tests reveal significant insights, as Ink 1 (COL) demonstrates both low and consistent forces. This characteristic is highly advantageous for achieving precise bioprinting at high resolutions, especially when using small diameter needles. On the contrary, the characteristics of Ink 2 (COLHA_0.05% ) demonstrate a sudden increase in force, which strongly suggests clogging, and then a sharp decrease that indicates a possible failure in extrusion. The inconsistent force profile of Ink 3 (COLHA_0.5% ) highlights significant problems with its ability to be injected, making it unlikely to be suited for bioprinting applications until it undergoes additional modifications.

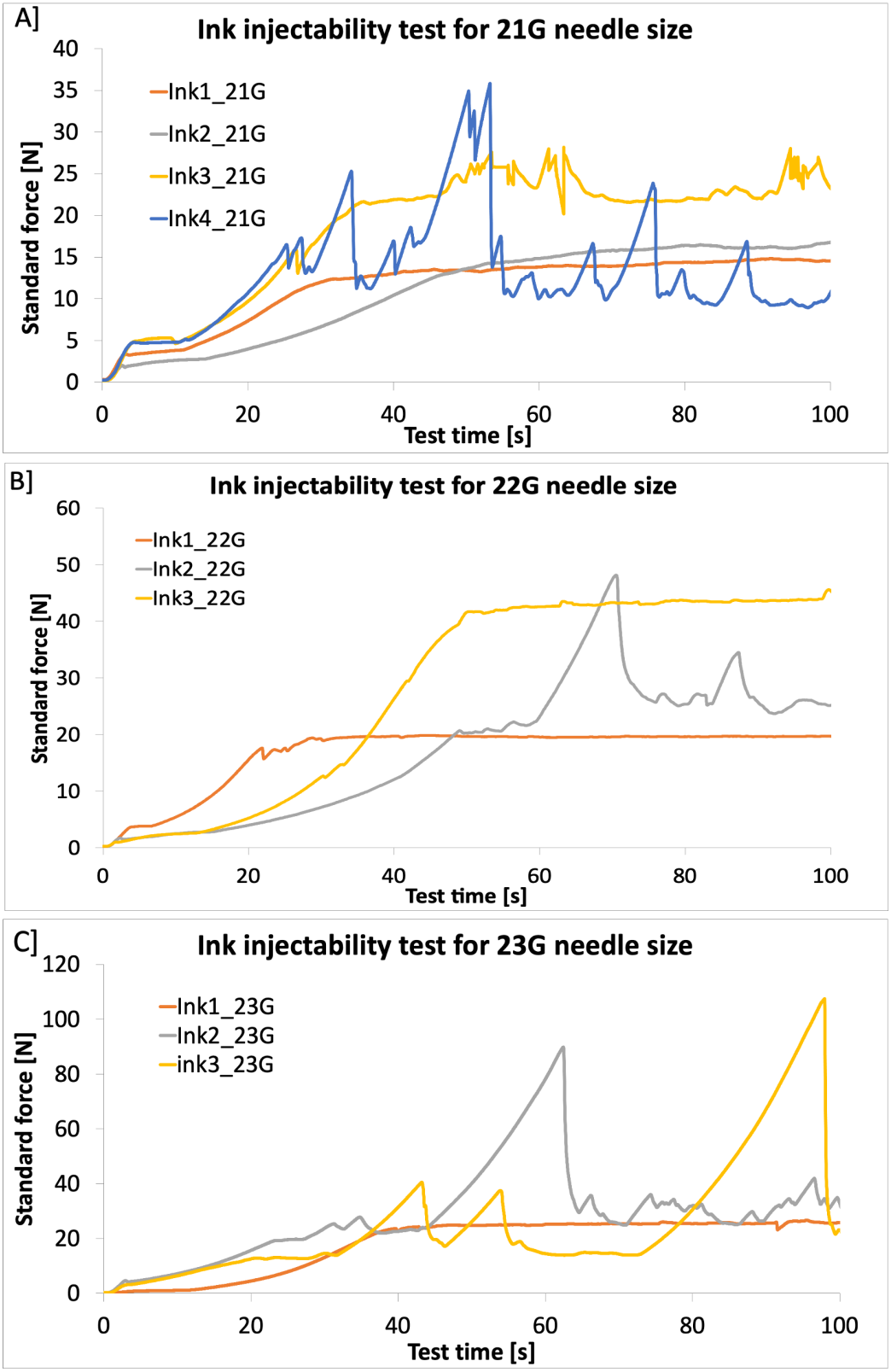



**Figure 3.25:** Standard force vs extrusion of collagen injectability test for four different inks tested with three needle sizes 21G, 22G and 23G.

### *3.5.1.3. Ink rheological behaviour*

Due to the more complex force profiles observed from the injectability testing for the collagen/HA inks, a more detailed rheological assessment was carried out using rheometry. The graph in **Figure 3.26**-A shows the storage modulus (G') and loss modulus (G") for collage/HA Inks 1 through 4. These moduli represent the elastic and viscous properties of the inks, respectively. A higher storage modulus indicates a more solid-like behaviour, while a higher loss modulus indicates more liquid-like behaviour. The dotted lines represent the storage modulus, and the solid lines represent the loss modulus across varying frequencies. The moduli are relatively stable across the frequencies tested, which suggests that the inks have consistent viscoelastic properties under the conditions studied. **Figure 3.26**-B presents the complex viscosity ($\eta^*$) of the inks across the same range of frequencies. Complex viscosity is a measure of a fluid's resistance to deformation. It encompasses both the viscous and elastic aspects of the ink's rheology. A lower complex viscosity indicates that the ink is less resistant to flow, which may affect its ability to maintain structure after extrusion. In the evaluation of complex viscosity, Ink 1 (COL) stands out with the highest measured value at 55.4 Pa.s, which correlates with a significant resistance to flow. This characteristic implies that Ink 1 (COL) has an ability to maintain its shape post-extrusion, potentially making it the most suitable candidate for applications requiring structural integrity. On the other hand, Ink 2 (COLHA_0.05% ) exhibits a reduced complex viscosity of 47.28 Pa.s, indicating a lesser resistance to flow in comparison to Ink 1 (COL). Despite this reduction in complex viscosity, Ink 2 (COLHA_0.05% ) and Ink (COLHA_0.5% ) could still effectively retain its shape, marking it as a viable option for various printing conditions. Ink 4 (COLHA_1% ), which demonstrates the lowest complex viscosity at 24.1 Pa.s. This low resistance to flow was evidenced by its inability to maintain structure during the printing process. The rheological behaviour of these inks indicates that Inks 1, 2 and 3, with higher complex viscosities, are likely to be more suitable for printing applications that require the maintenance of shape and structure post-extrusion. In contrast, Ink 4, with lower viscosity, may have issues to maintain object structure in complex designs without additional support or modifications to the printing process.

These findings are supported by several studies that have explored the rheological properties of bioinks. For instance collagen-based bioinks with appropriate viscoelastic properties are crucial for maintaining structural integrity during and after printing, particularly when combined with other materials like hydroxyapatite (HA) to collagen bioinks can improve the mechanical properties and stability of the printed constructs [253], [254].

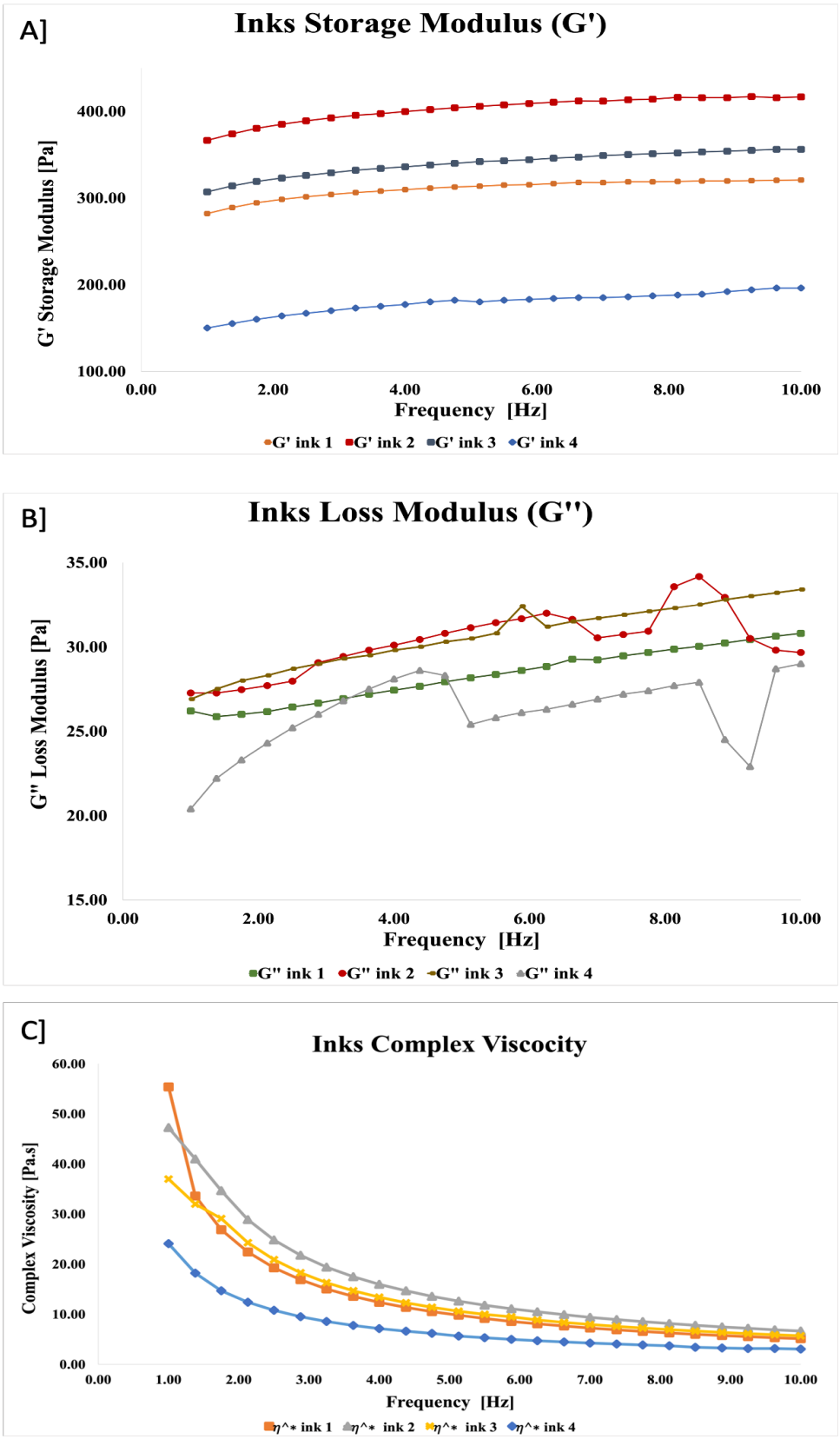



**Figure 3.26:** Rheological Characterisation of Collagen Inks – A-B] A comparison of storage modulus (G') and loss modulus (G'') across a frequency sweep. C] complex viscosity across the same frequency range for Inks 1 to 4, demonstrating the viscoelastic properties.

The rheological properties of the bioinks were characterised using the power law model, which describes the flow behaviour of non-Newtonian fluids. The parameters obtained, n and k, are indicative of the fluid's flow behaviour index and consistency coefficient, respectively. For the inks under study, **Table 3.8** displays these values, which were subsequently used to inform the pressure calculations necessary for the 3D bioprinting process. The data in **Figure 3.27** indicate a consistent increase in shear stress with shear rate for all four inks, establishing a positive correlation that verifies the non-Newtonian (Power law model) nature of the bioinks. The close alignment of predicted and actual measured data underscores the power law model's ability to accurately predict the rheological behaviour of the inks.

**Table 3.8:** Flow Behaviour Index (n) and Consistency Coefficient (k).

| Inks | n | k |
|---|---|---|
| **Ink 1 (COL)** | 0.0660 | 4.174 |
| **Ink 2 (COLHA_0.05% )** | 0.0650 | 5.474 |
| **Ink 3 (COLHA_0.5% )** | 0.0649 | 3.692 |
| **Ink 4** | 0.0935 | 2.007 |

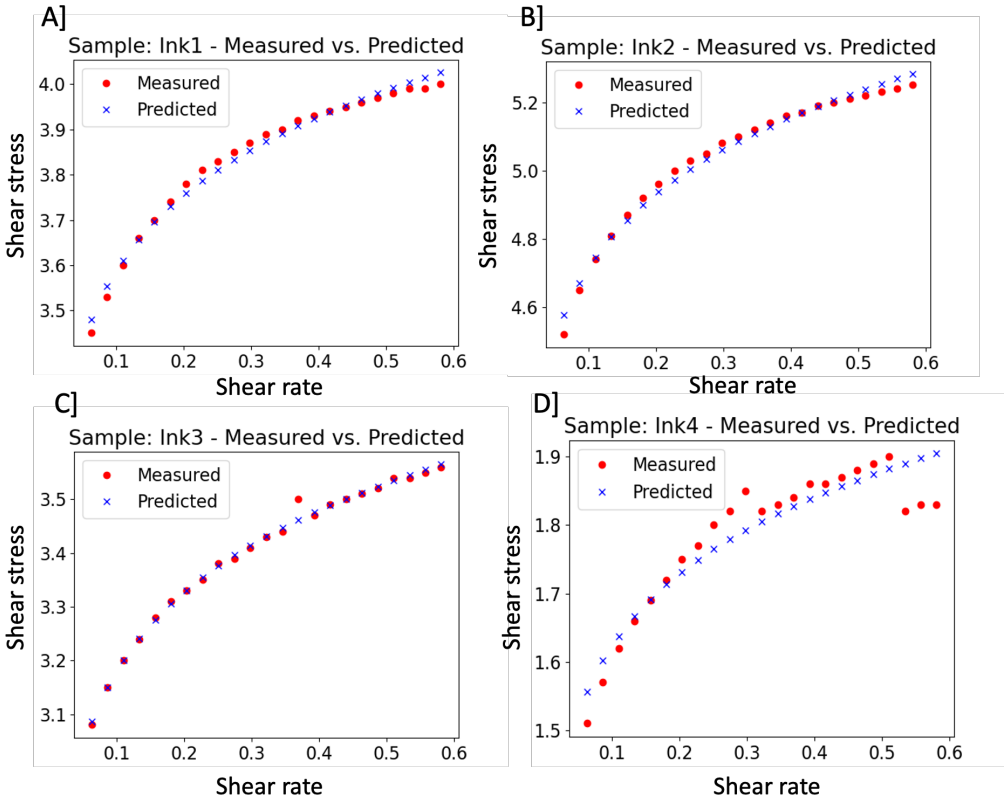



**Figure 3.27:** Correlation Plots of Measured vs. Predicted Shear Stress for Bioinks 1-4 Across Increasing Shear Rates.

### *Pressure calculation*

When using the power law parameters n and k to calculate the extrusion pressure (**Equation 3.1**), the theoretical pressures for Ink 1 (COL), which displays the highest viscosity, were slightly lower than the applied pressures during printing for all needle sizes. This could imply the practical need for greater force for extrusion than what theoretical models suggest. In contrast, for Inks 2 and 3, with their reduced viscosities and increased HA content, there is a better alignment between theoretical and applied pressures. This suggests that the non-Newtonian characteristics are more pronounced, rendering the power law model more appropriate. However, Ink 4, which has the lowest viscosity, predicts the required applied pressure well at lower shear rate values but shows a significant gap between theoretical and applied pressures at higher shear rate values, particularly for the smaller diameter needle sizes. This discrepancy may be attributed to unexpected resistive forces in practice or to compensatory adjustments made by the bioprinter for factors like surface tension and ink adhesion properties, which are not captured within the power law equation.

The comparison of calculated pressure using power law (**Equation 3.2**) to the applied printing pressures on the Incredible$^{+}$ 3D bioprinter for different inks and needle sizes reveals essential insights into the interplay between theoretical predictions and practical application. For Ink 1 (COL) (**Table 3.9**), with the highest viscosity, the theoretical pressures are slightly lower than the applied pressures across all needles, which could suggest that the ink's behaviour in the practical setting requires slightly more force to extrude than theory predicts.

As we move to Inks 2 and 3 (**Table 3.9**), which have progressively lower viscosities due to increased HA concentration, the theoretical pressures remain fairly close to the applied pressures, especially for the 21G needle. This could indicate a more non-Newtonian behaviour in these inks, where the power law is more applicable. However, for Ink 4 (**Table 3.9**), which has the lowest viscosity, the theoretical pressures are significantly lower than the applied pressures for the smaller needle sizes (22G and 23G), suggesting that in practice, the ink may be encountering unexpected resistance or that the bioprinter compensates for other factors such as surface tension and ink adhesion properties that are not considered in the power law calculation. Overall, these results underscore the importance of empirically tuning the bioprinting parameters for each ink and needle combination. The theoretical calculations provide a baseline for expected pressures, but real-world application requires adjustments to ensure the quality and accuracy of the 3D printed structures (**Table 3.9**). It is also indicative of the complex nature of bioprinting, where multiple variables must be finely balanced to achieve the desired outcome.

**Table 3.9**: Comparison of calculated power law pressures to the applied pressures on the CELLINK 3D bioprinter for different inks and needle sizes.

| | 21G | | 22G | | 23G | |
|---|---|---|---|---|---|---|
| | Theoretical pressure [kPa] | 3D Bioprinter pressure [kPa] | Theoretical pressure [kPa] | 3D Bioprinter pressure [kPa] | Theoretical pressure [kPa] | 3D Bioprinter pressure [kPa] |
| **Ink 1 (COL)** | 94.72 | 90 | 112.89 | 200 | 132.89 | 394 |
| **Ink 2 (COLHA_0.05%)** | 125.97 | 78 | 150.22 | 178 | 176.94 | 334 |
| **Ink 3 (COLHA_0.5%)** | 86.49 | 61 | 103.15 | 120 | 121.50 | 243 |
| **Ink 4** | 20 | 40 | 41.23 | 74 | 47.73 | 210 |

#### *3.5.1.4. Ink shape fidelity/printability assessments*

To gain a more comprehensive understanding of the printability of the collagen/HA ink a range of tests were carried out to assess the print fidelity of these materials including string/filament testing, filament collapse testing and the 'Plus' test.

String / filament test

Following the assessment of the forces required for extrusion of the different ink compositions, the ability to form a continuous filament upon extrusion was then assessed using the bioprinter. In the tests with Ink 1 (COL) and Ink 2 (COLHA_0.05% ) using 23G and 22G needles, all trials were marked as 'PASS' as shown in **Figure 3.28**, indicating that under the applied pressure, the inks could be extruded smoothly, forming a continuous filament. The successful extrusion in these instances suggests that the viscosity and rheological properties of these inks are well-tuned for the applied pressures and needle sizes, resulting in uninterrupted flow and high filament fidelity.

However, for Ink 4 (COLHA_1% ) using a 21G needle, the test results in a 'FAIL' (**Figure 3.28**), indicating that the ink was unable to maintain a continuous extrusion, likely due to clogging within the needle. This failure indicates that for Ink 4 (COLHA_1% ), either the viscosity is too low to maintain structure under the forces of extrusion, or that particulate components within the ink may be causing blockages, or the ink's properties are not compatible with the larger internal diameter of the 21G needle. The pressures required to print the inks, as outlined in **Table 3.10**, are pivotal for understanding the printability of each ink formulation. A balanced pressure setting is essential; too low, and the ink will not extrude, too high, and the ink may cause clogging or be extruded too rapidly, compromising the print's resolution and structural integrity.

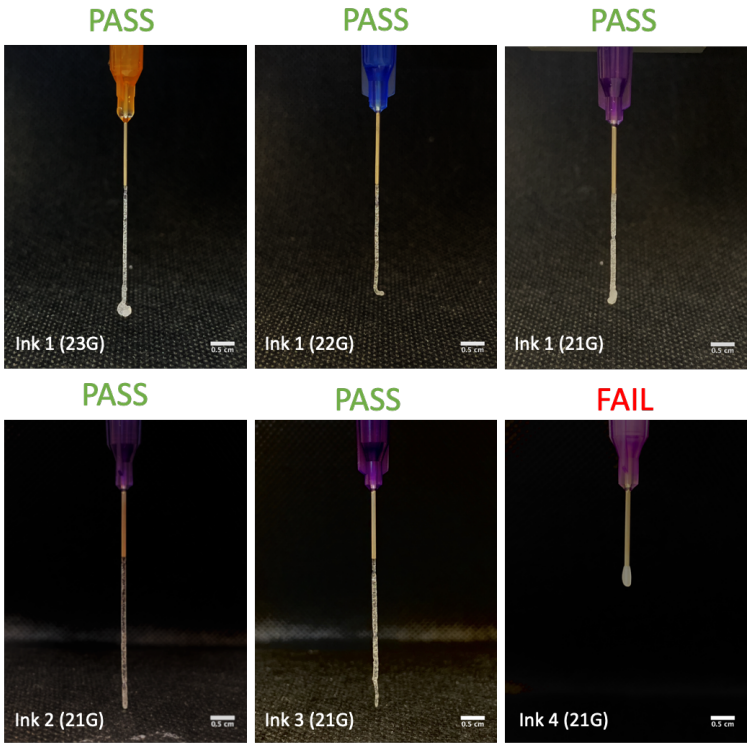



**Figure 3.28:** Evaluation of extrusion consistency for various inks across different needle gauges, with classification of PASS or FAIL based on the continuous flow of the ink through the needle. (scale bar 1mm).

**Table 3.10:** Measured extrusion pressures from the filament string test for Inks (Ink 1 (COL) , Ink 2 (COLHA_0.05% ), Ink 3 (COLHA_0.5% ) and Ink 4 (COLHA_1% ))., using 23G, 22G, and 21G needles, as recorded from the 3D Bioprinter.

| Needle size / Ink | Ink 1 | Ink 2 | Ink 3 | Ink 4 |
|---|---|---|---|---|
| 23G | 394 kPa | 334 kPa | 243 kPa | 210 kPa |
| 22G | 200 kPa | 178 kPa | 120 kPa | 74 kPa |
| 21G | 90 kPa | 78 kPa | 61 kPa | 40 kPa |

Pass Fail

Filament collapse test

In the filament collapse test, the performance of the inks can be evaluated based on their ability to maintain structural integrity between two points, simulating the demands of more complex 3D bioprinting structures. The test results suggest that Inks 2 and 3 have demonstrated a commendable degree of filament stability with collapse percentages of 13% and 17% respectively (**Figure 3.29**), indicating that they possess suitable viscoelastic properties that allow them to form and hold strands across gaps without significant deformation. These characteristics are indicative of a balance between viscosity and elasticity, enabling the inks to withstand the stresses of extrusion and subsequent span without immediate sagging or breaking.

In contrast, Ink 4 (COLHA_1%) exhibits a notable failure in this test, as it is unable to form a continuous filament between the two bridges as shown in **Figure 3.29**. This is attributed to its lower viscosity, which implies a less resistant flow under the force of gravity and the absence of sufficient internal structural strength to support its own weight. The inability to form and maintain a strand over time suggests that Ink 4 (COLHA_1%) lacks the necessary viscoelastic balance to create and sustain complex structures. For Ink 1 (COL), the filament appears to hold, yet with noticeable sagging, indicating that while it may have a higher viscosity than Ink 4 (COLHA_1%), adjustments may still be needed to optimize its performance for complex structural applications. This result emphasises the importance of optimising the rheological properties of the ink, particularly its viscosity, to ensure successful 3D bioprinting outcomes.

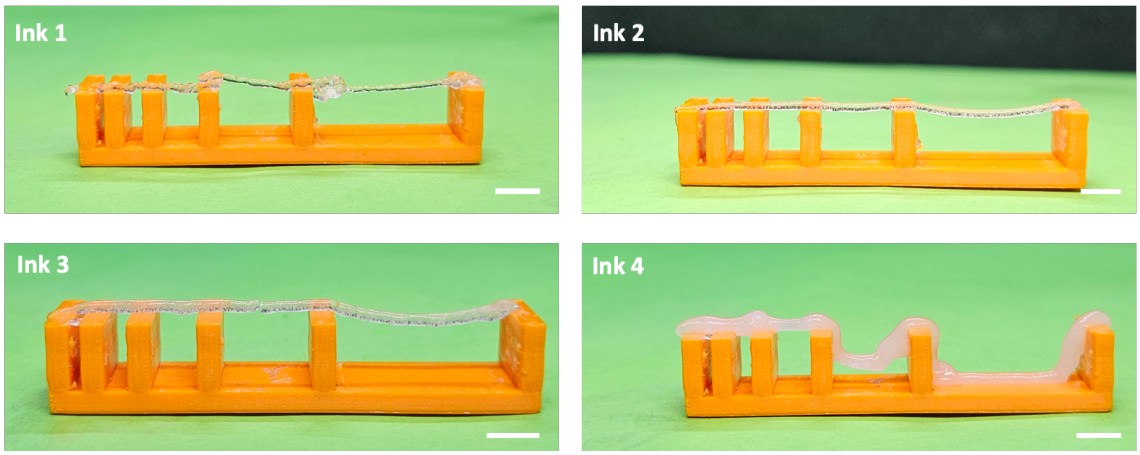



**Figure 3.29:** Filament collapse test for evaluating the rheological performance of bioprinting inks. This figure illustrates the comparative results of a filament collapse test for four different bioprinting inks (Ink 1 (COL) , Ink 2 (COLHA_0.05%), Ink 3 (COLHA_0.5%) and Ink 4 (COLHA_1%). (scale bar 1mm).

Layer stacking test

The layer stacking or 'plus' test evaluates the capacity of various inks to stack layers on top of each other, an essential feature for 3D bioprinting applications that demand dimensional stability and accuracy in multi-layered structures. Ink 1 (COL) and Ink 2 (COLHA_0.05% ) (**Figure 3.30**) demonstrate an important degree of structural integrity, characterised by accurate and well-defined lines at the points where the layers intersect. This indicates that Ink 1 (COL) and Ink 2 (COLHA_0.05%) have appropriate rheological characteristics, facilitating efficient layering without significant spreading or merging between layers. For Ink 3 (COLHA_0.5% ), increased merging and spreading at the intersections is evident (**Figure 3.30**). The observed behaviour indicates a decrease in viscosity and the possibility of structural degradation as further layers are incorporated. Although Ink 3 (COLHA_0.5%) can still be used for bioprinting, its versatility may be restricted to materials that can handle some layer merging.

Ink 4 (COLHA_1%) exhibits significant merging and deformation at the intersections, with the layers losing distinctness and the overall structure appearing flattened (**Figure 3.30**). This suggests that Ink 4 (COLHA_1%), has insufficient viscosity to maintain layer separation, resulting in a collapse or merging of layers. Ink 4 (COLHA_1%), properties suggest it may not be suitable for constructing complex or intricate multi-layered 3D structures where dimensional fidelity is crucial. Overall, Ink 1 (COL) and Ink 2 (COLHA_0.05%) showed outstanding results in layer stacking formation. Ink 3 (COLHA_0.5%) and Ink 4 (COLHA_1%), particularly Ink 4 (COLHA_1%), could encounter difficulties when printing intricate structures because they lack the capacity to preserve layer separation and structural integrity.

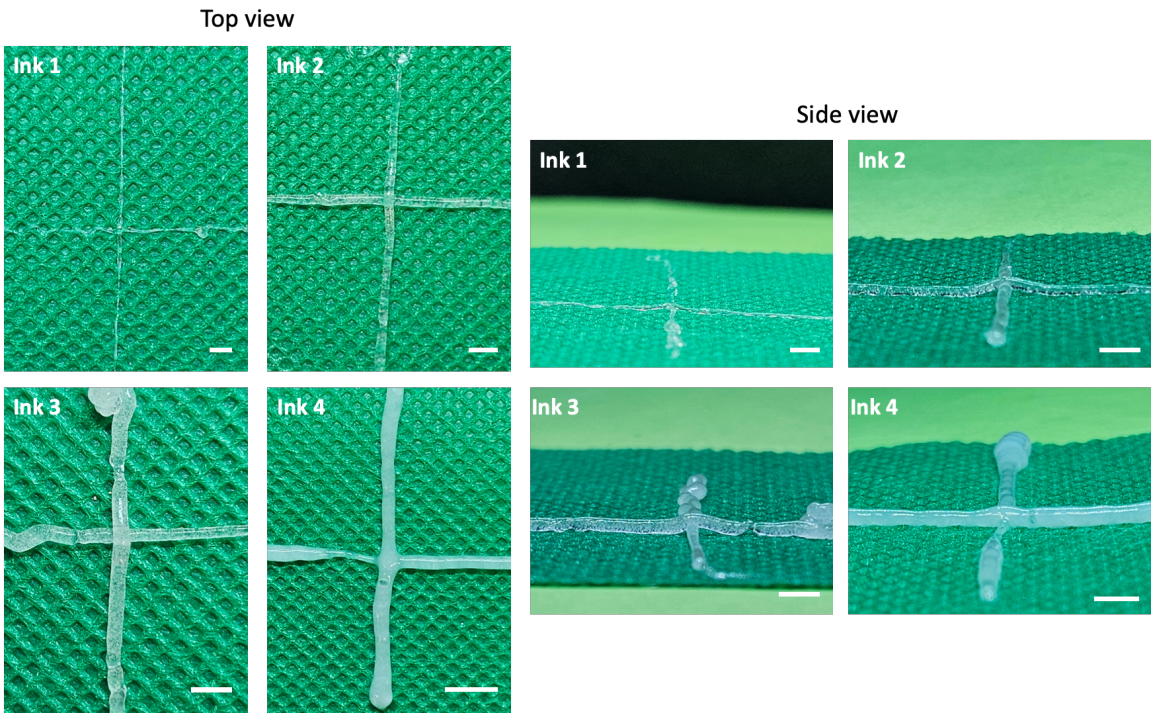



**Figure 3.30**: 'Plus' test comparison for ink's 1 through 4, illustrating the ability of each ink to maintain structural integrity when printed in a layered cross pattern (scale bar 1mm 21G).

## Scaffold porosity

The porosity of the scaffolds printed using Inks 1, 2 and 3 ranged from 79 to 98%. At the slowest print speed of 1 mm/s (**Figure 3.31**-A), a consistent pattern was observed across all inks whereby the porosity of the scaffolds decreases as the number of layers increases. Specifically, the 5-layer scaffolds demonstrate the highest porosity, with a lower in the 10-layer scaffolds and further lower porosity in the 15-layer scaffolds. This is due to the weight and pressure of subsequent layers compressing the underlying ones before the material fully solidifies, thereby reducing the porosity.

When the printing speed is increased to 3.5 mm/s (**Figure 3.31**-B), the trend remains the same; however, the overall porosity for all layers is generally higher than that observed at the 1 mm/s speed. This indicates that the increased speed may allow for less compaction between layers, as there is less time for the ink to flow and settle before the next layer is deposited. At a further increased speed of 6 mm/s (**Figure 3.31**-C), the porosity among scaffolds with different numbers of layers seems to even out, especially between the 10- and 15-layer scaffolds for Inks 2 and 3. The highest porosity is observed in the 5-layer scaffolds across all inks. The results suggest that at higher speeds, the effect of layering on porosity is minimised, likely due to even less time for the material to settle and compress. This result agrees with previous findings reported in the literature by Loskot *et. al*, who reported that printing speed affected scaffold porosity showing higher porosity for lower printing

speed and multi-layered can increase the density of the scaffold which then decrease the scaffold porosity [255].

The relationship between layer number and porosity was statistically significant, with a p-value below 0.0001, as determined by a two-way ANOVA. This finding highlights the importance of layer management in scaffold design, emphasising that careful consideration must be given to the intended porosity level when deciding on the number of layers, especially when working with various inks that might respond differently to layer adjustments.

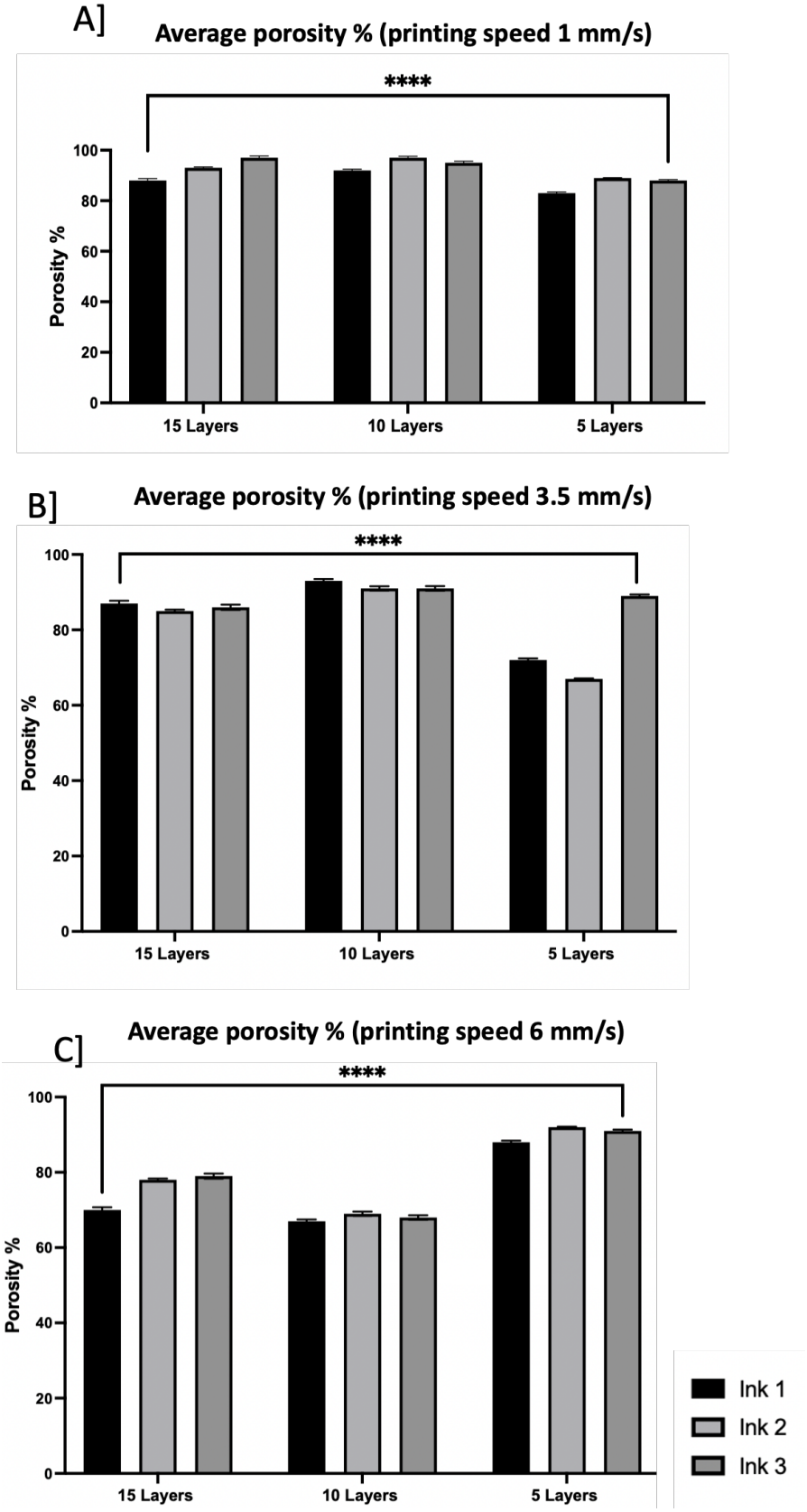



**Figure 3.31:**Effect of print speed and number of layers on scaffold porosity. For print speeds of A] Average porosity for scaffold printed at 1 mm/s. B] Average porosity for scaffold printed at 3.5 mm/s. C] Average porosity for scaffold printed at 6 mm/s. (**** $p<0.0001$, n=3).

### 3.5.2. DoE Study 2: COL/HA printing parameter optimisation

#### *3.5.2.1. Response Models*

The ANOVA for the scaffold properties, printing pressure, degradation, Young's modulus, and pore size, is summarised below **Table 3.11**, considering the same criteria for significance as indicated by p-values less than 0.05. The Lack of Fit p-values greater than 0.05 for all responses demonstrate that the models have a good fit to the experimental data and are capable of accurately representing the process. The determination coefficients ($R^2$) for all responses are above 0.9, signifying that over 90% of the data variability is explained by the models. The adjusted $R^2$ values, which account for the number of predictors in the model and are less sensitive to sample size, are also high, indicating excellent fit to the adjusted model terms. Specifically, for printing pressure, Young's modulus, and pore size, both $R^2$ and adjusted $R^2$ values are greater than 0.9 and 0.8, respectively. Although the predicted $R^2$ for degradation is lower, it remains in reasonable agreement with the adjusted $R^2$ as recommended by best practices. For printing pressure, the HA concentration and printing speed are dominant factors. Degradation is primarily influenced by HA concentration, and to a lesser extent, the number of layers. Young's modulus is most strongly affected by HA concentration, while pore size is primarily dictated by the number of layers, with printing speed also playing a significant role. The significance of the interaction and quadratic terms indicates complex relationships between factors, necessitating a multifaceted approach to optimisation. These models provide a robust framework for understanding and predicting the behaviour of 3D bioprinted collagen/HA scaffolds.

Printing Pressure (R1)

The ANOVA results show a highly significant model with a F-value of 382.79 and a negligible probability of F-value being due to noise, as indicated by a p-value less than 0.0001. HA concentration (A) and printing speed (C) are found to be highly significant factors, with printing speed having the highest sum of squares (SS), signifying its greater impact on the response. The interaction term AC is also significant, indicating that the effect of HA concentration on printing pressure changes at different printing speeds. The $R^2$ value of 0.9922 shows that almost all the variability in printing pressure is explained by the model, which is further corroborated by a high adjusted $R^2$ of 0.9896 and a high predicted $R^2$ of 0.9751, indicating that the model's predictions are consistent with the observed data.

Degradation (R2)

The model is significant with a lower $R^2$ value of 0.9767 compared to R1, suggesting slightly less variability explained by the model but still extremely high. HA concentration (A) again has a large impact, with a significant F-value. The number of layers (B) and the interaction between HA concentration and the number of layers (AB) also affect the degradation rate, although their individual impacts are smaller. The predicted $R^2$ of 0.6996 is lower, which might indicate the

presence of other factors influencing degradation that are not included in the model or potential variability in the experimental data.

Young's Modulus (R3)

The model for Young's modulus is highly significant with an F-value of 199.24. Here, the HA concentration (A) is the predominant factor, and its quadratic term ($A^2$) is also significant, indicating a non-linear relationship between HA concentration and Young's modulus. This could imply an optimum HA concentration for maximum Young's modulus. The $R^2$ value of 0.9891 and the adjusted $R^2$ of 0.9841 suggest a very strong model fit, and the high predicted $R^2$ of 0.9514 indicates that the model can reliably predict Young's modulus.

Pore Size (R4)

The ANOVA indicates the model is highly significant for predicting pore size with an F-value of 47.06. The number of layers (B) is the most influential factor with the highest F-value, and it is significantly impacting pore size. The interaction terms BC and the quadratic term $B^2$ are also significant, suggesting that the relationship between the number of layers and pore size is affected by printing speed and is non-linear. With an $R^2$ of 0.9837, the model explains a large proportion of the variance in pore size, and the high adjusted $R^2$ of 0.9628, along with a predicted $R^2$ of 0.937, indicate that the model predictions are robust.

**Table 3.11:** Study 2 ANOVA for response surface quadratic model for printing pressure, Degradation, Young's modulus and pore sizes

| **R1- printing pressure** | **Sum of Squares** | **F-value** | **p-value** | **Comment** | **$R^2$** | **Adjusted $R^2$** | **Predicted** |
|---|---|---|---|---|---|---|---|
| **Model** | 9954.22 | 382.79 | < 0.0001 | significant | 0.9922 | 0.9896 | 0.9751 |
| A-HA concentration | 544.5 | 83.75 | < 0.0001 | | | | |
| C-Printing speed | 6328.13 | 973.38 | < 0.0001 | | | | |
| AC | 132.25 | 20.34 | 0.0007 | | | | |
| $A^2$ | 2949.35 | 453.66 | < 0.0001 | | | | |
| **Residual** | 78.01 | | | | | | |
| Lack of Fit | 66.81 | 2.98 | 0.1531 | not significant | | | |
| **R2-Degradation** | | | | | | | |
| **Model** | 1322.21 | 32.6 | < 0.0001 | significant | 0.9767 | 0.9467 | 0.6996 |
| A-HA concentration | 820.12 | 181.96 | < 0.0001 | | | | |
| B-Layers no. | 45.13 | 10.01 | 0.0158 | | | | |
| C-Printing speed | 4.5 | 0.9984 | 0.351 | | | | |
| AB | 30.25 | 6.71 | 0.0359 | | | | |
| AC | 1 | 0.2219 | 0.6519 | | | | |
| BC | 1 | 0.2219 | 0.6519 | | | | |
| $A^2$ | 418.95 | 92.95 | < 0.0001 | | | | |
| $B^2$ | 4.42 | 0.9815 | 0.3548 | | | | |

| | | | | | | | |
|---|---|---|---|---|---|---|---|
| $C^2$ | 0.3184 | 0.0706 | 0.7981 | | | | |
| **Residual** | 31.55 | | | | | | |
| Lack of Fit | 24.75 | 4.85 | 0.0806 | not significant | | | |
| **R3- Young's modulus** | | | | | | | |
| **Model** | 2.05 | 199.24 | < 0.0001 | significant | 0.9891 | 0.9841 | 0.9514 |
| A-HA concentration | 1.91 | 931.12 | < 0.0001 | | | | |
| B-Layers no. | 0.0511 | 24.87 | 0.0004 | | | | |
| AB | 0.0045 | 2.19 | 0.167 | | | | |
| $A^2$ | 0.0701 | 34.14 | 0.0001 | | | | |
| $B^2$ | 0.0056 | 2.71 | 0.1277 | | | | |
| **Residual** | 0.0226 | | | | | | |
| Lack of Fit | 0.0159 | 1.35 | 0.407 | not significant | | | |
| **R4- Pore size** | | | | | | | |
| **Model** | 0.3758 | 47.06 | < 0.0001 | significant | 0.9837 | 0.9628 | 0.937 |
| A-HA concentration | 0.0065 | 7.32 | 0.0304 | | | | |
| B-Layers no. | 0.3313 | 373.4 | < 0.0001 | | | | |
| C-Printing speed | 0.0085 | 9.52 | 0.0177 | | | | |
| AB | 0.0037 | 4.19 | 0.0798 | | | | |
| AC | 0.0018 | 1.99 | 0.2014 | | | | |
| BC | 0.0072 | 8.14 | 0.0246 | | | | |
| $A^2$ | 0.0001 | 0.0817 | 0.7832 | | | | |
| $B^2$ | 0.0096 | 10.87 | 0.0132 | | | | |
| $C^2$ | 0.008 | 9.04 | 0.0197 | | | | |
| **Residual** | 0.0062 | | | | | | |
| Lack of Fit | 0.001 | 0.2541 | 0.8553 | not significant | | | |

#### *3.5.2.2. Validation and verification of the model*

The diagnostic plots, including the normal probability of residuals and predicted versus actual values, were investigated for model verification across all response models of the 3D bioprinted scaffolds. The normal probability plot, which is depicted in **Figure 3.32** for pressure, allows for the assessment of whether the residuals conform to a normal distribution. This agreement is typically visualised as a clustering of points around a straight line. The plot likely shows that, except for some minor deviations, the majority of data points fall within an acceptable range of this line. **Figure 3.33**, illustrates the predicted versus actual values for degradation, demonstrating the model's predictive capacity. The random scattering of data points around the diagonal reference line indicates that the model's predictions correspond closely to the actual observed values, which confirms the model's reliability in capturing the true underlying relationship.

**Figure 3.34** displays externally studentised residuals plotted against predicted values for Young's modulus. The absence of indicates that there is a constant variance across all levels of the predicted values, suggesting homoscedasticity. The data points, predominantly lying within the range of [ -2, +2], reinforce the assumption that no transformation of the model is necessary, and that the error

variance is stable. Lastly, **Figure 3.35** shows how the residuals vary for each run number regarding pore size.

Together, these diagnostic plots substantiate that the models employed for evaluating the scaffold properties are highly adequate, confirming the models' suitability for approximating the developed quadratic regressions. The data align well with the critical assumptions of regression analysis, providing a robust framework for predicting and optimising the characteristics of 3D bioprinted scaffolds.

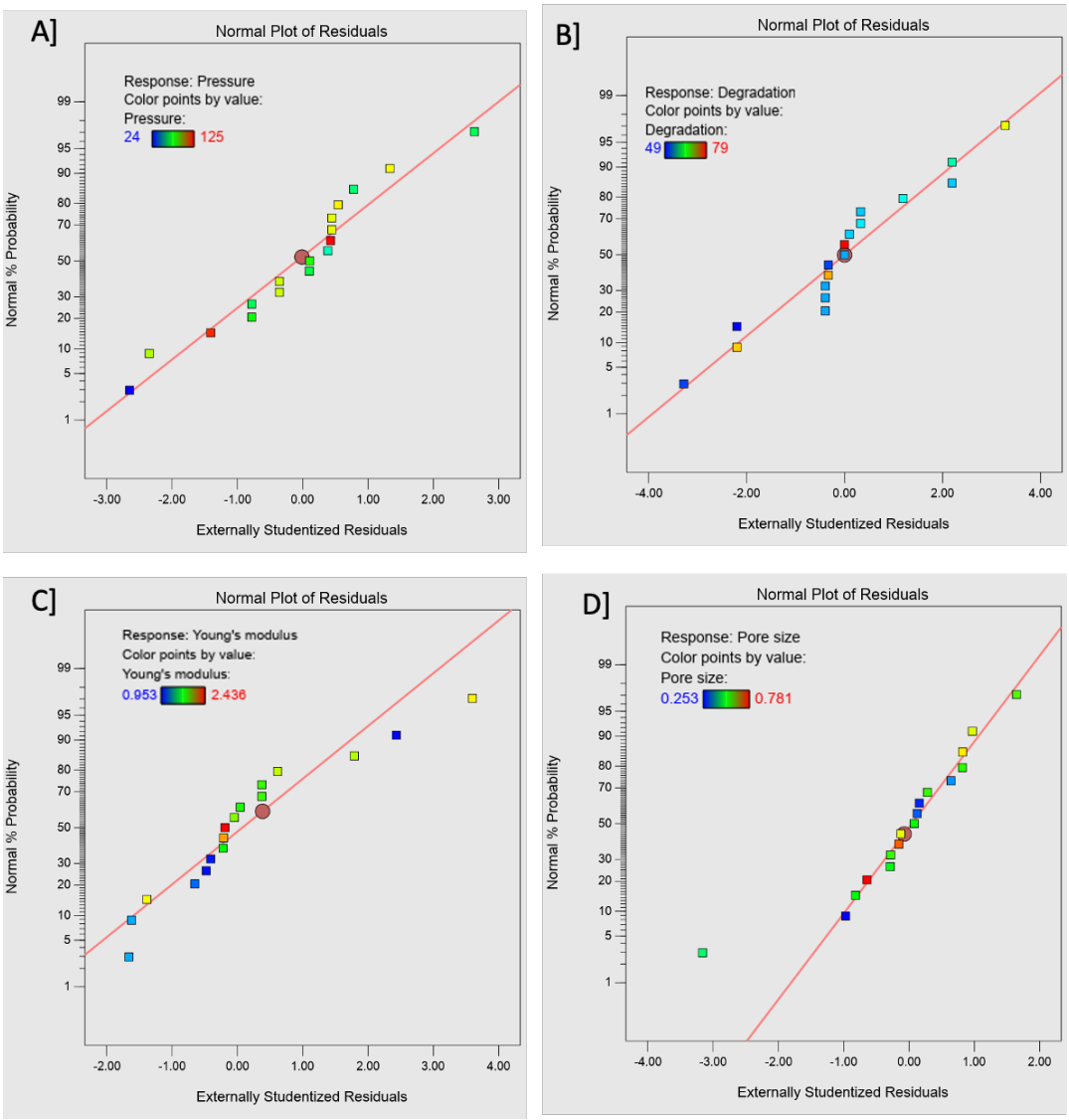



**Figure 3.32:** Normal probability plots for A] printing pressure, B] scaffold degradation C] Young's modulus and D] pore sizes for 3D bioprinted pure collagen scaffold.

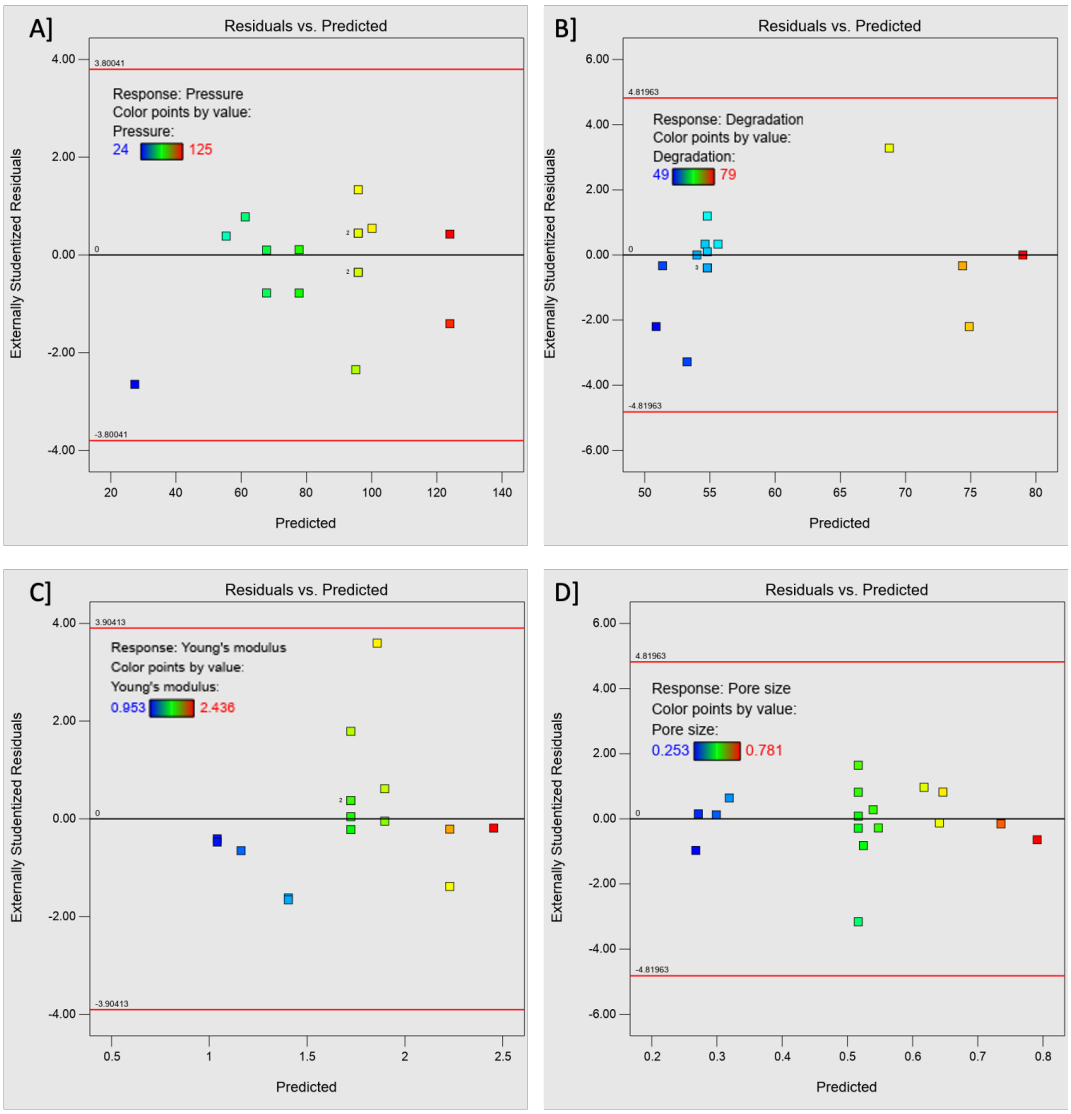



**Figure 3.33:** Studentised residuals versus predicted values plots for A] printing pressure, B] scaffold degradation C] Young's modulus and D] pore sizes for 3D bioprinted pure collagen scaffold.

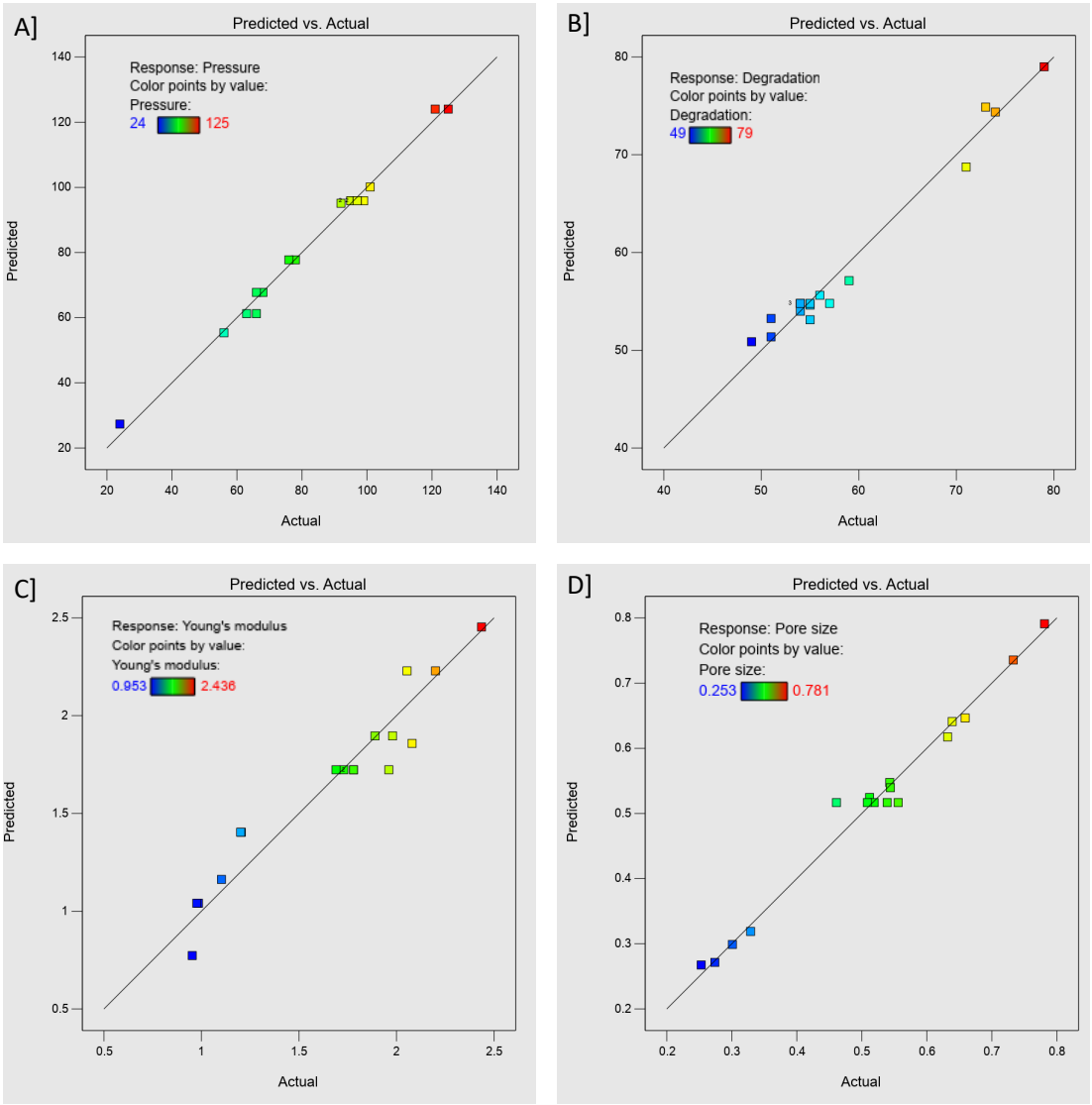



**Figure 3.34:** Predicted versus actual values plots for A] printing pressure, B] scaffold degradation C] Young's modulus and D] pore sizes for 3D bioprinted pure collagen scaffold.

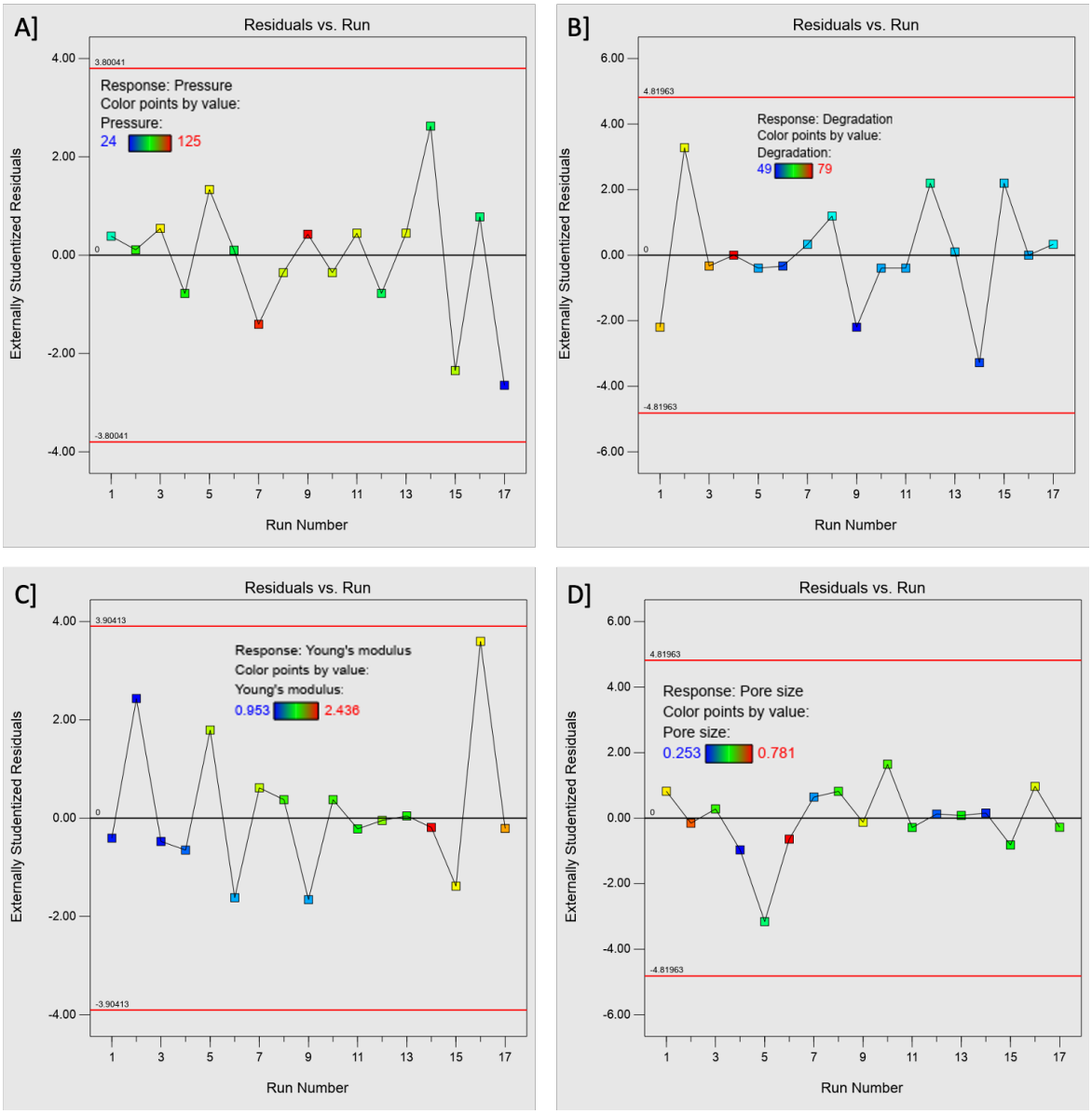



**Figure 3.35:** Studentised residuals versus run number plots for A] printing pressure, B] scaffold degradation C] Young's modulus and D] pore sizes for 3D bioprinted pure collagen scaffold.

### *3.5.2.3. Responses analysis study 2*

Printing pressure

**Figure 3.36** presents the perturbation plot for the printing pressure response. The plot illustrates the relative influence of HA concentration (HA concentration ) and printing speed on the printing pressure of 3D bioprinted scaffolds. The plot indicates that printing speed exerts a more pronounced effect on the printing pressure compared to the HA concentration. Specifically, as the HA concentration deviates from the reference point (set at zero in coded units), there is a discernible increase in printing pressure, albeit less steep than that of printing speed. This suggests that the

viscosity of the material increases with higher concentrations of HA, which can be anticipated as more particulate matter is added to the solution, potentially increasing the force required for injection. Conversely, the plot shows a steep downward trend for printing speed, implying that higher speeds significantly decrease the pressure needed for injection. This could be due to faster printing speeds facilitating the material's extrusion, thus requiring less pressure. The response surface and contour plots in **Figure 3.37** provide a deeper insight into the combined effects of HA concentration and printing speed on printing pressure. The three-dimensional surface plot shows a clear interaction between the two variables, where the printing pressure appears to be at its highest when the HA concentration is high, and printing speed is low. This aligns with the theory that a more viscous solution (higher HA concentration) combined with a slower extrusion process requires greater pressure for injection. The contour plot, on the other hand, translates this interaction into levels of printing pressure indicated by the colour gradient and contour lines. Areas where the lines are closer together represent steeper gradients of pressure change, highlighting regions of greater sensitivity to changes in HA concentration and printing speed.

The shape of the response surface and contour lines (**Figure 3.37**) indicates that there is not a simple linear relationship between the factors and the response; instead, there is a more complex interaction at play. The nature of this curvature suggests an optimal region of operation may exist, where a balance between HA concentration and printing speed minimises the printing pressure, potentially leading to an improved printing process.

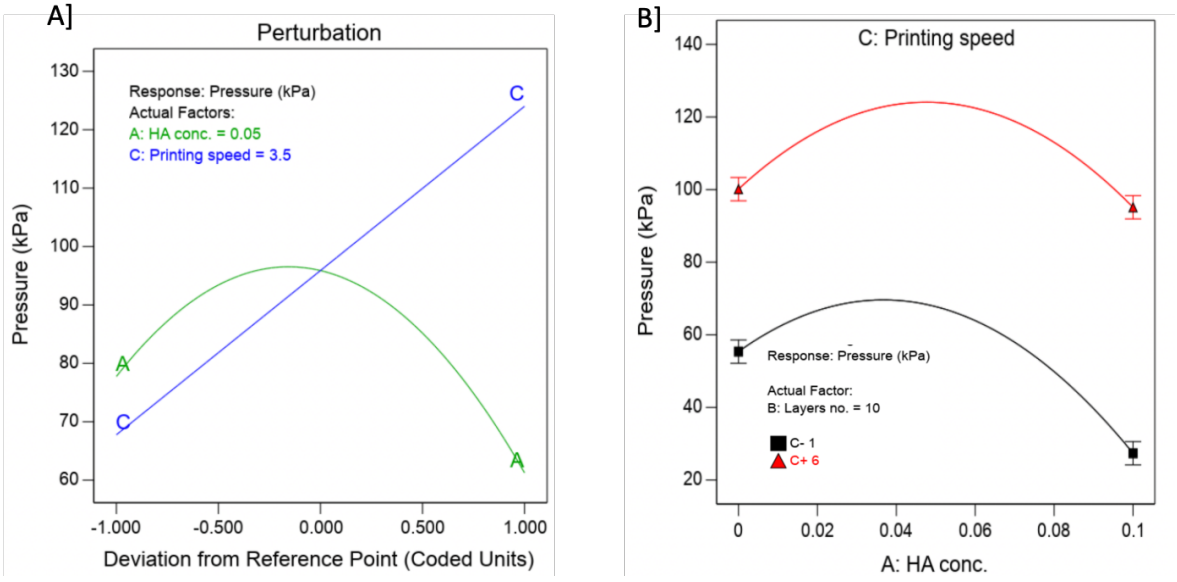



**Figure 3.36:** Perturbation plot demonstrating the individual effects of HA concentration and printing speed on the printing pressure of a 3D bioprinted scaffold, along with an interaction plot highlighting their combined impact.

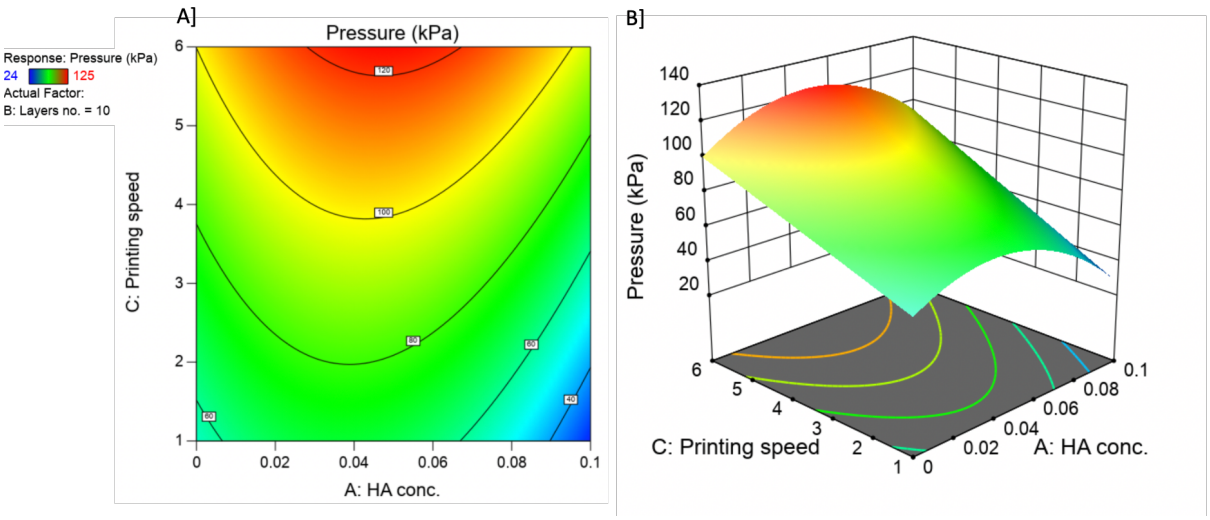



**Figure 3.37:** Contour and 3D response surface plots demonstrating the effects of HA concentration and printing speed on the printing pressure of 3D bioprinted scaffolds.

In summary, the perturbation and response surface plots together indicate that both HA concentration and printing speed are significant factors influencing the printing pressure of 3D bioprinted scaffolds. However, it is the interplay between these two factors that ultimately dictates the optimal printing conditions, balancing material properties with machine operation parameters to ensure efficient and effective scaffold production.

## Degradation response

The perturbation plot illustrates **Figure 3.38**-A the sensitivity of the degradation response to changes in the levels of HA concentration (A), number of layers (B), and printing speed (C) from a chosen reference point. The plot shows a significant increase in degradation percentage with the increase in HA concentration, suggesting a more rapid breakdown of the scaffold structure in the presence of a higher amount of HA. This is indicative of the role of HA in the biodegradation process, possibly due to its interaction with the biological environment or changes it induces in the scaffold's microstructure. The degradation response to changes in the number of layers shows a contrasting trend. The increase in the number of layers appears to contribute to a decrease in the degradation rate. This could be attributed to the incremental mass that must be broken down as the number of layers increases, which naturally could slow the degradation process due to a more complex structure. The factor of printing speed presents a less pronounced effect. The degradation rate slightly increases with a decrease in printing speed. A possible explanation for this could be that slower printing speeds result in a denser scaffold with potentially less porosity, which may retain more moisture and thus be more susceptible to hydrolytic degradation.

The interaction plots provide a visual representation of how two factors simultaneously affect the degradation response (**Figure 3.38**-B to D). The interaction plot for HA concentration and the number of layers (**Figure 3.38**-B) reveals a notable interdependency. It suggests that scaffolds with fewer layers are more affected by changes in HA concentration than those with more layers. For scaffolds with a higher number of layers, the degradation rate is less responsive to the HA concentration. This might be due to the physical barrier provided by additional layers, which could protect the scaffold's core and reduce the accessibility of the degrading agents. The relationship between HA concentration and printing speed (**Figure 3.38**-C) demonstrates an interesting interaction. With increasing HA concentration, the degradation rate rises, and this trend is more pronounced at slower printing speeds. The synergistic effect at lower printing speeds and higher HA concentrations may suggest a structural characteristic of the scaffold that is conducive to faster degradation, such as increased porosity or surface area exposed to the degrading environment.

Finally, the interaction between the number of layers and printing speed indicates that degradation is lowest when both factors are at mid-range levels (**Figure 3.38**-D). A faster printing speed with an insufficient number of layers may not allow adequate fusion between the layers, potentially leading to a more fragile scaffold structure that degrades quickly. Conversely, slower printing speeds may enhance layer adhesion, reducing degradation if the layer number is not too low. These interaction effects are crucial for understanding the multiplicative impact that the factors may have on degradation. Optimisation of these parameters is therefore not straightforward and requires a balance to be struck between HA concentration, printing speed, and layer number to achieve a scaffold with the desired rate of degradation.

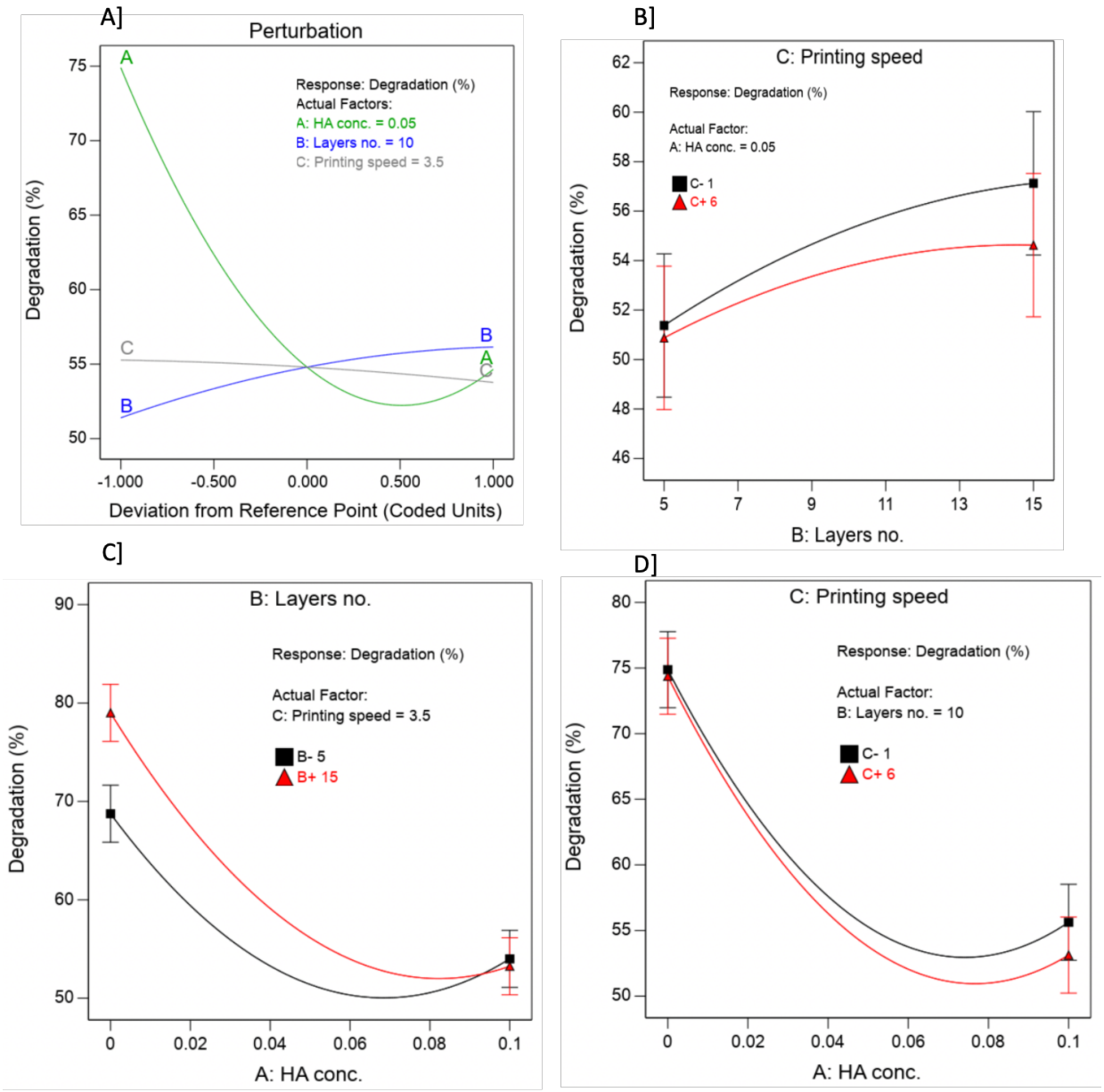



**Figure 3.38:** Perturbation and interaction plots showing the effect of HA concentration, layer number, and printing speed on scaffold degradation, with individual factor impacts and their two-way interactions.

**Figure 3.39** A and B showcase the interaction between the number of layers and printing speed on degradation. The contour plot (**Figure 3.39**-A) and the corresponding 3D surface plot (**Figure 3.39**-B) reveal that the degradation rate decreases as the number of layers increases, which can be inferred from the colour gradient shifting from warmer to cooler colours with an increase in the number of layers. Furthermore, there is a valley in the 3D plot at intermediate printing speeds across all layers, indicating an optimal printing speed that minimises degradation regardless of the layer count. This suggests that there is a synergy between the speed at which the material is printed and the accumulated thickness from the number of layers that influences how quickly the material degrades. **Figure 3.39** C and D focus on the interaction between HA concentration and the number

of layers. The contour plot (**Figure 3.39**-C) illustrates that higher HA concentrations generally lead to increased degradation, seen in the shift toward warmer colours as HA concentration rises. The response surface plot (**Figure 3.39**-D) further emphasises this relationship, showing an inclined plane where degradation ascends with an increase in HA concentration across all layer numbers. The influence of layer numbers appears to moderate the degradation response at higher HA concentrations, indicating the complexity of interplay between structural and compositional factors in determining the degradation behaviour.

**Figure 3.39** E and F depict the relationship between HA concentration and printing speed. The plots convey that an increase in HA concentration leads to a higher degradation rate, which is consistent across different printing speeds. Both the contour (**Figure 3.39** E) and 3D surface (**Figure 3.39** F) plots show this positive relationship. However, the printing speed seems to have a dual effect: at lower HA concentrations, the degradation rate is relatively unaffected by the printing speed, but as HA concentration increases, the degradation rate becomes more sensitive to changes in printing speed, seen in the steeper gradient on the surface plot.

These plots collectively provide a visual and quantitative analysis of how scaffold fabrication parameters can be tuned to control the degradation rate, which is a critical feature for designing scaffolds with predetermined degradation profiles suitable for various tissue engineering applications. The interdependent effects underscored by the contour and surface plots emphasise the need for an integrated approach when setting fabrication parameters to achieve the desired degradation characteristics of 3D bioprinted scaffolds.

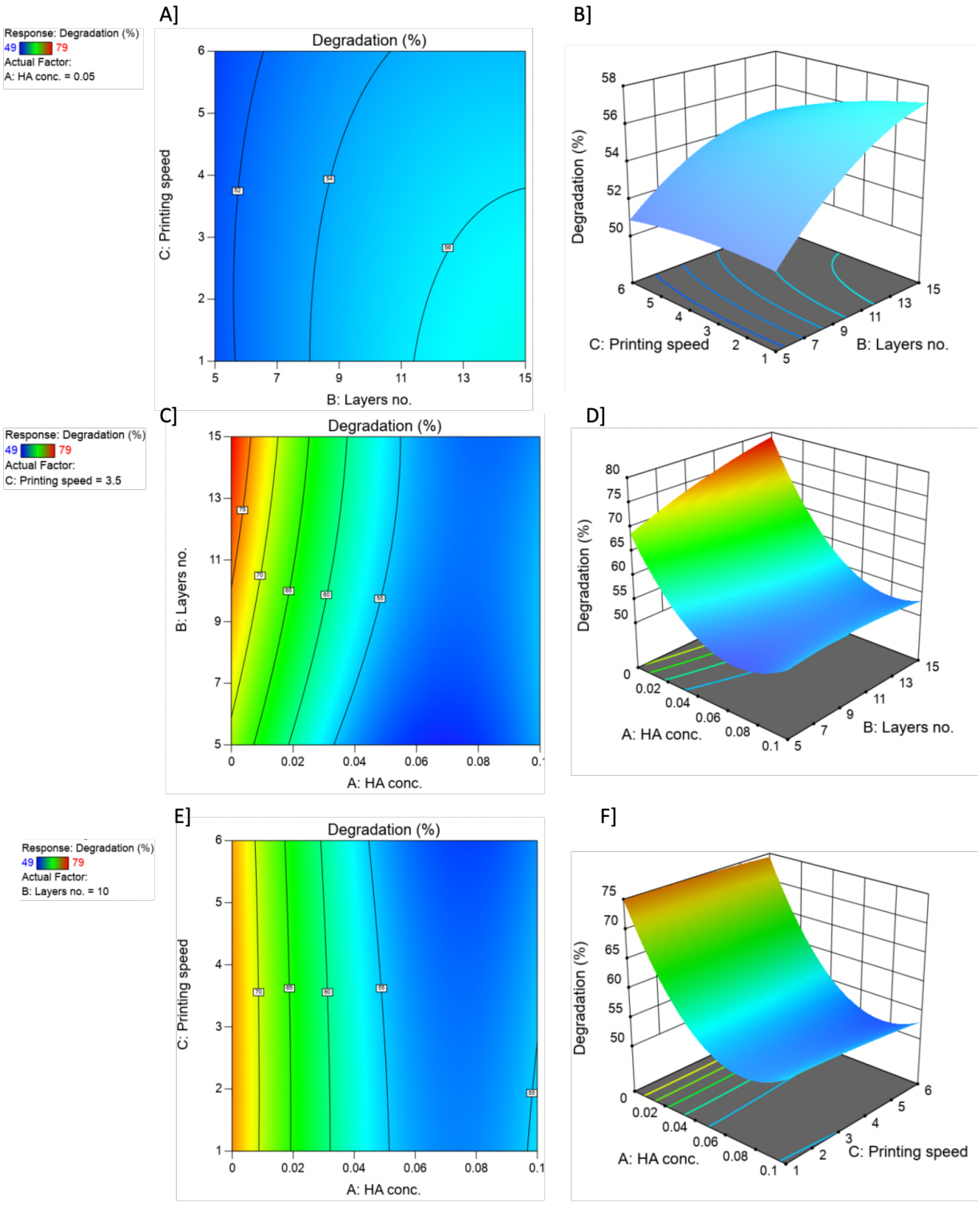



**Figure 3.39:** Contour and 3D response surface plots illustrating the impact of HA concentration, number of layers, and printing speed on the degradation percentage of 3D bioprinted scaffolds.

## Young's modulus response

The perturbation plot (**Figure 3.40**-A) indicates how variations from a central reference point in HA concentration (A) and the number of layers (B) influence Young's modulus. Young's modulus appears to increase with higher HA concentration and more layers. The steepness of the curve

associated with HA concentration suggests that it has a more pronounced effect, indicating that incorporating more HA into the scaffold increases rigidity. On the other hand, the number of layers also has a positive impact on Young's modulus, though to a lesser extent, suggesting that multi-layered structures enhance mechanical stability.

The interaction plot (**Figure 3.40**-B) highlights the combined effect of HA concentration and the number of layers. There is a noticeable trend of increasing Young's modulus with both an increase in HA concentration and number of layers, suggesting that these factors work synergistically achieve a stiffer scaffold structure. The plot also reveals that the influence of HA concentration on Young's modulus is more pronounced at higher layer numbers, potentially indicating a compounded effect when both factors are increased simultaneously.

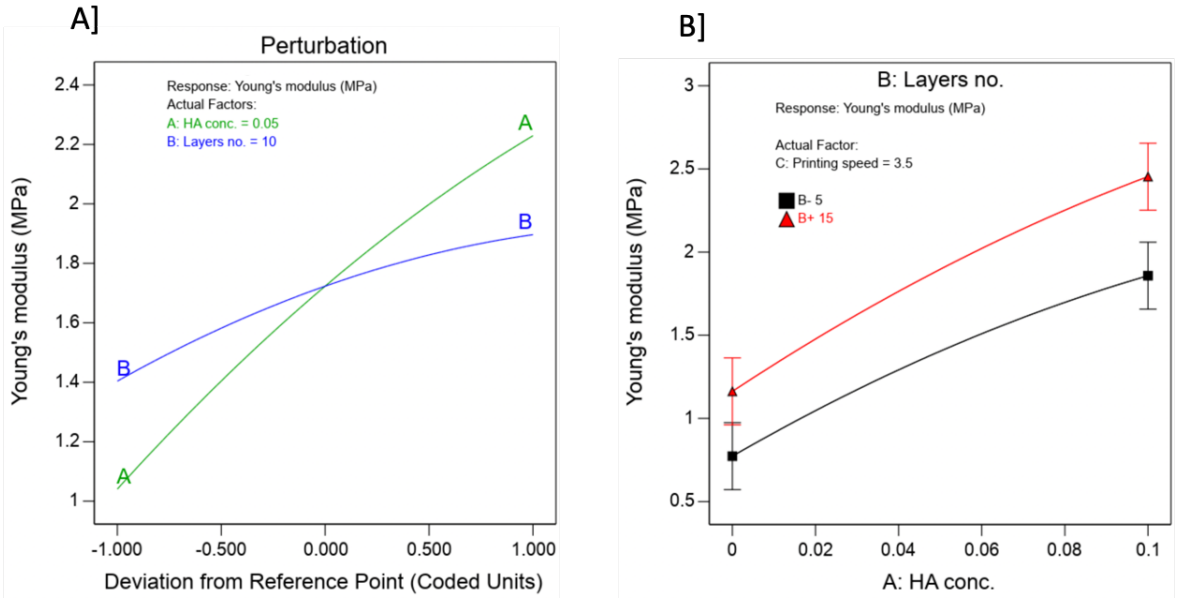



**Figure 3.40:** Perturbation and interaction plots showing the influence of HA concentration and the number of layers on the Young's modulus of 3D bioprinted scaffolds.

The contour plot (**Figure 3.41**-A) showcases a gradient of colours indicating varying levels of Young's modulus across different HA concentrations and layer numbers. The transition from cool to warm colours with increasing HA concentration and layer number suggests a direct correlation where both factors contribute to an increase in the mechanical stiffness of the scaffold. The highest Young's modulus values are found in the upper right corner of the plot, where both the HA concentration and the number of layers are at their maximum, implying that these conditions are most conducive to achieving a stiffer scaffold structure. The 3D response surface plot (**Figure 3.41**-B) provides a visual representation of the data from the contour plot. It displays a rising plane, confirming that Young's modulus increases with both HA concentration and the number of layers. The surface shows that while each factor individually contributes to the increase in stiffness, there is

a pronounced interaction between them, leading to a more substantial effect when both factors are increased together.

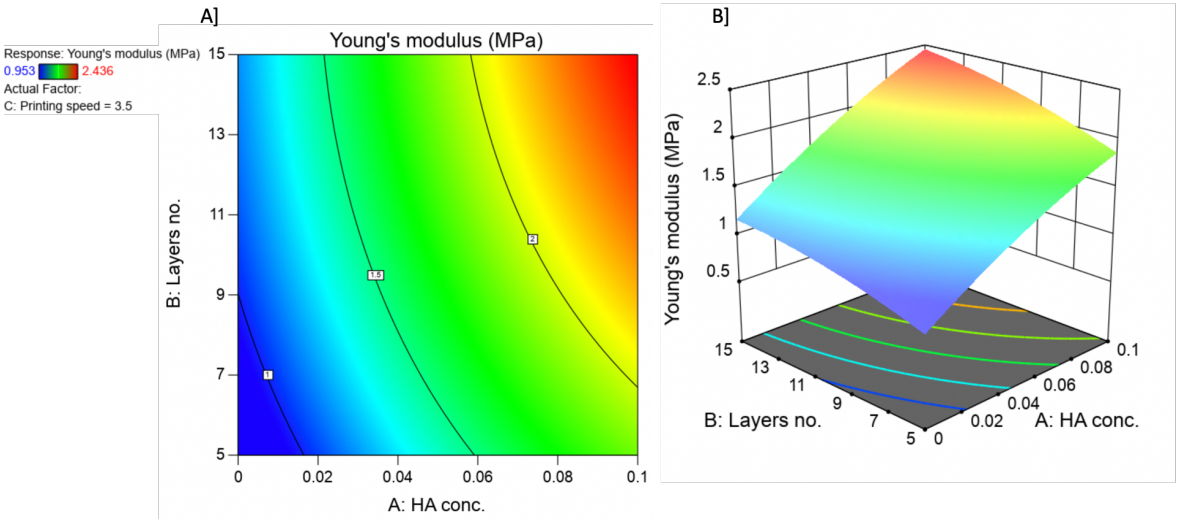



**Figure 3.41:** Contour and 3D response surface plots revealing the relationship between HA concentration, the number of layers, and the resultant Young's modulus of 3D bioprinted scaffolds.

## Pore size response

The perturbation plot (**Figure 3.42**-A) provides insights into how each factor deviating from a central reference point impacts the pore size. The plot suggests that pore size is inversely related to HA concentration and printing speed. As HA concentration increases or the printing speed decreases, pore size diminishes, suggesting denser scaffold structures under these conditions. Conversely, an increase in the number of layers leads to an increase in pore size, potentially due to the additive nature of layering in the bioprinting process, which might introduce more space between layers. The interaction plot for layer number and printing speed (**Figure 3.42**-B) shows that as the number of layers increases, the pore size decreases, particularly at higher printing speeds. This trend may be due to a more compact layering at higher speeds, which reduces pore size. Finally, the interaction plot for HA concentration and printing speed (**Figure 3.42**-C) further demonstrates that higher HA concentrations tend to decrease pore size across all printing speeds, with the effect being more pronounced at slower speeds.

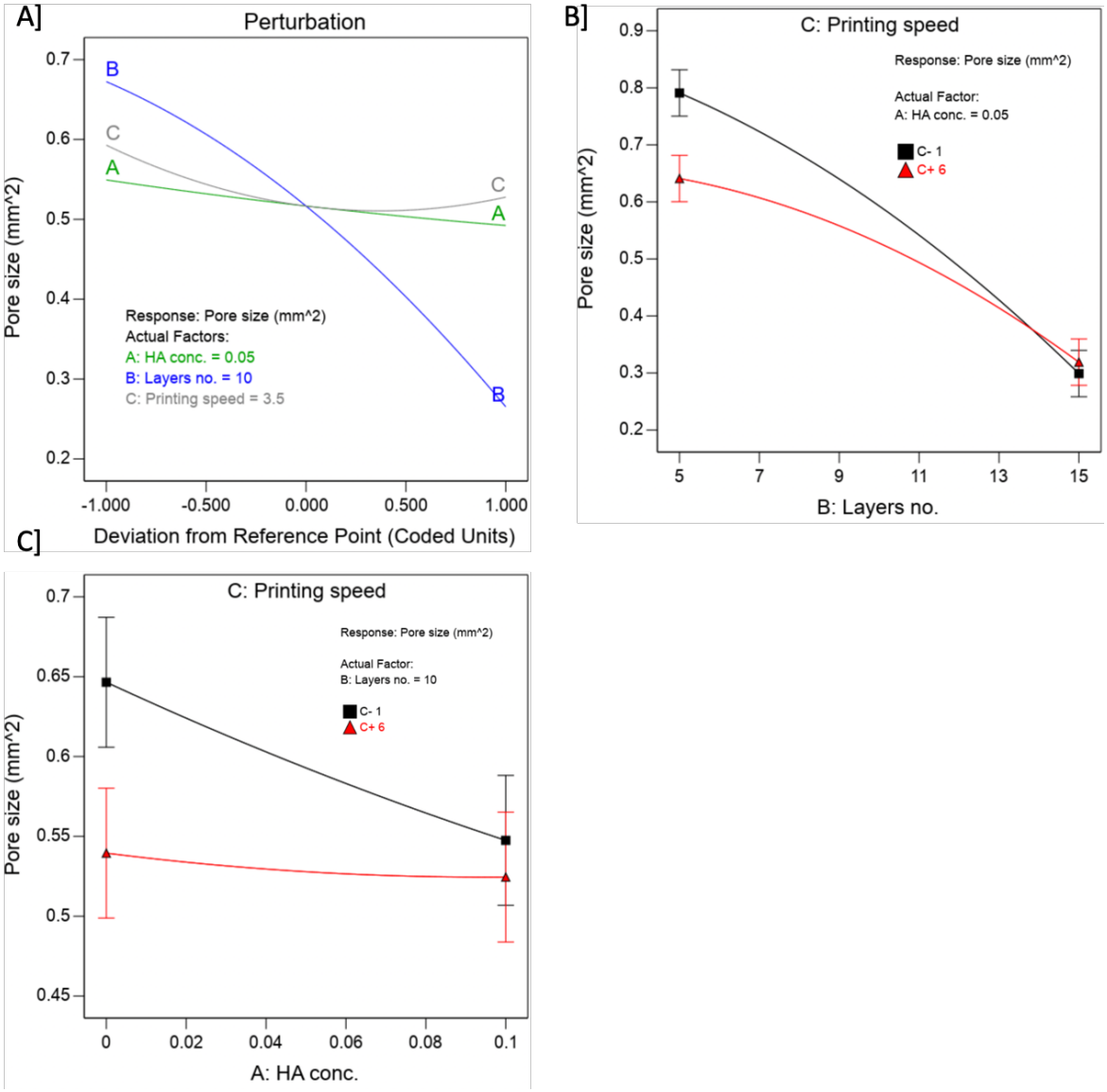



**Figure 3.42:** Perturbation and interaction plots showing the influence of HA concentration, number of layers and printing speed on the pore sizes of 3D bioprinted scaffolds.

The contour plot **Figure 3.43**-A and its corresponding 3D surface plot **Figure 3.43**-B represent how varying the number of layers and the printing speed can affect pore size. The contour lines indicate that increasing the number of layers and reducing the printing speed results in larger pore sizes. The surface plot shows this relationship three-dimensionally, with a pronounced peak in pore size at high layer numbers and lower printing speeds, suggesting a significant interaction between these two factors.

**Figure 3.43**-C (contour plot) and **Figure 3.43**-D (3D surface plot) examine the impact of HA concentration and printing speed. The gradient on the contour plot indicates that lower printing speeds and higher HA concentrations contribute to larger pore sizes. The response surface plot

illustrates this relationship, with the peak shifting towards the higher HA concentrations and lower printing speeds. These graphs suggest that to achieve larger pore sizes, which are often necessary for cell migration and nutrient diffusion in tissue engineering applications, one might consider scaffolds with higher HA concentration, more layers, and slower printing speeds. Conversely, smaller pore sizes could be obtained with lower HA concentration, fewer layers, and faster printing speeds.

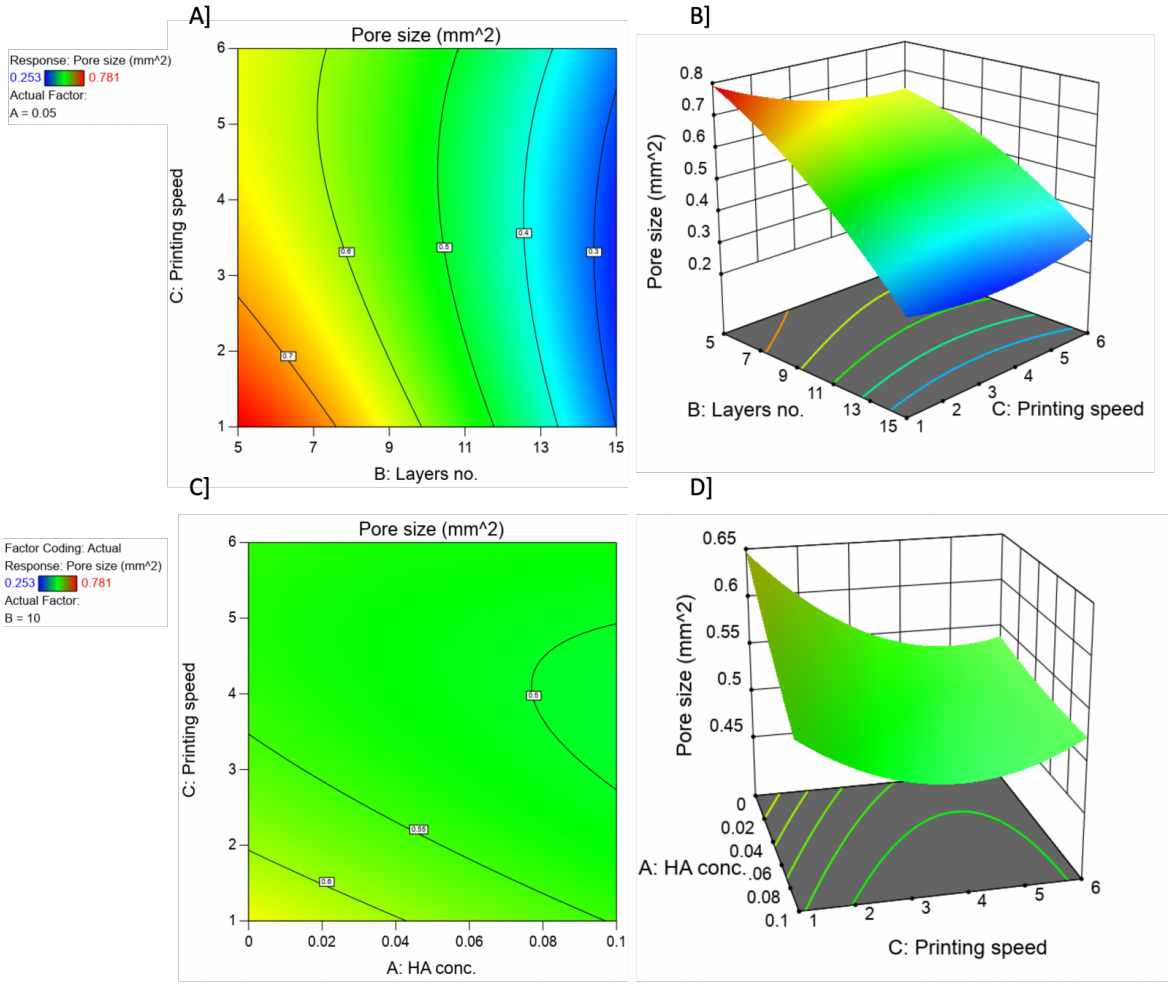



**Figure 3.43:** Contour and 3D response surface plots illustrating the effect of HA concentration, layer number, and printing speed on the pore size of 3D bioprinted scaffolds.

### *3.5.2.4. Study 2 Optimisation*

The optimisation of 3D bioprinted scaffolds using HA concentration, number of layers, and printing speed is crucial for creating structures tailored for specific tissue engineering needs. The results of the RSM in Study 2 are directed at finding the optimal combination of these variables to achieve the desired scaffold properties particularly focusing on printing pressure, Young's modulus, pore size

and degradation. Using a numerical optimisation strategy, goals were set for each response, with the parameters allowed to vary within established limits (

**Table 3.12**).The aim was to fabricate scaffolds with ideal degradation rates and mechanical properties while considering pore size, which influences cell integration and tissue growth. A desirability function approach was used to convert each response into a dimensionless measure of performance, where a desirability index close to 1 indicates a highly desirable outcome. In this context, the highest importance was given to degradation, signifying a particular emphasis on the longevity and stability of the scaffold in biological environments. HA concentration, layers number, and printing speed were also deemed critical, as indicated by their assigned importance, reflecting the necessity to balance printability with structural and functional integrity of the scaffold. Young's modulus was targeted for maximisation to ensure the scaffold's rigidity aligned with that of natural tissue, and pore size was to be maximised within the given range to facilitate nutrient flow and cell migration.

**Table 3.12:** Study 2 optimisation criteria for scaffold properties.

| Name | Goal | Lower Limit | Upper Limit | Importance |
|---|---|---|---|---|
| A: HA concentration [%(w/v)] | is in range | 0 | 0.1 | 3 |
| B: Layers no. | is in range | 5 | 15 | 3 |
| C: Printing speed [mm/s] | is in range | 1 | 6 | 3 |
| Pressure [kPa] | minimise | 24 | 125 | 2 |
| Young's modulus [MPa] | maximise | 0.953 | 2.436 | 3 |
| Pore size [$mm^2$] | maximise | 0.253 | 0.781 | 2 |
| Degradation [%] | minimise | 49 | 79 | 4 |

The optimisation results (**Table 3.13**) indicate that an HA concentration of 0.076 %(w/v), a layer number just over 6 layers, and a printing speed of approximately 1.5 mm/s leads to desirable scaffold properties. These conditions result in a scaffold with pressure and degradation rates within optimal limits, an enhanced Young's modulus for structural support, and a pore size conducive to tissue integration. The desirability index for the top solutions is consistently 0.801, signifying a high level of overall desirability for the predefined objectives. This balanced approach prioritises the fine-tuning of degradation and mechanical properties, providing a scaffold conducive to supporting tissue growth while ensuring ease of manufacturing and structural reliability.

**Table 3.13:** Optimal scaffold configurations derived from the RSM study, showcasing HA concentration, number of layers, printing speed, pressure, degradation, Young's modulus, pore size, and overall desirability.

| Number | HA concentration (%(w/v)) | Layers no. | Printing speed (mm/s) | Pressure (kPa) | Degradation (%) | Young's modulus (MPa) | Pore size ($mm^2$) | Desirability |
|---|---|---|---|---|---|---|---|---|
| **1** | **0.076** | **6** | **1.574** | **60** | **51.39** | **1.779** | **0.678** | **0.801** |
| 2 | 0.076 | 6 | 1.563 | 60 | 51.352 | 1.773 | 0.68 | 0.801 |
| 3 | 0.077 | 6 | 1.595 | 60 | 51.395 | 1.78 | 0.677 | 0.801 |
| 4 | 0.076 | 6 | 1.549 | 60 | 51.368 | 1.774 | 0.68 | 0.801 |
| 5 | 0.076 | 6 | 1.553 | 60 | 51.406 | 1.78 | 0.678 | 0.801 |

#### *3.5.2.5. Study 2 Confirmation*

To confirm the accuracy of the models produced from the DoE a confirmation run was completed using the parameters with the highest desirability values from Table 3.1.2. Specifically, the scaffold was fabricated using 4 %(w/v) collagen and 0.076 %(w/v) HA concentration a printing speed of 1.574 mm/s, 6 layers were printed and the scaffold was crosslinked using 6 %(w/v) TA for 37 min. The pressure, degradation, Young's modulus and pore size were all quantified. The degradation profile over a span of 15 days is presented in Figure 3.44-A.

Two measurements are employed: the percentage of weight loss and the percentage of dimensional change. Both measurements exhibit a parallel pattern, with a clear increase in degradation over time. The dimensional stability seems to exceed weight loss somewhat until Day 7, at which point the rates become similar. These findings indicate that the initial phases of degradation mostly consist of surface erosion, which eventually progresses to overall degradation, impacting both the weight and dimensions. The average degradation rates approximately 3.71% and 3.37% each day for weight loss and dimensional change, respectively. To place these figures within the context of bone repair, it is imperative to take into account the biological alignment that is necessary between the degradation of scaffolds and the resulting regeneration of bone. The degradation rate allows the scaffold to maintain its supportive role throughout the 6 to 8 weeks [232], [256]. The goal is for the scaffold to provide a temporary support structure that degrades at a rate that allows new bone tissue to replace it gradually, without losing mechanical integrity before the healing process is sufficiently advanced. The scaffold should maintain stability throughout the critical initial weeks of healing and then degrade in a controlled manner to allow complete integration and remodelling of the bone tissue [256]. Furthermore, the concentrations of HA were found to have a direct impact on the compressive stress, leading to a notable decrease in degradation [257].

The stress-strain curve represents the mechanical testing of the optimal scaffold, providing insight into its tensile properties. The curve is characteristic of a material that exhibits elasticity at the initial part of the graph, followed by plastic deformation as the slope increases. The modulus of elasticity,

given by the initial slope of the stress-strain curve, is calculated to be 1.931±0.05 MPa (Figure **3.44** B). This value indicates the stiffness of the scaffold and correlates with the Young's modulus desired in the optimisation criteria. The histogram illustrates the distribution of pore sizes in the optimal scaffold configuration. It presents a normal distribution centred around a mean pore area of 0.537±1.24 $mm^2$ and pore diameter of 350-400 µm (Figure 3.44-C and D), signifying a consistent pore size throughout the samples. The literature strongly supports this range, frequently citing 250 – 500 µm as the ideal pore size for facilitating bone ingrowth [251]. As a result, these conformation tests validate the DoE optimisation by demonstrating that the selected parameters indeed lead to a scaffold with a controlled degradation rate, desirable mechanical properties, and a consistent pore size distribution. The results confirm the success of the optimisation strategy and underscore the capability to finely tune the scaffold characteristics to meet specific biomechanical and biological requirements.

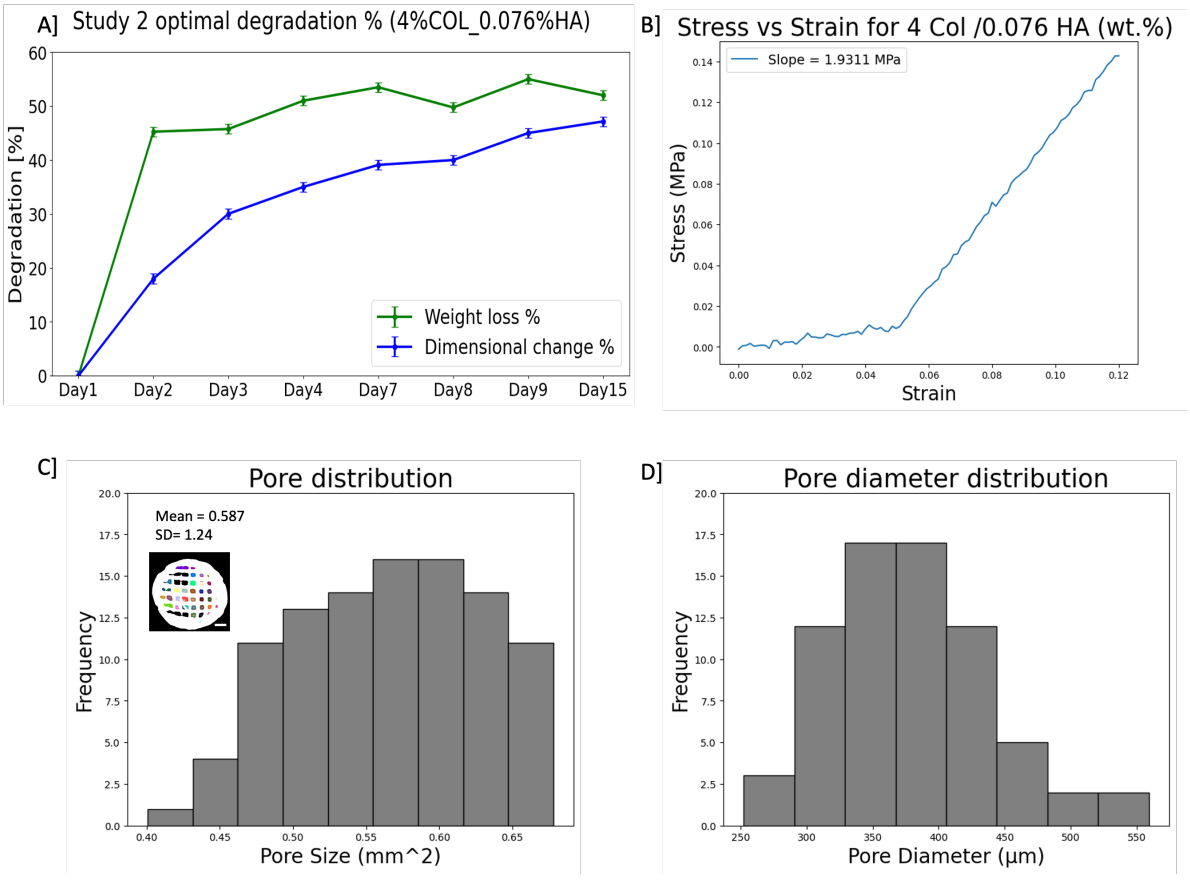



**Figure 3.44:** Conformation results of the optimal scaffold properties identified in Study 2 of the DOE, with each test conducted in triplicate (n=3) for reliability and statistical significance

The percentage differences between predicted and actual values across various metrics indicate a generally close alignment, with some deviations. For printing pressure, the experimental value exceeded the DoE prediction by 18.9% (Table 3.14), suggesting factors in the experimental setup

that may have influenced the pressure needed. The degradation rate showed a minimal difference of 1.173% (Table 3.14), reflecting a high level of accuracy in predicting how the scaffold would behave under physiological conditions. The Young's Modulus, a measure of stiffness, was higher in the experimental results by 7.87% (Table 3.14 Lastly, the pore sizes observed were smaller than predicted, with a 15.5% (Table 3.14).

**Table 3.14:** Results of the DoE optimisation of the COL/HA bioink composition demonstrate. The models were validated by comparing the difference between the expected responses for the optimal COL/HA composition and the actual values obtained from experimental data.

| Response | DoE Prediction | Experimental values | Difference (%) |
|---|---|---|---|
| **Printing pressure (kPa)** | 60 | 74 | 18.9 |
| **Degradation (%)** | 51.39 | 52 | 1.173 |
| **Young's Modulus (MPa)** | 1.779 | 1.931 | 7.87 |
| **Pore sizes ($mm^2$)** | 0.678 | 0.587 | 15.5 |

## 3.6. Conclusion

This chapter addresses Objective 1 of the thesis by systematically modifying and evaluating various parameters that influence the printability, degradation, mechanical, and rheological properties of COL/HA bioprinted scaffolds using DoE. The DoE findings have pinpointed the upper and lower bounds of various critical parameters such as ink formulation, crosslinking duration, and mechanical strength, which are vital for the integrity and functionality of the scaffolds. The chapter initially applied DoE methodology to identify the optimal collagen concentration , crosslinking concentration and crosslinking time for a collagen-based bioprinted scaffold. Regression models relating to the print pressure, Young's modulus and pore size the collagen concentration were successfully developed, enabling optimisation of the process.

The DoE clarified significant relationships, mainly highlighting the direct influence of collagen concentration on printing pressure and scaffold stiffness, which were quantified using Young's modulus. The elevated collagen concentration not only increased the viscosity of the bioink, requiring an increase in printing pressure, but also significantly improved the mechanical strength of the scaffold. Furthermore, the relationship between the concentration of collagen and the duration of crosslinking was found to be a determining factor in the size of the pores. Specifically, longer crosslinking times at higher collagen concentrations led to a finer pore structure. The key parameters that define the responses and predict the performance of scaffolds precise balance between the composition, mechanical characteristics, and porosity of the bioink used. Expanding upon the initial results of Study 1, Study 2 enhanced the previously determined best parameters for the collagen bioprinted scaffold. These parameters include a collagen concentration of 4 % (w/v), the highest

concentration of tannic acid at 6 % (w/v), a crosslinking time of approximately 37 minutes, and the utilisation of a 21G needle size. The parameters were established to achieve an ideal balance between the ease of extrusion, mechanical rigidity, and control over pore size in collagen scaffolds produced via bioprinting.

Following the identification of the optimal collagen concentration and crosslinking conditions, a second DoE was implemented with the goal of developing an optimised bioprinted collagen/HA scaffold. Regression models were developed relating the printing pressure, degradation, Young's modulus and pore size to the HA concentration The DoE highlighted a complex interplay of factors influencing scaffold properties, where HA concentration enhanced Young's modulus for stiffness, but optimal printing speeds and layer numbers were essential to modify degradation rates and pore sizes, ensuring structural integrity. Overall, the in-depth analysis preformed in this chapter provides new insight into the factors that have the greatest impact on the properties of bioprinted collagen scaffolds and inter-relationships between different factors which will help to acceleration the development of collagen-based bioprinted scaffolds for bone tissue engineering applications. From this analysis, the optimal conditions were found to be a HA concentration of 0.076 %(w/v), printing speed of 1.574 mm/s printed at 6 layers. The quality of the printed scaffold is shown to be depending upon these controlled conditions, emphasising the nuanced balance necessary for optimal bioink behaviour during the 3D bioprinting process. Overall, the study has led to the development of a COL/HA bioprinted scaffold that poses significant potential for bone tissue engineering applications.

The scaffold degradation analysis was one analytical aspect explored within this study. However, the numerical measurements included within the DoE did not fully capture the degradation process that the scaffold was undergoing. This reinforces the understanding that while DoE is robust in handling numerical data, other data formats are more difficult to incorporate into the optimisation process.

The potential of ML to overcome this limitation is acknowledged, with its capability to integrate numerical data and images, offering a more comprehensive forecast of scaffold properties. The predictive power of ML could be instrumental in advancing the field beyond the numerical constraints of DoE. Chapter 4 is set to evaluate the application of ML in predicting the degradation behaviour of 3D bioprinted scaffolds, potentially setting a new precedent for the assessment and optimisation of scaffold performance in regenerative medicine.

# Chapter 4: Predicting degradation of three tissue engineering scaffold applications from image data using convolutional neural network (CNN) model and Long short-term memory (LSTM)

## 4.1. Introduction

Central to the success of bone tissue engineering is the development of effective scaffolds that provide an effective support structure for cell attachment, proliferation, and differentiation during the healing process [258], [259]. Thus, the scaffold degradation properties are a critical design parameter. The pace of degradation plays a critical role in the process of tissue creation. Fast degradation can may not provide sufficient support for tissue regeneration, while slow degradation may delay the synthesis of new tissue. Hence, it is crucial to effectively control the degradation profile to align it with the rate of development of new tissue for specific applications [260]. Currently, scaffold design processes primarily rely on trial-and-error experimentation for degradation regulation. Traditionally, the evaluation of scaffold degradation has relied on (1) analytical models based on governing equations [261], and (2) data-driven models methods [262]; that are often destructive, time-consuming, and lack the ability to provide real-time information [263].

As a result, there is a growing need for more efficient methods, image-based methods that can accurately predict the degradation rate of tissue engineering scaffolds. In recent years, deep learning techniques, specifically convolutional neural network (CNN) and long short-term memory (LSTM) models, have shown remarkable success in various computer vision tasks, including image classification [264], object detection [265], and segmentation [266], [267]. CNNs and LSTM are a class of deep learning models specifically designed for analysing visual data, such as images, by automatically learning hierarchical representations of image features. CNNs consist of multiple layers, (i) convolutional layers that extract local patterns, (ii) pooling layers that down sample the data, and (iii) fully connected layers that make predictions based on the learned features [268]. CNN models have demonstrated potential in the analysis of scaffold architectures in the field of tissue engineering. CNNs have been effectively used in earlier studies to measure the essential scaffold characterisation parameters such as porosity and pore size [269]. It is possible to accurately estimate these features from new, unseen photos by training CNN models using a library of scaffold images with known pore diameters or porosity values [270],[271]. Researchers may now optimise the design and production of scaffolds because this method can facilitate effective non-destructive scaffold structural analysis [272],[273], [274]. While CNN models have received a lot of attention for their use in evaluating the pore diameters and porosity of scaffolds [270],[271], predicting scaffold degradation is a relatively new and emerging field [263]. The success of tissue engineering implants and their ability to perform functionally are directly impacted by scaffold degradation, which is defined as the degradation of scaffold material over time [275]. The utilisation of imaging data to forecast the rate of scaffold degradation would yield significant benefits in enhancing implant design, production techniques, and therapeutic interventions.

Currently, LSTM models are extensively employed in diverse domains like speech recognition, time series modelling, video classification, and traffic flow prediction [276]. In addition, LSTM technique has been utilised to forecast bearing degradation by examining the relationship between bearing degradation data and time [277], [278]. These examples that uses LSTM model to forecast bearing degradation illustrates the potential use of this model to forecast scaffold degradation. LSTM networks are a type of Recurrent Neural Network (RNN) designed to overcome the limitations of traditional RNNs in handling long-term dependencies. Traditional RNNs struggle to retain information from inputs that are separated by long time intervals, which can be crucial in sequential data processing [276]. The LSTM's ability to remember long-term dependencies means it can consider the entire history of the material's condition, rather than just the most recent changes, leading to more accurate predictions [279].

Furthermore, LSTM networks, when integrated with the Visual Geometry Group 16 layers (VGG16) architecture, create a powerful hybrid model for analysing complex data like images combined with sequential numerical information [280], [281]. VGG16 is a CNN architecture known for its simplicity and deep structure. The "16" refers to the number of layers in the network that have weights (this includes convolutional layers and fully connected layers) [282]. VGG16 is notable for its architecture, which consists of small (3x3) convolutional filters stacked in increasing depth, allowing it to capture complex features at multiple scales [282]. VGG16 was originally trained on the ImageNet dataset [283], a large database of millions of images across thousands of categories, for the task of image recognition [284]. VGG16's capability for high-level feature extraction from images, and LSTM's proficiency in processing sequential data [279], [281].

The literature review identifies a noticeable lack of utilisation of ML approaches such as CNN and LSTM, in the field of tissue engineering, particularly in the examination of scaffold degradation. This thesis aims to close this gap by examining the capacity of these computational models to improve techniques for assessing both imaging and time-series data on scaffold integrity.

### 4.1.1. Chapter Aims

This chapter focuses on the development of new approaches for assessing and predicting scaffold degradation. The chapter addresses thesis Objective 2: To automate the measurement of scaffold degradation rates using image analysis tools and compare various machine learning models for predicting scaffold degradation with a combination of image-derived and numerical data, and Thesis Objective 3: To build interface platform to predict scaffold degradation.

To accomplish this goal, the following specific objectives investigated were to:

(1) gather a large dataset of scaffold images at different stages of degradation,
(2) assess of the effect of HA concentration on the degradation rate of bioprinted collagen/HA scaffolds

(3) develop and train CNN and LSTM model to predict degradation rates based on these images,

(4) evaluate the performance of the trained models and comparing them with traditional degradation assessment techniques.

(5) build an interface platform for the prediction of scaffold degradation at different time points.

This study aims to give a more precise and timely assessment of scaffold degradation using deep learning and image analysis, allowing researchers and clinicians to make well-informed decisions about implant performance and patient care. The construction of more durable and long-lasting tissue engineering scaffolds can be made easier by understanding the underlying mechanisms driving scaffold degradation using image-based analysis, ultimately leading to better patient outcomes in bone fracture repair and regeneration. To address this objective, a number of different scaffolds were investigated including 3D bioprinted scaffolds, electrospun scaffolds, and an injectable cement. An overview of the study is presented in (Figure 4.1).

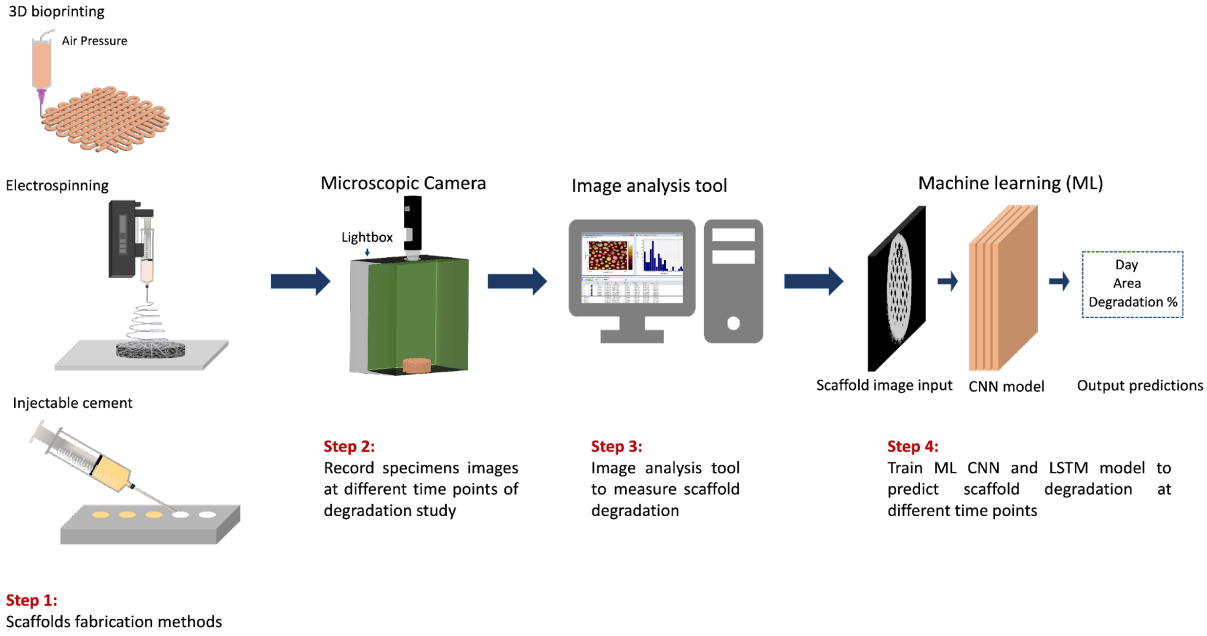



Figure 4.1: Scaffold degradation analysis methods in tissue engineering.

## 4.2. Methodology

### 4.2.1. Material fabrication

Four different types of scaffolds were assessed in this chapter. Firstly, the collagen and collagen /HA scaffolds developed in Chapter 4 were assessed. Following this, three additional scaffolds provided by our collaborators in Italy at Politecnico di Torino, University of Pisa and MERLN Institute for

Technology in the Netherlands, part of GIOTTO project (H2020-NMBP-TR-IND-2018, 814410-GIOTTO), were also included in the study to show the wider applicability of the developed degradation assessment tool. These materials were a 3D printed polymer scaffold (Device 1), an electrospun scaffold (Device 2) and an injectable cement (Device 3). The composition and properties of the scaffolds explored in the study are described here.

#### *4.2.1.1. 3D bioprinted scaffolds*

Collagen and collagen/HA scaffolds were fabricated using the methodologies described in Section 3.2. Specifically, three collagen/HA based bioinks were fabricated containing 4 %(w/v) collagen and 0.05 %(w/v) and 0.5 %(w/v) HA. Briefly, the fabrication process was as follows: collagen type I (milled bovine tendon long fibre powder, Collagen Solutions, United Kingdom) was dispersed in 0.5 M acetic acid (Sigma-Aldrich, Wicklow, Ireland) at a concentration of 4%(w/v). The COL solution was homogenised using an overhead blender (IKA, Ultra-Turrax, T-25) for 30 min to 1 h at 4 ºC. Then the COL solution was passed through two stainless steel meshes with sizes of 30 and 50 mesh to remove any clumps and ensure the hydrogel printability through small needles sizes. For the micro-particles of HA were initially added to 0.5M acetic acid at concentrations of 0.05 or 0.5 %(w/v) and sonicated (BRANSON digital sonifier, USA) for 10 min to allow solubilisation of the HA. Then, COL type I was added to this HA solution at concentration of 4 %(w/v) and placed in a fridge for 24 h, to achieve a collagen suspension. After 24 h the overhead blender/mesh was used to homogenies the inks. The inks were printed under the same parameters in study 2 in chapter 3.

#### *4.2.1.2. 3D printed polymers (Device 1)*

Device 1 was a 3D printed polymer scaffold fabricated by our collaborators using existing protocols [20]. The first step in the fabrication process involved the synthesis of nano-hydroxyapatite particles (nHA) using a reactor to mix solutions of calcium and phosphate ions. A version of this material was also made with added strontium (Sr). The resulting materials were gathered through a chemical process and thoroughly cleaned before being concentrated. An extrusion technique was then used to create filaments from a blend of three polymers, Poly l-lactide/ polycaprolactone/ Poly(3-hydroxybutyrate-co-3-hydroxyvalerate) (PLLA/PCL/PHBV) in a ratio of 90/5/5 %(w/v). After extrusion, the filaments were cut to appropriate lengths. In addition to the base blend, two variations were made that incorporated nHA and Sr-nHA powders. These powders were pre-mixed with PLLA pellets, combined with PCL and PHBV, and then extruded under the same conditions as the base blend. The concentration of nanoparticles was carefully chosen to achieve the required mechanical properties for the composite material [285].

#### *4.2.1.3. Electrospinning scaffold (Device 2)*

Device 2 provided by collaborators through the GIOTTO project is an electrospun scaffold. These composite scaffolds were fabricated by incorporating varying particle concentrations (from 5 to 15 %(w/v) into poly(ethylene oxide terephthalate)/poly(butylene terephthalate) (PEOT/PBT) scaffolds as previously reported [286].

The spinning process involved setting the polymer flow at 0.12 ml/h, spinning at 20kV through a 0.8 mm spinneret, 12 cm from the collector, at 25°C with 35% humidity. The distribution of particles in the meshes was optimised by testing different particle concentrations, from 5% to 15%. The spun composites were collected on a flat stainless-steel platform for 15 minutes. Scaffolds for lab tests were created using a punched polypropylene sheet, which was mounted on a rotating mandrel. The spun composite was then collected on this mandrel at 1500 rpm. Samples were punched from the sheet using 15 mm puncher, resulting in a sample supported by a polypropylene ring [286].

The resultant porous scaffolds showed a random fibre alignment with the absence of beads. The fibre diameters vary between 1.06 ± 0.11 μm for PEOT/PBT and about 0.67 ± 0.14 μm for 15 nHA scaffolds. No significant difference in fibre size was observed between the 15 nHA and 15 nHA_Sr scaffolds, with the latter having a dimension of 0.68 ± 0.15 μm. The average fibre diameters for the Mesoporous bioactive glass (MBGs) particles containing of strontium (Si/Ca/Sr) [287]. are 0.59 ± 0.25 μm and 0.76 ± 0.27 μm for 12.5 SD and 12.5 SG, respectively. Lastly, particles in all composites meshes seem to be evenly distributed, forming small clusters around 10 μm in size [286].

#### *4.2.1.4. Injectable cements (Device 3)*

Device 3 was an injectable cement samples were fabricated by our collaborators in Torino. The procedure involved creating a homogeneous paste by mixing a precisely measured powder phase with double-distilled water ($ddH_2O$), which acted as the liquid phase. The powder phase consisted of α-type calcium sulphate hemihydrate (α-CSH; GC Fujirock EP Classic, GC Europe, San Giuliano Milanese, Italy) for the matrix, as a resorbable matrix, along with commercially available $ZrO_2$ nanoparticles (particle size: 200-500 nm, Anhui Rencheng Technology CO, Hefei, China) and Sr - MBG particles containing 10 mol% of strontium (Si/Ca/Sr = 85/5/10) [287]. These components were added to enhance radiopacity, bioactive characteristics, and pro-osteogenic qualities. The Sr-MBG particles were synthesised by a base-catalysed sol-gel technique. The powder phase of the cement was composed of 75% CSH, 20% Sr-MBG, and 5% $ZrO_2$ using a volumetric formulation. The dry phase was mixed with $ddH_2O$ for 90 seconds at 20°C to simulate circumstances in an operating room and ensure full injection of the cement. The liquid-to-powder ratio is 0.40. The formulation was labelled as 75CSH-MBG, with pure CSH (100CSH) serving as the control under the name 100CSH. Following the mixing process, degradation studies were performed on cylindrical specimens with dimensions of 13 mm in diameter and 5 mm in height. The specimens were formed

by forcing the paste through a 13 G needle into cylindrical moulds. The materials were left to solidify at 37 °C and 100% humidity for 24 h [287].

### 4.2.2. Data collection

The data collection method employed in this study was divided into two distinct measurements: manual measurements and image recording. Each measurement contributed to a comprehensive understanding of scaffold degradation. Manual measurements were conducted to record the dimensional and weight changes of the scaffolds (**Figure 4.2**-A). For the 3D bioprinted collagen-based scaffolds: the degradation rate was assessed by immersing them into phosphate-buffered saline (PBS) solution at a pH of 7.4 and a temperature of 37°C for up to 15 days. Dimensional changes, and changes in weight were recorded at time intervals of 28 days. For the 3D bioprinted polymer-based scaffolds: the degradation rate was assessed by immersing them into phosphate-buffered saline (PBS) solution at a pH of 7.4 and a temperature of 70°C for up to 28 days. Dimensional changes and changes in weight were recorded at specific time intervals of 28 days. Cement-based samples: (CSH)-based cements in solid cylindrical form (13 x 5 mm) were placed in a tris-HCL solution (0.1M, pH 7.4) and subjected to orbital shaking at 37 °C for up to 28 days, following ISO 5833-2002 guidelines [288]. Dimensional changes and weight measurements were recorded periodically throughout the degradation process.

In parallel, images of the scaffolds were recorded to capture their visual characteristics and degradation progression. A microscopic camera (RS Pro Wi-Fi Digital Microscope) was used to capture daily images of the scaffolds over a time course **Figure 4.2**-B. This imaging process resulted in a total of 958 images for the four groups under investigation. The captured images served as the basis for further analysis and assessment of scaffold degradation.

A]

| Sample | Dimensional change [%] | Weight change [%] |
|---|---|---|
| Scaffold 1 Day 1 | 50 | 35 |
| Scaffold 2 Day 1 | 40 | 44 |
| : | : | : |
| : | : | : |
| Scaffold(n) Day n | .. | .. |

B]

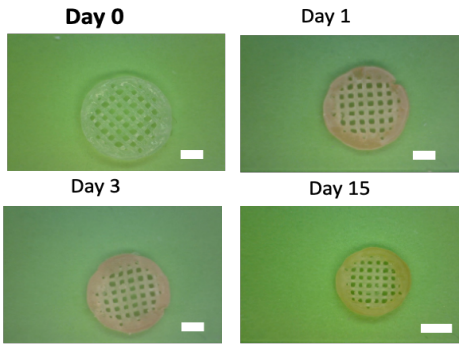



**Figure 4.2:** A] manual measurements collected from the lab and B] Image-based data taken from 3D bioprinted (scale bar 1 mm).

### 4.2.3. Image analysis method

The development of the image analysis tool was carried out using Google Colab, an open-source platform that allows users to write and execute Python code in an interactive environment. Google Colab was chosen for its ease of use, accessibility, and ability to use cloud-based resources, which is particularly useful for computationally intensive tasks such as image processing and analysis.

Following image capture, an image pre-processing phase was carried out. This involved a series of carefully designed steps to prepare the images for subsequent analysis and feature extraction. Initially, the images were loaded using the widely-used OpenCV library (OpenCV version 4.8.0, [289]), ensuring consistent and reliable access to the image data. To standardise the colour representation across all images, a conversion from the default BGR colour space to RGB was performed. This conversion step was particularly important to ensure accurate interpretation and comparison of colour-related features. Following the colour conversion, the grayscale conversion step was implemented to simplify subsequent analysis and reduce computational complexity. The grayscale images retain only the intensity information, effectively eliminating the colour information and reducing the dimensionality of the data. This transformation proved essential in focusing the subsequent processing on the inherent intensity variations within the images.

To facilitate image segmentation, a thresholding operation was employed to convert the grayscale images into binary images. A carefully chosen threshold value of 200 (grayscale value) was applied to distinguish between foreground and background regions. Pixels with intensity values above the threshold were classified as the foreground, while those below were classified as the background. This step effectively separated the objects of interest from the background and laid the foundation for subsequent feature extraction. To further refine the binary images and improve the overall quality, a series of morphological operations were applied. Specifically, morphological opening, closing, and erosion were sequentially performed using structuring elements with a shape of an ellipse and a size of 3 x 3 pixels (**Figure 4.3**-A). These morphological operations, guided by the chosen structuring elements, effectively eliminated noise, filled in small gaps, and smoothed the object boundaries, resulting in cleaner and more accurate binary images (**Figure 4.3**-B and C). To reduce noise and enhance the image quality, a Gaussian blur was applied to the processed binary images. By utilising a kernel size of 5 x 5 pixels and appropriate parameter settings, the Gaussian blur operation effectively reduced high-frequency noise, smoothed intensity variations, and enhanced the overall coherency of the images. This step proved essential in further refining the images and preparing them for subsequent analysis.

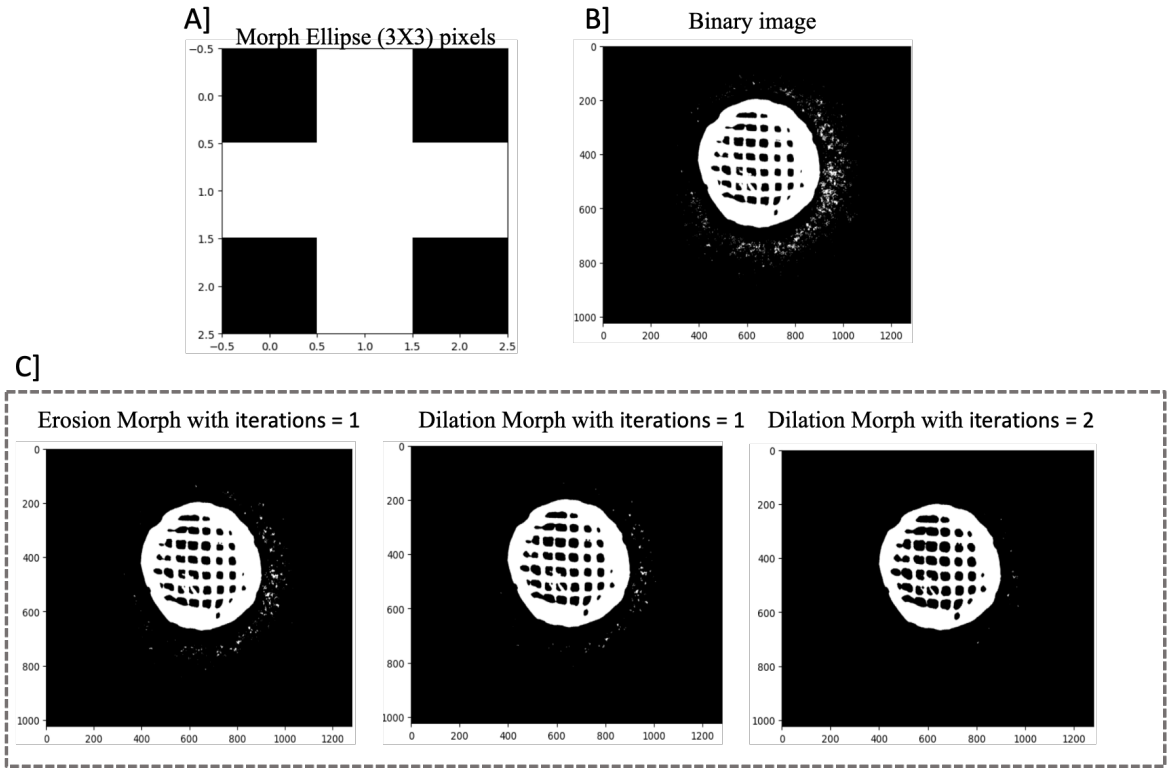



**Figure 4.3:** A] Noise A 3x3 morphological ellipse structuring element. B] Initial scaffold binary image displaying noise artifacts. C] Result of morphological opening and closing using the ellipse, which cleans noise and closes gaps. Image axes are in pixels.

To improve the contrast and visibility of the images, intensity rescaling was performed. By applying the '`rescale_intensity`' function from the scikit-image library (scikit-image version 0.19.3, [290]), an open-source image processing library for the Python programming language [290], the intensity values of the images were rescaled to a desired range. This rescaling step significantly enhanced the visibility of image features, making them more distinguishable and amenable to subsequent analysis and interpretation. Contour extraction, a fundamental step in image analysis, was then carried out to identify and outline the boundaries of connected regions within the binary images. The '`findContours`' function from OpenCV was utilised, employing a tree-based retrieval mode and a simple chain approximation method. This approach successfully identified the contours corresponding to the objects of interest in the images. To identify the most prominent object or region, the contour with the largest area was determined by computing the area of each contour using the '`contourArea`' function. The maximum area contour was then stored and recorded in a '`DataFrame`', associating it with the corresponding image for future analysis and comparisons (**Figure 4.4**).

Finally, to visually assess the effectiveness of the pre-processing steps, the resulting images with the outlined contours were displayed. This visualisation aided in verifying the accuracy of the image

segmentation, evaluating the quality of the pre-processing operations, and ensuring that the subsequent analysis would be based on appropriately processed images.

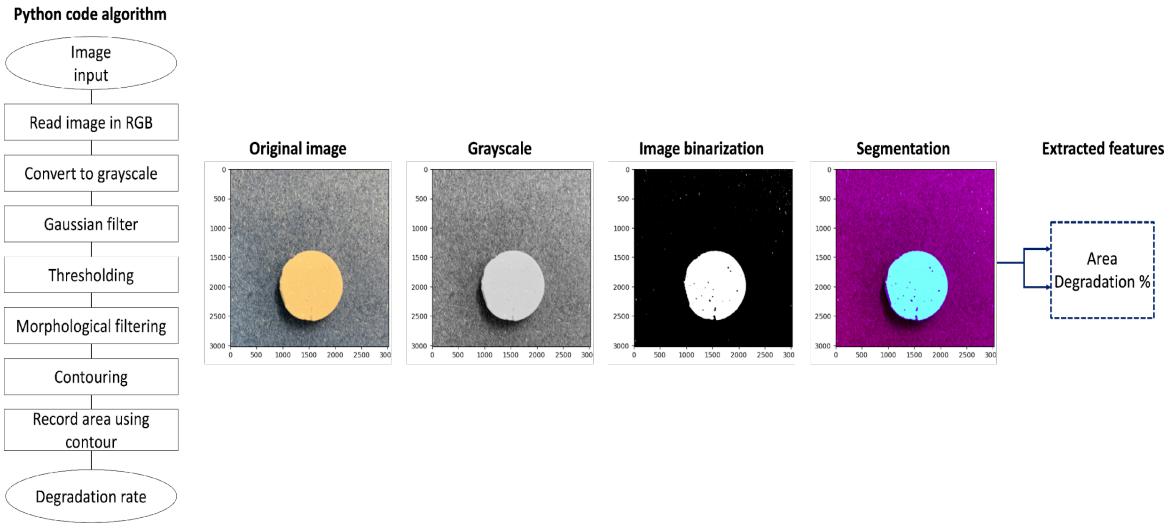



**Figure 4.4:** Pre-processing steps involved in extracting the scaffold area and computing degradation. It includes converting the image to grayscale, applying morphological filters, thresholding, segmenting the scaffold, and measuring its area and scaffold degradation (Device 3). Images axes are in pixels.

### 4.2.4. ML application to predict scaffold degradation

#### *4.2.4.1. Data Exploratory*

In the data exploration phase depicted by **Figure 4.5**, a preliminary analysis was conducted to assess the volume of images available for model training. The bar graph represents the distribution of images across different devices, with Device 1 accounting for approximately 188 images, Device 2 for about 48 images, Device 3 for around 36 images, and the 3D bioprinted collagen providing a substantially larger set of approximately 686 images. This initial inventory of data was critical for understanding the scale and diversity of the dataset available for feeding into the CNN and LSTM models. The considerable variation in the number of images per category suggests a potential class imbalance, which is an important factor to consider during model training. Adequate pre-processing steps, such as data augmentation or class weighting, was necessary to ensure that the models did not become biased towards the more represented classes. Additionally, the abundant data from the 3D bioprinted collagen group offers an extensive set for potential deep feature extraction, which is pivotal for the robust performance of CNNs in image recognition tasks and for LSTMs in understanding sequence and patterns over time.

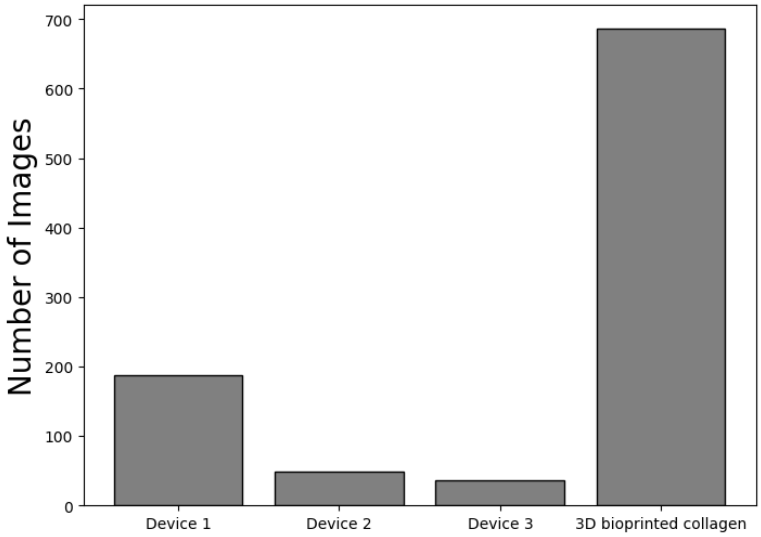



**Figure 4.5:** Data exploration

#### *4.2.4.2. Convolutional Neural Network (CNN) model for degradation prediction*

CNN model data preparation

The data loading process in this study involved two main components: image-based data and experimental data stored in an Excel file. The image-based data consisted of scaffold images captured at different experimental conditions, while the experimental data provided additional information related to each scaffold sample. To facilitate the integration of these data sources, a custom dataset class called 'CustomDataset' was implemented. This class served as the interface for loading and pre-processing the dataset. In the data loading phase, the experimental data from the Excel file was read and stored in a structured format. Additionally, any rows with missing values were removed to ensure data integrity and consistency. The dataset class was designed to handle the retrieval of individual samples. For each sample, the corresponding image was accessed using the provided file path. The experimental features, such as the day of the experiment, composition, area, area degradation, weight, and weight degradation, were extracted from the dataset. These features were subsequently converted into a suitable format for analysis and model training. Additionally, the target values, representing the next day's degradation by dimensions and weight, were stored as a dictionary. This dictionary structure facilitated the organisation and retrieval of target values during the model training and evaluation stages.

Model architecture

The CNN model was specifically designed to analyse image-based data in the context of the provided dataset. The model architecture consists of different layers that collectively enable effective feature extraction and prediction. The architectural design of the model incorporates a dual-input strategy

(**Table 4.1**). Utilising the innate attributes of CNN, like shared weights and local receptive fields, the model can detect patterns and spatial data from the provided imagery. The model starts with two convolutional layers (self.conv1 and self.conv2) that perform feature extraction by convolving filters with the input images. These filters convolve with the images, performing element-wise multiplications and summations to generate feature maps. The filters' weights are learned during the training process, allowing the model to automatically extract meaningful features. Mathematically, the convolution operation can be represented as follows:

$$Feature\ Maps = \sum_{i=1}^{N} (Input\ Image * Filter_i)$$

**Equation 4.1:** Feature Maps Generation

Following each convolutional layer, the Rectified Linear Unit (ReLU) (self.relu1 and self.relu2) activation function is applied elementwise to introduce non-linearity. ReLU sets negative values to zero, preserving positive values and enabling the model to learn complex relationships. Mathematically, ReLU can be defined as:

$$ReLU(x) = \max(0, x)$$

**Equation 4.2:** Rectified Linear Unit (ReLU) Activation

Max pooling layers (self.pool1 and self.pool2) are incorporated to down-sample the feature maps, reducing the spatial dimensions and retaining the most salient information. This pooling operation helps in capturing the most important features while reducing computational complexity. Max-pooling is commonly used, which partitions the feature maps into non-overlapping regions and selects the maximum value within each region. Mathematically, max pooling can be represented as

$$Max\ Pooling = max\ (Feature\ Map)$$

**Equation 4.3:** Max Pooling Operation equation

After the pooling layers, the feature maps are flattened into a one-dimensional tensor using `'Flatten()'`(PyTorch 1.8.0). This flattening operation reshapes the feature maps into a vector, allowing the model to process them through fully connected layers. These layers connect every

neuron in the current layer to every neuron in the subsequent layer, allowing the model to learn high-level representations and make predictions based on the extracted features. The model then has two fully connected layers (self.fc1 and self.fc2) that take the flattened feature vector as input. The first fully connected layer (self.fc1) has a size determined by the output shape of the last convolutional layer (32 * 56 * 56) plus 6 additional features. The ReLU activation function `('self.relu3')` is applied again to introduce non-linearity before passing the data to the final fully connected layer `('self.fc2')`. The size of self.fc2 corresponds to the desired output size, which in this case is the degradation prediction.

By utilising this model architecture, the model can effectively extract relevant features from the input images and combine them with the additional experimental data to make predictions regarding the degradation of the scaffolds as shown in **Figure 4.6**.

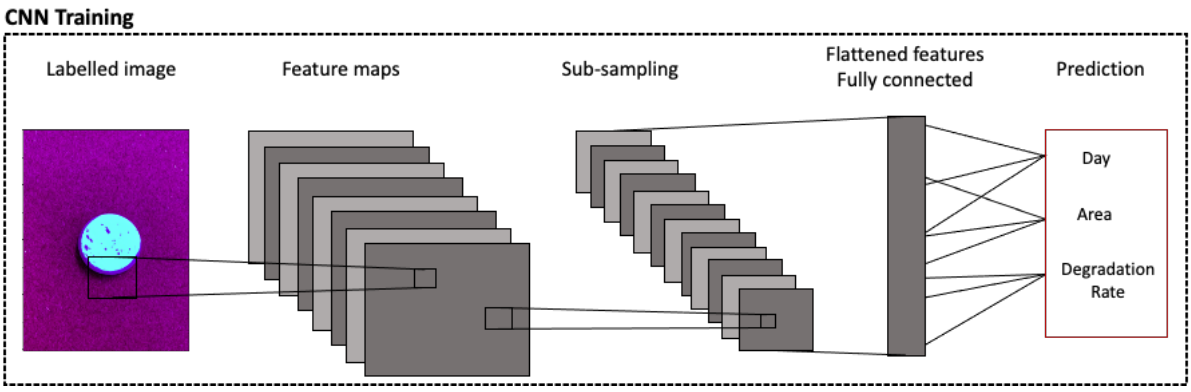



**Figure 4.6:** The training process involves feature maps, sub-sampling, and flattened features, which capture important patterns related to degradation rate. Fully connected layers further learn complex relationships within the extracted features. The CNN model's output layer provides predictions for scaffold degradation rate.

**Table 4.1:** Layers parameter used to build CNN model

| **Model Parameters** | **Parameter Values** | **Description** |
|---|---|---|
| Input Channels | 3 | Number of channels in the input image |
| Output size | 2 | Number of output values |
| Conv1 | Kernel Size: 3, Stride: 1, Padding: 1 | Convolutional layer 1 |
| Relu1 | - | ReLU activation function after Conv1 |
| Pool1 | Kernel Size: 2, Stride: 2 | Max pooling layer 1 |
| Conv2 | Kernel Size: 3, Stride: 1, Padding: 1 | Convolutional layer 2 |
| Relu2 | - | ReLU activation function after Conv2 |
| Pool2 | Kernel Size: 2, Stride: 2 | Max pooling layer 2 |
| Flatten | - | Flatten layer |
| FC1 | Input size: (32*56*56+6), output size: 100 | Fully connected layer 1 |
| Relu3 | - | ReLU activation function after FC1 |
| FC2 | Input size:100, Output size: 2 | Fully connected layer 2 (Output layer) |

CNN training and hyperparameter selection

The necessary hyperparameters, as shown in **Table 4.2**, were defined for the training process, such as the learning rate, number of epochs, and batch size. The training data is loaded from the `'CustomDataset'`, which combines the image-based data and experimental data from an Excel file. The dataset is split into train and test indices, with 80 % of the data allocated for training. During each epoch of training, the model is iteratively optimised using mini batches of data. The inputs and targets are extracted from the batch, where the inputs correspond to the image data and the features encompass the experimental data. These inputs and targets are then transformed and transferred to the model. The features and targets are scaled using standard scalars to normalise the data and improve training performance.

The model was then trained using the Adam optimiser and the mean squared error (MSE) loss function. The forward pass computes the outputs of the model, representing the predicted values for scaffold degradation. The loss is calculated as the sum of individual losses for each output value, reflecting the discrepancy between the predicted and target values. The backward pass computes the gradients of the model parameters with respect to the loss, and the optimiser updates the parameters accordingly. The running loss and root mean square error (RMSE) values for each output value were calculated to monitor the training progress. The RMSE quantifies the average deviation between the predicted and true values, providing a measure of the model's performance. After training, the model's state dictionary was saved to a file, allowing it to be loaded and used for future predictions.

In addition to this, the feature scaler and target scaler, tools vital for preparing input data by scaling it to a consistent range for the model, were preserved using the Python library pickle. This method of serialisation transforms these scalars into a format that can be saved to a file and later retrieved, ensuring that any future data fed into the model for predictions undergoes the same scaling process. This careful preservation of the model's state and the scaling tools is a testament to the foresight in maintaining the integrity and repeatability of the model's predictive capabilities, allowing it to be efficiently deployed for future predictions without the necessity of retraining.

**Table 4.2:** Summary of model hyperparameters.

| **Hyperparameters** | **Values** | **Description** |
|---|---|---|
| Learning Rate | 0.001 | Step size for model parameter updates |
| Number of Epochs | 100 | Number of times to iterate over the dataset |
| Batch size | 32 | Number of samples in each mini-batch |

#### *4.1.1.1. Long short-term memory (LSTM) model for degradation prediction*

LSTM model data preparation

To achieve the uniformity necessary for the image processing of the VGG16 neural network, data exploration began with standardising picture file formats to '.jpeg'. The pictures were then put into a data frame with image paths and counts, describing the size of the dataset and ensuring that the images had been categorised correctly. Next, temporal elements were extracted from image filenames, converted into a numerical sequence, and standardised. This demonstrated the LSTM networks needed for time-series analysis preparations. To preserve data integrity for effective model training, missing values were resolved. Following this, the combination of image data and structured data weight and diameter was done to create a dataset that was prepared for predictive modelling using the LSTM and VGG16 frameworks. This dataset was further divided into four categories: 'X_numerical,' 'X_image,' 'y_weight,' and 'y_diameter.' This suggests a method for handling different data formats and prediction goals, which result in the creation of distinct or multi-output models.

LSTM Model architecture

The LSTM model presented for this application represents an advanced combination of neural network technologies, designed to employ the power of both image-based and numerical data inputs for the prediction of material degradation characteristics. The architectural design of the model incorporates a dual-input strategy (**Table 4.3**). The first input, designed for image data, employs the pre-trained VGG16 model as a feature extractor (**Figure 4.7**-B). VGG16, renowned for its effectiveness in image recognition, operates without its top layer of fully connected neurons. The convolutional base of VGG16 used here, uses weights that have been pre-trained on the expansive ImageNet dataset. This approach allows for the extraction of a high-level feature set from input images, which is crucial for subsequent processing stages. Once the image features are extracted, they undergo a flattening process to convert the multidimensional tensors into a single vector of values. This vector is then reshaped to fit the input requirements of the LSTM layer, aligning with the LSTM's inherent ability to process sequential data (**Figure 4.7**-C). The LSTM layer, equipped with 256 units and using a ReLU activation function, processes the time-series representation of the image features, enabling the model to understand and influence the temporal dynamics inherent in the sequential data (**Figure 4.7**-D).

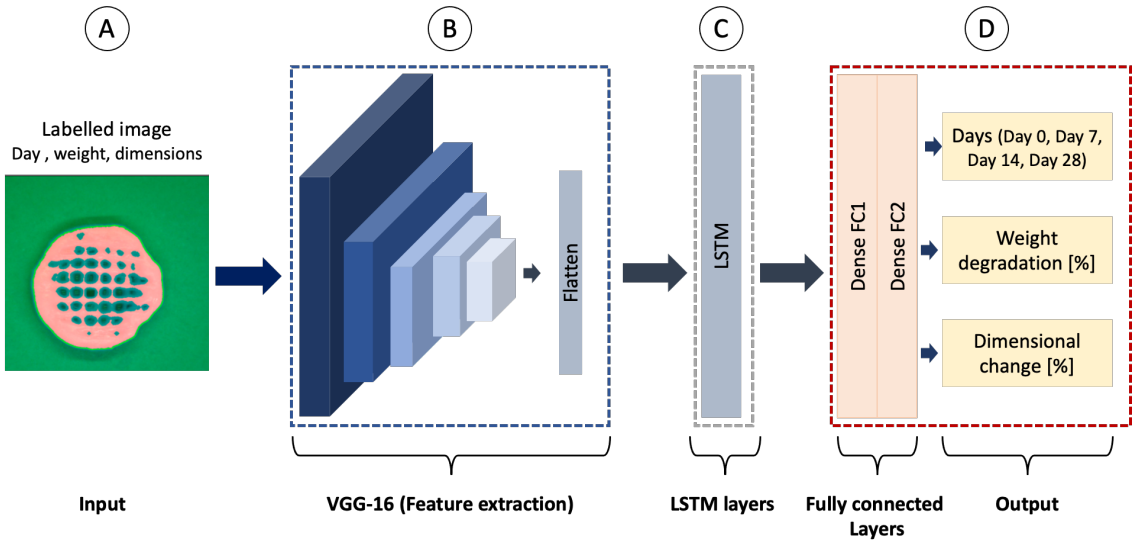



**Figure 4.7:** Illustrates of the use of VGG-16 and LSTM to forecast scaffold degradation at different time points.

LSTM training

In combination with the image-based pathway, the model receives a secondary input stream dedicated to numerical data. This stream feeds directly into the LSTM architecture, ensuring that both image and numerical data are concurrently processed, capturing the complex interdependencies between the two. The fusion of these two data streams is achieved through concatenation, resulting in a composite feature matrix that combines the strengths of both inputs. This matrix serves as the foundation for the prediction process, passing through a dense layer of 128 neurons that also employs the ReLU activation function to maintain non-linearity within the network. The predictive capability of the model is realised through two separate dense layers. Each layer is dedicated to predicting a specific output parameter: 'weight' and 'diameter.' These layers utilise a linear activation function, suitable for the model's regression-based tasks.

During the model training phase, mean absolute error is selected as the loss function, reflecting the average magnitude of errors between the predicted and actual values without considering their direction. The optimisation of the model parameters is guided by the Adam optimiser (is a method used in ML that helps computers get better at making decisions, adjusting how they learn from data more efficiently over time), a choice driven by its adaptive learning rate capabilities and proficiency in handling sparse gradients. An innovative aspect of the training process is the incorporation of a learning rate reduction strategy. The learning rate is decreased by a factor of 0.1 if the validation loss does not improve during a period of five epochs. This methodical approach ensures a more precise and controlled optimisation path, enhancing the model's ability to generalise to new, unseen data. The training regimen is carried out over eighty epochs, with a batch size of eight, striking a balance

between computational demands and the learning capacity of the model. This careful calibration of epochs and batch size is instrumental in driving the convergence of the model parameters, which is crucial for the reliability of the predictive outcomes. The model parameters and hyperparameters used summarised in **Table 4.3**.

**Table 4.3:** layers. parameters and hyperparameters to build LSTM model

| Model Parameters | Parameter Values | Description |
|---|---|---|
| Numerical Input | Shape: (2,) | Input layer for numerical data. |
| Image Input | Shape: (224, 224, 3) | Input layer for image data formatted for VGG16. |
| VGG16 Feature Extractor | Weights: 'imagenet' | Pre-trained VGG16 for feature extraction. |
| Flatten | | Flattens VGG16 output to 1D array. |
| Reshape | Shape: (7, 7*512) | Reshapes features for LSTM input. |
| LSTM | Units: 256, Activation: 'relu' | Processes sequential image features. |
| Concatenate | | Merges numerical input and LSTM features. |
| Dense (ReLU) | Units: 128 | Dense layer with ReLU activation. |
| Output Weight | Units: 4, Activation: 'linear' | Predicts the weight with linear activation. |
| Output Diameter | | Predicts the diameter with linear activation. |
| Loss Function | Mean Absolute Error | Calculates the mean absolute error between prediction and target. |
| Optimiser | Adam | Optimises the model weights. |
| Learning Rate Adjustment | ReduceLROnPlateau | Reduces learning rate when a plateau in validation loss is detected. |
| Training Epochs | 80 | Number of training cycles. |
| Batch Size | 8 | Number of samples per training batch. |

#### *4.1.1.2. Model performance and evolution*

The performance of the model was evaluated using the Mean Squared Error (MSE) loss function during the training process to assess how close the segmented result was to the provided ground truth segmentation. At each epoch, the model's predictions were compared to the actual values, and the MSE was calculated. The equation for MSE is given by:

$$MSE = \frac{1}{N}\sum_{i=1}^{N}\left(Y_i - \widehat{Y}_i\right)^2$$

**Equation 4.4:** Mean Squared Error equation

Where $N$ is the total number of data points, $Y_i$ is the actual value, and $\widehat{Y}_i$ is the predicted value. A smaller MSE indicates that the model's predictions are closer to the actual values.

In addition to the MSE, the Root Mean Squared Error (RMSE) was used to evaluate the model's performance for each of the ten outputs. RMSE provides a measure of the average magnitude of the errors between predicted and observed values. It is computed as the square root of the MSE:

$$RMSE = \sqrt{MSE}$$

**Equation 4.5:** Root Mean Squared Error equation

The RMSE has the advantage of being in the same units as the predicted and actual values, making it more interpretable. For each epoch, both the training loss MSE and the RMSE for the ten outputs were printed, providing a detailed view of how the model performed over time. Finally, a visual representation of the training loss over all epochs was saved as a graph, providing a clear illustration of the model's convergence behaviour.

#### *4.1.1.3. LSTM model evolution (WebApp)*

To get started, the Flask (Pallets Projects) application sets up directories for pictures and provides the path to the pretrained model. Multiple pre-processing steps are performed to ensure the images meets the input specification. These tasks include scaling the image to 224 x 224 pixels, turning it into an array, and applying specific pre-processing procedures designed for the VGG16 model. This guarantees that the image is in the appropriate format for feature extraction by the neural network. The application combines visual characteristics obtained from images uploaded by the user with quantitative inputs, specifically weight and diameter, to predict scaffold degradation. By using a multi-faceted method, the model's capacity to predict accurately is significantly enhanced. The data are carefully converted into understandable percentage values, providing a measurable view of scaffold degradation. An essential component of this study involves the visualisation of the predicted degradation patterns. The application generates graphs that show the degradation percentages of the scaffold over time, providing a clear and visual picture of its degradation journey. This visual analysis tool is essential for comprehending the degrading behaviour of the material, hence enhancing the interpretability of the model's predictions.

## 4.3. Results and Discussion

### 4.3.1. Computational vs traditional methods (Image analysis tool)

#### *4.3.1.1. Collagen-based scaffold*

The degradation rates of 3D bioprinted collagen-based scaffolds, as measured by image analysis (D_c), weight loss (D_w), and dimensional change (D_d), provide valuable insights into the performance and stability of these scaffolds over time, particularly in the context of bone tissue engineering. The scaffold with no HA (**Figure 4.8**-A) showed degradation rates of 3.96 % for D_c and 3.98 % for D_d. Highlighting the similarity between these two rates emphasises the accuracy of

the image analysis tool in accurately detecting the exterior degradation of the scaffold, including surface erosion and dimensional reduction, with the same level of sensitivity as the traditional dimensional change measurements. This is especially important considering that D_c, an automated and apparently less labour-intensive approach, is comparable to the more manual D_d in monitoring the structural soundness of the scaffold over a period of time. The weight loss technique (D_w), however, exhibits a higher rate of degradation at 4.77 % each day, indicating an inconsistency between the decrease in mass and the noticeable decrease in dimensions. The difference suggests internal alterations inside the scaffold, potentially at the microscopic scale, that are not evident in the scaffold's outward measurements. These changes may occur due to the degradation of internal scaffold components or the release of soluble elements, which would affect the weight of the scaffold before its overall shape.

By introducing HA into the collagen matrix, starting with a concentration of 0.05 %(w/v) (**Figure 4.8**-B) and 0.5 %(w/v) (**Figure 4.8**-C), a consistent decrease in degradation rates shown in the results using all measuring methods. The degradation rates for the scaffolds in **Figure 4.8**-B are as follows: D_c has a rate of 3.14 %, D_d has a rate of 3.21 %, and D_w has a higher rate of 4.00 %. When the concentration of HA is increased to 0.5 %(w/v), the rates decline even more. Specifically, D_c shows a decrease of 2.89 %, D_d shows a decrease of 3.13 %, and D_w reports a decrease of 3.57%. The observed decreases suggest that HA increases the structure of the scaffold by potentially creating a crystalline framework that enhances the collagen, so preventing both internal degradation and external damage.

The appropriate degradation rate of a scaffold should match with the rate of new bone production [256]. If the scaffold undergoes rapid degradation, it may not be able to offer the essential mechanical support needed during the initial and crucial stages of bone healing [256]. On the other hand, if the degradation rate is too slow it might delay the integration and remodelling of new bone tissue [291]. The degradation rate appears to be influenced by the presence of HA, indicating that the concentration of HA in collagen scaffolds can be adjusted to enhance the performance of the scaffold [257].

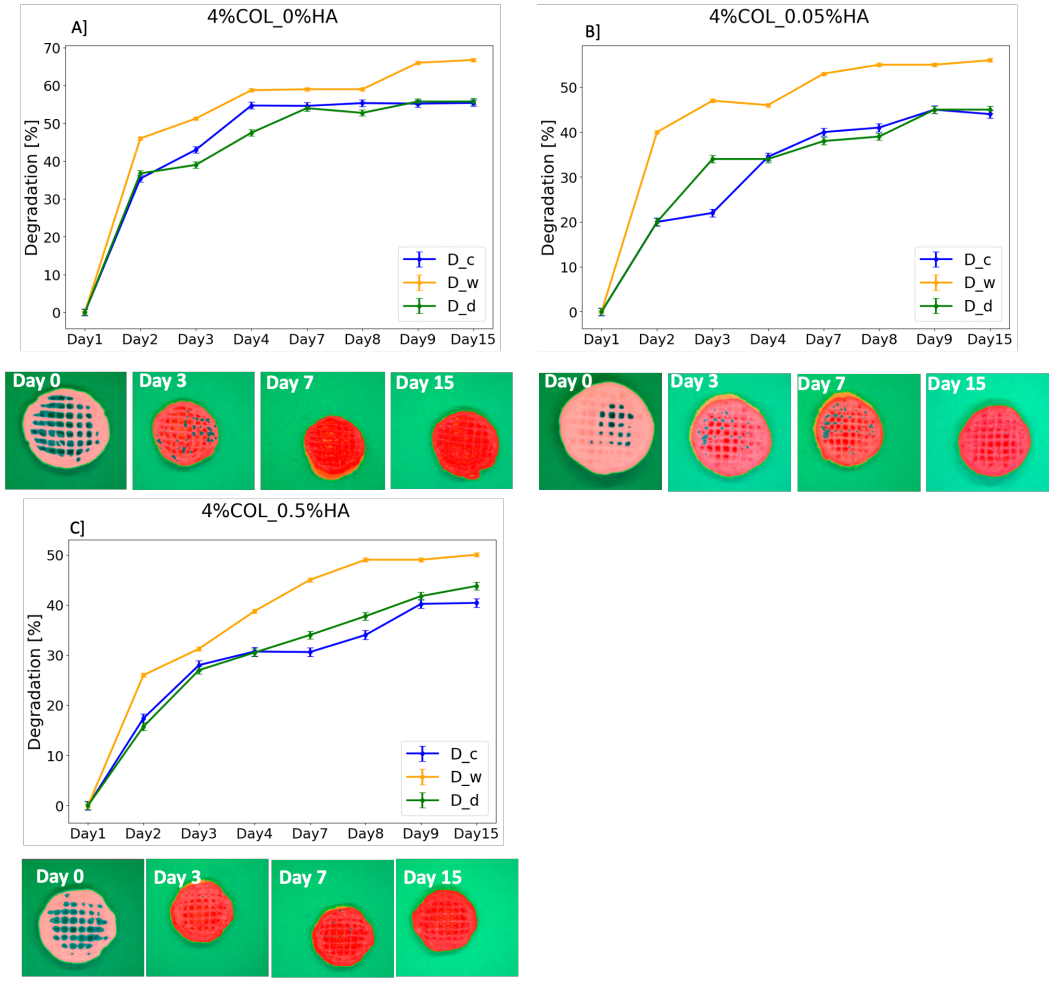



**Figure 4.8:** Comparison between image analysis (D_c), weight loss (D_w), and dimensional change (D_d) from Day 0 to 15 with images for . A] 4% COL/0%HA B] 4% COL/0.05%HA and C] 4% COL/0.5%HA.

#### *4.1.1.1. Device 1*

A comparison of degradation measurements obtained via different methodologies: image analysis tool (D_c), weight loss measurement (D_w), and dimensional change measurement (D_d) is shown in **Figure 4.9**. These methodologies were employed to analyse the degradation behaviour of three distinct compositions of 3D bioprinted polymer scaffolds: PLLA/PCL/PHBV (5 x 3 mm and 5 x 5 mm), PLLA/PCL/PHBV_nHA, and PLLA/PCL/PHBV_Sr_nHA, across multiple time intervals: Day 0, Day 7, Day 14, and Day 28 (Figure 4.6). The congruence between D_c and D_d degradation measurements can be observed. In several instances, both D_c and D_d exhibit a parallel trend, with degradation measurements peaking at approximately 20 %. This consistency in trends between image analysis and dimensional change measurements further demonstrates the accuracy and reliability of the image analysis tool in capturing the dimensional alterations of the scaffolds over time.

On the contrary, the weight loss degradation measurements (D_w) manifest a different degradation trajectory with values not surpassing 5 %, D_w suggests a slower degradation rate. This disparity between D_w and the other two measures could be attributed to various factors. Weight loss may be a more gradual process, or the mechanism of degradation ascertained through weight may differ from that of dimensional changes. Moreover, there might be elements within the scaffold that degrade but do not significantly affect its weight in the early stages. Furthermore the scaffold likely contract and shrink during the initial stages of the degradation study, while the mass stays relatively consistent. The overarching significance of these findings is the evident utility of image analysis tools for scaffold degradation measurement.

The degradation behaviour observed in the study was consistent with findings reported in the literature, particularly in the work by Kontogianni *et al* investigated PLLA/PCL/PHBV scaffolds enriched with nano-hydroxyapatite (nano-HA) and strontium-substituted nano-hydroxyapatite (Sr-nano-HA) [285]. Mass loss was observed within the first eight weeks, with values within ±3% of the initial mass. The slower degradation rates indicated by weight loss measurements in both studies suggest that internal structural changes may not significantly affect overall mass during the early stages of degradation.

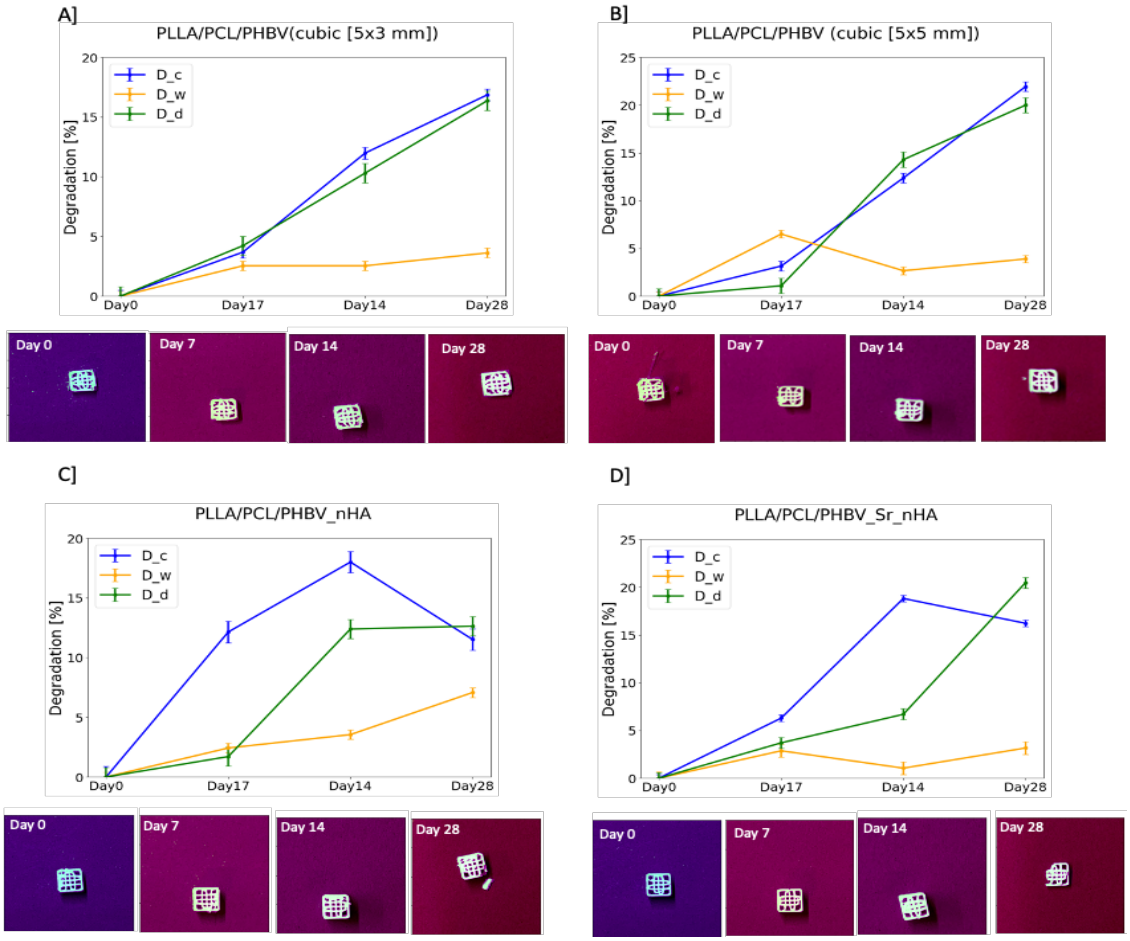



**Figure 4.9:** Device 1 comparison between image analysis (D_c), weight loss (D_w), and dimensional change (D_d) from Day 0 to 28 with scaffold images for A] PLLA/PCL/PHBV (5 x 3 mm) B] PLLA/PCL/PHBV (5 x 5 mm) C] PLLA/PCL/PHBV_nHA D] PLLA/PCL/PHBV_Sr_nHA.

#### *4.1.1.2. Device 2*

In **Figure 4.10**-A, both D_d and D_c shows similar degradation patterns, with levels between 34 % and 56 %. In contrast, D_w indicates a much higher degradation at around 80 %. This observation indicates that, although the superficial morphology of the scaffold exhibits a specific degradation trajectory, the internal structural integrity could be compromised at a potentially accelerated rate.

In **Figure 4.10**-B, the addition of MBG slows down the degradation. Both D_d and D_c has degradation rates between 20 % and 26 %. However, D_w again shows a higher value, this time at around 60%. This difference between external (D_d and D_c) and internal (D_w) degradation rates is again evident, as was seen in **Figure 4.10**-A. What is clear from both figures is that the image tool is good at capturing the general degradation trend of the scaffold's outer part. Especially for studies around electrospinning scaffolds, this tool offers a faster way to measure degradation based on the scaffold images. However, one limitation of the approach is that degradation related changes to the internal scaffold structure, like changes in the scaffold's fibre structures, cannot be easily detected. The imaging tool presents an efficacious methodology for elucidating external scaffold degradation dynamics for this device. However, for a comprehensive understanding of internal structural alterations, supplementary investigative techniques are imperative.

The results presented in **Figure 4.10**, showing the degradation patterns of PEOT/PBT and PEOT/PBT_MBG scaffolds, are consistent with observations in the literature. Specifically, the study by Tomasina *et al.* on the incorporation of strontium-containing bioactive particles into PEOT/PBT electrospun scaffolds provides relevant comparisons [286]. The research found that PEOT/PBT scaffolds exhibited a degradation rate of around 17% mass loss in vitro over 14 days, aligning with the degradation percentages observed in the study at hand for PEOT/PBT without MBG. Furthermore, the inclusion of mesoporous bioactive glasses (MBG) in the scaffolds significantly altered the degradation behaviour, resulting in lower degradation rates.

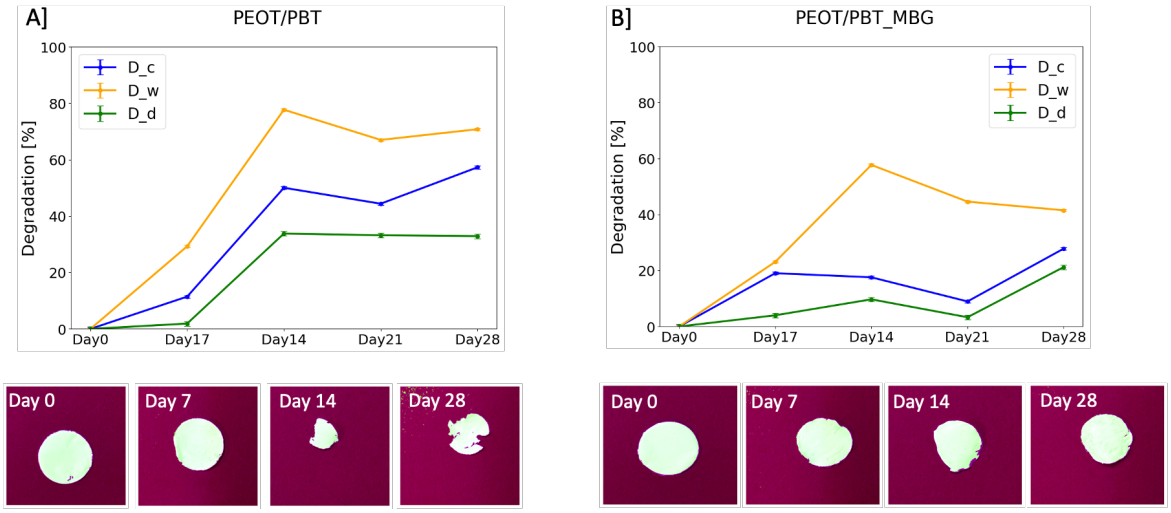



**Figure 4.10:** Device 2 comparison image analysis (D_c), weight loss (D_w), and dimensional change (D_d) degradation measurements from Day 0 to 28 with images from each day for A] PEOT/PBT. B] PEOT/PBT_MBG.

### *4.1.1.3. Device 3*

For Device 3, the injectable cements, **Figure 4.11** provides a comparison of deterioration measures between the image analysis tool and traditional manual approaches. The injectable cements confirmed findings for earlier devices by showing a closer congruence between D_d and D_c. A notable finding in **Figure 4.11**-A is the near alignment of the deterioration trajectories observed using all three techniques, which points to a consistent degradation pattern across measurements. In contrast, **Figure 4.11**-B introduces an inherently porous structure of the MBG, D_w degrades at a slightly faster rate than D_c and D_d. This distinction may indicate underlying internal alterations in the scaffold material, which may have been influenced by porous properties of the MBG. The paired graphs in this image, which exhibit the study's findings, give important insights into the many ways injectable cements degrade. This emphasises the significance of using a variety of techniques to get a comprehensive understanding of scaffold degradation.

The degradation behaviour observed for Device 3, particularly with the 100CSH and 70CSH_MBG injectable cements, shows a close alignment with findings reported in the literature. The study by Banche-Niclot et al. demonstrated that cements containing mesoporous bioactive glass (MBG) exhibited an accelerated degradation rate compared to non-MBG formulations, particularly when measuring weight loss [30], [287]. These similarities between the current findings and the literature underscore the critical role of MBG in modulating the degradation behaviour of injectable cements, validating the use of multiple measurement techniques to gain a comprehensive understanding of scaffold degradation

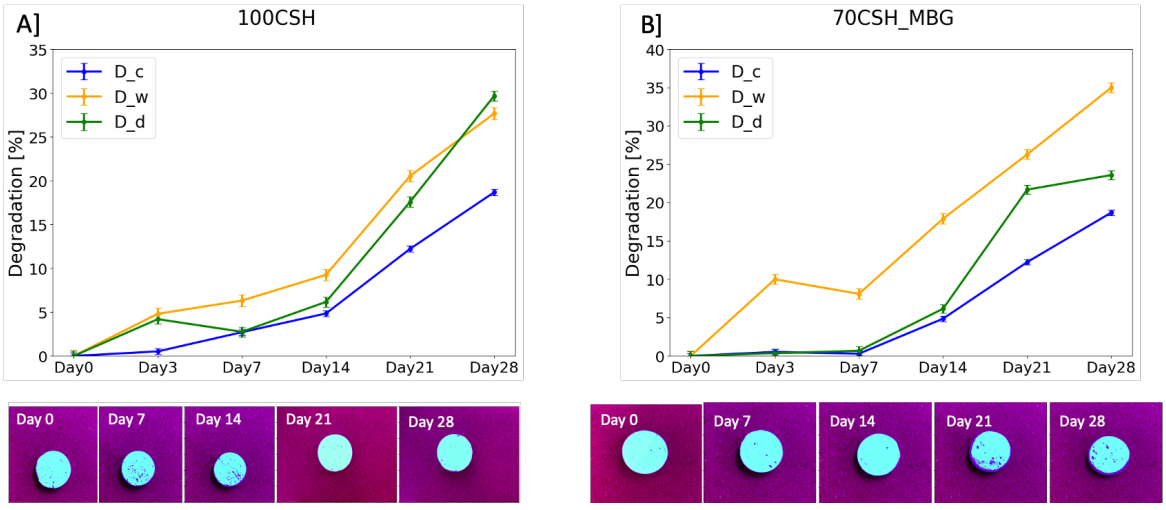



**Figure 4.11:** Device 3 comparison between image analysis (D_c), weight loss (D_w), and dimensional change (D_d) degradation measurements from Day 0 to 28 with images from each day. for A] 100 CSH B] 70CSH_MBG.

The Python-based image analysis tool developed here has several benefits for evaluating the degradation rate of scaffolds in bone tissue engineering applications. First, it allows for more accurate and precise measurements compared to traditional manual methods. Second, it reduces the time and effort required for data analysis, as the tool can automatically calculate dimensional changes using image analysis algorithm. Third, it enables researchers to compare the performance of different types of scaffolds in a more systematic and objective manner. Furthermore, the tool can be used to optimise the manufacturing process for scaffolds by identifying factors that impact the degradation rate. By adjusting the material composition or manufacturing process, researchers can improve the performance of the scaffolds and ultimately the success of bone fracture implants. In addition, the tool can be used to assess the stability and degradation rate of scaffolds over time, which is important for long-term implant success.

**Table 4.4:** Comparison between scaffold degradation traditional manual methods vs image analysis tool

| **Criteria** | **Manual analysis** | **Computational image analysis tool** |
|---|---|---|
| **Accuracy** | Subject to human error, less consistent | High precision through algorithms, consistent results (87% accuracy) |
| **Efficiency** | Time-consuming, analysis per scaffold can vary significantly (for high volume if samples take minimum 2 h to record data) | Rapid processing, uniform time for analysing each scaffold (5-10 min) |
| **User Dependency** | High; requires expert knowledge and can vary between users | Low; minimal training required, user-independent |
| **Systematic Analysis** | Difficult to standardise due to manual handling | Easy to standardise and automate for bulk analysis |
| **Long-term Analysis** | Labour-intensive to monitor degradation over time | Automated tracking over time with minimal effort |

### 4.3.2. CNN and LSTM models

This section presents a description of how the degradation prediction was carried out using LSTM networks combined with CNN. The method incorporates data from experiments, such as weight and diameter measurements, along with images, to effectively model and predict degradation. The

training, evaluation, and performance of the models will be covered, as well as the creation of a user-friendly web application interface.

#### *4.3.2.1. Training and validation losses*

CNN model (**Figure 4.12**-A), the curve shows a dramatic initial decrease in training loss, which flattens out as epochs increase, a typical pattern indicating that the model is learning from the training data. Nevertheless, the validation loss shows a less significant decrease and displays more variation and an increasing pattern as the learning process advances, indicating the possibility of overfitting in the model. The gap between the training and validation losses indicates the model performs well on the training data but does not generalise as effectively to the validation data. This could be a sign that the model is too complex or that the dataset is not diverse enough, causing the model to memorise the training data rather than learning general patterns.

LSTM model (**Figure 4.12**-B), both training and validation losses plummet swiftly and then level off, staying in close proximity throughout the training process. This pattern is indicative of a well-performing model with good generalisability to unseen data. The slight convergence of training and validation loss towards the end suggests that the model may benefit from further training, more data, or perhaps a different set of hyperparameters to reduce the gap further and improve performance. Comparing the two, the model on the LSTM (Figure 4.10-B), appears to be more effective, achieving lower loss values with better alignment between training and validation, which is **Figure 4.12**-A), while initially showing promise, would benefit from strategies to reduce overfitting.

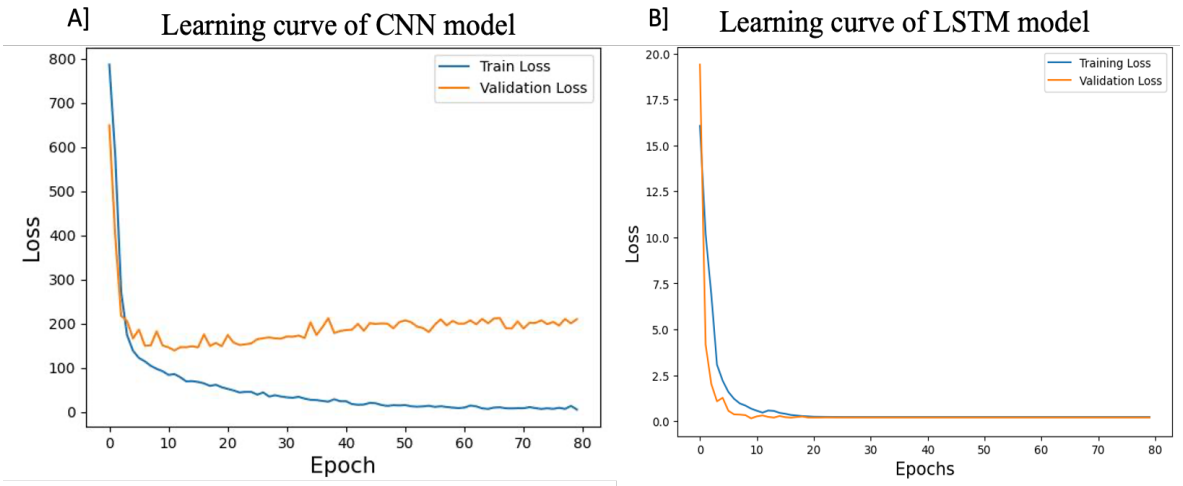



**Figure 4.12:** CNN and LSTM models efficacy was gauged during their training phases using the mean squared error as the benchmark metric. A] CNN learning curve. B] LSTM learning curve.

#### *4.3.2.2. Model performance*

The metrics in **Table 4.5** offer a direct comparison between the performance of CNN and LSTM network across several common evaluative measures. The Mean Squared Error (MSE) for the LSTM is substantially lower than that of the CNN, suggesting that the LSTM model has a much tighter fit to the data. The Mean Absolute Error (MAE) follows a similar trend, with the LSTM achieving a markedly lower score than the CNN. This indicates that, on average, the LSTM's predictions are closer to the true values, which is particularly significant given that MAE provides a clear and interpretable measure of prediction accuracy in the same units as the predicted variable. The R-squared ($R^2$) values provide insight into the proportion of variance in the dependent variable that is predictable from the independent variables. Here, the LSTM model again outperforms the CNN, albeit more modestly. An $R^2$ of 0.665 implies that the LSTM captures a greater portion of the variance than the CNN, which achieves an $R^2$ of 0.569.

Finally, the accuracy measure further demonstrates the superiority of the LSTM in this context, with an accuracy of 0.79 compared to 0.61 for the CNN. It is important to note, however, that accuracy is more often used for classification tasks, so its interpretation for regression models (typically those evaluated by MSE and MAE) should be treated with caution unless the accuracy here is defined in a context-specific manner (e.g., percentage of predictions within a certain range of the true values). Overall, these results suggest that the LSTM model not only predicts more accurately but also captures the underlying data structure more effectively than the CNN model. This could be due to the ability of the LSTM to model sequential or time-dependent patterns in the data, which is often where it excels in comparison to CNNs that are more suited to spatial pattern recognition.

**Table 4.5:** Performance metrics comparison between CNN and LSTM models, including Mean Squared Error (MSE), Mean Absolute Error (MAE), R-squared (R2), and Accuracy.

| | **CNN** | **LSTM** |
|---|---|---|
| **MSE** | 0.032 | 0.006 |
| **MAE** | 2.10227 | 0.061 |
| **$R^2$** | 0.569 | 0.665 |
| **Accuracy** | 0.61 | 0.79 |

Recent literature on the application of machine learning models, such as LSTM and CNN, to predict scaffold degradation using image-based data highlights the growing interest in combining computational tools with material science to enhance prediction accuracy. Entekhabi *et al.* predicted the degradation rate of genipin cross-linked gelatin scaffolds demonstrates the utility of machine learning in estimating the degradation behaviour of biomaterials, which parallels the approach taken

in this study [263]. Specifically, the article compares artificial neural networks (ANN) and kernel ridge regression (KRR) models, showing that ANN outperforms KRR in predicting degradation rates, with an MSE of 2.68% versus 4.78% [263]. This outcome supports the effectiveness of machine learning in capturing complex degradation patterns, a finding that resonates with the results obtained using CNN and LSTM models in this study.

#### *4.3.2.3. CNN model evaluation*

In the evaluation phase, 10% of the data was reserved to test the model's predictive prowess, with the inputs being images from Day 0, accompanying weight, and diameter values (**Figure 4.13**). When compared, the actual versus predicted outcomes unveiled an accuracy of 65% in forecasting weight loss and a slightly more promising 78% in predicting the dimensional change degradation of the scaffold. One significant factor underlying these results is the constrained dataset used to train the model. An ML model's proficiency is directly contingent on the richness and diversity of the dataset it is trained on. In this study, the lack of data, especially with diverse scaffold shapes and material types, could have contributed to the model's inability to generalise more effectively. To enhance prediction accuracy, particularly in the domain of image-based degradation analysis, amassing a more voluminous and varied dataset becomes imperative.

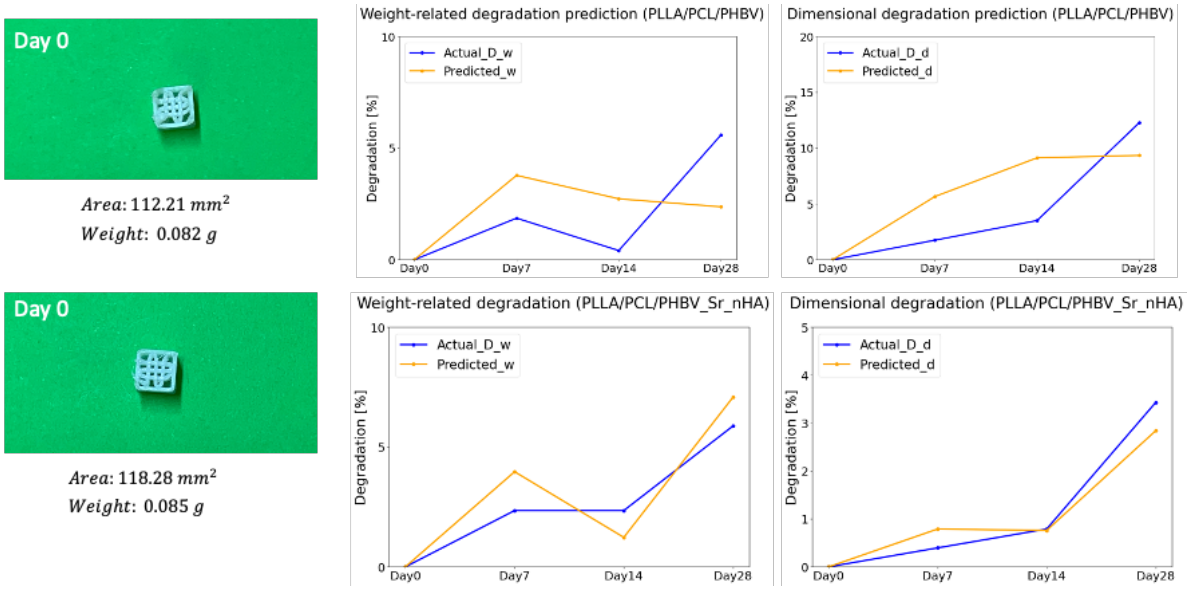



**Figure 4.13:** Device 1 degradation prediction testing and comparing it with actual data.

User interface and interactive analysis

The Flask framework is essential for this research. It provides a user-centric web interface, allowing for direct interaction with the prediction model. This WebApp allows users to upload images of scaffolds and enter pertinent metadata. The uploaded data is analysed to generate predictive and visual evaluations of scaffold degradation. This interactive platform greatly improves the practical use of the predictive model, making advanced deep learning insights accessible to both researchers and practitioners in the field of material science. The combination of predicting scaffold degradation with a user-friendly visualisation and interactive interface (**Figure 4.14**) represents the interdisciplinary nature of current scientific research. This novel approach not only emphasises the practicality and usefulness of using ML for analysing material degradation, but also shows the cutting-edge capability of integrating artificial intelligence with online technologies to tackle intricate scientific research.

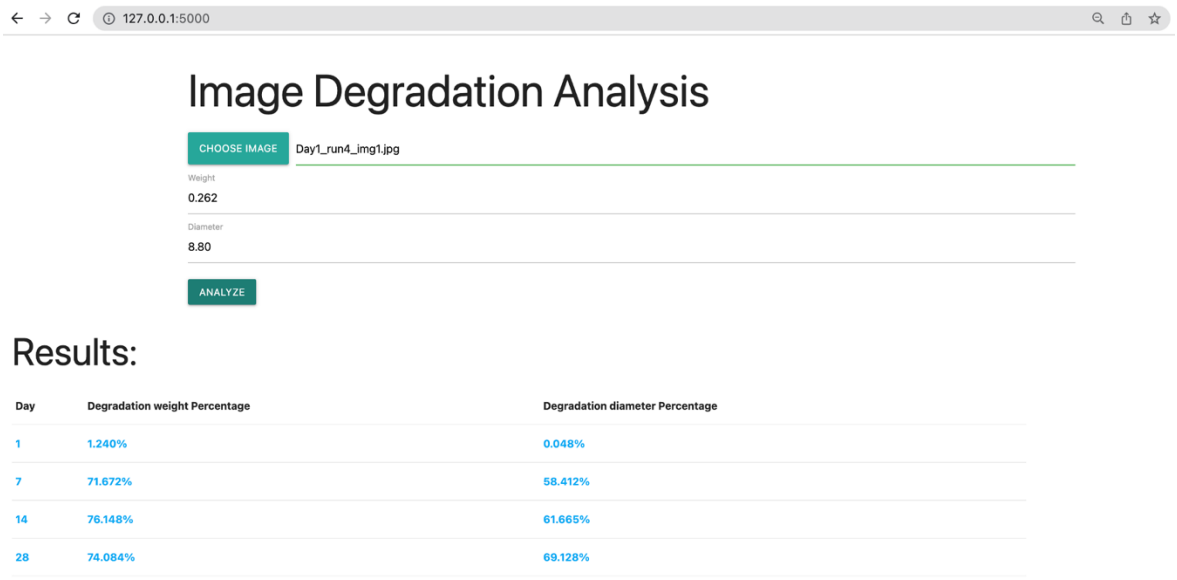



**Figure 4.14:** Web Interface displaying image degradation analysis results. The interface presents degradation weight and diameter percentages for selected days.

## 4.4 Conclusions

In this chapter, Objective 2 of the thesis, to automate scaffold degradation rate measurements through advanced image analysis, has been successfully achieved. The implementation of these novel computational techniques has resulted in a significant improvement over conventional methods, offering enhanced precision and speed. Furthermore, the fulfilment of Objective 3 has seen the successful integration of CNN and LSTM ML models into a user-centric interface, facilitating advanced predictive analysis of scaffold degradation.

Our Python-driven image analysis programme proves to be an important tool for determining the rate at which scaffolds degrade. This tool is faster, more accurate, and provides a more thorough understanding as compared to conventional manual approaches, particularly when focusing on dimensional changes. Researchers can benefit greatly from this technical development since it gives them a thorough understanding of how scaffolds degrade, which can then be used to improve the fabrication of scaffolds and maximise their performance in bone fracture implants. Traditionally, weight-based measurements were the most often used manual measurements for degradation analysis. But as our work shows, these measurements might not always be accurate, especially when there is a clear distinction between dimensions and weight changes during the degradation process. The need for several samples to be produced for each time point is minimised by image analysis approaches that are capable of real-time, non-destructive analyses. This guarantees resource conservation and a more streamlined degradation assessment method.

One challenge in the use of the image analysis approach applied here for assessment of degradation is that while the subtleties of outward degradation can be effectively captured, underlying structural changes cannot be detected. Therefore, it is obvious that to gain a true picture of scaffold degradation microstructural investigations must be incorporated into our evaluation processes. This approach would allow a thorough grasp of both the internal and external deterioration processes by utilising a variety of imaging techniques and cutting-edge image analysis tools. By focusing on the development of complex image analysis algorithms specifically made for scaffold degradation investigations, future research can expand on this foundation. A thorough investigation of scaffold microstructures utilising a variety of imaging techniques will offer a full view of degradation, taking into account both internal and exterior aspects. Additionally, the prospective uses of such instruments go beyond bone scaffolds, offering breakthroughs in a number of tissue engineering fields.

Furthermore, the integration of CNN and LSTM models represents a significant stride forward in predictive analytics for scaffold degradation. The LSTM model, especially when used in conjunction with VGG16 architecture for image feature extraction, shows superior performance over the CNN in all metrics mean squared error, mean absolute error, R-squared values, and accuracy. These metrics

indicate the LSTM's enhanced ability to capture the temporal sequences in the data, offering a more nuanced understanding of degradation patterns that can inform future scaffold designs.

Although the results show promise, the quality and variety of the training dataset significantly impact the performance of the models. The existing constraints in the quantity and diversity of data may impede the models' capacity to generalise across diverse scaffold architectures and materials. Therefore, it is recommended that future research should prioritise the expansion of the dataset by incorporating a wider variety of scaffold types and conditions to improve the accuracy and dependability of the models. Overall, the use of ML methods for the examination of scaffold degradation has created fresh opportunities for advancement in tissue engineering. By utilising the capabilities of these computational models, researchers can enhance their understanding of material behaviour, thereby advancing the field towards the creation of stronger and more efficient scaffolds for bone fracture implants. The increasing size of the dataset and the continuous improvement of the models have the potential to greatly transform scaffold design and performance evaluation. The prospects for bone tissue engineering are promising, as these computational technologies are at the forefront of improving patient outcomes.

In the upcoming Chapter 5, the focus will turn to using micro-CT imaging to measure scaffold porosity and monitor microstructural changes during degradation, providing a deeper insight into scaffold performance and enhancing the predictive modelling established in this chapter.

# Chapter 5: Predicting pore sizes and porosity in Micro-CT images of degraded injectable cements using CNN model

Sections of this Chapter have previously been presented in a scientific article published in Open Ceramics, Elsevier (2024): **I. Corvaglia, G. Al- Kharusi, F. Banche- Niclot, A. Manca, T. j. Lev ingstone, S. Little, S.Fiorilli, N. Dunne , C. Vitale-Brovaron "Comprehensive study through imaging techniques of the degradation of a resorbable calcium sulphate-based composite bone cement," vol. 17.**

## 5.1. Introduction

Degradation of injectable cements holds paramount importance in biomaterials and medical research. Properly monitoring the degradation process and comprehending its implications is essential for guaranteeing the long-term efficacy and safety of these materials in medical applications. While many studies, including a preceding chapter, relied on 2D microscopic images to gauge degradation, such an approach provides only a surface-level perspective of the samples [292]. The inherent limitations of 2D microscopic images underscore the importance of a deeper exploration, necessitating an examination of the internal intricacies of degraded cements. Truly understanding degradation requires an internal view of the scaffold microstructure. Micro-CT imaging emerges as a solution, offering a 3D visualisation of the entire scaffold. Micro-CT, or micro-computed tomography, revolutionised research capabilities, delivering high-resolution, non-destructive insights into internal structures [293]. The literature has numerous examples of the application of micro-CT for the detailed characterisation of biomaterials [294], [295] .

Micro-CT imaging is a reliable technique for producing a large amount of data, which is essential for the development of ML applications in biomaterials research. The detailed 3D data sets acquired from micro-CT scans provide a highly detailed perspective of the interior structures [296]. When combined with ML methods, these data sets can significantly improve the accuracy of predictive modelling for material behaviours. The extensive data sets associated with micro-CT imaging are highly suitable for ML as the effectiveness and precision of algorithms such as CNN are greatly enhanced with increased quality and quantity of accessible data [297], [298]. Designed to learn spatial hierarchies of features from images automatically and adaptively, CNN models are well suited for tasks such as predicting pore sizes and porosity [269].

The integration of micro-CT images into ML models enables intricate pattern identification and in-depth analysis that would be impractical with alone 2D pictures [294]. Furthermore, the combination of micro-CT data with automated deep learning pipelines demonstrates the ability to simplify the analysis of biomaterial degradation, enabling a more advanced comprehension of the underlying processes [299]. The integration of extensive data sets produced by micro-CT with the sophisticated analytical capabilities of ML models holds the potential to unveil novel boundaries in biomaterials research and medical applications [292], [296]. The combination of high-resolution imaging and computational intelligence has the potential to result in significant advancements in the prediction of material degradation, the enhancement of injectable cement design and safety, and ultimately the improvement of patient outcomes [298].

### 5.1.1. Chapter Aims

This chapter aims to fulfil Thesis Objective 4 by developing a sophisticated image analysis tool specifically designed to determine and quantify porosity and pore characteristics within scaffold

structures. Additionally, this chapter focuses on the implementation of a CNN model that uses micro-CT images to predict alterations in pore size within degraded cement scaffolds.

To successfully achieve this objective, the chapter will concentrate on the following specific aims:

(1) Design and create an image analysis tool capable of detecting pores and quantifying porosity in scaffold structures.

(2) compile a detailed dataset of micro-CT images capturing the morphological evolution of scaffold microstructures over time, specifically focusing on porosity and pore size variations.

(3) develop a CNN model optimised for the interpretation of micro-CT images to accurately detect changes in the pore size of cement scaffolds as they degrade.

(4) evaluate and refine the image analysis tool and CNN model to ensure high efficacy and accuracy, with the aim to surpass the performance of current methods used in scaffold pore sizes and porosity analysis.

## 5.2. Methodology

The cement samples and micro-CT images were fabricated and captured by our collaborators in Politecnico di Torino.

### 5.2.1. Sample fabrication

Injectable cement samples were fabricated by our collaborators in Torino using the methodology described in 4.3.1.4. The procedure involved creating a homogeneous paste by mixing a precisely measured powder phase with double-distilled water ($ddH_2O$), which acted as the liquid phase. The powder phase consisted of α-type calcium sulphate hemihydrate (α-CSH; GC Fujirock EP Classic, GC Europe, San Giuliano Milanese, Italy) for the matrix, as a resorbable matrix, along with commercially available $ZrO_2$ nanoparticles (particle size: 200-500 nm, Anhui Rencheng Technology CO, Hefei, China) and Sr-MBG particles containing 10 mol% of strontium (Si/Ca/Sr = 85/5/10) [30].

These components were added to enhance radiopacity, bioactive characteristics, and pro-osteogenic qualities. The Sr-MBG particles were synthesised by a base-catalysed sol-gel technique. The powder phase of the cement was composed of 75% CSH, 20% Sr-MBG, and 5% $ZrO_2$ using a volumetric formulation. The dry phase was mixed with $ddH_2O$ for 90 secs at 20 °C to simulate circumstances in an operating room and ensure full injection of the cement. The liquid-to-powder ratio is 0.40. The formulation was labelled as 75CSH-MBG, with pure CSH (100CSH) serving as the control under the name 100CSH. Following the mixing process, degradation studies were performed on cylindrical specimens with dimensions of 13 mm in diameter and 5 mm in height. The specimens were formed by forcing the paste through a 13 G needle into cylindrical moulds. The materials were left to solidify at 37 °C and 100% humidity for 24 h [30].

### 5.2.2. *In vitro* degradation test

The cement's degradation was evaluated according to ISO 10999-14 standard [30] using the protocol described in Section 4.2.2. Cylindrical cement samples were created and placed in a Tris-HCl solution with a concentration of 0.1 M and pH 7.4, using 1 g of material for every 20 mL of buffer. The samples were placed in an orbital shaker (Excella E24, Eppendorf, Hamburg, Germany) and agitated at 120 rpm at 37 °C for up to 28 days. Every week, the degradation buffer was fully replenished, and the samples from the given time point were gathered. The samples were washed twice with dd$H_2O$, dried in an oven at 70 °C for 2 h , and the residual weight percentage of each sample was calculated. The residual weight percentage is calculated using the formula:

$$residual\ weight\ (\%) = \left(1 - \frac{w_0 - w_t}{w_0}\right) \times\ 100$$

**Equation 5.1:** Residual weight percentage

where $w_0$ is the initial weight of the sample (g) and $w_t$ is the weight recorded in the specific time point $t$ (g) [30].

### 5.2.3. Micro-CT images

The microarchitecture of the cement was thoroughly analyzed using a high-resolution X-ray Micro-CT Skyscan 1272 scanner (Skyscan; Bruker, Ettlingen, Germany), which allowed for detailed visualization and quantification of the internal structure of the samples at various stages of degradation. The samples were meticulously prepared and scanned at a resolution of 7 µm per pixel, ensuring that even the smallest features within the cement's microstructure could be accurately captured. The scanning process was carried out under controlled conditions, with an applied voltage of 100 kV and a current of 100 µA, optimizing the contrast and sharpness of the images. A 0.11 mm thick copper filter was employed to enhance image quality by reducing beam hardening effects, which could otherwise distort the reconstructed images. The rotation increment was finely tuned to 0.3° to allow for the acquisition of a high number of projections, ensuring that the 3D reconstructions were highly accurate and detailed. These high-resolution scans provided critical insights into the microstructural changes occurring within the cement over time, contributing to a better understanding of its degradation behaviour and mechanical properties.

### 5.2.4. Pore detection and porosity measurements using image analysis tool

An image analysis function was developed using OpenCV (Python 3.9) to process images obtained from micro-CT, as schematised in **Figure 5.1**A. The initial step involved collecting the micro-CT

reconstructed images (**Figure 5.1**B). These images were then converted to grayscale and resized to one-fourth of their original size while maintaining their aspect ratio. This resizing was done to eliminate variations in image size that could potentially affect the model's object detection accuracy. Subsequently, a Gaussian filter with a kernel size of 3x3 was applied to reduce noise and enhance the image edges. To convert the images into binary form, Otsu's thresholding method was employed. This method automatically determines an optimal threshold value that separates the pixel intensity histogram into two classes, maximising the variance between them. As a result, the threshold value varies dynamically for each image based on its pixel intensity distribution (**Figure 5.1**C, left). After generating the binary images, morphological operations such as dilation and erosion were applied to remove noise from the object boundaries. The edges of these features were detected using Canny edge detection with threshold values of 1 and 2 (**Figure 5.1**C, right). Finally, the dimensions of each pore were calculated using contour detection, which measures the distance between pore boundaries. Only contours representing pore areas greater than 800 square pixels (adjusted based on the resized image) were considered in the analysis. Additionally, the code identifies the largest pore, highlights it in the image, and calculates the average pore size. The area of each pore was determined based on the detected contours, and this data was used to calculate the porosity.

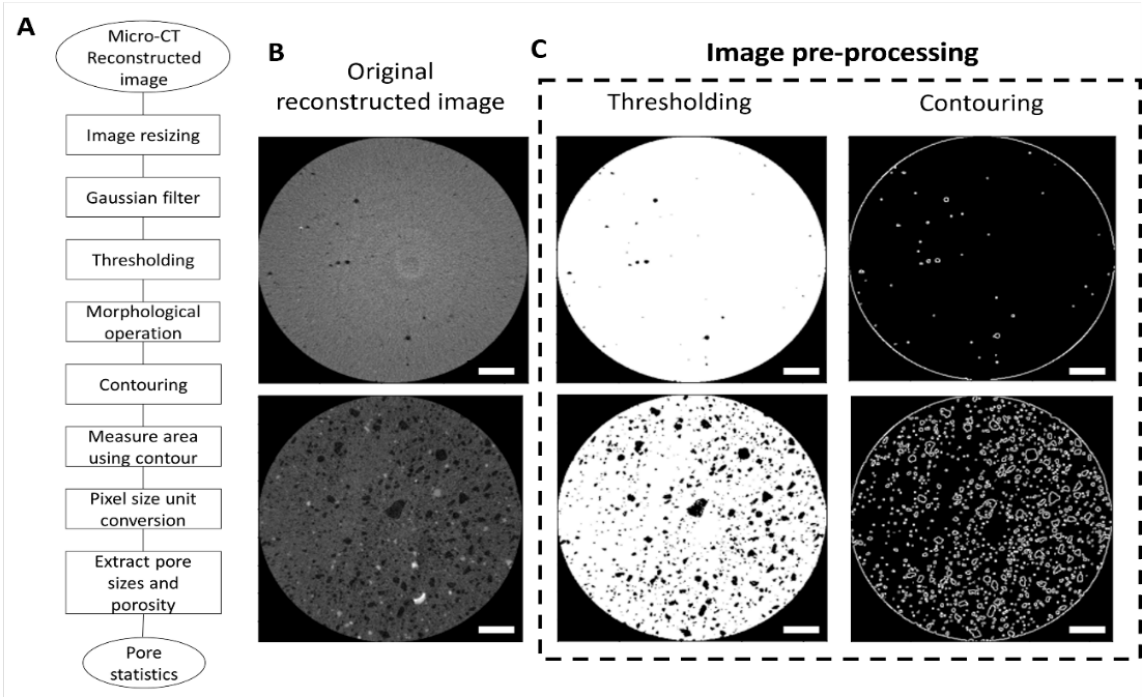



**Figure 5.1:** A] Workflow of the pore detection algorithm coded in Phyton 3.9. B] Raw images of the reconstructed 100CSH (top) and 75CSH-MBG (bottom) formulations. C] Pre-processing methods (thresholding, contouring) applied to the reconstructed images. Scale bar represents 1 mm.

#### *5.2.4.1. Datasets*

The quantitative analysis of the study was based on a collection of about 5,222 micro-CT images that were taken over the course of 28 days. The dataset was captured using a micro-CT scanner and documents the comprehensive physicochemical degradation processes experienced by injectable cement samples in a controlled environment. The high-resolution photographs provide a detailed visual record of the time-dependent morphological changes in the cement structure. Every micro-CT image presents an in-depth cross-sectional representation of the cement's microarchitecture, showing important details including pore distribution, size, and interconnectivity within the cement matrix.

#### *5.2.4.2. Labelling and train-test splitting*

Each image represents the microstructure of the cement and is accompanied by associated metadata, which is read from a CSV file. The metadata serves as labels for the image dataset, providing ground truth values against which the model's predictions are compared. One of the initial steps involves organising the data into training, validation, and testing datasets. The validation dataset is used to fine-tune the model parameters and hyperparameters without exposing the model to the test data. The division is done as follows:

- 80% (around 4,178 images) of the data was utilised for training, ensuring that the model has a comprehensive understanding of the underlying data distribution.
- 10% (approximately 522 images) was reserved for validation. This subset aids in the model's hyperparameter tuning, providing an unbiased evaluation of the model's performance during the training phase.
- The remaining 10% (also about 522 images) was set aside for testing, serving as a completely unseen dataset for the final evaluation of the model's predictive capabilities.

This ensures that the model was trained on a large portion of the data while also having separate sets to fine-tune and evaluate its performance.

### 5.2.5. CNN model to predict pore sizes and porosity

#### *5.2.5.1. CNN architecture*

The PoreNet, a deep Convolutional Neural Network (CNN) architecture **Table 5.1**, was specifically designed to predict pore sizes and porosity from micro-CT images. Each layer within this architecture serves a unique role, playing a pivotal part in the extraction of hierarchical features from the input data.

Convolutional Layers:

The initial layers in this model consist of two convolutional layers (`'conv1'` and `'conv2'`). These are the workhorses of the CNN, responsible for the extraction of local features from the input image. `'conv1'` Layer: The first convolutional layer (`'conv1'`) has a single input channel (as the images are grayscale) and 16 output channels, utilising a 3x3 kernel size. The padding is set to 1 to maintain the spatial dimensions of the image post convolution. This layer scans the image with its kernels and identifies local patterns, which can be basic edges or textures. Building on the features identified by conv1, the second convolutional layer (`'conv2'`) takes the 16 output channels from conv1 and extends it to 32 channels. It continues the pattern detection process by identifying more complex features and combinations of the simpler patterns recognised by the preceding layer.

Pooling Layer:

Following each convolutional layer, a max-pooling operation (`'pool'`) is applied using a 2x2 kernel. This step reduces the spatial dimensions of the feature maps by half, ensuring computational efficiency and allowing the model to gain a more abstract representation of the features. It is a standard technique to prevent overfitting by providing an abstracted form of the representation.

Fully Connected Layers

After the convolutional and pooling layers, the data flows through two fully connected layers `'fc1'` and `'fc2'`). The `'fc1'` layer takes the flattened output from the previous layers (32 channels of 56x56 feature maps) and reduces the dimensionality to 128 nodes. Here, global patterns in the image are identified, combining the local features learned by the convolutional layers. The subsequent and final layer, `'fc2'`, narrows down the 128 nodes to 3 output nodes. Each of these nodes corresponds to a specific prediction: one for each of the two pore sizes and one for porosity.

Activation Functions and Data Transformation

Relu (Rectified Linear Unit) activation functions are incorporated post each convolutional and the first fully connected layer. These introduce non-linearity into the model, enabling it to learn from the error and make adjustments, which is essential for learning complex patterns. Additionally, before inputting the micro-CT images into the model, they undergo a series of transformations. These images are resized to a uniform dimension of 224x224 pixels, ensuring consistency in input data. Subsequently, they are converted to tensors and normalised, making the training process more efficient and stable.

**Table 5.1:** PoreNet CNN model architecture summary

| Model Parameters | Parameter Values | Description |
|---|---|---|
| Input Image | 224 x 224 x1 | Size of the input image |
| Output size | 3 | Number of output values |
| Conv1 | Kernel Size: 3, Stride: 1, Padding: 1 | Convolutional layer 1 |
| Pool1 | Kernel Size: 2, Stride: 2 | Max pooling layer 1 |
| Conv2 | Kernel Size: 3, Stride: 1, Padding: 1 | Convolutional layer 2 |
| Flatten | - | Flatten layer |
| FC1 | Input feature: (32*56*56), output feature: 128 | Fully connected layer 1 |
| FC2 | Input feature:128, Output feature: 3 | Fully connected layer 2 (Output layer) |

#### *5.1.1.1. CNN training and hyperparameter selection*

Hyperparameters are critical values that influence the training process but are not updated during training. Proper selection of these values can significantly affect the performance of the model. The model undergoes training using the training dataset. For each epoch (an epoch is one full forward and backward pass of all the training examples), the model's predictions are compared to the actual outcomes, and the error is back-propagated through the model to adjust the model's internal parameters. This iterative process aims to minimise the Mean Squared Error (MSE), which quantifies the difference between the predicted and actual values. The specific implementation is summarised in **Table 5.2**:

**Table 5.2:** Summarised hyperparameters

| Hyperparameters | Value | Description |
|---|---|---|
| Learning rate | 0.001 | Number of samples propagated through the network at once. |
| Batch size | 4 | Number of samples propagated through the network at once. |
| Number of epochs | 20 | Number of times the entire dataset is passed through the neural network. |
| Optimiser | Adam | Optimisation algorithm used to minimise the loss function. Combines benefits of AdaGrad and RMSProp. |

#### *5.1.1.2. Performance*

The performance evaluation of the model is multi-faceted and relies on various metrics to understand both its efficacy during training and its ultimate performance on unseen test data. During the training phase, the model's performance is primarily assessed using the MSE equation that was presented in chapter 4 section 4.3 (**Equation 4.4**).

For each training epoch, this loss is computed, giving an insight into how well the model is fitting the training data over time. Additionally, the loss on a validation set is tracked, ensuring that the model generalises well and is not overfitting. Post-training, the model's performance on the test dataset is gauged using three primary metrics: Mean Absolute Error (MAE), R-squared ($R^2$) and a custom "accuracy" metric for regression tasks. The MAE, calculated for various outputs like average pore diameter, biggest pore diameter, and porosity, gives an absolute difference between predicted and actual values. It is defined as:

$$MAE = \frac{1}{N}\sum_{i=1}^{N} \left|Y_i - \widehat{Y_i}\right|$$

**Equation 5.2:** Mean Absolute Error equation.

The $R^2$ score, also computed for each output, provides a measure of how well the predicted values explain the variance in the true values. It ranges from 0 to 1, with 1 indicating perfect predictions. Finally, the custom regression "accuracy" is calculated. It is a unique metric that defines a prediction as "accurate" if the difference between the predicted and true value is within a certain threshold (in this case, 10% of the true value). This offers a practical perspective on how often the model's predictions are reasonably close to the actual values. Together, these metrics provide a comprehensive overview of the model's performance, capturing both the magnitude of errors and the model's ability to capture the underlying patterns in the data.

## 5.3. Results and Discussion

### 5.3.1. Image analysis tool

#### *5.3.1.1. Porosity measurements*

**Figure 5.2**A and **Figure 5.2**B present the evaluation of the total porosity over time for the 100CSH and 75CSH-MBG formulations, respectively, using the image analysis tool. Both formulations exhibited a slight increase in the total porosity over time. The as prepared 100CSH formulation had an estimated porosity of approximately 2%, which increased to about 3% by Day 28 of immersion in the degradation buffer. Similarly, the as-prepared 75CSH-MBG formulation had a porosity of around 15%, which increased to roughly 18% by Day 28.

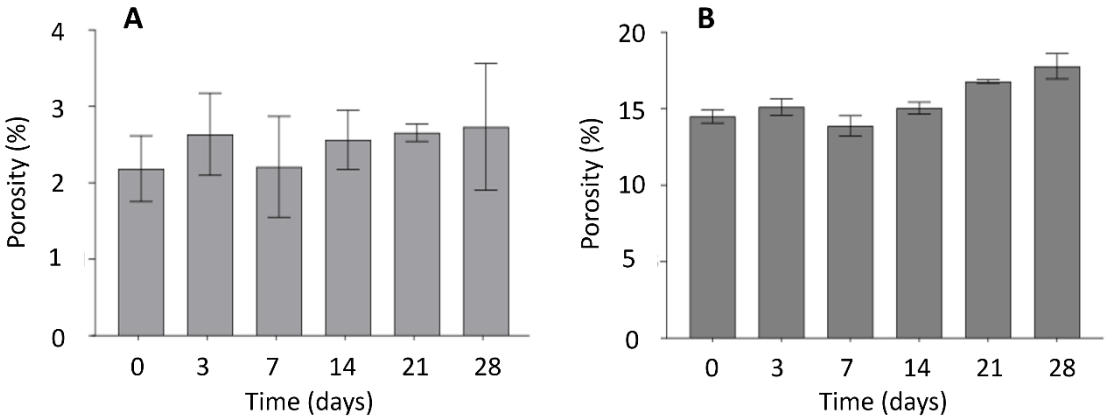



**Figure 5.2:** Microstructural parameters obtained using the image analysis tool. A] Porosity percentage of 100CSH formulation over time. B] Porosity percentage of 75CSH-MBG formulation over time.

The study examines the changes in porosity of 100CSH and 75CSH-MBG formulations using micro- CT image analysis for a duration of 28 days. The results demonstrate subtle modifications that suggest material degradation. The marginal rise in overall porosity corresponds to the anticipated response of cementitious substances in a deteriorating environment. The rise in porosity in the 75CSH-MBG formulation from 15% to around 18% indicates a heightened interaction with the immersion environment, maybe due to the nature of the material or the reactivity of the microglass beads. The consistent pore size distribution observed in the 100CSH formulation, except for the appearance of bigger pores after two weeks, prompts inquiries regarding the degradation kinetics and its homogeneity throughout the sample matrix. The 100CSH formulation has a rather stable microstructure, suggesting a regulated degradation process that is advantageous for applications that necessitate progressive bio-resorption [30].

On the other hand, the formulation of 75CSH-MBG exhibits a larger initial porosity and subsequent increase, which can be beneficial in applications that need quicker integration of the material with surrounding tissues. Nevertheless, the identification of progressively larger pores may indicate uneven degradation, which could result in varied mechanical characteristics within the substance.

#### *5.1.1.1. Pore distribution*

The image analysis tool was also used to assess pore size distribution at different time points. **Figure 5.3** and **Figure 5.4** present the pore size distribution for the 100CSH and 75CSH-MBG formulations, respectively. The as prepared 100CSH samples exhibited small pores (below 100 µm), with the majority being between 50-100 µm in size. The pore size distribution remained relatively unchanged over time, except for the increase in the number of larger pores (greater than 150 µm in diameter) at Day 14.

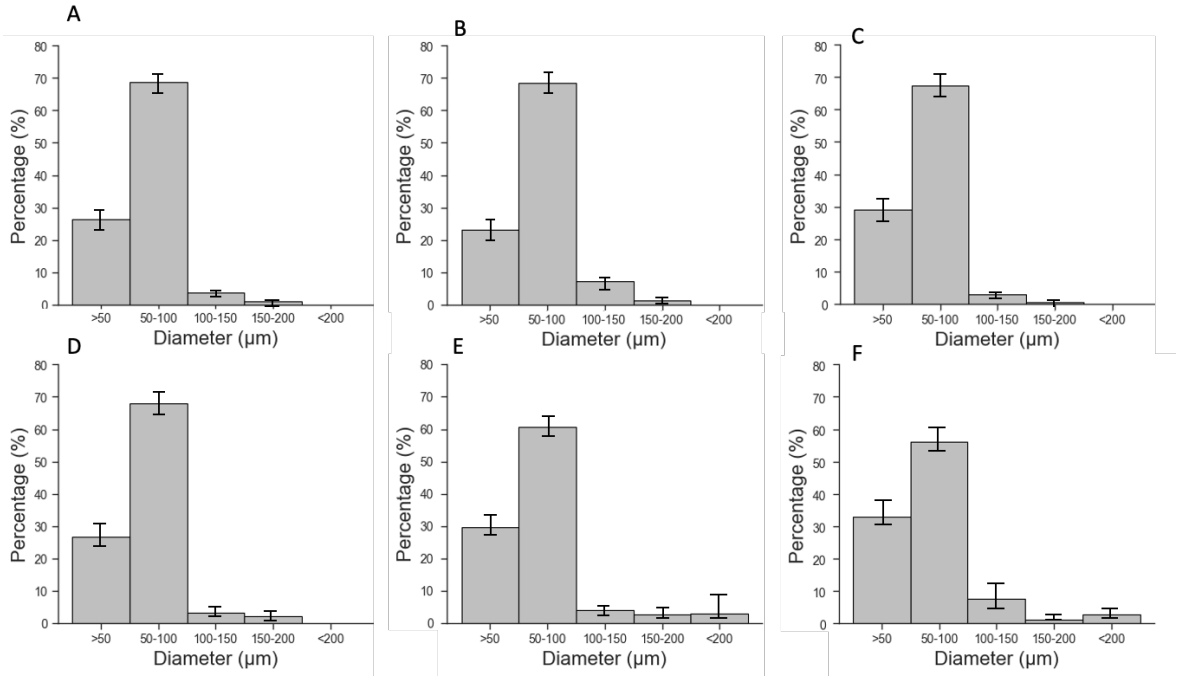



**Figure 5.3:** Pore size distribution over time for 100CSH formulation analysed using image analysis tool. A] Pore size distribution of the cement before degradation testing. B] Pore size distribution at Day 3. C] Pore size distribution at Day 7. D] Pore size distribution at Day 14. E] Pore size distribution at Day 21. F] Pore size distribution at Day 28.

In contrast, the as-prepared 75CSH-MBG formulation had a considerable portion of pores below 50 µm in diameter (constituting over 70% of all detected pores), as shown in **Figure 5.4**. Only a few pores exceeding 100 µm in diameter were observed in the as-prepared samples. As the degradation progressed, the pore size distribution did not undergo substantial changes, with many detected pores

remaining below 50 µm in diameter (slightly less than 60% after Day 28). Like the 100CSH formulation, an increase in the number of larger pores (greater than 100 µm in diameter) was detected by Day 14.

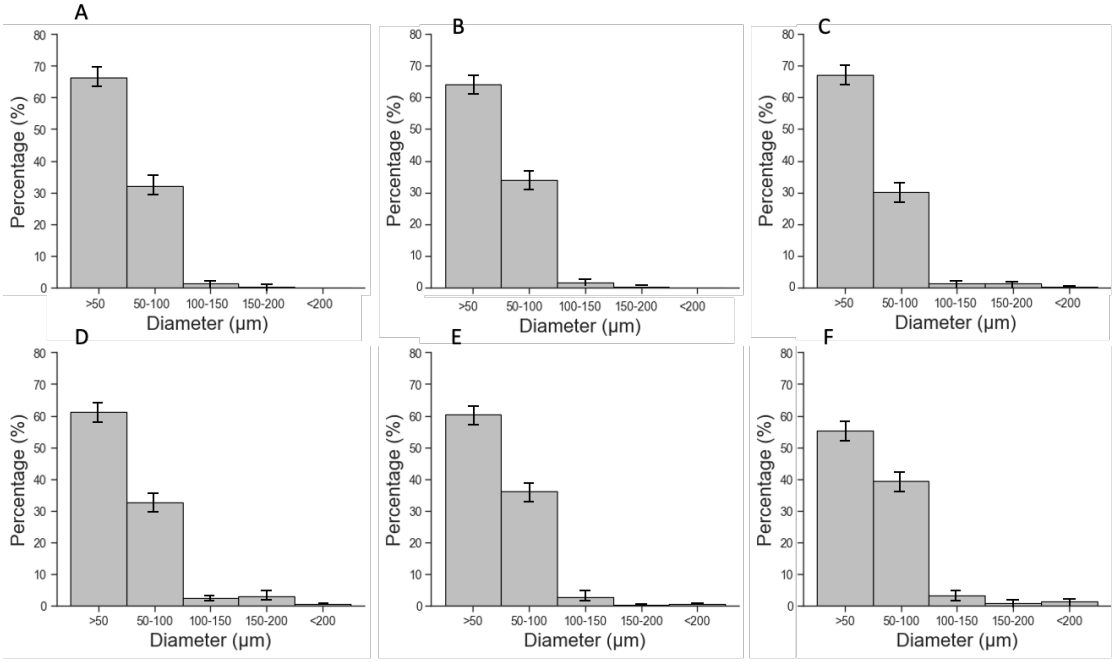



**Figure 5.4:** Pore size distribution over time for 75CSH-MBG formulation using image analysis tool. A: Pore size distribution of the cement before degradation test. B: Pore size distribution at Day 3. C: Pore size distribution at Day 7. D: Pore size distribution at Day 14. E: Pore size distribution at Day 21. F: Pore size distribution at Day 28.

### 5.3.2. CNN evaluation

The model's learning progression over the course of the 20 epochs is insightfully visualised in the loss graph (**Figure 5.5**). The graph shows how the model adjusts its internal parameters in response to the data it is exposed to (**Figure 5.5**), with each epoch representing a full run through the training data. Higher loss numbers at first may be seen, indicating significant differences between the model's predictions and the actual results. This is to be expected as the model's initial predictions are mostly arbitrary because it starts off with random or uninitialised parameters. However, a declining trend in the loss is anticipated as the epochs go on, showing that the model is evolving and that its forecasts are steadily becoming more accurate.

A steady decrease in the loss indicates that the model is successfully picking up new information from the training set of data. However, it is crucial to pay close attention to the decline's gradient. It is frequently a sign that the model has reached its optimisation limit with the given data and architecture when the initial epochs decline quickly and then plateau. On the other hand, any sudden

oscillations or spikes in the loss could be a sign of problems like an excessive learning rate or possible data anomalies. Comparing the loss graph with the validation loss is also crucial. As the number of epochs increases, a significant divergence between training and validation loss may indicate overfitting, in which the model excels on the training data but struggles on fresh, untried data.

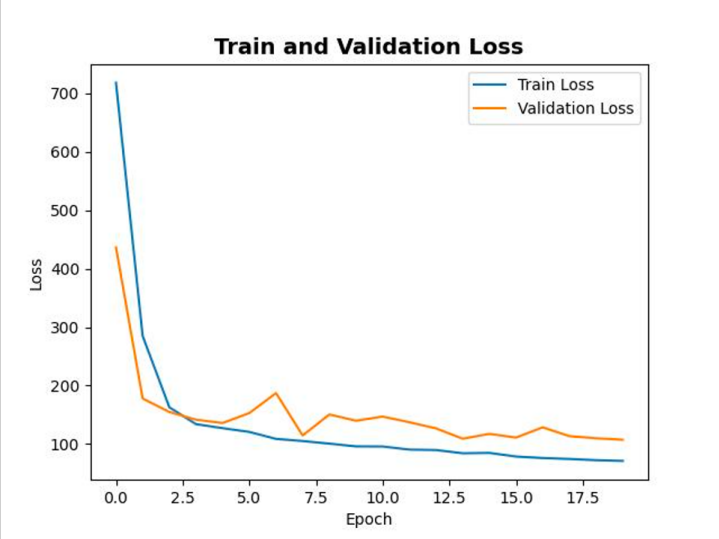



**Figure 5.5:** The CNN model performance during training using mean absolute error as the evaluation metric. The blue and orange lines depict the training and validation errors, respectively.

The Mean Absolute Error (MAE) gives an insight into the average magnitude of the errors between predicted and observed outcomes. For the average pore diameter, the MAE is recorded at 2.54%, suggesting that, on average, the model's predictions are off by this value. In terms of the biggest pore diameter, the error is considerably larger MAE at 13.16 %. This could suggest that predicting the maximum pore size is inherently more challenging or that there are certain outliers in the dataset that make this task more complex. In contrast, the MAE for porosity stands MAE at 3.33%, indicating a moderate level of prediction accuracy (**Table 5.3**).

The $R^2$ score, which measures the percentage of the dependent variable's variance that can be explained by the model's independent variables, is another crucial metric. The $R^2$ value is commendably high for the average pore diameter, 0.89, indicating that the model can account for about 88.8% of the variability, which is a sign of a good model fit. With a lower $R^2$ value of 0.69 for the largest pore diameter, the model only captures about 68.8% of the variability. The model may not be suited for forecasting porosity, or there may be other external factors or data anomalies affecting this specific outcome, as indicated by the negative $R^2$ score for porosity at 0.62.

Lastly, the model exhibits high level of accuracy performance for average pore diameter and porosity, with accuracies of 95.9% and 99.8%, respectively, while taking into account the test accuracy within a 10% margin. Due to the model's high accuracy, it can be assumed that its

predictions for these two parameters are often within 10% of the actual values. The accuracy lowers to 70.5% at the largest pore diameter, however, showing the need to improve the model or perhaps reevaluate the features for this particular prediction.

**Table 5.3:** Model performance metric summery

| | Mean absolute error [%] | Accuracy | $R^2$ |
|---|---|---|---|
| Average pore size | 2.54 | 0.95 | 0.89 |
| Porosity | 3.33 | 0.99 | 0.62 |

The CNN model exhibits commendable prediction capability for average pore sizes, as indicated by the mean absolute error and $R^2$ score. However, it reveals a discrepancy in accurately predicting the biggest pore sizes. This discrepancy may be attributed to the inherent challenge in accurately measuring the outliers of a distribution or could indicate the irregular occurrence of greater pore development in these materials. The negative $R^2$ score for porosity predictions may suggest that the model's learning approach oversimplifies complicated physiological processes or fails to adequately reflect influential variables in the dataset.

The CNN model, one of the most powerful ML algorithms, has proven to be a vital tool for assessing and forecasting the microstructure of deteriorated scaffolds. This is because it combines the use of modern imaging technologies. The results demonstrate the precision and effectiveness of the Python 3.9-coded image analysis tool. It shed insight on the subtle rise in porosity over time and the emergence of bigger pores during degradation by revealing subtle details regarding porosity and pore distribution. These insights may not be as easily and precisely ascertained using conventional techniques, but they are essential for comprehending scaffold behaviour.

The CNN model's examination highlighted its potential for predicting complex microstructural aspects further. While there were certain areas where the performance was remarkable, such as the precision in estimating average pore diameter and porosity, there were also some areas where improvement was needed. The loss graph across 20 epochs, which shows the model's adaptability and learning progression, emphasises the dynamic nature of ML in raising prediction accuracy. The difficulties encountered in forecasting the largest pore diameter, however, point to the dataset's inherent complexity or the need for more precise model topologies.

Alqahtani *et al.* employed CNN to predict key physical properties such as porosity, specific surface area, and average pore size based on micro-CT images. The CNN model demonstrated high accuracy, particularly in predicting porosity with a relative error of less than 3% using binary images. The relaive error matches the CNN performance in predicting pore sizes and porosity of injectable cements. This research highlights the effectiveness of CNNs in accurately characterizing porous media, providing a valuable comparison point for the performance of similar models in predicting microstructural features like porosity and pore sizes in biodegradable scaffolds. The study's findings support the robustness and applicability of CNNs in complex image analysis tasks related to material science.

## 5.4. Conclusion

In this pivotal chapter, the completion of Objective 4 has been effectively represented, marking a significant milestone in tissue engineering. The successful development and application of an automated image analysis tool, custom-made for the task of detecting pore sizes and porosity within scaffolds, signifies a considerable leap forward. Coupled with a CNN model, this tool has utilised micro-CT images to predict changes in pore sizes in degraded cement scaffolds.

In summary, the application of an automated image analysis tool for the assessment of pore size distribution in cement materials proved to be highly effective. Notably, the tool demonstrated superior accuracy in pore detection, successfully identifying pore structures that manual measurement methods might overlook. This increased sensitivity is particularly evident in the heightened detection rate of smaller pores, which manual methods may not consistently highlight due to their limited sensitivity and potential for human error. Furthermore, the automated method showed an advanced capability in recording a higher count of pores, suggesting a more comprehensive analysis of the pore distribution within the cement matrix. The use of Python-based image analysis tools, with their high sensitivity to detect every black spot as a pore, contributed to the accurate quantification of the pore sizes.

The utilisation of CNN to evaluate the pore size and porosity of degrading cement samples via micro-CT image analysis represents an important advancement in the field of material science research. CNNs' capability to analyse and derive insights from intricate datasets shows great potential for improving our comprehension of material degradation mechanisms. The models have shown their capacity to distinguish small differences in the microstructures of biomaterials, which helps forecast their mechanical behaviour and lifespan more accurately.

Although CNNs have strong analytical powers, they have limits when used in the study of biomaterial degradation. The main limitation is the dependence on the quality and variety of the dataset. CNN need diverse and abundant data for efficient training. Any absence of

representativeness in the data may result in biased or imprecise models. For cement degradation, the micro-CT images should cover various degradation phases and pore distributions to let the CNN perform effectively with new data. Another limitation is the potential for overfitting, where the model performs exceptionally well on the training data but fails to predict accurately on unseen data. This challenge necessitates careful hyperparameter tuning and validation strategies to ensure the model's robustness. Furthermore, CNNs may struggle to predict outliers within the dataset, such as the largest pore sizes, which can be essential for determining the structural integrity of the cement.

In conclusion, combining image tools with ML models, particularly for micro-CT images, is a promising way for scientists to learn more about the subtleties of microstructural changes during scaffold degradation. Such integrative techniques not only speed up the research procedure but also improve the accuracy and breadth of the conclusions drawn. Adopting this strategy can be crucial in expediting discoveries and breakthroughs in the fields of biomaterials and tissue engineering research.

# Chapter 6: Overall thesis discussion, conclusions and future work

## 6.1. Overall discussion

The overall aim of this thesis was to apply DoE and ML approaches for the optimisation of bioprinted scaffolds for bone tissue engineering applications, focusing specifically on the measurement of scaffold properties including degradation rate, pore size and porosity. In Chapter 3, we thoroughly interrogated the parameters that influence the printability of collagen-based inks, thereby addressing Objective 1. The modification and evaluation conducted through DoE were pivotal for optimising their degradation, mechanical, and rheological properties. The study showed interaction between collagen concentrations, HA incorporation, and crosslinking conditions. By employing a RSM it has been determined that the mechanical properties of the scaffolds may be greatly improved by optimising the collagen content and crosslinking conditions with a specific concentration of HA. The DoE findings indicated that an optimal ratio of 4 %(w/v) collagen to 0.076 %(w/v) HA resulted in favourable scaffold properties and crosslinked with tannic acid for 60 min at a concentration of 5 %(w/v) . This formulation demonstrated an ideal balance, displaying regulated degradation patterns that are suitable for tissue engineering applications where transitory mechanical strength is essential for tissue regeneration.

The optimised blend demonstrated a modulus of elasticity of 1.931±0.05 MPa, indicating its ability to provide mechanical support within the predicted range for bone tissue scaffolds at a physiological level. The tensile tests proved the material's robustness by establishing a stress-strain relationship that closely aligns with the existing literature on effective scaffold compositions for bone regeneration. The distribution of pore sizes is a crucial characteristic of scaffolds that plays a significant role in facilitating efficient cell migration and nutrient diffusion. The results of DoE analysis revealed a consistent average pore size of 0.537±1.24 mm² across the best scaffolds. These factors collectively informed the viscoelastic behaviour of the inks, which in turn dictated the scaffolds' structural and functional integrities. Notably, the rheological analysis provided insights into the shear-thinning behaviour of the bioinks, crucial for their extrudability and shape fidelity post-printing. By systematically varying and examining these parameters, the research advanced the understanding of the material science underpinning scaffold design, offering a foundation for more predictive and controllable 3D bioprinting processes.

Chapter 4 extended the thesis narrative by tackling Objectives 2 and 3. It took a leap from the manual, time-intensive measurement of scaffold degradation rates to an automated, image analysis-driven method. The work done in this chapter compared various ML models, laying out a clear path toward the most effective prediction of scaffold degradation using a combination of image-derived and numerical data. By constructing an interface platform to predict scaffold degradation, the chapter brought to the fore the transformative potential of integrating computational tools into TE. The platform showcased the feasibility of employing ML for the proactive adjustment of scaffold

properties, paving the way for a new era in scaffold design where proactive measures could ensure longevity and performance custom-made to specific biomedical applications.

Chapter 5 fulfilled Objective 4 by creating an image analysis tool adept at detecting changes in pore size and porosity within scaffolds, using the power of CNNs and Micro-CT images. This chapter underscored the significance of pore architecture in influencing scaffold functionality and, ultimately, the success of bone regeneration strategies. The implementation of CNNs facilitated the unravelling of complex relationships between pore characteristics and scaffold degradation, signifying a major stride in computational TE. The precision of prediction models in this chapter was a testament to the sophisticated algorithmic structures of CNNs, which could identify subtle shifts in pore morphology over time, allowing the scaffold's degradation properties to be predicted. This achievement not only illustrates the thesis's contribution to the field's methodological arsenal but also exemplifies a successful marriage of ML with imaging techniques to address longstanding challenges in scaffold characterisation. The comprehensive synthesis of these chapters highlights the transformative journey from empirical experimentation to predictive modelling. Each chapter incrementally builds upon the last, laying down a mosaic of insights that address the critical gaps in the literature. The DoE provided a systematic and robust framework for experimentation, while ML offered the necessary computational prowess to handle the complexity of image and numerical data.

While DoE has proved invaluable in systematically evaluating and optimising the printability of collagen-based inks and scaffolds, its application is not without limitations. One of the primary constraints is the extensive data requirements. DoE often necessitates a considerable number of experiments to ensure the robustness of the findings, which can be resource-intensive in terms of materials, time, and labour. Furthermore, DoE typically demands a prior assumption about the experimental domain and the nature of the interactions between variables, which may not always encapsulate the complexities of scaffold behaviour. In the context of scaffold property characterisation, the iterative nature of DoE can lead to a protracted experimental phase before arriving at the desired outcomes. Each experimental run requires careful planning, execution, and analysis, which can be a time-consuming process. Moreover, in cases where the parameter space is vast, DoE might become inefficient, leading to an exhaustive search through the experimental conditions rather than a targeted approach.

ML, on the other hand, can offer a paradigm shift in this regard. ML's predictive capabilities provide an attractive alternative to the traditional DoE constraints by enabling the assessment of scaffold properties before the empirical phase. Through the analysis of existing data, ML algorithms can forecast how a scaffold might behave under various conditions. This predictive modelling can greatly reduce the number of physical experiments required by informing the researcher of the most promising conditions to test, leading to a more efficient use of resources.

For instance, CNN models used in Chapter 5 did not simply analyse Micro-CT images post-experimentation; they offered a prospective view, predicting the structural evolution of pore sizes over time. Such predictions have the potential to shape pre-experimental planning significantly, reducing the trial-and-error approach often associated with scaffold optimisation.

## 6.2. Concluding Remarks

This thesis was to employ both DoE and ML to enhance the fabrication and predictive understanding of bioprinted scaffolds for bone tissue engineering. Each chapter methodically tackled a distinct objective, building towards a comprehensive framework for scaffold optimisation and analysis. The initial chapters laid the groundwork with a focused DoE study. Objective 1 was achieved by the creation of a customised collagen-HA scaffold designed for the purpose of bone regeneration. The application of systematic optimisation using DoE has established a robust experimental basis for scaffold design, with a specific emphasis on printability, degradation, and mechanical qualities. The DoE study did not just optimise the scaffold's empirical attributes but also generated a wealth of numerical and image data. This dataset formed the backbone of the subsequent ML applications.

In a progression from the foundational work, the thesis moved to the automation of scaffold degradation measurements in Chapter 4. Objective 2 focused on enhancing the accuracy and effectiveness of measuring the degradation of scaffolds. The utilisation of image analysis technologies facilitated this measurement, switching from manual techniques to advanced, ML-driven forecasts. This facilitated the comparative examination of ML models, utilising both image-derived and numerical data to forecast scaffold degradation. The aim in this chapter to replace the labour-intensive manual methods with automated image analysis tools; and secondly, to apply various ML models to predict scaffold degradation. However, the study in Chapter 4 is limited by the type of images available, particularly in quantifying the internal structural changes during scaffold degradation. This highlighted an essential need for advanced imaging techniques to obtain a more comprehensive understanding of these changes. Therefore, Chapter 5 introduced the application of Micro-CT imaging, a technique capable of revealing the microstructural evolution within degrading scaffolds. This technology not only offered a solution to the limitations encountered but also presented a method to circumvent the issue of data type, by providing a voluminous and detailed dataset for the refinement and validation of ML algorithms.

Objective 4 was realised with the development of an image analysis tool and the implementation of a CNN model in Chapter 5. Future perspectives

Future research should focus on expanding the datasets available for ML modelling. Richer datasets will allow for the creation of more accurate and generalisable models. Additionally, the development of real-time ML algorithms that can offer in-process adjustments during the bioprinting phase can also be explored. These algorithms could potentially integrate with bioprinting hardware, creating a

feedback loop that provides real-time correction to the printing parameters. Advanced ML-driven bioprinting technology have the potential to completely transform personalised medicine in a clinical context. The capability to continuously monitor and modify printing parameters in real-time guarantees that the bioprinted scaffolds conform accurately to the specified design standards, specifically customised to the individual patient's unique anatomy and tissue needs. The importance of precision cannot be overstated, as it has the potential to greatly enhance the functionality, fit, and integration of the implanted scaffolds, hence resulting in better results in regenerative therapies. Furthermore, this technique holds the potential to simplify the process of moving from the experimental stage to practical clinical implementations, providing optimism for more effective and successful approaches to tissue repair and regeneration.

Another promising direction is the integration of ML models with multiscale simulations. Such models can combine the molecular interactions within the bioink material with macro-level scaffold behaviour to provide a holistic view of scaffold performance, spanning from the initial material selection to the final tissue regeneration outcome. Ultimately, extending the application of ML to personalised medicine would represent a significant leap forward. Tailoring scaffold designs using patient-specific data would optimise therapeutic outcomes, bringing the field closer to realising the full promise of regenerative medicine.

# References


[1] T. Sozen, L. Ozisik, and N. Calik Basaran, “An overview and management of osteoporosis,” *Eur J Rheumatol*, vol. 4, no. 1, pp. 46–56, Mar. 2017, doi: 10.5152/eurjrheum.2016.048.

[2] Y. Li, S. K. Chen, L. Li, L. Qin, X. L. Wang, and Y. X. Lai, “Bone defect animal models for testing efficacy of bone substitute biomaterials,” *J Orthop Translat*, vol. 3, no. 3, pp. 95–104, 2015, doi: 10.1016/j.jot.2015.05.002.

[3] D. L. and H. Z. Hélder A. Santos, “Droplet-based microfluidics for cell encapsulation and delivery,” in *Microfluidics for Pharmaceutical Applications*, Hangzhou: William Andrew, 2019, ch. Chapter 11, pp. 307–335. doi: https://doi.org/10.1016/B978-0-12-812659-2.00011-9.

[4] L. Saunders and P. X. Ma, “Self-Healing Supramolecular Hydrogels for Tissue Engineering Applications,” *Macromol Biosci*, vol. 19, no. 1, pp. 1–11, 2019, doi: 10.1002/mabi.201800313.

[5] I. Goldfracht *et al.*, “Engineered heart tissue models from hiPSC-derived cardiomyocytes and cardiac ECM for disease modeling and drug testing applications,” *Acta Biomater*, vol. 92, pp. 145–159, 2019, doi: 10.1016/j.actbio.2019.05.016.

[6] D. N. Heo, M. Hospodiuk, and I. T. Ozbolat, “Synergistic interplay between human MSCs and HUVECs in 3D spheroids laden in collagen/fibrin hydrogels for bone tissue engineering,” *Acta Biomater*, vol. 95, pp. 348–356, 2019, doi: 10.1016/j.actbio.2019.02.046.

[7] A. R. Amini, C. T. Laurencin, and S. P. Nukavarapu, “Bone tissue engineering: Recent advances and challenges,” *Crit Rev Biomed Eng*, vol. 40, no. 5, pp. 363–408, 2012, doi: 10.1615/CritRevBiomedEng.v40.i5.10.

[8] F. J. O’Brien, “Biomaterials & scaffolds for tissue engineering,” *Materials Today*, vol. 14, no. 3, pp. 88–95, 2011, doi: 10.1016/S1369-7021(11)70058-X.

[9] S. Bose, S. Vahabzadeh, and A. Bandyopadhyay, “Bone tissue engineering using 3D printing,” *Materials Today*, vol. 16, no. 12, pp. 496–504, 2013, doi: 10.1016/j.mattod.2013.11.017.

[10] S. J. Hollister, “Porous scaffold design for tissue engineering,” *Nat Mater*, vol. 4, no. 7, pp. 518–524, 2005, doi: 10.1038/nmat1421.

[11] K. Rezwan, Q. Z. Chen, J. J. Blaker, and A. R. Boccaccini, “Biodegradable and bioactive porous polymer/inorganic composite scaffolds for bone tissue engineering,” *Biomaterials*, vol. 27, no. 18, pp. 3413–3431, 2006, doi: 10.1016/j.biomaterials.2006.01.039.

[12] D. C. Montgomery, *Design and Analysis of Experiments*, Eighth. New Jersey: John Wiley & Sons, Incorporated, 2019.

[13] S. Zhang, S. Vijayavenkataraman, W. F. Lu, and J. Y. H. Fuh, "A review on the use of computational methods to characterize, design, and optimize tissue engineering scaffolds, with a potential in 3D printing fabrication," *J Biomed Mater Res B Appl Biomater*, vol. 107, no. 5, pp. 1329–1351, 2019, doi: 10.1002/jbm.b.34226.

[14] J. Kim, J. A. McKee, J. J. Fontenot, and J. P. Jung, "Engineering Tissue Fabrication With Machine Intelligence: Generating a Blueprint for Regeneration," *Front Bioeng Biotechnol*, vol. 7, no. January, pp. 1–9, 2020, doi: 10.3389/fbioe.2019.00443.

[15] O. Hakimi, M. Krallinger, and M. P. Ginebra, "Time to kick-start text mining for biomaterials," *Nat Rev Mater*, vol. 5, no. 8, pp. 553–556, 2020, doi: 10.1038/s41578-020-0215-z.

[16] C. Sharpe, T. Wiest, P. Wang, and C. C. Seepersad, "A comparative evaluation of supervised machine learning classification techniques for engineering design applications," *Journal of Mechanical Design*, vol. 141, no. 12, p. 12, 2019, doi: 10.1115/1.4044524.

[17] R. V. Ghaemi, L. C. Siang, and V. G. Yadav, "Improving the Rate of Translation of Tissue Engineering Products," *Adv Healthc Mater*, vol. 8, no. 19, pp. 1–9, 2019, doi: 10.1002/adhm.201900538.

[18] W. L. Ng, A. Chan, Y. S. Ong, and C. K. Chua, "Deep learning for fabrication and maturation of 3D bioprinted tissues and organs," *Virtual Phys Prototyp*, vol. 15, no. 3, pp. 340–358, 2020, doi: 10.1080/17452759.2020.1771741.

[19] C. Yu and J. Jiang, "A perspective on using machine learning in 3D bioprinting," *Int J Bioprint*, vol. 6, no. 1, pp. 4–11, 2020, doi: 10.18063/ijb.v6i1.253.

[20] K. Ruberu *et al.*, "Coupling machine learning with 3D bioprinting to fast track optimisation of extrusion printing," *Appl Mater Today*, vol. 22, p. 100914, 2021, doi: 10.1016/j.apmt.2020.100914.

[21] J. M. Bone *et al.*, "Hierarchical Machine Learning for High-Fidelity 3D Printed Biopolymers," *ACS Biomater Sci Eng*, vol. 6, no. 12, pp. 7021–7031, 2020, doi: 10.1021/acsbiomaterials.0c00755.

[22] J. Lee, S. J. Oh, S. H. An, W. D. Kim, S. H. Kim, and S. H. Kim, "Machine learning-based design strategy for 3D printable bioink: Elastic modulus and yield stress determine printability," *Biofabrication*, vol. 12, no. 3, p. 13, 2020, doi: 10.1088/1758-5090/ab8707.

[23] B. Cao *et al.*, “How to optimize materials and devices via design of experiments and machine learning: Demonstration using organic photovoltaics,” *ACS Nano*, vol. 12, no. 8, pp. 7434–7444, 2018, doi: 10.1021/acsnano.8b04726.

[24] E. Entekhabi, M. Haghbin Nazarpak, M. Sedighi, and A. Kazemzadeh, “Predicting degradation rate of genipin cross-linked gelatin scaffolds with machine learning,” *Materials Science and Engineering C*, vol. 107, no. June 2019, p. 110362, 2020, doi: 10.1016/j.msec.2019.110362.

[25] A. Koeppe, C. A. Hernandez Padilla, M. Voshage, J. H. Schleifenbaum, and B. Markert, “Efficient numerical modeling of 3D-printed lattice-cell structures using neural networks,” *Manuf Lett*, vol. 15, pp. 147–150, 2018, doi: 10.1016/j.mfglet.2018.01.002.

[26] M. M. Kareem and K. E. Tanner, “Optimising micro-hydroxyapatite reinforced poly(lactide acid) electrospun scaffolds for bone tissue engineering,” *J Mater Sci Mater Med*, vol. 31, no. 4, 2020, doi: 10.1007/s10856-020-06376-8.

[27] F. Li *et al.*, “Design of self-assembly dipeptide hydrogels and machine learning via their chemical features,” *Proc Natl Acad Sci U S A*, vol. 166, no. 23, pp. 11259–11264, 2019, doi: 10.1073/pnas.1903376116.

[28] Y. Robles-Bykbaev *et al.*, “An artificial-vision- And statistical-learning-based method for studying the biodegradation of type I collagen scaffolds in bone regeneration systems,” *PeerJ*, no. 7, pp. 1–39, 2019, doi: 10.7717/peerj.7233.

[29] G. Al-Kharusi, N. J. Dunne, S. Little, and T. J. Levingstone, “The Role of Machine Learning and Design of Experiments in the Advancement of Biomaterial and Tissue Engineering Research,” *Bioengineering*, vol. 9, no. 10, 2022, doi: 10.3390/bioengineering9100561.

[30] I. Corvaglia *et al.*, “Comprehensive study through imaging techniques of the degradation of a resorbable calcium sulphate-based composite bone cement,” *Open Ceramics*, vol. 17, Mar. 2024, doi: 10.1016/j.oceram.2024.100542.

[31] A. M. Weatherholt, R. K. Fuchs, and S. J. Warden, “Specialized connective tissue: Bone, the structural framework of the upper extremity,” *Journal of Hand Therapy*, vol. 25, no. 2, pp. 123–132, 2012, doi: 10.1016/j.jht.2011.08.003.

[32] T. D. Seeley, Rod R; Tate, Philip; Stephens, *Anatomy & Physiology*, 2nd ed. London: McGraw Hill Higher Education, 1992.

[33] C. Le Meng Bao, E. Y.L., M. S.K., Y. Liu, M. Choolani, and J. K.Y., “Advances in Osteoporotic Bone Tissue Engineering,” *Regenerative Medicine and Tissue Engineering*, pp. 1–27, 2021, doi: 10.5772/55916.

[34] OpenStax, “Bone Tissue and the Skeletal System,” in *Anatomy and Physiology*, Rice University, 2013, ch. 6.

[35] J. Sheen and G. Vishnu, “Fracture Healing Overview,” *StatPearls*, 2021.

[36] P. V. Giannoudis, “Fracture reduction and fixation techniques: Upper extremities,” *Fracture Reduction and Fixation Techniques: Upper Extremities*, pp. 1–277, 2018, doi: 10.1007/978-3-319-68628-8.

[37] “38.2E: Bone Remodeling and Repair,” Biology Libretexts. [Online]. Available: https://bio.libretexts.org/Bookshelves/Introductory_and_General_Biology/Book%3A_General_Biology_(Boundless)/38%3A_The_Musculoskeletal_System/38.2%3A_Bone/38.2E%3A_Bone_Remodeling_and_Repair

[38] H. Yang, J. Pan, and G. Wang, “A review of osteoporotic vertebral fracture nonunion management,” Dec. 15, 2014, *Lippincott Williams and Wilkins*. doi: 10.1097/BRS.0000000000000538.

[39] T. Sozen, L. Ozisik, and N. Calik Basaran, “An overview and management of osteoporosis,” *Eur J Rheumatol*, vol. 4, no. 1, pp. 46–56, 2017, doi: 10.5152/eurjrheum.2016.048.

[40] S. K. Stewart, “Fracture non-union: A review of clinical challenges and future research needs,” Jul. 01, 2019, *Malaysian Orthopaedic Association*. doi: 10.5704/MOJ.1907.001.

[41] NIH Consensus Development Panel on Osteoporosis Prevention, “Osteoporosis Prevention, Diagnosis, and Therapy,” *South Med J*, vol. 94, no. 6, pp. 569–573, 2001, doi: 10.1097/00007611-200106000-00005.

[42] J. A. Kanis *et al.*, “The use of clinical risk factors enhances the performance of BMD in the prediction of hip and osteoporotic fractures in men and women,” *Osteoporosis International*, vol. 18, no. 8, pp. 1033–1046, 2007, doi: 10.1007/s00198-007-0343-y.

[43] WHO, “Who Scientific Group on the Assessment of Osteoporosis At Primary Health,” *WHO scientific group on the assessment of osteoprosis at primary health care level*, no. May 2004, pp. 1–17, 2007.

[44] J. E. Compston, M. R. McClung, and W. D. Leslie, “Osteoporosis,” *The Lancet*, vol. 393, no. 10169, pp. 364–376, 2019, doi: 10.1016/S0140-6736(18)32112-3.

[45] J. A. Sterling and S. A. Guelcher, “Biomaterial scaffolds for treating osteoporotic bone Human and Animal Rights and Informed Consent,” *Curr Osteoporos Rep*, vol. 12, no. 1, pp. 48–54, 2014, doi: 10.1007/s11914-014-0187-2.Biomaterial.

[46] A. A. Mark E. Furth, *Principles of Tissue Engineering*, Fifth. San Diego: Elsevier Science Publishing Co Inc, 2014. doi: https://doi.org/10.1016/C2011-0-07193-4.

[47] P. Zhu *et al.*, "Fabrication of three-dimensional nanofibrous macrostructures by electrospinning," *AIP Adv*, vol. 6, no. 5, 2016, doi: 10.1063/1.4948797.

[48] S. M. Damaraju *et al.*, "Three-dimensional piezoelectric fibrous scaffolds selectively promote mesenchymal stem cell differentiation," *Biomaterials*, vol. 149, pp. 51–62, 2017, doi: 10.1016/j.biomaterials.2017.09.024.

[49] F. Banche-Niclot *et al.*, "Optimization of an Injectable, Resorbable, Bioactive Cement Able to Release the Anti-Osteoclastogenic Biomolecule ICOS-Fc for the Treatment of Osteoporotic Vertebral Compression Fractures," *Biomolecules*, vol. 13, no. 1, 2023, doi: 10.3390/biom13010094.

[50] W. N. L. W. Jusoh, M. S. Sajab, P. M. Abdul, and H. Kaco, "Recent Advances in 3D Bioprinting: A Review of Cellulose-Based Biomaterials Ink," *Polymers (Basel)*, vol. 14, no. 11, pp. 1–25, 2022, doi: 10.3390/polym14112260.

[51] Ž. P. Kačarević *et al.*, "An introduction to 3D bioprinting: Possibilities, challenges and future aspects," *Materials*, vol. 11, no. 11, 2018, doi: 10.3390/ma11112199.

[52] Y. B. Kim, H. Lee, and G. H. Kim, "Strategy to Achieve Highly Porous/Biocompatible Macroscale Cell Blocks, Using a Collagen/Genipin-bioink and an Optimal 3D Printing Process," *ACS Appl Mater Interfaces*, vol. 8, no. 47, pp. 32230–32240, 2016, doi: 10.1021/acsami.6b11669.

[53] K. E. Drzewiecki, J. N. Malavade, I. Ahmed, C. J. Lowe, and I. David, "A thermoreversible, photocrosslinkable collagen bio-ink for freeform fabrication of scaffolds for regenerative medicine," *Technology (Singap World Sci)*, vol. 5, no. 4, pp. 185–195, 2018, doi: 10.1142/S2339547817500091.A.

[54] L. Zhang, G. Yang, B. N. Johnson, and X. Jia, "Three-dimensional (3D) printed scaffold and material selection for bone repair," *Acta Biomater*, vol. 84, pp. 16–33, 2019, doi: 10.1016/j.actbio.2018.11.039.

[55] J. Li, M. Chen, X. Wei, Y. Hao, and J. Wang, "Evaluation of 3D-printed polycaprolactone scaffolds coated with freeze-dried platelet-rich plasma for bone regeneration," *Materials*, vol. 10, no. 7, Jul. 2017, doi: 10.3390/ma10070831.

[56] P. R. K-Hasuwan, P. Pavasant, and P. Supaphol, "Effect of the surface topography of electrospun poly(ε-caprolactone)/ Poly(3-hydroxybuterate-co-3-hydroxyvalerate) fibrous substrates on cultured bone cell behavior," *Langmuir*, vol. 27, no. 17, pp. 10938–10946, 2011, doi: 10.1021/la202255w.

[57] M. Sadat-Shojai, M. T. Khorasani, and A. Jamshidi, “A new strategy for fabrication of bone scaffolds using electrospun nano-HAp/PHB fibers and protein hydrogels,” *Chemical Engineering Journal*, vol. 289, pp. 38–47, 2016, doi: 10.1016/j.cej.2015.12.079.

[58] Y. Wang *et al.*, “The differential effects of aligned electrospun PHBHHx fibers on adipogenic and osteogenic potential of MSCs through the regulation of PPARγ signaling,” *Biomaterials*, vol. 33, no. 2, pp. 485–493, 2012, doi: 10.1016/j.biomaterials.2011.09.089.

[59] T. J. Sill and H. A. von Recum, “Electrospinning: Applications in drug delivery and tissue engineering,” *Biomaterials*, vol. 29, no. 13, pp. 1989–2006, 2008, doi: 10.1016/j.biomaterials.2008.01.011.

[60] K. Chen *et al.*, “Recent advances in electrospun nanofibers for wound dressing,” *Eur Polym J*, vol. 178, no. June, p. 111490, 2022, doi: 10.1016/j.eurpolymj.2022.111490.

[61] M. Bohner, “Calcium orthophosphates in medicine: From ceramics to calcium phosphate cements,” *Injury*, vol. 31, no. SUPPL. 4, 2000, doi: 10.1016/S0020-1383(00)80022-4.

[62] M. P. Ginebra, C. Canal, M. Espanol, D. Pastorino, and E. B. Montufar, “Calcium phosphate cements as drug delivery materials,” *Adv Drug Deliv Rev*, vol. 64, no. 12, pp. 1090–1110, 2012, doi: 10.1016/j.addr.2012.01.008.

[63] F. Tamimi, Z. Sheikh, and J. Barralet, “Dicalcium phosphate cements: Brushite and monetite,” *Acta Biomater*, vol. 8, no. 2, pp. 474–487, 2012, doi: 10.1016/j.actbio.2011.08.005.

[64] M. Hospodiuk, M. Dey, D. Sosnoski, and I. T. Ozbolat, “The bioink: A comprehensive review on bioprintable materials,” *Biotechnol Adv*, vol. 35, no. 2, pp. 217–239, 2017, doi: 10.1016/j.biotechadv.2016.12.006.

[65] C. Mandrycky, Z. Wang, K. Kim, and D. H. Kim, “3D bioprinting for engineering complex tissues,” *Biotechnol Adv*, vol. 34, no. 4, pp. 422–434, 2016, doi: 10.1016/j.biotechadv.2015.12.011.

[66] Z. Zheng, D. Eglin, M. Alini, G. R. Richards, L. Qin, and Y. Lai, “Visible Light-Induced 3D Bioprinting Technologies and Corresponding Bioink Materials for Tissue Engineering: A Review,” *Engineering*, vol. 7, no. 7, pp. 966–978, 2021, doi: 10.1016/j.eng.2020.05.021.

[67] A. Lee *et al.*, “3D bioprinting of collagen to rebuild components of the human heart,” *Science (1979)*, vol. 365, pp. 482–487, 2019, doi: 10.1126/science.aav9051.

[68] J. Gopinathan and I. Noh, “Recent trends in bioinks for 3D printing,” *Biomater Res*, vol. 22, no. 1, pp. 1–15, 2018, doi: 10.1186/s40824-018-0122-1.

[69] S. McGivern, H. Boutouil, G. Al-Kharusi, S. Little, N. J. Dunne, and T. J. Levingstone, "Translational Application of 3D Bioprinting for Cartilage Tissue Engineering," *Bioengineering*, vol. 8, no. 10, p. 144, 2021, doi: 10.3390/bioengineering8100144.

[70] I. T. Ozbolat and M. Hospodiuk, "Current advances and future perspectives in extrusion-based bioprinting," *Biomaterials*, vol. 76, pp. 321–343, 2016, doi: 10.1016/j.biomaterials.2015.10.076.

[71] A. T. Khalaf *et al.*, "Bone Tissue Engineering through 3D Bioprinting of Bioceramic Scaffolds: A Review and Update," Jun. 01, 2022, *MDPI*. doi: 10.3390/life12060903.

[72] M. Z. A. Zulkifli, D. Nordin, N. Shaari, and S. K. Kamarudin, "Overview of Electrospinning for Tissue Engineering Applications," Jun. 01, 2023, *MDPI*. doi: 10.3390/polym15112418.

[73] S. Vanaei, M. S. Parizi, S. Vanaei, F. Salemizadehparizi, and H. R. Vanaei, "An Overview on Materials and Techniques in 3D Bioprinting Toward Biomedical Application," *Engineered Regeneration*, vol. 2, no. December 2020, pp. 1–18, 2021, doi: 10.1016/j.engreg.2020.12.001.

[74] G. Turnbull *et al.*, "3D bioactive composite scaffolds for bone tissue engineering," *Bioact Mater*, vol. 3, no. 3, pp. 278–314, 2018, doi: 10.1016/j.bioactmat.2017.10.001.

[75] J. Li, M. Chen, X. Fan, and H. Zhou, "Recent advances in bioprinting techniques: Approaches, applications and future prospects," *J Transl Med*, vol. 14, no. 1, pp. 1–15, 2016, doi: 10.1186/s12967-016-1028-0.

[76] X. Li *et al.*, "Inkjet Bioprinting of Biomaterials," *Chem Rev*, vol. 120, no. 19, pp. 10793–10833, 2020, doi: 10.1021/acs.chemrev.0c00008.

[77] P. Zhang *et al.*, "Lightweight 3D bioprinting with point by point photocuring," *Bioact Mater*, vol. 6, no. 5, pp. 1402–1412, 2021, doi: 10.1016/j.bioactmat.2020.10.023.

[78] Q. Gu *et al.*, "Three-dimensional bioprinting speeds up smart regenerative medicine," *Natl Sci Rev*, vol. 3, no. 3, pp. 331–344, 2016, doi: 10.1093/nsr/nww037.

[79] W. Liu *et al.*, "Rapid Continuous Multi-Material Extrusion Bioprinting," *Advanced Materials*, vol. 176, no. 3, pp. 139–148, 2017, doi: 10.1053/j.gastro.2016.08.014.CagY.

[80] S. Sakai, A. Yoshii, S. Sakurai, K. Horii, and O. Nagasuna, "Silk fibroin nanofibers: a promising ink additive for extrusion three-dimensional bioprinting," *Mater Today Bio*, vol. 8, no. July, 2020, doi: 10.1016/j.mtbio.2020.100078.

[81] Y. Yu, Y. Zhang, J. A. Martin, and I. T. Ozbolat, "Evaluation of cell viability and functionality in vessel-like bioprintable cell-laden tubular channels," *J Biomech Eng*, vol. 135, no. 9, pp. 1–9, 2013, doi: 10.1115/1.4024575.

[82] I. T. Ozbolat and Y. Yu, “Bioprinting toward organ fabrication: Challenges and future trends,” *IEEE Trans Biomed Eng*, vol. 60, no. 3, pp. 691–699, 2013, doi: 10.1109/TBME.2013.2243912.

[83] H. Gudapati, M. Dey, and I. Ozbolat, “A comprehensive review on droplet-based bioprinting: Past, present and future,” *Biomaterials*, vol. 102, pp. 20–42, 2016, doi: 10.1016/j.biomaterials.2016.06.012.

[84] M. E. Cooke and D. H. Rosenzweig, “The rheology of direct and suspended extrusion bioprinting,” *APL Bioeng*, vol. 5, no. 1, 2021, doi: 10.1063/5.0031475.

[85] D. Nguyen *et al.*, “Cartilage Tissue Engineering by the 3D Bioprinting of iPS Cells in a Nanocellulose/Alginate Bioink,” *Sci Rep*, vol. 7, no. 1, pp. 1–10, 2017, doi: 10.1038/s41598-017-00690-y.

[86] G. Cidonio, M. Glinka, J. I. Dawson, and R. O. C. Oreffo, “The cell in the ink: Improving biofabrication by printing stem cells for skeletal regenerative medicine,” *Biomaterials*, vol. 209, no. March, pp. 10–24, 2019, doi: 10.1016/j.biomaterials.2019.04.009.

[87] H. Zhang, L. Zhou, and W. Zhang, “Control of scaffold degradation in tissue engineering: A review,” *Tissue Eng Part B Rev*, vol. 20, no. 5, pp. 492–502, 2014, doi: 10.1089/ten.teb.2013.0452.

[88] A. J. Salgado, O. P. Coutinho, and R. L. Reis, “Bone tissue engineering: State of the art and future trends,” Aug. 09, 2004. doi: 10.1002/mabi.200400026.

[89] Y. S. Zhang *et al.*, “3D Bioprinting for Tissue and Organ Fabrication,” *Ann Biomed Eng*, vol. 45, no. 1, pp. 148–163, Jan. 2017, doi: 10.1007/s10439-016-1612-8.

[90] J. Huang *et al.*, “BMSCs-laden gelatin/sodium alginate/carboxymethyl chitosan hydrogel for 3D bioprinting,” *RSC Adv*, vol. 6, no. 110, pp. 108423–108430, 2016, doi: 10.1039/c6ra24231f.

[91] Z. Fu, S. Naghieh, C. Xu, C. Wang, W. Sun, and X. Chen, “Printability in extrusion bioprinting,” Jul. 01, 2021, *IOP Publishing Ltd*. doi: 10.1088/1758-5090/abe7ab.

[92] E. S. Bishop *et al.*, “3-D bioprinting technologies in tissue engineering and regenerative medicine: Current and future trends,” Dec. 01, 2017, *Chongqing University*. doi: 10.1016/j.gendis.2017.10.002.

[93] M. Du *et al.*, “3D bioprinting of BMSC-laden methacrylamide gelatin scaffolds with CBD-BMP2-collagen microfibers,” *Biofabrication*, vol. 7, no. 4, Dec. 2015, doi: 10.1088/1758-5090/7/4/044104.

[94] Y. B. Kim and G. H. Kim, “PCL/alginate composite scaffolds for hard tissue engineering: Fabrication, characterization, and cellular activities,” *ACS Comb Sci*, vol. 17, no. 2, pp. 87–99, Feb. 2015, doi: 10.1021/co500033h.

[95] M. Neufurth *et al.*, “Engineering a morphogenetically active hydrogel for bioprinting of bioartificial tissue derived from human osteoblast-like SaOS-2 cells,” *Biomaterials*, vol. 35, no. 31, pp. 8810–8819, 2014, doi: 10.1016/j.biomaterials.2014.07.002.

[96] D. Chimene, K. K. Lennox, R. R. Kaunas, and A. K. Gaharwar, “Advanced Bioinks for 3D Printing: A Materials Science Perspective,” Jun. 01, 2016, *Springer New York LLC*. doi: 10.1007/s10439-016-1638-y.

[97] M. Di Giuseppe *et al.*, “Mechanical behaviour of alginate-gelatin hydrogels for 3D bioprinting,” *J Mech Behav Biomed Mater*, vol. 79, pp. 150–157, Mar. 2018, doi: 10.1016/j.jmbbm.2017.12.018.

[98] J. Park *et al.*, “Cell-laden 3D bioprinting hydrogel matrix depending on different compositions for soft tissue engineering: Characterization and evaluation,” *Materials Science and Engineering C*, vol. 71, pp. 678–684, Feb. 2017, doi: 10.1016/j.msec.2016.10.069.

[99] Y. Luo, G. Luo, M. Gelinsky, P. Huang, and C. Ruan, “3D bioprinting scaffold using alginate/polyvinyl alcohol bioinks,” *Mater Lett*, vol. 189, pp. 295–298, Feb. 2017, doi: 10.1016/j.matlet.2016.12.009.

[100] A. Aldaadaa, N. Owji, and J. Knowles, “Three-dimensional Printing in Maxillofacial Surgery: Hype versus Reality,” *J Tissue Eng*, vol. 9, Apr. 2018, doi: 10.1177/2041731418770909.

[101] M. Neufurth *et al.*, “Engineering a morphogenetically active hydrogel for bioprinting of bioartificial tissue derived from human osteoblast-like SaOS-2 cells,” *Biomaterials*, vol. 35, no. 31, pp. 8810–8819, 2014, doi: 10.1016/j.biomaterials.2014.07.002.

[102] M. Milazzo *et al.*, “Additive Manufacturing Approaches for Hydroxyapatite-Reinforced Composites,” Aug. 01, 2019, *Wiley-VCH Verlag*. doi: 10.1002/adfm.201903055.

[103] F. You, X. Wu, N. Zhu, M. Lei, B. F. Eames, and X. Chen, “3D Printing of Porous Cell-Laden Hydrogel Constructs for Potential Applications in Cartilage Tissue Engineering,” *ACS Biomater Sci Eng*, vol. 2, no. 7, pp. 1200–1210, Jul. 2016, doi: 10.1021/acsbiomaterials.6b00258.

[104] Y. Luo, A. Lode, A. R. Akkineni, and M. Gelinsky, “Concentrated gelatin/alginate composites for fabrication of predesigned scaffolds with a favorable cell response by 3D plotting,” *RSC Adv*, vol. 5, no. 54, pp. 43480–43488, 2015, doi: 10.1039/c5ra04308e.

[105] J.-K. F. Suh and H. W. T. Matthew, “Application of chitosan-based polysaccharide biomaterials in cartilage tissue engineering: a review,” 2000.

[106] R. A. A. Muzzarelli, F. Greco, A. Busilacchi, V. Sollazzo, and A. Gigante, “Chitosan, hyaluronan and chondroitin sulfate in tissue engineering for cartilage regeneration: A review,” Jul. 01, 2012. doi: 10.1016/j.carbpol.2012.04.057.

[107] S. Rhee, J. L. Puetzer, B. N. Mason, C. A. Reinhart-King, and L. J. Bonassar, “3D Bioprinting of Spatially Heterogeneous Collagen Constructs for Cartilage Tissue Engineering,” *ACS Biomater Sci Eng*, vol. 2, no. 10, pp. 1800–1805, Oct. 2016, doi: 10.1021/acsbiomaterials.6b00288.

[108] M. Mohseni, A. Jahandideh, G. Abedi, A. Akbarzadeh, and S. Hesaraki, “Assessment of tricalcium phosphate/collagen (TCP/collagene)nanocomposite scaffold compared with hydroxyapatite (HA) on healing of segmental femur bone defect in rabbits,” *Artif Cells Nanomed Biotechnol*, vol. 46, no. 2, pp. 242–249, Feb. 2018, doi: 10.1080/21691401.2017.1324463.

[109] G. Turnbull *et al.*, “3D bioactive composite scaffolds for bone tissue engineering,” Sep. 01, 2018, *KeAi Communications Co.* doi: 10.1016/j.bioactmat.2017.10.001.

[110] N. Ashammakhi *et al.*, “Advancing Frontiers in Bone Bioprinting,” Apr. 11, 2019, *Wiley-VCH Verlag*. doi: 10.1002/adhm.201801048.

[111] P. Zhai, X. Peng, B. Li, Y. Liu, H. Sun, and X. Li, “The application of hyaluronic acid in bone regeneration,” May 15, 2020, *Elsevier B.V.* doi: 10.1016/j.ijbiomac.2019.10.169.

[112] J. Kim *et al.*, “Bone regeneration using hyaluronic acid-based hydrogel with bone morphogenic protein-2 and human mesenchymal stem cells,” *Biomaterials*, vol. 28, no. 10, pp. 1830–1837, Apr. 2007, doi: 10.1016/j.biomaterials.2006.11.050.

[113] Z. Zhu, Y.-M. Wang, J. Yang, and X.-S. Luo, “Hyaluronic acid: a versatile biomaterial in tissue engineering,” *Plast Aesthet Res*, vol. 4, no. 12, p. 219, Dec. 2017, doi: 10.20517/2347-9264.2017.71.

[114] W. K. and G. Kim, “Collagen/bioceramic-based composite bioink to fabricate a porous 3D hASCs-laden structure for bone tissue regeneration,” *Biofabrication*, pp. 0–31, 2019.

[115] W. J. Kim, H. S. Yun, and G. H. Kim, “An innovative cell-laden α-TCP/collagen scaffold fabricated using a two-step printing process for potential application in regenerating hard tissues,” *Sci Rep*, vol. 7, no. 1, pp. 1–12, 2017, doi: 10.1038/s41598-017-03455-9.

[116] L. Muthukrishnan, “Imminent antimicrobial bioink deploying cellulose, alginate, EPS and synthetic polymers for 3D bioprinting of tissue constructs,” *Carbohydr Polym*, vol. 260, no. December 2020, p. 117774, 2021, doi: 10.1016/j.carbpol.2021.117774.

[117] I. Levental, P. C. Georges, and P. A. Janmey, “Soft biological materials and their impact on cell function,” *Soft Matter*, vol. 3, no. 3, pp. 299–306, 2007, doi: 10.1039/b610522j.

[118] S. Cai, Y. Liu, Z. S. Xiao, and G. D. Prestwich, “Injectable glycosaminoglycan hydrogels for controlled release of human basic fibroblast growth factor,” *Biomaterials*, vol. 26, no. 30, pp. 6054–6067, 2005, doi: 10.1016/j.biomaterials.2005.03.012.

[119] K. Schenke-Layland *et al.*, “Impact of decellularization of xenogeneic tissue on extracellular matrix integrity for tissue engineering of heart valves,” *J Struct Biol*, vol. 143, no. 3, pp. 201–208, 2003, doi: 10.1016/j.jsb.2003.08.002.

[120] W. W. Chan, D. C. L. Yeo, V. Tan, S. Singh, D. Choudhury, and M. W. Naing, “Additive biomanufacturing with collagen inks,” *Bioengineering*, vol. 7, no. 3, pp. 1–23, 2020, doi: 10.3390/bioengineering7030066.

[121] J. Malda *et al.*, “25th anniversary article: Engineering hydrogels for biofabrication,” *Advanced Materials*, vol. 25, no. 36, pp. 5011–5028, 2013, doi: 10.1002/adma.201302042.

[122] A. Panwar and L. P. Tan, “Current status of bioinks for micro-extrusion-based 3D bioprinting,” *Molecules*, vol. 21, no. 6, 2016, doi: 10.3390/molecules21060685.

[123] J. M. Townsend, E. C. Beck, S. H. Gehrke, C. J. Berkland, and M. S. Detamore, “Flow behavior prior to crosslinking: The need for precursor rheology for placement of hydrogels in medical applications and for 3D bioprinting,” *Prog Polym Sci*, vol. 91, pp. 126–140, 2019, doi: 10.1016/j.progpolymsci.2019.01.003.

[124] F. F. Cai, S. Heid, and A. R. Boccaccini, “Potential of Laponite incorporated oxidized alginate–gelatin (ADA-GEL) composite hydrogels for extrusion-based 3D printing,” *J Biomed Mater Res B Appl Biomater*, vol. 109, no. 8, pp. 1090–1104, Aug. 2021, doi: 10.1002/jbm.b.34771.

[125] L. Ouyang, R. Yao, Y. Zhao, and W. Sun, “Effect of bioink properties on printability and cell viability for 3D bioplotting of embryonic stem cells,” *Biofabrication*, vol. 8, no. 3, 2016, doi: 10.1088/1758-5090/8/3/035020.

[126] D. F. Duarte Campos *et al.*, “Bioprinting Organotypic Hydrogels with Improved Mesenchymal Stem Cell Remodeling and Mineralization Properties for Bone Tissue Engineering,” *Adv Healthc Mater*, vol. 5, no. 11, pp. 1336–1345, 2016, doi: 10.1002/adhm.201501033.

[127] G. Gao, A. F. Schilling, T. Yonezawa, J. Wang, G. Dai, and X. Cui, “Bioactive nanoparticles stimulate bone tissue formation in bioprinted three-dimensional scaffold and human mesenchymal stem cells,” *Biotechnol J*, vol. 9, no. 10, pp. 1304–1311, 2014, doi: 10.1002/biot.201400305.

[128] A. Habib, V. Sathish, S. Mallik, and B. Khoda, “3D printability of alginate-carboxymethyl cellulose hydrogel,” *Materials*, vol. 11, no. 3, 2018, doi: 10.3390/ma11030454.

[129] K. D. Roehm and S. V. Madihally, “Bioprinted chitosan-gelatin thermosensitive hydrogels using an inexpensive 3D printer,” *Biofabrication*, vol. 10, no. 1, 2018, doi: 10.1088/1758-5090/aa96dd.

[130] K. Hölzl, S. Lin, L. Tytgat, S. Van Vlierberghe, L. Gu, and A. Ovsianikov, “Bioink properties before, during and after 3D bioprinting,” *Biofabrication*, vol. 8, no. 3, 2016, doi: 10.1088/1758-5090/8/3/032002.

[131] A. S. Theus *et al.*, “Bioprintability: Physiomechanical and biological requirements of materials for 3d bioprinting processes,” *Polymers (Basel)*, vol. 12, no. 10, pp. 1–19, 2020, doi: 10.3390/polym12102262.

[132] N. Soltan, L. Ning, F. Mohabatpour, P. Papagerakis, and X. Chen, “Printability and Cell Viability in Bioprinting Alginate Dialdehyde-Gelatin Scaffolds,” *ACS Biomater Sci Eng*, vol. 5, no. 6, pp. 2976–2987, 2019, doi: 10.1021/acsbiomaterials.9b00167.

[133] T. Gao *et al.*, “Optimization of gelatin-alginate composite bioink printability using rheological parameters: A systematic approach,” *Biofabrication*, vol. 10, no. 3, 2018, doi: 10.1088/1758-5090/aacdc7.

[134] L. Ouyang, C. B. Highley, W. Sun, and J. A. Burdick, “A Generalizable Strategy for the 3D Bioprinting of Hydrogels from Nonviscous Photo-crosslinkable Inks,” *Advanced Materials*, vol. 29, no. 8, 2017, doi: 10.1002/adma.201604983.

[135] L. Ruiz-Cantu, A. Gleadall, C. Faris, J. Segal, K. Shakesheff, and J. Yang, “Characterisation of the surface structure of 3D printed scaffolds for cell infiltration and surgical suturing,” *Biofabrication*, vol. 8, no. 1, p. 0, 2016, doi: 10.1088/1758-5090/8/1/015016.

[136] N. Hojat, P. Gentile, A. M. Ferreira, and L. Šiller, “Automatic pore size measurements from scanning electron microscopy images of porous scaffolds,” *Journal of Porous Materials*, vol. 30, no. 1, pp. 93–101, 2023, doi: 10.1007/s10934-022-01309-y.

[137] A. Venkateshaiah, V. V. T. Padil, M. Nagalakshmaiah, S. Waclawek, M. Černík, and R. S. Varma, “Microscopic techniques for the analysis of micro and nanostructures of biopolymers and their derivatives,” *Polymers (Basel)*, vol. 12, no. 3, 2020, doi: 10.3390/polym12030512.

[138] M. Castilho *et al.*, “Melt Electrospinning Writing of Poly-Hydroxymethylglycolide-co-ε-Caprolactone-Based Scaffolds for Cardiac Tissue Engineering,” *Adv Healthc Mater*, vol. 6, no. 18, pp. 1–9, 2017, doi: 10.1002/adhm.201700311.

[139] J. Visser *et al.*, “Reinforcement of hydrogels using three-dimensionally printed microfibres,” *Nat Commun*, vol. 6, pp. 1–10, 2015, doi: 10.1038/ncomms7933.

[140] M. Bartoš, T. Suchý, and R. Foltán, “Note on the use of different approaches to determine the pore sizes of tissue engineering scaffolds: What do we measure?,” *Biomed Eng Online*, vol. 17, no. 1, pp. 1–15, 2018, doi: 10.1186/s12938-018-0543-z.

[141] C. E. P. Aronin *et al.*, “Comparative effects of scaffold pore size, pore volume, and total void volume on cranial bone healing patterns using microsphere-based scaffolds,” *J Biomed Mater Res A*, vol. 89, no. 3, pp. 632–641, 2009, doi: 10.1002/jbm.a.32015.

[142] X. Liu *et al.*, *Multifunctional 3D-printed bioceramic scaffolds: Recent strategies for osteosarcoma treatment*, vol. 14, no. 72. 2023. doi: 10.1177/20417314231170371.

[143] S. J. Hollister, R. D. Maddox, and J. M. Taboas, “Optimal design and fabrication of scaffolds to mimic tissue properties,” *Biomaterials*, vol. 23, pp. 4095–4103, 2002.

[144] J. Antons *et al.*, “Zone-dependent mechanical properties of human articular cartilage obtained by indentation measurements,” *J Mater Sci Mater Med*, vol. 29, no. 5, 2018, doi: 10.1007/s10856-018-6066-0.

[145] D. W. Hutmacher, “Scaffolds in tissue engineering bone and cartilage,” *The Biomaterials: Silver Jubilee Compendium*, vol. 21, pp. 175–189, 2000, doi: 10.1016/B978-008045154-1.50021-6.

[146] B. Durakovic, “Design of experiments application, concepts, examples: State of the art,” *Periodicals of Engineering and Natural Sciences*, vol. 5, no. 3, pp. 421–439, 2017, doi: 10.21533/pen.v5i3.145.

[147] J. Pietraszek, N. Radek, and A. V. Goroshko, “Challenges for the DOE methodology related to the introduction of Industry 4.0,” *Production Engineering Archives*, vol. 26, no. 4, pp. 190–194, 2020, doi: 10.30657/pea.2020.26.33.

[148] A. Uhoraningoga, G. K. Kinsella, G. T. Henehan, and B. J. Ryan, “The goldilocks approach: A review of employing design of experiments in prokaryotic recombinant protein production,” *Bioengineering*, vol. 5, no. 4, pp. 1–27, 2018, doi: 10.3390/bioengineering5040089.

[149] W. Sukthomya and J. Tannock, “The optimisation of neural network parameters using Taguchi’s design of experiments approach: An application in manufacturing process

modelling," *Neural Comput Appl*, vol. 14, no. 4, pp. 337–344, 2005, doi: 10.1007/s00521-005-0470-3.

[150] B. Sarvin *et al.*, "LC-MS determination of steroidal glycosides from Dioscorea deltoidea Wall cell suspension culture: Optimization of pre-LC-MS procedure parameters by Latin Square design," *J Chromatogr B Analyt Technol Biomed Life Sci*, vol. 1080, no. February, pp. 64–70, 2018, doi: 10.1016/j.jchromb.2018.02.012.

[151] L. Vaut, J. J. Juszczyk, K. Kamguyan, K. E. Jensen, G. Tosello, and A. Boisen, "3D Printing of Reservoir Devices for Oral Drug Delivery: From Concept to Functionality through Design Improvement for Enhanced Mucoadhesion," *ACS Biomater Sci Eng*, vol. 6, no. 4, pp. 2478–2486, 2020, doi: 10.1021/acsbiomaterials.9b01760.

[152] "NIST/SEMATECH e-Handbook of Statistical Methods," National Institute of Standards and Technology. Accessed: Oct. 01, 2022. [Online]. Available: http://www.itl.nist.gov/div898/handbook/

[153] E. Y. K. Ng and W. K. Ng, "Parametric study of the biopotential equation for breast tumour identification using ANOVA and Taguchi method," *Med Biol Eng Comput*, vol. 44, no. 1–2, pp. 131–139, 2006, doi: 10.1007/s11517-005-0006-0.

[154] O. F. Enoch, Ab. A. Shuaib, and A. H. bin Hasbullah, "Applying P-Diagram in Product Development Process: An Approach towards Design for Six Sigma," *Applied Mechanics and Materials*, vol. 789–790, pp. 1187–1191, 2015, doi: 10.4028/www.scientific.net/amm.789-790.1187.

[155] X. Shen, G. Zhang, and B. Bjerg, "Assessments of experimental designs in response surface modelling process: Estimating ventilation rate in naturally ventilated livestock buildings," *Energy Build*, vol. 62, pp. 570–580, 2013, doi: 10.1016/j.enbuild.2013.03.038.

[156] S. Karimifard and M. R. Alavi Moghaddam, "Application of response surface methodology in physicochemical removal of dyes from wastewater: A critical review," *Science of the Total Environment*, vol. 640–641, pp. 772–797, 2018, doi: 10.1016/j.scitotenv.2018.05.355.

[157] R. Scaffaro, F. Sutera, and F. Lopresti, "Using Taguchi method for the optimization of processing variables to prepare porous scaffolds by combined melt mixing/particulate leaching," *Mater Des*, vol. 131, pp. 334–342, 2017, doi: 10.1016/j.matdes.2017.06.025.

[158] H. C. J. Hoefsloot, D. J. Vis, J. A. Westerhuis, A. K. Smilde, and J. J. Jansen, "Multiset Data Analysis: ANOVA Simultaneous Component Analysis and Related Methods," *Comprehensive Chemometrics*, vol. 2, pp. 453–472, 2009, doi: 10.1016/B978-044452701-1.00054-5.

[159] J. D. Barrett, “Taguchi’s Quality Engineering Handbook,” *Technometrics*, vol. 49, no. 2, pp. 224–225, 2007, doi: 10.1198/tech.2007.s480.

[160] R. H. Myers, D. C. Montgomery, and C. M. Anderson-cook, *Response surface methodology: process and product optimization using designed experiments*, 4th editio. New Jersey: John Wiley & Sons., 2016.

[161] S. Saeedi Garakani *et al.*, “Fabrication of chitosan/agarose scaffolds containing extracellular matrix for tissue engineering applications,” *Int J Biol Macromol*, vol. 143, pp. 533–545, 2020, doi: 10.1016/j.ijbiomac.2019.12.040.

[162] L. Tan, M. Gong, F. Zheng, B. Zhang, and K. Yang, “Study on compression behavior of porous magnesium used as bone tissue engineering scaffolds,” *Biomedical Materials*, vol. 4, no. 1, p. 7, 2009, doi: 10.1088/1748-6041/4/1/015016.

[163] T. J. Levingstone, N. Barron, M. Ardhaoui, K. Benyounis, L. Looney, and J. Stokes, “Application of response surface methodology in the design of functionally graded plasma sprayed hydroxyapatite coatings,” *Surf Coat Technol*, vol. 313, pp. 307–318, 2017, doi: 10.1016/j.surfcoat.2017.01.113.

[164] T. J. Levingstone, M. Ardhaoui, K. Benyounis, L. Looney, and J. T. Stokes, “Plasma sprayed hydroxyapatite coatings: Understanding process relationships using design of experiment analysis,” *Surf Coat Technol*, vol. 283, pp. 29–36, 2015, doi: 10.1016/j.surfcoat.2015.10.044.

[165] S. Kehoe, M. Ardhaoui, and J. Stokes, “Design of experiments study of hydroxyapatite synthesis for orthopaedic application using fractional factorial design,” *J Mater Eng Perform*, vol. 20, no. 8, pp. 1423–1437, 2011, doi: 10.1007/s11665-010-9704-3.

[166] J. Lam, S. T. Carmichael, W. E. Lowry, and T. Segura, “Hydrogel design of experiments methodology to optimize hydrogel for iPSC-NPC culture,” *Adv Healthc Mater*, vol. 4, no. 4, pp. 534–539, 2015, doi: 10.1002/adhm.201400410.

[167] M. Blanco, J. A. Vázquez, R. I. Pérez-Martín, and C. G. Sotelo, “Collagen extraction optimization from the skin of the small-spotted catshark (S. Canicula) by response surface methodology,” *Mar Drugs*, vol. 17, no. 1, 2019, doi: 10.3390/md17010040.

[168] F. A. A. Ruiter, C. Alexander, F. R. A. J. Rose, and J. I. Segal, “A design of experiments approach to identify the influencing parameters that determine poly-D,L-lactic acid (PDLLA) electrospun scaffold morphologies,” *Biomedical Materials (Bristol)*, vol. 12, no. 5, 2017, doi: 10.1088/1748-605X/aa7b54.

[169] G. Marchiori *et al.*, “Design of a novel procedure for the optimization of the mechanical performances of 3D printed scaffolds for bone tissue engineering combining CAD, Taguchi

method and FEA," *Med Eng Phys*, vol. 69, pp. 92–99, 2019, doi: 10.1016/j.medengphy.2019.04.009.

[170] J. Y. F. Aishwarya Bhargav, Vinicius Rosa , Lu Wen Feng, "Optimization of Surface Scaffold Morphology and Structure Using Taguchi's Design of Experiments," Minneapolis, 2018.

[171] M. Shirzad, A. Zolfagharian, A. Matbouei, and M. Bodaghi, "Design, evaluation, and optimization of 3D printed truss scaffolds for bone tissue engineering," *J Mech Behav Biomed Mater*, vol. 120, no. May, p. 104594, 2021, doi: 10.1016/j.jmbbm.2021.104594.

[172] J. E. Trachtenberg *et al.*, "Extrusion-Based 3D Printing of Poly(propylene fumarate) in a Full-Factorial Design," *ACS Biomater Sci Eng*, vol. 2, no. 10, pp. 1771–1780, 2016, doi: 10.1021/acsbiomaterials.6b00026.

[173] Z. Bi, "Applications—Solid Mechanics Problems," in *Finite Element Analysis Applications*, Indiana: Elsevier Inc., 2018, ch. Chapter 8, pp. 281–339. doi: 10.1016/b978-0-12-809952-0.00008-x.

[174] B. A. Williams and S. Cremaschi, *Surrogate Model Selection for Design Space Approximation And Surrogatebased Optimization*, vol. 47. Elsevier Masson SAS, 2019. doi: 10.1016/B978-0-12-818597-1.50056-4.

[175] A. Jankovic, G. Chaudhary, and F. Goia, "Designing the design of experiments (DOE) – An investigation on the influence of different factorial designs on the characterization of complex systems," *Energy Build*, vol. 250, p. 111298, 2021, doi: 10.1016/j.enbuild.2021.111298.

[176] Z. Li, "Predicting bone regeneration from machine learning," *Nat Comput Sci*, vol. 1, no. 8, pp. 509–510, 2021, doi: 10.1038/s43588-021-00116-w.

[177] E. Alpaydin, *Introduction to Machine Learning*, Fourth. Massachusetts: The MIT Press, 2020.

[178] C. Park, C. C. Took, and J. K. Seong, "Machine learning in biomedical engineering," *Biomed Eng Lett*, vol. 8, no. 1, pp. 1–3, 2018, doi: 10.1007/s13534-018-0058-3.

[179] W. J. Murdoch, C. Singh, K. Kumbier, R. Abbasi-Asl, and B. Yu, "Definitions, methods, and applications in interpretable machine learning," *Proc Natl Acad Sci U S A*, vol. 116, no. 44, pp. 22071–22080, 2019, doi: 10.1073/pnas.1900654116.

[180] M. R. M. Talabis, R. McPherson, I. Miyamoto, J. L. Martin, and D. Kaye, "Analytics Defined," in *Information Security Analytics: Finding Security Insights, Patterns, and Anomalies in Big Data*, Waltham: Elsevier Inc., 2015, pp. 1–12. doi: 10.1016/b978-0-12-800207-0.00001-0.

[181] D. De Ridder, J. De Ridder, and M. J. T. Reinders, “Pattern recognition in bioinformatics,” *Brief Bioinform*, vol. 14, no. 5, pp. 633–647, 2013, doi: 10.1093/bib/bbt020.

[182] S. Balasubramanyam, “New Technologies and Environments,” *The IFPUG Guide to IT and Software Measurement*, pp. 385–386, 2012, doi: 10.1201/b11884-28.

[183] A. Conev, E. E. Litsa, M. R. Perez, M. Diba, A. G. Mikos, and L. E. Kavraki, “Machine learning-guided three-dimensional printing of tissue engineering scaffolds,” *Tissue Eng Part A*, vol. 26, no. 23–24, pp. 1359–1368, 2020, doi: 10.1089/ten.tea.2020.0191.

[184] T. Shaikhina, D. Lowe, S. Daga, D. Briggs, R. Higgins, and N. Khovanova, “Machine learning for predictive modelling based on small data in biomedical engineering,” *IFAC-PapersOnLine*, vol. 28, no. 20, pp. 469–474, 2015, doi: 10.1016/j.ifacol.2015.10.185.

[185] N. P. Tigga and S. Garg, “Prediction of Type 2 Diabetes using Machine Learning Classification Methods,” *Procedia Comput Sci*, vol. 167, no. 2019, pp. 706–716, 2020, doi: 10.1016/j.procs.2020.03.336.

[186] S. R. Gangadhar Shobha, “Chapter 8 - Machine Learning,” in *Computational Analysis and Understanding of Natural Languages: Principles, Methods and Applications*, vol. 38, V. N. Gudivada and C. R. Rao, Eds., 2018, pp. 197–228. doi: https://doi.org/10.1016/bs.host.2018.07.004.

[187] J. Patterson and A. Gibson, *Deep Learning: A Practitioner’s Approach*, First. O’Reilly Media, 2017. doi: 10.1016/B978-0-12-801775-3.00001-9.

[188] P. Suryachandra, “Comparison of Machine Learning Algorithms,” in *3rd International Conference on Science and Technology - Computer (ICST) Comparison*, IEEE, 2017, pp. 2241–2247.

[189] M. Mashayekhi and R. Gras, “Rule Extraction from Random Forest: The RF+HC Methods,” *Lecture Notes in Computer Science (including subseries Lecture Notes in Artificial Intelligence and Lecture Notes in Bioinformatics)*, vol. 9091, no. June, pp. 273–280, 2015, doi: 10.1007/978-3-319-18356-5.

[190] I. H. Witten, E. Frank, M. A. Hall, and C. J. Pal, “Extending instance-based and linear models,” in *Data Mining*, Fourth., I. H. Witten, E. Frank, M. A. Hall, and C. J. Pal, Eds., Morgan Kaufmann, 2017, pp. 243–284. doi: 10.1016/b978-0-12-804291-5.00007-6.

[191] K. Vu *et al.*, “Understanding kernel ridge regression: Common behaviors from simple functions to density functionals,” *Int J Quantum Chem*, vol. 115, no. 16, pp. 1115–1128, 2015, doi: 10.1002/qua.24939.

[192] D. Zhu *et al.*, “Training of Quantum Circuits on a Hybrid Quantum Computer,” *Sci Adv*, vol. 5, pp. 1–22, 2019.

[193] K. Swersky *et al.*, “Taking the Human Out of the Loop : A Review of Bayesian Optimization Citation Taking the Human Out of the Loop : A Review of Bayesian Optimization,” *Proceedings of the IEEE*, vol. 104, no. 1, pp. 148–175, 2016, doi: 10.1109/JPROC.2015.2494218.

[194] A. Siegel, “Chapter 11 - Correlation and Regression: Measuring and Predicting Relationships,” in *Practical Business Statistics*, Seattle: Elsevier Inc., 2016, pp. 299–354. doi: https://doi.org/10.1016/B978-0-12-804250-2.00011-0.

[195] V. Kotu, “Chapter 4: Classification,” in *Predictive Analytics and Data Mining*, V. Kotu and B. Deshpande, Eds., Morgan Kaufmann, 2015, pp. 63–163. doi: 10.3109/00016926109176097.

[196] M.-S. Mushtaq and A. Mellouk, “Methodologies for Subjective Video Streaming QoE Assessment,” in *Quality of Experience Paradigm in Multimedia Services*, M.-S. Mushtaq and A. Mellouk, Eds., Elsevier, 2017, pp. 27–57. doi: 10.1016/b978-1-78548-109-3.50002-3.

[197] R. Gholami and N. Fakhari, “Support Vector Machine: Principles, Parameters, and Applications,” in *Handbook of Neural Computation*, P. Samui, S. Sekhar, and V. E. Balas, Eds., Elsevier Inc., 2017, pp. 515–535. doi: 10.1016/B978-0-12-811318-9.00027-2.

[198] J. R. Quinlan, “Induction of decision trees,” *Mach Learn*, vol. 1, no. 1, pp. 81–106, 1986, doi: 10.1007/bf00116251.

[199] S. Misra and H. Li, “Noninvasive fracture characterization based on the classification of sonic wave travel times,” in *Machine Learning for Subsurface Characterization*, S. Misra, H. Li, and J. He, Eds., Gulf Professional Publishing, 2020, pp. 243–287. doi: 10.1016/b978-0-12-817736-5.00009-0.

[200] W. Mao and F.-Y. Wang, “Cultural Modeling for Behavior Analysis and Prediction,” in *New Advances in Intelligence and Security Informatics*, W. Mao and F.-Y. Wang, Eds., Academic Press, 2012, pp. 91–102. doi: 10.1016/b978-0-12-397200-2.00008-7.

[201] C. Reinders, H. Ackermann, M. Y. Yang, and B. Rosenhahn, “Chapter 4 - Learning Convolutional Neural Networks for Object Detection with Very Little Training Data,” in *Multimodal Scene Understanding*, M. Y. Yang, B. Rosenhahn, and V. Murino, Eds., Academic Press, 2019, pp. 65–100. doi: 10.1016/B978-0-12-817358-9.00010-X.

[202] H. P. N. Nagarajan *et al.*, “Knowledge-based design of artificial neural network topology for additive manufacturing process modeling: A new approach and case study for fused

deposition modeling," *Journal of Mechanical Design, Transactions of the ASME*, vol. 141, no. 2, pp. 1–12, 2019, doi: 10.1115/1.4042084.

[203] Z. Jin, Z. Zhang, and G. X. Gu, "Autonomous in-situ correction of fused deposition modeling printers using computer vision and deep learning," *Manuf Lett*, vol. 22, pp. 11–15, 2019, doi: 10.1016/j.mfglet.2019.09.005.

[204] S. A. Singh and K. A. Desai, "Automated surface defect detection framework using machine vision and convolutional neural networks," *J Intell Manuf*, 2022, doi: 10.1007/s10845-021-01878-w.

[205] T. P. Nguyen, S. Choi, S. J. Park, S. H. Park, and J. Yoon, "Inspecting Method for Defective Casting Products with Convolutional Neural Network (CNN)," *International Journal of Precision Engineering and Manufacturing - Green Technology*, vol. 8, no. 2, pp. 583–594, 2021, doi: 10.1007/s40684-020-00197-4.

[206] R. Gove and J. Faytong, "Machine Learning and Event-Based Software Testing: Classifiers for Identifying Infeasible GUI Event Sequences," in *Advances in Computers*, vol. 86, A. Hurson and A. Memon, Eds., Elsevier, 2012, pp. 109–135. doi: 10.1016/B978-0-12-396535-6.00004-1.

[207] J. Verrelst *et al.*, "Optical remote sensing and the retrieval of terrestrial vegetation bio-geophysical properties - A review," *ISPRS Journal of Photogrammetry and Remote Sensing*, vol. 108, pp. 273–290, 2015, doi: 10.1016/j.isprsjprs.2015.05.005.

[208] J. Wu, X. C. Hao, Z. L. Xiong, and H. Lei, "Hyperparameter Optimization for Machine Learning Models Based on Bayesian Optimization," *Journal of Electronic Science and Technology*, vol. 17, no. 1, pp. 26–40, 2019, doi: 10.11989/JEST.1674-862X.80904120.

[209] V. Nguyen and U. Kingdom, "Bayesian Optimization for Accelerating Hyper-parameter Tuning," in *IEEE Second International Conference on Artificial Intelligence and Knowledge Engineering (AIKE)*, Sardinia: IEEE, 2019. doi: 10.1109/AIKE.2019.00060.

[210] L. Zhang and B. Zhang, "Hierarchical Machine Learning – A Learning Methodology Inspired by Human Intelligence," in *Rough Sets and Knowledge Technology*, G. Wang, J. F.Peters, A. Skowron, and Y. Yao, Eds., Springer, 2006, pp. 28–30. doi: 10.1007/11595014_1.

[211] S. Subendran, "Using Natural Language Processing to Detect Breast Cancer Recurrence in Clinical Notes : A Hierarchical Machine Learning Approach," Masters thesis, University of Waterloo, 2021.

[212] Y. Jiang and Z. P. Jiang, “Robust adaptive dynamic programming and feedback stabilization of nonlinear systems,” *IEEE Trans Neural Netw Learn Syst*, vol. 25, no. 5, pp. 882–893, 2014, doi: 10.1109/TNNLS.2013.2294968.

[213] A. Cropper, S. Dumančić, R. Evans, and S. H. Muggleton, “Inductive logic programming at 30,” *Mach Learn*, vol. 111, no. 1, pp. 147–172, 2022, doi: 10.1007/s10994-021-06089-1.

[214] S. K. Panigrahy and K.-N. Chiang, “Study on an Artificial Intelligence Based Kernel Ridge Regression Algorithm for Wafer Level Package Reliability Prediction,” in *71st Electronic Components and Technology Conference (ECTC)*, IEEE, 2021, pp. 1435–1441. doi: 10.1109/ectc32696.2021.00229.

[215] A. Khadilkar, J. Wang, and R. Rai, “Deep learning–based stress prediction for bottom-up SLA 3D printing process,” *International Journal of Advanced Manufacturing Technology*, vol. 102, no. 5–8, pp. 2555–2569, 2019, doi: 10.1007/s00170-019-03363-4.

[216] J. Freiesleben, J. Keim, and M. Grutsch, “Machine learning and Design of Experiments: Alternative approaches or complementary methodologies for quality improvement?,” *Qual Reliab Eng Int*, no. August 2019, pp. 1–12, 2020, doi: 10.1002/qre.2579.

[217] A. Konrad Paul Kording, Ari S. Benjamin, Roozbeh Farhoodi and J. I. Glaser, “The Roles of Machine Learning in Biomedical Science,” in *Frontiers of Engineering*, National Academy of Sciences, 2017, pp. 61–71. doi: 10.17226/24906.

[218] R. Arboretti, R. Ceccato, L. Pegoraro, and L. Salmaso, “Design of Experiments and machine learning for product innovation: A systematic literature review,” *Qual Reliab Eng Int*, vol. 38, no. 2, pp. 1131–1156, 2021, doi: 10.1002/qre.3025.

[219] L. Khoshnevisan, F. Hourfar, F. Alhameli, and A. Elkamel, “Combining design of experiments, machine learning, and principal component analysis for predicting energy consumption and product quality of a natural gas processing plant,” *Int J Energy Res*, vol. 45, no. 4, pp. 5974–5987, 2021, doi: 10.1002/er.6217.

[220] J. Huang, L. J. Segura, T. Wang, G. Zhao, H. Sun, and C. Zhou, “Unsupervised learning for the droplet evolution prediction and process dynamics understanding in inkjet printing,” *Addit Manuf*, vol. 35, no. March, p. 101197, 2020, doi: 10.1016/j.addma.2020.101197.

[221] F. Olsson, “A literature survey of active machine learning in the context of natural language processing,” Kista, 2009.

[222] M. Duquesnoy, T. Lombardo, M. Chouchane, E. N. Primo, and A. A. Franco, “Data-driven assessment of electrode calendering process by combining experimental results, in silico

mesostructures generation and machine learning," *J Power Sources*, vol. 480, p. 229103, 2020, doi: 10.1016/j.jpowsour.2020.229103.

[223] A. L. Facklam, L. R. Volpatti, and D. G. Anderson, "Biomaterials for Personalized Cell Therapy," *Advanced Materials*, vol. 32, no. 13, 2020, doi: 10.1002/adma.201902005.

[224] S. V. Murphy and A. Atala, "3D bioprinting of tissues and organs," *Nat Biotechnol*, vol. 32, no. 8, pp. 773–785, 2014, doi: 10.1038/nbt.2958.

[225] X. Lin, S. Patil, Y. G. Gao, and A. Qian, "The Bone Extracellular Matrix in Bone Formation and Regeneration," *Front Pharmacol*, vol. 11, no. May, pp. 1–15, 2020, doi: 10.3389/fphar.2020.00757.

[226] L. Li, M. Zhao, J. Li, Y. Zuo, Q. Zou, and Y. Li, "Preparation and cell infiltration of lotus-type porous nano-hydroxyapatite/polyurethane scaffold for bone tissue regeneration," *Mater Lett*, vol. 149, pp. 25–28, 2015, doi: 10.1016/j.matlet.2015.02.106.

[227] K. Kobayashi *et al.*, "Osteoconductive property of a mechanical mixture of octacalcium phosphate and amorphous calcium phosphate," *ACS Appl Mater Interfaces*, vol. 6, no. 24, pp. 22602–22611, 2014, doi: 10.1021/am5067139.

[228] Z. Li, T. Du, C. Ruan, and X. Niu, "Bioinspired mineralized collagen scaffolds for bone tissue engineering," May 01, 2021, *KeAi Communications Co.* doi: 10.1016/j.bioactmat.2020.11.004.

[229] H. J. Lee *et al.*, "A New Approach for Fabricating Collagen/ECM-Based Bioinks Using Preosteoblasts and Human Adipose Stem Cells," *Adv Healthc Mater*, vol. 4, no. 9, pp. 1359–1368, 2015, doi: 10.1002/adhm.201500193.

[230] W. K. and G. Kim, "Collagen/bioceramic-based composite bioink to fabricate a porous 3D hASCs-laden structure for bone tissue regeneration," *Biofabrication*, pp. 0–31, 2019.

[231] M. G. Yeo and G. H. Kim, "A cell-printing approach for obtaining hASC-laden scaffolds by using a collagen/polyphenol bioink," *Biofabrication*, vol. 9, no. 2, 2017, doi: 10.1088/1758-5090/aa6997.

[232] J. U. Lee, M. Yeo, W. J. Kim, Y. W. Koo, and G. H. Kim, "Development of a tannic acid cross-linking process for obtaining 3D porous cell-laden collagen structure," *Int J Biol Macromol*, vol. 110, pp. 497–503, 2018, doi: 10.1016/j.ijbiomac.2017.10.105.

[233] E. Mancha Sánchez *et al.*, "Hydrogels for Bioprinting: A Systematic Review of Hydrogels Synthesis, Bioprinting Parameters, and Bioprinted Structures Behavior," *Front Bioeng Biotechnol*, vol. 8, no. August, 2020, doi: 10.3389/fbioe.2020.00776.

[234] F. H. Heijmen, J. S. Du Pont, E. Middelkoop, R. W. Kreisn, and M. J. Hoekstra, "Cross-linking of dermal sheep collagen with tannic acid," *Biomaterials*, vol. 18, no. 10, pp. 749–754, 1997, doi: 10.1016/S0142-9612(96)00202-5.

[235] W. C. Chin, "Transient, Three-Dimensional, Multiphase Pipe and Annular Flow," in *Managed Pressure Drilling*, Elsevier, 2012, pp. 315–385. doi: 10.1016/b978-0-12-385124-6.00009-5.

[236] J. M. Crook Editor, "3D Bioprinting Principles and Protocols." [Online]. Available: http://www.springer.com/series/7651

[237] A. Habib, V. Sathish, S. Mallik, and B. Khoda, "3D printability of alginate-carboxymethyl cellulose hydrogel," *Materials*, vol. 11, no. 3, 2018, doi: 10.3390/ma11030454.

[238] V. Guarino, F. Causa, and L. Ambrosio, "Porosity and mechanical properties relationship in PCL porous scaffolds," *Journal of Applied Biomaterials and Biomechanics*, vol. 5, no. 3, pp. 149–157, 2007, doi: 10.1177/228080000700500303.

[239] G. S. Offeddu, J. C. Ashworth, R. E. Cameron, and M. L. Oyen, "Structural determinants of hydration, mechanics and fluid flow in freeze-dried collagen scaffolds," *Acta Biomater*, vol. 41, pp. 193–203, 2016, doi: 10.1016/j.actbio.2016.05.024.

[240] E. Peon, G. Fuentes, J. A. Delgado, L. Morejon, A. Almirall, and R. García, "PREPARATION AND CHARACTERIZATION OF POROUS BLOCKS OF SYNTHETIC HYDROXYAPATITE," 2004.

[241] J. H. Muyonga, C. G. B. Cole, and K. G. Duodu, "Fourier transform infrared (FTIR) spectroscopic study of acid soluble collagen and gelatin from skins and bones of young and adult Nile perch (Lates niloticus)," *Food Chem*, vol. 86, no. 3, pp. 325–332, Jul. 2004, doi: 10.1016/j.foodchem.2003.09.038.

[242] V. Natarajan, N. Krithica, B. Madhan, and P. K. Sehgal, "Preparation and properties of tannic acid cross-linked collagen scaffold and its application in wound healing," *J Biomed Mater Res B Appl Biomater*, vol. 101, no. 4, pp. 560–567, 2013, doi: 10.1002/jbm.b.32856.

[243] S. Kyle, Z. M. Jessop, A. Al-Sabah, and I. S. Whitaker, "'Printability'' of Candidate Biomaterials for Extrusion Based 3D Printing: State-of-the-Art,'" Aug. 23, 2017, *Wiley-VCH Verlag*. doi: 10.1002/adhm.201700264.

[244] L. Ouyang, R. Yao, Y. Zhao, and W. Sun, "Effect of bioink properties on printability and cell viability for 3D bioplotting of embryonic stem cells," *Biofabrication*, vol. 8, no. 3, Sep. 2016, doi: 10.1088/1758-5090/8/3/035020.

[245] J. U. Lee, M. Yeo, W. J. Kim, Y. W. Koo, and G. H. Kim, “Development of a tannic acid cross-linking process for obtaining 3D porous cell-laden collagen structure,” *Int J Biol Macromol*, vol. 110, pp. 497–503, 2018, doi: 10.1016/j.ijbiomac.2017.10.105.

[246] C. Gao, S. Peng, P. Feng, and C. Shuai, “Bone biomaterials and interactions with stem cells,” Dec. 21, 2017, *Sichuan University*. doi: 10.1038/boneres.2017.59.

[247] Y. W. Koo, E. J. Choi, J. Y. Lee, H. J. Kim, G. H. Kim, and S. H. Do, “3D printed cell-laden collagen and hybrid scaffolds for in vivo articular cartilage tissue regeneration,” *Journal of Industrial and Engineering Chemistry*, vol. 66, pp. 343–355, Oct. 2018, doi: 10.1016/j.jiec.2018.05.049.

[248] W. J. Kim, H. S. Yun, and G. H. Kim, “An innovative cell-laden α-TCP/collagen scaffold fabricated using a two-step printing process for potential application in regenerating hard tissues,” *Sci Rep*, vol. 7, no. 1, Dec. 2017, doi: 10.1038/s41598-017-03455-9.

[249] R. A. Perez and G. Mestres, “Role of pore size and morphology in musculo-skeletal tissue regeneration,” Apr. 01, 2016, *Elsevier Ltd*. doi: 10.1016/j.msec.2015.12.087.

[250] J. Dong, H. Ding, Q. Wang, and L. Wang, “A 3D-Printed Scaffold for Repairing Bone Defects,” Mar. 01, 2024, *Multidisciplinary Digital Publishing Institute (MDPI)*. doi: 10.3390/polym16050706.

[251] D. J. Choi, S. J. Park, B. K. Gu, Y. J. Kim, S. Chung, and C. H. Kim, “Effect of the pore size in a 3D bioprinted gelatin scaffold on fibroblast proliferation,” *Journal of Industrial and Engineering Chemistry*, vol. 67, pp. 388–395, Nov. 2018, doi: 10.1016/j.jiec.2018.07.013.

[252] A. Serhiienko, T. Dontsova, O. Yanushevska, A. Lapinskyi, and G. Krymets, “Synthesis and characterization of hydroxyapatite and composite based on it with collagen/alginate,” *Chemical Papers*, vol. 76, no. 1, pp. 385–392, Jan. 2022, doi: 10.1007/s11696-021-01841-2.

[253] R. Rasouli, C. Sweeney, and J. P. Frampton, “Heterogeneous and Composite Bioinks for 3D-Bioprinting of Complex Tissue,” *Biomedical Materials & Devices*, Mar. 2024, doi: 10.1007/s44174-024-00171-7.

[254] C. Guo, J. Wu, Y. Zeng, and H. Li, “Construction of 3D bioprinting of HAP/collagen scaffold in gelation bath for bone tissue engineering,” *Regen Biomater*, vol. 10, 2023, doi: 10.1093/rb/rbad067.

[255] J. Loskot *et al.*, “Influence of print speed on the microstructure, morphology, and mechanical properties of 3D-printed PETG products,” *Polym Test*, vol. 123, Jun. 2023, doi: 10.1016/j.polymertesting.2023.108055.

[256] K. Zhou, F. A. Azaman, Z. Cao, M. Brennan Fournet, and D. M. Devine, “Bone Tissue Engineering Scaffold Optimisation through Modification of Chitosan/Ceramic Composition,” *Macromol*, vol. 3, no. 2, pp. 326–342, Jun. 2023, doi: 10.3390/macromol3020021.

[257] N. B. Allen, B. Abar, L. Johnson, J. Burbano, R. M. Danilkowicz, and S. B. Adams, “3D-bioprinted GelMA-gelatin-hydroxyapatite osteoblast-laden composite hydrogels for bone tissue engineering,” *Bioprinting*, vol. 26, Jun. 2022, doi: 10.1016/j.bprint.2022.e00196.

[258] H. Sung, C. Meredith, C. Johnson, and Z. S. Galis, “The effect of scaffold degradation rate on three-dimensional cell growth and angiogenesis,” *Biomaterials*, vol. 25, pp. 5735–5742, 2004, doi: 10.1016/j.biomaterials.2004.01.066.

[259] H. Mao *et al.*, “Progress in Natural Science : Materials International Recent advances and challenges in materials for 3D bioprinting,” *Progress in Natural Science: Materials International*, vol. 30, no. 5, pp. 618–634, 2020, doi: 10.1016/j.pnsc.2020.09.015.

[260] R. T. Tran, E. Naseri, A. Kolasnikov, X. Bai, and J. Yang, “A new generation of sodium chloride porogen for tissue engineering,” *Biotechnol Appl Biochem*, vol. 58, no. 5, pp. 335–344, Sep. 2011, doi: 10.1002/bab.44.

[261] F. Buchanan, *Degradation Rate of Bioresorbable Materials: Prediction and Evaluation*, Illustrate. Elsevier, 2008. doi: https://doi.org/10.1016/B978-1-84569-329-9.50016-2.

[262] L. Zeng, X. Deng, and J. Yang, “Constrained hierarchical modeling of degradation data in tissue-engineered scaffold fabrication,” *IIE Transactions (Institute of Industrial Engineers)*, vol. 48, no. 1, pp. 16–33, 2016, doi: 10.1080/0740817X.2015.1019164.

[263] E. Entekhabi, M. Haghbin Nazarpak, M. Sedighi, and A. Kazemzadeh, “Predicting degradation rate of genipin cross-linked gelatin scaffolds with machine learning,” *Materials Science and Engineering C*, vol. 107, no. June 2019, p. 110362, 2020, doi: 10.1016/j.msec.2019.110362.

[264] A. L. S. Meirelles, T. Kurc, J. Kong, R. Ferreira, and J. H. Saltz, “Building Efficient CNN Architectures for Histopathology Images Analysis : A Case-Study in Tumor-Infiltrating Lymphocytes Classification,” vol. 9, no. May, pp. 1–10, 2022, doi: 10.3389/fmed.2022.894430.

[265] P. Stavroulakis *et al.*, “Rapid tracking of extrinsic projector parameters in fringe projection using machine learning,” *Opt Lasers Eng*, vol. 114, no. April 2018, pp. 7–14, 2019, doi: 10.1016/j.optlaseng.2018.08.018.

[266] G. Litjens *et al.*, “A survey on deep learning in medical image analysis,” *Med Image Anal*, vol. 42, no. December 2012, pp. 60–88, 2017, doi: 10.1016/j.media.2017.07.005.

[267] P. Malhotra, S. Gupta, D. Koundal, A. Zaguia, and W. Enbeyle, “Deep Neural Networks for Medical Image Segmentation,” *Healthcare Engineering*, 2022.

[268] R. Yamashita, M. Nishio, R. Kinh, G. Do, and K. Togashi, “Convolutional neural networks : an overview and application in radiology,” pp. 611–629, 2018.

[269] N. Alqahtani, F. Alzubaidi, R. T. Armstrong, P. Swietojanski, and P. Mostaghimi, “Machine learning for predicting properties of porous media from 2d X-ray images,” *J Pet Sci Eng*, vol. 184, Jan. 2020, doi: 10.1016/j.petrol.2019.106514.

[270] C. L. Reedy and C. L. Reedy, “High-resolution micro-CT with 3D image analysis for porosity characterization of historic bricks,” *Herit Sci*, vol. 10, no. 1, pp. 1–22, 2022, doi: 10.1186/s40494-022-00723-4.

[271] N. Alqahtani, F. Alzubaidi, R. T. Armstrong, P. Swietojanski, and P. Mostaghimi, “Journal of Petroleum Science and Engineering Machine learning for predicting properties of porous media from 2d X-ray images,” *J Pet Sci Eng*, vol. 184, no. March 2019, p. 106514, 2020, doi: 10.1016/j.petrol.2019.106514.

[272] H. Yong, R. Maruta, D. Huanca, and W. Salcedo, “Correlation-based multi-shape granulometry with application in porous silicon nanomaterial characterization,” *Porous Materials*, vol. 20, pp. 375–385, 2013, doi: 10.1007/s10934-012-9607-9.

[273] G. Lo Re, F. Lopresti, G. Petrucci, and R. Scaffaro, “A facile method to determine pore size distribution in porous scaffold by using image processing,” vol. 76, pp. 37–45, 2015, doi: 10.1016/j.micron.2015.05.001.

[274] N. Hojat, P. Gentile, A. M. Ferreira, and L. Šiller, “Automatic pore size measurements from scanning electron microscopy images of porous scaffolds,” *Journal of Porous Materials*, vol. 30, no. 1, pp. 93–101, 2023, doi: 10.1007/s10934-022-01309-y.

[275] H. Zhang, L. Zhou, and W. Zhang, “Control of scaffold degradation in tissue engineering: A review,” *Tissue Eng Part B Rev*, vol. 20, no. 5, pp. 492–502, 2014, doi: 10.1089/ten.teb.2013.0452.

[276] Y. Hu *et al.*, “Performance Degradation Prediction Using LSTM with Optimized Parameters,” *Sensors*, vol. 22, no. 6, Mar. 2022, doi: 10.3390/s22062407.

[277] N. Ding, H. Li, Z. Yin, N. Zhong, and L. Zhang, “Journal bearing seizure degradation assessment and remaining useful life prediction based on long short-term memory neural

network," *Measurement (Lond)*, vol. 166, Dec. 2020, doi: 10.1016/j.measurement.2020.108215.

[278] B. Zhang, S. Zhang, and W. Li, "Bearing performance degradation assessment using long short-term memory recurrent network," *Comput Ind*, vol. 106, pp. 14–29, Apr. 2019, doi: 10.1016/j.compind.2018.12.016.

[279] W. Nash, T. Drummond, and N. Birbilis, "A review of deep learning in the study of materials degradation," Dec. 01, 2018, *Nature*. doi: 10.1038/s41529-018-0058-x.

[280] B. Barros, P. Lacerda, C. Albuquerque, and A. Conci, "Pulmonary COVID-19: Learning spatiotemporal features combining CNN and LSTM networks for lung ultrasound video classification," *Sensors*, vol. 21, no. 16, Aug. 2021, doi: 10.3390/s21165486.

[281] D. Bychkov *et al.*, "Deep learning based tissue analysis predicts outcome in colorectal cancer," *Sci Rep*, vol. 8, no. 1, Dec. 2018, doi: 10.1038/s41598-018-21758-3.

[282] A. Younis, L. Qiang, C. O. Nyatega, M. J. Adamu, and H. B. Kawuwa, "Brain Tumor Analysis Using Deep Learning and VGG-16 Ensembling Learning Approaches," *Applied Sciences (Switzerland)*, vol. 12, no. 14, Jul. 2022, doi: 10.3390/app12147282.

[283] O. Russakovsky *et al.*, "ImageNet Large Scale Visual Recognition Challenge," Sep. 2014, [Online]. Available: http://arxiv.org/abs/1409.0575

[284] P. Gayathri, A. Dhavileswarapu, S. Ibrahim, R. Paul, and R. Gupta, "Exploring the Potential of VGG-16 Architecture for Accurate Brain Tumor Detection Using Deep Learning," *Journal of Computers, Mechanical and Management*, vol. 2, no. 2, Jun. 2023, doi: 10.57159/gadl.jcmm.2.2.23056.

[285] G. I. Kontogianni *et al.*, "Promotion of In Vitro Osteogenic Activity by Melt Extrusion-Based PLLA/PCL/PHBV Scaffolds Enriched with Nano-Hydroxyapatite and Strontium Substituted Nano-Hydroxyapatite," *Polymers (Basel)*, vol. 15, no. 4, Feb. 2023, doi: 10.3390/polym15041052.

[286] C. Tomasina *et al.*, "Incorporation of strontium-containing bioactive particles into PEOT/PBT electrospun scaffolds for bone tissue regeneration," *Biomaterials Advances*, vol. 149, Jun. 2023, doi: 10.1016/j.bioadv.2023.213406.

[287] F. Banche-Niclot *et al.*, "Optimization of an Injectable, Resorbable, Bioactive Cement Able to Release the Anti-Osteoclastogenic Biomolecule ICOS-Fc for the Treatment of Osteoporotic Vertebral Compression Fractures," *Biomolecules*, vol. 13, no. 1, Jan. 2023, doi: 10.3390/biom13010094.

[288] “INTERNATIONAL STANDARD ISO 5833 Implants for surgery-Acrylic resin cements,” 2002.

[289] G. Bradsky, “OpenCv.” Accessed: Apr. 04, 2022. [Online]. Available: https://opencv.org/license/

[290] S. van der Walt, “sickit-image.” Accessed: Mar. 27, 2022. [Online]. Available: https://scikit-image.org/

[291] M. I. Echeverria Molina, K. G. Malollari, and K. Komvopoulos, “Design Challenges in Polymeric Scaffolds for Tissue Engineering,” Jun. 14, 2021, *Frontiers Media S.A.* doi: 10.3389/fbioe.2021.617141.

[292] A. C. Jones, C. H. Arns, A. P. Sheppard, D. W. Hutmacher, B. K. Milthorpe, and M. A. Knackstedt, “Assessment of bone ingrowth into porous biomaterials using MICRO-CT,” *Biomaterials*, vol. 28, no. 15, pp. 2491–2504, May 2007, doi: 10.1016/j.biomaterials.2007.01.046.

[293] S. Rosenhain, Z. A. Magnuska, G. G. Yamoah, W. Al Rawashdeh, F. Kiessling, and F. Gremse, “A preclinical micro-computed tomography database including 3D whole body organ segmentations,” *Sci Data*, vol. 5, 2018, doi: 10.1038/sdata.2018.294.

[294] S. T. Ho and D. W. Hutmacher, “A comparison of micro CT with other techniques used in the characterization of scaffolds,” Mar. 2006. doi: 10.1016/j.biomaterials.2005.08.035.

[295] O. Gauthier *et al.*, “In vivo bone regeneration with injectable calcium phosphate biomaterial: A three-dimensional micro-computed tomographic, biomechanical and SEM study,” *Biomaterials*, vol. 26, no. 27, pp. 5444–5453, 2005, doi: 10.1016/j.biomaterials.2005.01.072.

[296] F. Peyrin, “Evaluation of bone scaffolds by micro-CT,” in *Osteoporosis International*, Jun. 2011, pp. 2043–2048. doi: 10.1007/s00198-011-1609-y.

[297] Y. Lecun, Y. Bengio, and G. Hinton, “Deep learning,” May 27, 2015, *Nature Publishing Group*. doi: 10.1038/nature14539.

[298] A. Suwardi *et al.*, “Machine Learning-Driven Biomaterials Evolution,” Jan. 01, 2022, *John Wiley and Sons Inc*. doi: 10.1002/adma.202102703.

[299] E. Vincenzi *et al.*, “A fully automated deep learning pipeline for micro-CT-imaging-based densitometry of lung fibrosis murine models,” *Respir Res*, vol. 23, no. 1, Dec. 2022, doi: 10.1186/s12931-022-02236-x.

# Appendix A

## Plus test G-code

```
G90
G0 Z30
G0 X0 Y0
G0 Z0.40
T0
G1 Z0.4 F800
G0 X5 Y
M760;
G1 X-5 E1
M761;
```

```
G0 X0.5 Y6
G1 Z0.8 F800
M760;
G1 Y-6 E9
M761;
M84 ;disable motors
;END
```

# Appendix- B

Table 1.B: Initial design layout produced from DoE software for COL ink formulation (Study 1)

| | Factors | | | | Responses | |
|---|---|---|---|---|---|---|
| | A | B | C | D | R1 | R2 |
| Run | Collagen %(w/v) | Tannic acid %(w/v) | Crosslinking time min | Needle size G | Printing pressure kPa | Young's modulus MPa |
| 1 | 4 | 5 | 37.5 | 21 | 185 | 0.0716 |
| 2 | 4 | 5 | 37.5 | 23 | 326 | 0.0823 |
| 3 | 4 | 5 | 60 | 22 | 309 | 0.0896 |
| 4 | 4 | 5 | 15 | 22 | 332 | 0.0225 |
| 5 | 4 | 4 | 37.5 | 22 | 313 | 0.0702 |

| | | | | | | |
|---|---|---|---|---|---|---|
| **6** | 4 | 6 | 37.5 | 22 | 302 | 0.1263 |
| **7** | 5 | 5 | 37.5 | 22 | 337 | 0.0800 |
| **8** | 5 | 6 | 60 | 22 | 364 | 0.1207 |
| **9** | 5 | 5 | 37.5 | 22 | 400 | 0.0947 |
| **10** | 5 | 4 | 37.5 | 21 | 251 | 0.0602 |
| **11** | 5 | 4 | 37.5 | 23 | 330 | 0.0746 |
| **12** | 5 | 4 | 60 | 22 | 306 | 0.0994 |
| **13** | 5 | 5 | 37.5 | 22 | 373 | 0.1086 |
| **14** | 5 | 5 | 60 | 23 | 340 | 0.1198 |
| **15** | 5 | 6 | 15 | 22 | 322 | 0.0750 |
| **16** | 5 | 5 | 37.5 | 22 | 336 | 0.0784 |
| **17** | 5 | 6 | 37.5 | 21 | 241 | 0.0826 |
| **18** | 5 | 5 | 60 | 21 | 212 | 0.0703 |
| **19** | 5 | 4 | 15 | 22 | 336 | 0.0460 |
| **20** | 5 | 5 | 37.5 | 22 | 369 | 0.0935 |
| **21** | 5 | 5 | 15 | 21 | 270 | 0.0560 |
| **22** | 5 | 5 | 15 | 23 | 381 | 0.0673 |
| **23** | 5 | 6 | 37.5 | 23 | 354 | 0.0699 |
| **24** | 6 | 5 | 37.5 | 23 | 373 | 0.0633 |
| **25** | 6 | 4 | 37.5 | 22 | 306 | 0.0503 |
| **26** | 6 | 5 | 37.5 | 21 | 263 | 0.0864 |
| **27** | 6 | 6 | 37.5 | 22 | 298 | 0.0967 |
| **28** | 6 | 5 | 60 | 22 | 337 | 0.1508 |
| **29** | 6 | 5 | 15 | 22 | 307 | 0.0218 |

Table 2.B: Initial design layout produced from DoE software for printing parameters optimisation for COL/HA ink (Study 2)

| | Factors | | | Responses | | | |
|---|---|---|---|---|---|---|---|
| | **A** | **B** | **C** | **R1** | **R2** | **R3** | |
| **Run** | **HA concentration %(w/v)** | **Layers no.** | **Printing speed mm/s** | **Pressure kPa** | **Degradation %** | **Young's modulus MPa** | **Por n** |
| **1** | 0 | 10 | 1 | 56 | 73 | 0.985 | 0 |
| **2** | 0 | 5 | 3.5 | 78 | 71 | 0.953 | 0 |
| **3** | 0 | 10 | 6 | 101 | 74 | 0.976 | 0 |
| **4** | 0 | 15 | 3.5 | 76 | 79 | 1.103 | 0 |
| **5** | 0.05 | 10 | 3.5 | 99 | 54 | 1.961 | 0 |
| **6** | 0.05 | 5 | 1 | 68 | 51 | 1.205 | 0 |
| **7** | 0.05 | 15 | 6 | 121 | 55 | 1.98 | 0 |
| **8** | 0.05 | 10 | 3.5 | 95 | 57 | 1.78 | 0 |
| **9** | 0.05 | 5 | 6 | 125 | 49 | 1.201 | 0 |
| **10** | 0.05 | 10 | 3.5 | 95 | 54 | 1.78 | 0 |
| **11** | 0.05 | 10 | 3.5 | 97 | 54 | 1.69 | 0. |
| **12** | 0.05 | 15 | 1 | 66 | 59 | 1.89 | 0 |
| **13** | 0.05 | 10 | 3.5 | 97 | 55 | 1.73 | 0 |
| **14** | 0.1 | 15 | 3.5 | 66 | 51 | 2.436 | 0 |
| **15** | 0.1 | 10 | 6 | 92 | 55 | 2.054 | 0 |
| **16** | 0.1 | 5 | 3.5 | 63 | 54 | 2.08 | 0 |
| **17** | 0.1 | 10 | 1 | 24 | 56 | 2.2 | 0 |